Laser Ultrasonic Characterization of Contact Dynamics in Single- and Few-Layer Self-Assembled Microscale Granular Crystals

Amey Rajendra Khanolkar

A dissertation
submitted in partial fulfillment of the
requirements for the degree of

Doctor of Philosophy

University of Washington

2018

Reading Committee:

Nicholas S. Boechler, Chair

Peter H. Dahl

Jonathan T.C. Liu

Program Authorized to Offer Degree:
Mechanical Engineering

University of Washington

Abstract

Laser Ultrasonic Characterization of Contact Dynamics in Single- and Few-Layer Self-Assembled Microscale Granular Crystals

Amey Rajendra Khanolkar

Chair of the Supervisory Committee:

Professor Nicholas S. Boechler

Department of Mechanical Engineering

Materials with designed structural discreteness and local resonances have garnered significant interest in recent years due their ability to manipulate waves in new ways. A number of studies over the past decade have explored mechanical wave phenomena in one such system, composed of ordered, close-packed arrays of elastic particles in contact, referred to as 'granular crystals'. Proposed applications for such acoustic wave tailoring designer materials include vibration isolation, frequency-selective acoustic wave filtering, and acoustic wave guiding and focusing. Besides serving as a platform to gain new insight into the complex dynamic behavior of granular media, macroscale granular crystals (composed of millimeter- to centimeter-sized units) have also shown potential for use as such a designed composite material. Granular crystals also exhibit additional capabilities over some other types of other types of wave-tailoring designer materials, in that they exhibit a tunable dynamic response in the linear, weakly nonlinear and strongly nonlinear regimes to tailor acoustic waves. While macroscale granular crystals are designed to affect sonic frequency acoustic waves, extending granular crystals to the micro- and nanoscale has the potential to enable granular-based devices that operate at megahertz and gigahertz frequencies. In addition,

microscale granular crystals also serve as a platform for exploring and developing a more general class of high, frequency, and micro- to nanostructured designer wave-tailoring materials, wherein large-scale fabrication presents significant challenges. Micro- and nanoscale granular crystals, however, cannot be thought of as simply scaled down versions of their macroscale counterparts since effects such as adhesion between particles, which are negligible at the macroscale, become significant at reduced length scales, and can drastically alter the granular crystal dynamics. This thesis focuses on addressing open questions relating to the contact-based dynamics of self-assembled, single- and few-layer-thick microscale granular crystals using an experimentally-driven approach. Convective colloidal self-assembly techniques are used to fabricate mono- and multilayer granular crystals comprised of micron- and sub-micron-sized particles. The vibrational dynamics of the microparticle arrays and the interaction of the contact resonances of the particles with surface, bulk and Lamb waves are studied experimentally using photoacoustic techniques. The applicability of adhesive contact models at the microscale, including the effects of adhesion-induced plasticity, is also discussed. Novel mechanisms to tune the interparticle and particle-substrate contact stiffness via nanoscale solid bridges and local ablation of the contact zone are also explored. This work sheds new light on our understanding of the contact-based dynamics of micro- to nanoscale particles, and particle assemblies, and opens avenues for developing a new class of locally-resonant granular acoustic metamaterials with applications such as signal processing and ultrasonic wave imaging, and offers new insights into the mechanical properties of self-assembled materials.

TABLE OF CONTENTS

LIST OF FIGURES

LIST OF TABLES

DEDICATION

To my parents, for their infinite love and encouragement, and for giving me the wonderful gift of education;

To my sister Gauri, and brother-in-law, Hrishikesh, for being mentors at every step of the way.

ACKNOWLEDGMENTS

I'd like to express my immense and sincere gratitude to my advisor, Professor Nicholas Boechler, for giving me a chance, and for introducing me to the wonderful world of vibrations and phononics. Dr. Boechler's enthusiasm for research was infectious, and I have learned tremendously under his guidance over the past five years. I'd like to thank Dr. Boechler for giving me the freedom to explore different areas of research, listening to my ideas, and providing guidance at every step of the way. I am forever indebted to him for shaping me as a researcher.

I thank the members of my thesis committee: Professors Vincent Holmberg, Peter Dahl and Jonathan Liu. I found the few meetings with Dr. Holmberg and his group very insightful. Dr. Dahl's Mechanical Engineering Analysis was the first course I took as a student at the UW. It was always fascinating to learn from his examples of underwater acoustics while learning differential equations. Many thanks to Dr. Liu, and his wonderful Optics class, which helped me tremendously, particularly in the early part of my time in graduate school, when I was learning about various photoacoustic techniques. I sincerely appreciate the invaluable feedback provided by the members of the thesis committee towards improving the quality of this work. I would also like to thank the members of my qualifying exam committee, Professors Minoru Taya and Jae-Hyun Chung.

My sincere gratitude to Professor Nicolas Vogel, for providing invaluable guidance on colloidal self-assembly, and promptly answering my endless questions. I would also like to thank Professor Ashley Emery, who provided guidance on contact mechanics models and numer-

ical modeling techniques. My discussions with Dr. Emery have been very insightful. I'd like to thank Professor Keith Nelson and his group at MIT for the wonderful collaboration we have had throughout my time as a graduate student. My thanks to Dr. Alex Maznev, through whom I have learned immensely about experimental and analytical methods. Dr. Jeff Eliason, thank you very much for having me over at MIT, and for patiently teaching me the ropes of laser ultrasonic experiments. I'd also like to extend my gratitude to Dr. Alejandro Vega-Flick. I'd like to thank Professors Pierre Deymier and Pierre Lucas, under whose guidance I had the exciting opportunity to work on optically tunable materials. I would also like to thank Professor Arka Majumdar and his students, Jiajiu Zheng and Shane Colburn, for the opportunity to work on phase change materials. My thanks to Professor Vipin Kumar, and his students, Andrei Nicolae and Huimin Guo, for the opportunity to work on laser-induced foaming of plastics. Professor Junlan Wang and Melicent Stossel - it was a pleasure working with you on the microsphere spallation project.

A big thank you to all the members of the Boechler Research Group. Dr. Maroun Abi Ghanem - you have been a friend and mentor to be throughout, and I have been incredibly fortunate to work on several research projects under your guidance. I cannot thank you enough for your guidance both inside and outside the lab! To Sam Wallen and Morgan Hiraiwa, it has been an incredible honor of sharing the joys of being one of the first graduate students in the group with you. Thank you for your insightful discussions, and for always being available! To Samantha Hoang, Ariana Mendible, Morgan Bassford, and Apoorva Lele - thank you for making the lab such a fun place! I'd like to thank the numerous undergraduate students I had the privilege of mentoring and learning from: Jennifer Jenks, Henry Aller, Mary Helwig, Liam Potocsnack, Brittany Lydon, Cece Landau, Chloe McBurney, Suraj Bhosale, Radhika Apte and Vinod Ramakrishnan.

I'd like to thank the Mechanical Engineering Department for the immense support throughout my time as a graduate student. My thanks to Professor John Kramlich and Wanwisa Kisalang for their guidance with choosing courses and navigating the academic program. Bill Kuykendall and Michelle Hickener - thank you very much for all the equipment-related help. Several of the experiments described here wouldn't have been made possible without your guidance. Nancy Moses and Hazel Valdez, thank you for your help with purchasing and accounts, particularly in the initial phase of my research. I'd like to thank Dr. Mike Khbeis and the staff at the Washington Nanofabrication Facility, Dr. Darick Baker, Dr. Andy Lingley, and Dr. Rick Bojko in particular, for their help and training with the cleanroom fabrication aspects of this work. Many thanks to Dr. Micah Glaz and Dr. Liam Bradshaw at the Molecular Analysis Facility for training me on various metrology tools, and always being available for guidance.

I'd like to thank my mentors from Drexel: Professors Jonathan Awerbuch and Tein-Min Tan. I would not be in graduate school had you not introduced me to research, back when I was just a sophomore in college. Many thanks to Professor Didem Ozevin for her guidance towards the latter half of my time as a student at Drexel. Dr. John Bakuckas - thank you very much for being a mentor, and motivating me to always do my best. I'd also like to thank Dr. Andrew Bergan, Dr. Reewanshu Chadha, and Dr. Deepak Siromani for your guidance with approaching research.

I'd like to thank numerous friends who have made my time as a graduate school extremely fulfilling. To Sivaramakrishnan Natarajan Ramamoorthy and Karthik Iyer - I couldn't have asked for better roommates and friends. My thanks to Rajan Pawar, Armando Diaz Tolentino, Arvind Mallikeswaran, Arun Prashanth, Praveen Sekar, Prashanth Srikanthan, Amit Sonar, Tuhin Ghosh, Scott Roy, Aman Ved Kalia, Rishi Pahuja, Anamol Pundle, Aditya

Sankar, Iswar Patel, Abhishek De, Rajesh Chaunsali, Amir Amini, Mete Yurtoglu, David Schipf, Kapil Gangwar, Trevor Harrison, and many others, for being great friends, for the wonderful hikes and the fun-filled road-trips! My thanks to Ankit Gupta and Naveen Kumar Sharma for the intense squash matches at the IMA!

Above all, I would like to thank my parents, Rajendra and Sujata, and my sister, Gauri, and brother-in-law, Hrishikesh, for their constant encouragement, love and support. They have motivated me to put in my best effort as a student and as a researcher.

Chapter 1

INTRODUCTION

This thesis describes acoustic wave phenomena in granular crystals composed of single- and few-layer microscale particles in contact, and explores the potential of using microscale granular crystal systems to manipulate ultrasonic waves. This introduction briefly describes the motivation and historical setting for this research, some of the experimental and conceptual elements common to each of these projects, the significance of this work, and the organization of the thesis.

1.1 Motivation

The ability to control and manipulate electrons and photons has led to major technological revolutions that have transformed society and our daily lives. Control over the flow of electrons, fundamental subatomic particles, led to the discovery of electricity that powers numerous appliances and devices. The ability to control electrons in specific energy states in semiconductors has also formed the basis of modern semiconductor electronics that can be found in devices such as laptops, smartphones and tablets. Analogous control over photons, packets of light energy, has given birth to fields such as wireless communication, X-ray imaging and ultraviolet light therapy. The extent of photon-based technology development is evidenced by the successful management of photons over a wide range of the electromagnetic spectrum spanning over fourteen orders of magnitude in frequency. While technologies based on the control of electrons and photons are mature and ubiquitous in our daily lives, there

remains tremendous potential in developing devices that manipulate another fundamental component - the phonon [1].

The concept of phonons was introduced in 1930 by physicist Igor Tamm [14,15]. The phonon is a quantized packet of mechanical vibration responsible for the transmission of sound and heat, and can be considered an elastic/ vibration analog of photons in electromagnetic waves. Phonons are often designated as quasiparticles [16], and represent the normal vibrational modes of a lattice of atoms or molecules [17]. Phonons propagate through mechanical waves, i.e., waves that are an oscillation of matter, and therefore transfer energy through the medium. Mechanical waves can take different forms dependent on the medium of propagation (referred to as acoustic waves and elastic waves when propagating in fluids and solids, respectively) as well as the wavelength/frequency. In general, the wavelength of a mechanical wave is inversely proportional to the frequency. Low frequency waves typically propagate over long distances compared to higher frequency waves, which travel only relatively short distances. The mechanical wave spectrum, shown in Figure 1.1, encompasses waves ranging from the infrasound (frequency less than 1 Hz) such as seismic waves, sonic or "audible" waves (frequency between 20 Hz and 20 kHz), ultrasound (frequency between 20 kHz to 500 MHz), hypersound (frequency between 500 MHz to 100 GHz), and finally, heat (100 GHz to 100 THz) [1,2,18]. In crystalline solids, high-frequency, shorter-wavelength phonons, with wavelength on the order of the lattice constant, propagate via "lattice waves" and are associated with the transmission of heat in the material [19]. While phonons have been widely used to describe heat-carrying lattice waves [19], the concept of phonons has also been more generally used to describe the propagation of lower-frequency, longer-wavelength mechanical waves [1, 20]. The quantized energy states of an elastic vibrational mode of angular frequency ω are given by,

$$E_n = \left(n + \frac{1}{2}\right)\hbar\omega \tag{1.1}$$

where $\hbar$ is the reduced Planck constant, $(1/2)\hbar\omega$ is the minimum energy state of vibration (referred to as the zero-point energy), and $n = 0, 1, 2, ...,$ is the quantum number to which the mode is excited [20, 21]. We can see from Equation 1.1 that the energy states between adjacent modes, i.e., $\Delta n = \pm 1$, differ by $\Delta E = \pm\hbar\omega$. An exact amount of energy $\hbar\omega$ must be supplied to an atomic lattice vibrating at an angular frequency ω to excite it to the next energy level. Equation 1.1 also indicates that phonons, like photons, are not conserved and can be created or destroyed; phonons are created when atoms or molecules start to oscillate, and are destroyed when the oscillation stops.

Some of the most common techniques to control low frequency mechanical waves in the infrasonic and sonic regimes include the use of dissipative foams, and viscous and tuned mass dampers [22]. Mechanical waves in the ultrasonic regime are used in numerous settings such as in health care, for biomedical imaging devices and ultrasound therapy [23], in non-destructive evaluation of structures [24, 25], and even for surface cleaning and contaminant removal [26, 27]. Numerous electronic devices employ surface acoustic wave filters for signal processing that operate in the ultrasonic regime [28]. At the far end of the phonon spectrum, heat transport in both amorphous and crystalline dielectric solids is achieved via transfer of elastic vibrations of atoms in the lattice about their equilibrium position [29, 30].

Over the past three decades, there has been a rapidly growing interest in manipulating mechanical waves using materials engineered with designed structural discreteness and local resonances [1, 18, 31, 32]. The interaction of mechanical waves with the structural periodicty or local resonances in such materials, generally referred to as phononic structures [32], results in the dispersion of mechanical waves. Tailoring the dispersion of mechanical waves in phononic materials can give rise to frequency band gaps, ranges of frequencies where mechanical wave propagation is forbidden [1, 18], as well as pass bands with unique refractive properties such as negative refraction [31, 33–37]. Controlling mechanical waves using phononic materials could lead to devices that could bend earthquakes around cities [38–42],

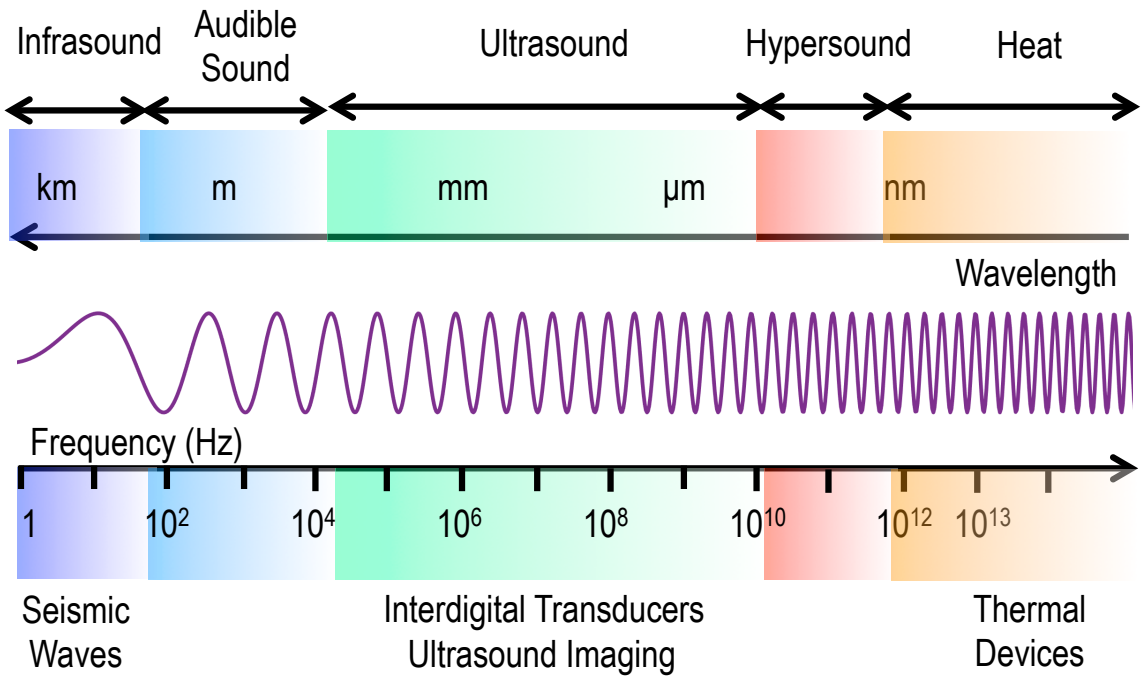

Figure 1.1: The mechanical wave spectrum. Adapted from [1, 2].

"cloak" military vehicles and soldiers from blast and shock waves [43], sound-proof buildings from certain frequencies [44], or even enhance thermoelectric devices to efficiently convert waste heat from our bodies into usable electricity [1, 45]. The introduction of nonlinearities in phononic materials can offer increased flexibility over mechanical wave control, including new ways to localize energy and convert energy between frequencies [32, 46].

Granular crystals have emerged as a promising type of phononic material for mechanical wave control [47]. Granular crystals are arrays of tightly packed solid particles that deform on contact with each other. The contact interactions between constitutive particles are nonlinear and are described by the Hertz theory of elastic contact, giving rise to a nonlinear effective constitutive response for granular media. [3,48]. The ability to tune the static precompression in macroscale granular crystals (composed of millimeter- to centimeter-sized units), coupled

with dispersion induced by structural discreteness, local resonances and nonlinearity has resulted in several interesting wave phenomena in the linear, weakly nonlinear and strongly nonlinear regimes. These include the demonstration of tunable frequency bandgaps [49, 50], discrete breathers [51] and nonlinear localized modes [52]. These novel wave phenomena in macroscale granular crystals have resulted in prototype devices for vibration filtering and tunable acoustic rectification [53], focusing acoustic waves to generate sound bullets [54], and absorb and attenuate impact energy [43, 55]. Downsizing granular crystals to the micron and sub-micron length scale brings potential to similarly control high frequency mechanical waves in the ultrasonic and hypersonic regimes [56]. However, microscale granular crystals cannot be treated as simply scaled down versions of their macroscale counterparts, since the relevant physics change drastically from the macro- to microscales. For instance, short-range adhesive forces between particles, that are negligible at macroscale, are several orders of magnitude stronger than gravity at microscale [57]. The balance of adhesive and contact forces between the particles in microscale granular crystals, as well as between the particles and the substrate, gives a characteristic stiffness to the interparticle and particle-substrate contacts which governs the dynamic response of the granular crystal. This thesis aims at addressing the open questions relating to the contact-based dynamics of microscale granular crystals, with the overall aim of developing granular crystal-based phononic materials for tailoring mechanical waves in the ultrasonic regime (MHz-GHz frequencies). Using a combination of colloidal self-assembly methods [58–61] to fabricate single- and few-layer microscale granular crystals, and photoacoustic techniques [62, 63] to excite and detect the vibrational resonances of the microparticle arrays, the contact behavior of isolated micron- and sub-micron-sized spheres adhered to substrates is also explored. The coupling of the vibrational resonances of microparticles to surface acoustic waves and Lamb waves, and methods to tune these resonances, are also studied in the context of developing tunable, locally-resonant phononic materials for ultrasonic wave control. The following sections provide a brief historical account of the development of phononic materials for mechanical wave control, followed by a review of the contact mechanics principles applicable to granular crystals for mechanical

wave tailoring.

1.1.1 Phononic Crystals and Acoustic Metamaterials

The earliest studies on mechanical waves in periodic structures can be traced back to the works of Newton in the seventeenth century [64] and to Rayleigh in the mid-twentieth century [65]. Although studies of wave propagation in periodic media began over a century ago [66], concepts concerning the use of artificially engineered periodic materials for mechanical wave control properties began to experience a resurgence in the early 1990s [32,67]. The development of 'phononic crystals', i.e., artificially structured composite materials composed of periodic inclusions used to control the propagation of elastic and acoustic waves, was inspired by progress made in their electromagnetic wave counterparts [32]. Phononic crystals are designed to control the dispersion of acoustic waves as they propagate through the medium, through a phenomenon known as Bragg scattering - the scattering of waves by a periodic arrangement of inclusions in a host medium with dimensions and periods comparable to the wavelength of the propagating wave [66]. The dispersion induced by periodicity in phononic crystals can be used to manipulate waves through unique ways, such as by the formation of absolute band-gaps - spectral bands where the propagation of waves is forbidden irrespective of the direction of propagation. Moreover, the presence of defects or voids in phononic crystals can result in mode localization [67]. The functionalities of phononic crystals can therefore be extended to applications in frequency filtering and wave-guiding.

Based on the characteristic dimensions and the length-scale of the periodicity in the medium, phononic crystals can be designed to control the propagation of elastic and acoustic waves with wavelengths ranging from the macroscale to the nanoscale. As stated previously, the mechanism of wave control in phononic crystals relies on spatially periodic variations in density and/or elasticity, and is analogous to the periodic variations of refractive index in pho-

tonic crystals, whose underlying concepts were independently proposed by Yablonovitch [68] and John [69] in the late 1980s [70]. The lattice parameter of a phononic crystal is inversely proportional to the band-gap center frequency, and as a result, the size of the phononic crystal unit cell dictates the band-gap frequency. Furthermore, structural periodicity and order are critical for the propagating waves to undergo Bragg interferences [71]. The position and width of the band gap depend on the direction of wave propagation since lattice parameter depends on the angle of incidence. Some phononic crystals form band gaps for waves propagating in any direction - these are known as absolute or complete band gaps. Other materials possess partial and gaps that only stop waves travelling in certain directions [18]. Also, the width of the band-gap is directly related to the ratio of the densities and sound velocities in the inclusions and the host medium - the larger the ratio, the wider the gap [18]. The audible sound filtering capability of a phononic crystal was first experimentally observed by researchers in 1995 in a minimalist sculpture designed by Eusebio Sempere in a park in Madrid, Spain [67, 72]. The phononic crystal in this study comprised of a two-dimensional periodic arrangement of steel tubes in air. With advances in nanofabrication and lithography techniques, phononic crystals have been developed to control hypersonic waves with gigahertz to terahertz frequencies [1]. Examples of hypersonic phononic crystals include lithographically etched periodic arrangements of 100 nm diameter holes in an epoxy layer [73] and self-assembled three-dimensional colloidal crystals consisting of monodisperse polystyrene nanospheres [74]. It is worth noting that these hypersonic phononic crystals were designed to tailor acoustic waves propagating in the air or fluid between the nanostructured inclusions, and did not undergo any interactions with the contact-based modes or intrinsic resonances of the nanometric elements themselves.

Just like the acoustics community drew inspiration from the optics and electromagnetic waves communities to develop phononic crystals with similar working principles as photonic crystals, studies focusing on the development of another class of composite materials for novel

acoustic and elastic wave tailoring strategies were based on innovations in the optics and electromagnetic waves communities [31, 32]. The composite materials for electromagnetic wave tailoring were termed as "metamaterials", and defined as "*macroscopic composites of periodic or non-periodic structure, whose function is both due to the cellular architecture and the chemical composition* [75]". Although several theoretical concepts of metamaterials for electromagnetic wave control were proposed as early as the 1960s [76, 77], the first experimental realization of metamaterial-based cloaks for electromagnetic waves at microwave frequencies was presented by Smith and coworkers in 2000 [78]. In the same year, Liu and coworkers presented a new class of sonic crystals that exhibited spectral gaps with lattice constants two orders of magnitude smaller than the relevant wavelength [79]. The 'sonic crystal' developed comprised of a three-dimensional cubic arrangement of centimeter-sized lead spheres, coated with a soft silicone layer, and embedded in a hard epoxy matrix. Measurements of sound transmission through the structure revealed attenuation dips associated with the resonance of the silicone-coated spheres. This observation of band-gaps in such materials, stemming from locally resonant structures within the host medium, gave birth to the study of a new class of composite materials for wave control, termed as 'acoustic metamaterials' [67]. In such materials, the wavelength of interest is much larger than the lattice constant of the structure and periodicity is not required for the formation of a band-gap. Acoustic metamaterials have been the subject of intense research due to their ability to design materials with tailorable local effective properties (such as density and modulus) that can be anisotropic, or even be zero or negative [32, 67]. Metamaterials with negative effective properties have been of particular interest due to their potential use as superlenses and cloaks. The architecture and constitutive resonant elements of acoustic metamaterials studied so far have differed drastically - a few examples include acoustic metamaterials comprising of arrays of soda-cans acting as Helmholtz resonators in the sonic regime [80, 81], to micron-sized locally-resonant pillars interacting with surface acoustic waves in the megahertz frequency regime [82–84]. Cummer and coworkers recently reviewed the progress and future directions in the field of acoustic metamaterials [31]. While acoustic metamaterials have shown promise

in manipulating waves over a broad frequency range, and act as frequency filters, cloaks, superlenses, and possess numerous other properties not found in naturally occurring materials, several challenges remain in the development of efficient techniques to fabricate metamaterial structures on a large-scale, particularly for those with micro- to nanoscale elements. These challenges have limited the conversion of laboratory-scale prototypes into useful devices [31]. Furthermore, while the majority of acoustic metamaterials studied so far are based on linear dynamics, the development of nonlinear metamaterials and phononic structures can offer potential for greater versatility in wave control with novel applications such as frequency conversion and acoustic rectification [85].

1.1.2 Nonlinear Acoustic Metamaterials

As stated previously, nonlinear metamaterials have the potential for greater versatility in wave control, owing to phenomena which may appear chaotic or counter-intuitive compared to those in linear systems [86]. Kivshar and coworkers first analyzed the nonlinear properties of an electromagnetic metamaterial, composed of a lattice of the split-ring resonators and wires with a nonlinear dielectric material, whose response could be switched based on the intensity of the macroscopic magnetic field [85]. The use of nonlinear effects in acoustic metamaterials is an emerging field study, where a number of recent studies have suggested the use of nonlinearity for acoustical applications [87]. Nonlinear phenomena have been employed in acoustic metamaterials for non-reciprocal (or one-way) wave propagation applications, analogous to the function of a semiconductor diode that permits the flow of electric current in only one direction. Liang and coworkers presented a numerical model of an acoustic diode formed by coupling a superlattice with a strong nonlinear medium [88, 89]. Fleury and coworkers introduced the acoustic analog of the Zeeman effect [90] in a metamaterial consisting of a resonant ring cavity biased by a circulating fluid [91]. The angular momentum bias from the circulating fluid split the rings azimuthal resonant modes, producing giant acoustic nonre-

ciprocity in the metamaterial. Popa and Cummer [92] presented an acoustic metamaterial with nonreciprocity using nonlinear electrically active components. Boechler and coworkers presented a concept of an acoustic rectifier based on an array of one-dimensional array of particles in contact, that contained a light mass defect particle near the boundary [93]. As a result of the defect, vibrations at select frequencies caused bifurcations and jumped to chaotic states with broadband frequency content [93]. In addition to applications in nonreciprocal wave propagation, nonlinear phenomena have also been utilized in acoustic metamaterials for other applications, such as high-intensity sound focusing [54], and in materials with a reconfigurable and reprogrammable dynamic response [94, 95]. Reviews on the development of nonlinear acoustic metamaterials are presented in references [31, 87, 96].

1.1.3 Granular Crystals as Nonlinear Acoustic Metamaterials and Phononic Crystals

Granular media, which are aggregates of elastic particles, are ubiquitous in nature [48, 97]. Common examples of granular media include sand, rocks, grains, seeds and powders. Granular materials are widely used in a variety of industries such as in mining, pharmaceuticals, and powder processing [97]. Granular media are also studied in geophysics, to understand the mechanics of avalanche formation, sedimentation of soil, propagation of seismic waves [98], and even the formation of planets [99]. Granular media are known to support a rich array of acoustic phenomena that stem from the interactions between constituent particles in the medium [48]. They have also generated significant interest in applications involving impulse and shock wave mitigation, as is seen by the use of granular beds of iron shot for damping high-amplitude shocks in explosive chambers [48]. Despite the prevalence of granular media in nature and their vast industrial applications, the physics of granular is extremely complex and not completely understood. An example of the unique behavior of granular media is their rate and amplitude dependence, for instance, sand-bags can effectively stop a bullet, yet, a pencil can be slowly pushed through the very same sand-bag. Some researchers have also sug-

gested classifying granular media as a fourth state of matter due to its unique behavior [100].

An approach to study the rich and complex dynamics of granular media is to study simplified, ordered granular systems referred to as 'granular crystals' [47, 48]. Granular crystals are ordered, close-packed arrays of elastic particles. The vast majority of studies on granular crystals have entailed millimeter or centimeter-sized particles, typically spherical in geometry (such as ball- bearings), which support waves in the sonic frequency regime [47]. We refer to these conventional granular crystals as 'macroscale granular crystals'. Just like atoms in a crystalline solid interact through chemical bonds, the transfer of forces and momenta in granular crystals occurs through geometric contact interactions. These interactions stem from the nonlinear Hertz law for elastic particles in contact [3], wherein a nonlinear power law dependence exists between the contact force and the penetration distance between the two bodies. The Hertzian nonlinear force- displacement (F - δ) relationship is given as:

$$F = E^* R^{1/2} [\delta]_+^{3/2} \tag{1.2}$$

Here, E^* is the effective modulus of contact and contains the Young's modulus (E_1 and E_2) and Poisson's ratio (ν_1 and ν_2) of the two contacting bodies, $E^* = [(3/4)\{((1-\nu_1^2)/E_1) + ((1-\nu_2^2)/E_2)\}]^{-1}$. R is the effective radius of contact, and for two contacting bodies with radii R_1 and R_2, the effective radius is defined as $R = [(1/R_1) + (1/R_2)]^{-1}$. It is important to note that only compressive forces are supported in granular crystals, in accordance with the Hertz contact law. The Hertz contact law is valid for deformations within the elastic limit, and assumes a frictionless contact with only normal forces acting between the particles in contact, and that the contact area is much smaller than the dimensions of the particles in contact [3]. One of the key features of macroscale granular crystals is that the dynamic behavior of the system can be tuned to encompass linear, weakly nonlinear and strongly linear regimes by varying the static pre-compression applied to the structure [48]. Under the absence of an external pre-compression, one- dimensional granular crystals are often referred

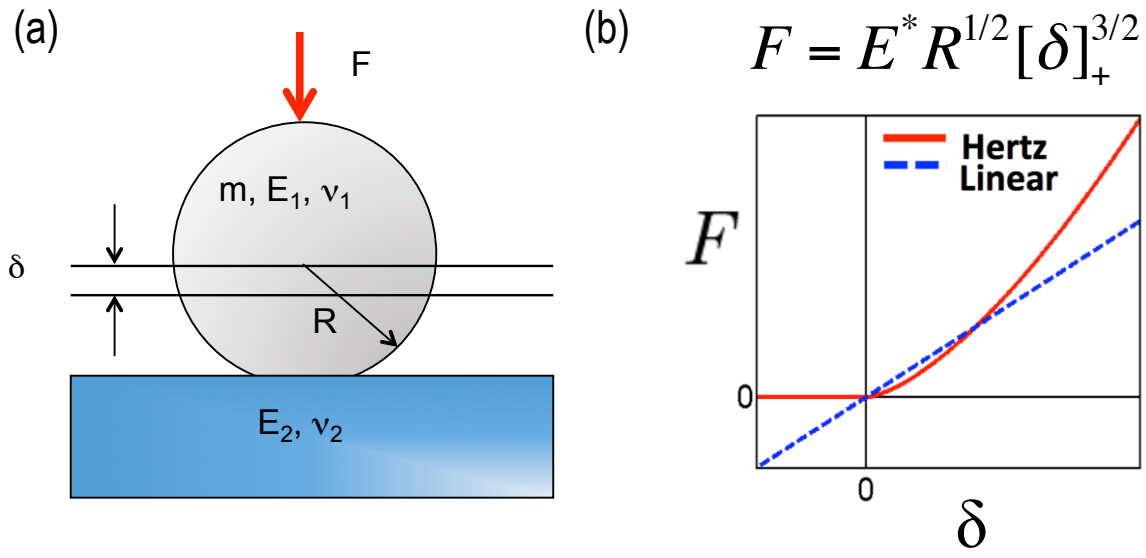

Figure 1.2: (a) Schematic of the contact between an elastic sphere and a substrate with denoted elastic properties; (b) Nonlinear force-displacement relationship predicted by the Hertz model of elastic particles in contact [3], where only compressive forces are supported. A linear force-displacement relationship is also shown for reference.

to as a sonic vacuum, because the speed of sound is zero in a system whose interparticle interactions are purely nonlinear [47]. The existence of highly nonlinear solitary waves was first shown analytically [101] and experimentally [102] in 1985. Since the seminal works of Nesterenko [101, 102], there has been a significant interest in the study of wave propagation in macroscale granular crystals [47, 48].

In addition to yielding insights in to the dynamics of granular media, granular crystals can also be thought of as a type of as a type of nonlinear acoustic metamaterial and phononic crystal. In such systems, wave propagation is affected by the nonlinear contact interactions and the dispersion induced by the structural periodicity in the granular crystal [47], or also with the addition of locally resonant elements to the particles in the granular crystal [50]. This

has lead to the development of granular crystal-based phononic crystals and metamaterials with unique features that leverage nonlinearity such as tunable frequency band-gaps [49,50], nonlinear intrinsic localized modes (referred to as 'discrete breathers') and non-reciprocal acoustic wave propagation [93], as well as prototypes for use as acoustic switches and logic elements [103] and acoustic lenses [54].

1.1.4 Downsizing Granular Crystals to the Micro- and Nanoscale

As described previously, the majority of studies on granular crystals have focused on macroscale granular crystals with millimeter or centimeter-sized constitutive particles that are designed to typically manipulate waves in the sonic regime [47]. Scaling down granular crystals to the micro- and nanoscales offers potential to manipulate waves and develop devices that operate in the megahertz and gigahertz frequency regime. At these length-scales, the effects of adhesion, which are negligible at the macroscale, will be significant [57] and are expected to alter the underlying physics of microscale granular crystals.

While the field of microscale granular crystals for ultrasonic wave tailoring is just in its nascent stage, there has been much interest in understanding the adhesion and contact mechanics of individual microparticles adhered to elastic substrates [104–106]. Several models have been proposed to describe the contact mechanics of microparticles subject to adhesive forces [107]. Of these, the Derjaguin-Muller-Toporov (DMT) [108] and the Johnson-Kendall-Roberts (JKR) [109] models of adhesive elastic normal contact are used most widely. The DMT model assumes the deformation profile follows that of the Hertz model and that long-range adhesive forces act outside the contact area. The force-displacement (F - δ) relationship in the DMT model is given by:

$$F = E^* R^{1/2} \delta^{3/2} - 2\pi w R \tag{1.3}$$

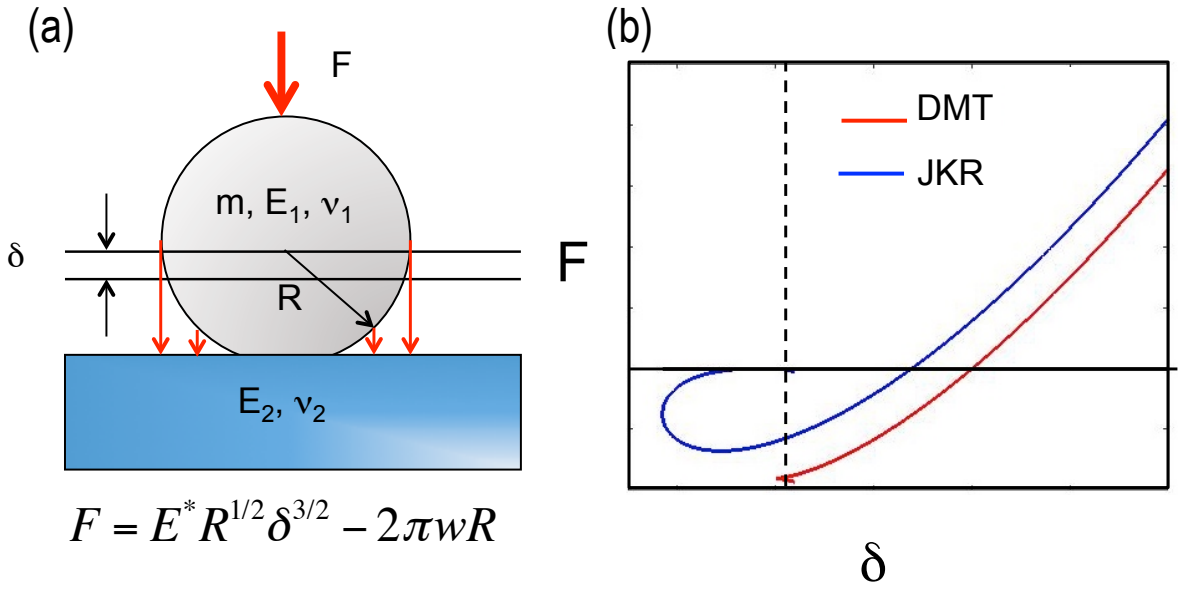

Figure 1.3: a) Schematic of the adhesive forces (indicated by the small red arrows) acting outside the contact region between the sphere and the substrate; (b) Force-displacement curves predicted by the DMT and JKR adhesive elastic contact models.

In equation 1.3, E^* and R are the effective modulus of contact the effective radius of contact, which dependent on the elastic properties and geometries of the two surfaces in contact, and w is the work of adhesion between the two surfaces in contact. It can be seen from the force-displacement relationship that the DMT model follows a similar trend as the Hertz model, with the addition of an offset corresponding to the adhesive force. The JKR model, on the other hand, assumes that short-ranged adhesive forces act only within the contact area, and the deformation profile is not constrained to remain Hertzian. The relationship between the contact force (F) and the resultant contact radius (a), and that between the normal displacement (δ) and the contact radius (a), as predicted by the JKR model, are

given by:

$$F = \frac{E^* a^3}{R} - \sqrt{6\pi w E^* a^3}, \ \delta = \frac{a^2}{R} - \frac{2}{3}\sqrt{\frac{6\pi w a}{E^*}} \tag{1.4}$$

It should be noted the DMT model is better suited for very small and stiff particles, while the JKR model is valid for comparatively larger and more compliant particles than what is valid for the DMT model [104]. From the force-displacement relationship of the JKR model, we see that during unloading (i.e., negative displacements), a connective neck is formed between the two surfaces in contact, and the contact is ruptured at negative loads. In addition to the DMT and JKR models, several additional adhesive elastic and elasto-plastic contact models incorporating normal and shear deformations have been studied [104].

Due to adhesion, microparticles are pulled towards the substrate. At equilibrium, the balance of contact and adhesive forces yields a particular contact area and a characteristic contact stiffness between the microparticle and the substrate. Consequently, the characteristic contact stiffness gives rise to a 'contact resonance', which depends on the elastic properties of the microparticle and the substrate, the adhesive force, and the mass of the microparticle [110–112]. A scanning electron microscopy image of a zoomed-in side view of a 1 μm diameter polystyrene sphere adhered an to aluminum-coated glass substrate is shown in Figure 1.4. The local deformation around the point of contact is clearly seen. Guillet and coworkers used an all-optical method to measure the axial contact resonance frequencies of single gold nanoparticles ranging from 50 nm to 1 μm in radius [34]. They found that the measured axial resonance frequencies measured for the different sized nanoparticles scaled to the same exponent as predicted by the DMT and JKR adhesive elastic contact models [110]. Murthy Peri and Cetinkaya measured a rocking motion induced by the contact stiffness in 20 μm diameter polystyrene microspheres by subjecting the substrate to a base acoustic excitation of up to 3.5 MHz, and measuring the displacement of the microspheres with an interferometer [111]. The resonance frequency associated with lateral motion of 5 to 20 μm

diameter glass spheres was measured using a quartz-crystal-microbalance [112]. Shifts in the lateral resonance frequency were seen by changing the coupling between the sphere and the substrate [112].

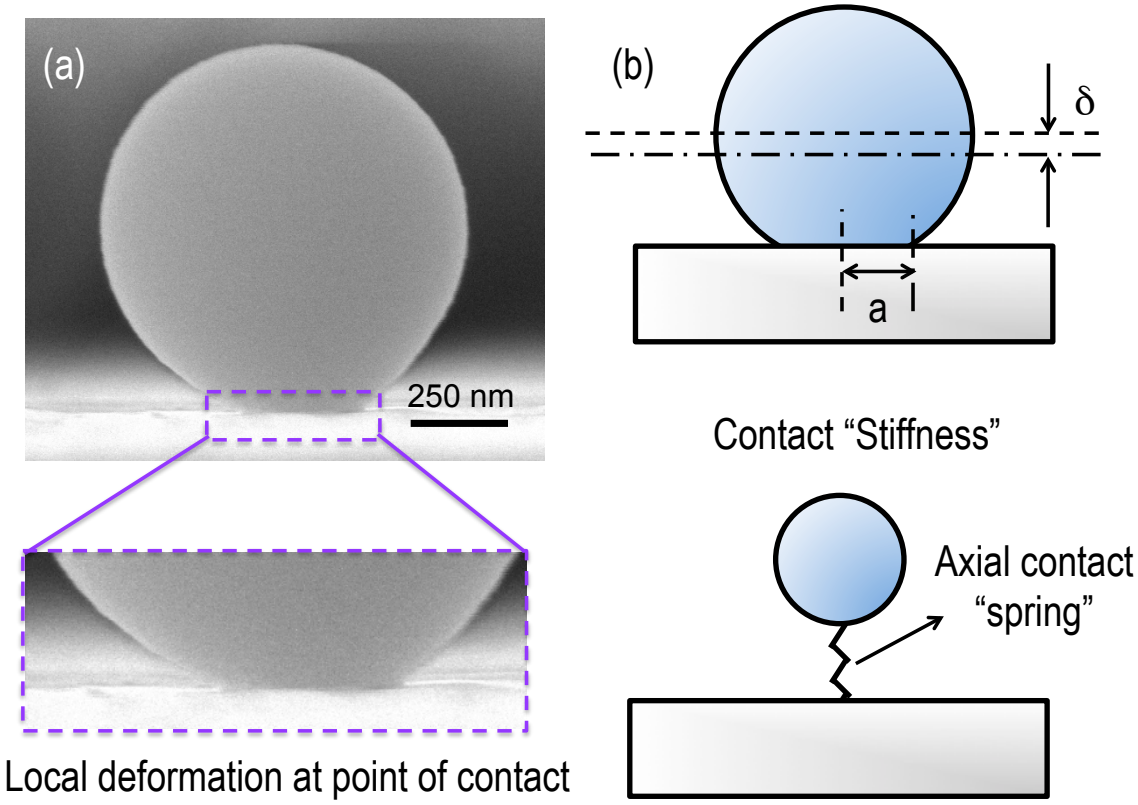

Figure 1.4: (a) Side-view scanning electron microscope image of a 1 μm polystyrene adhered to an aluminum-coated glass substrate. The local deformation induced by adhesive forces is visible in the particle-substrate contact area. (b) Schematic of the deformation of the sphere towards the substrate, which shows the axial displacement δ of the sphere towards the substrate, and the contact radius a. The deformation at the point of contact gives the contact a characteristic stiffness, and the contact can be modeled as a spring.

In addition to studies on the adhesion and contact resonances of individual microspheres,

recent studies have also explored the contact-based dynamics of three-dimensional nanoparticle assemblies [113–118]. However, these have been either in disordered settings [113–115], or in nanoparticle assemblies interacting via ligands [116–118] or polymer tethers [113].

1.1.5 Contact Mechanics at the Macro- and Microscale

Contact mechanics describes the behavior of solid bodies in contact under the action of external loads. The field of contact mechanics is said to have been started in 1882 by the seminal work of Heinrich Hertz [3], whose interest in the problem was aroused by observations of changes in optical fringe patterns induced by the elastic deformation of a stack of spherical glass lenses in contact [119]. Hertz showed, by analogy to the electrostatic potential theory, that an ellipsoidal distribution of contact pressure would produce elastic displacements in the two bodies in the form of an elliptical contact area. The Hertz contact theory predicts a nonlinear relationship between the force exerted on the contacting bodies and the relative displacement between them. This nonlinearity arises purely from geometric effects (assuming elastic behavior of the particles), and is restricted to the contact between frictionless nonadhering elastic solids. Motivated by the applicability of contact problems in numerous industrial settings that gained prominence in the early twentieth century, including locomotive wheel-rail contacts, mechanical linkages and gears, and bearing systems, a number of works developed theories to remove the restrictions of the original Hertz theory. These included studies that described the contact between viscoelastic solids [120–122], and the role of friction between the contacting surfaces [123]. These early contact mechanics models, however, were applicable only to the contact between macroscale bodies, and neglected the effects of interfacial adhesive interactions.

Rapid developments in the fields of pharmaceutical tableting, cosmetics, semiconductor manufacturing, powder processing, xerography, surface coatings, and additive manufacturing

over the past few decades have been directly linked to advances in particle technology and the understanding of contact-based interactions between particles at the micro- and nanoscale [27]. Studying the contact-based interactions and adhesion between micrometer and submicrometer-sized particles is also central to disciplines such as self-assembly [124], geology and rock formation, contaminant removal [27], and granular flow [97]. Contact characteristics between constitutive particles also govern the dynamic and shock-wave response of heterogeneous materials [48]. At the micro- and nanometer length scales, the magnitude of adhesive forces, which is negligible at the macroscale, exceeds the weight of the particles by several orders of magnitude [27, 57]. Consequently, micro- and nanoparticles in contact with each other and with other surfaces experience strong adhesive forces that induce deformation near the points of contact (as shown in Figure 1.4). These localized deformations at the points of contact yield vibrational resonances, wherein the particles move like rigid bodies and the deformed region around the contact acts as a spring [9, 11, 110–112]. These contact-based vibrational resonances in two-dimesional particle arrays have also been used to tailor the dispersion of surface acoustic waves [9–11, 125] and Lamb waves [12], giving rise to a new class of colloidal crystal-based acoustic metamaterial [31]. Exploring the contact-based dynamics in such systems has also opened the frontier of "micro-scale granular crystals" [47], enabling the possibility to extend unique wave control phenomena such as tunable frequency bandgaps [49] and non-reciprocal acoustic wave propagation [93], observed previously in the sonic frequency range in macro-scale granular crystals, to the megahertz and gigahertz frequencies [56].

In light of the increasing applications of particle technology and processes in a variety of industrial settings, a number of contact mechanics models have been developed to further understand and predict the fundamental physics of micro- and nanoparticles in contact. Early experiments with a soft rubber sphere in contact with glass revealed the importance of adhesion and led to the development of mechanical theories of adhesion of elastic spher-

ical surfaces [119]. Bradley, in 1932 [126], derived an expression for the total force between two rigid spheres, and showed that the maximum adhesive force F_a (or the pull-off force) was given by $F_a = 2\pi wR$, where $R = [(1/R_1) + (1/R_2)]^{-1}$ is the effective radius of the two spheres, each with radius R_1 and R_2, and $w = \gamma_1 + \gamma_2 - \gamma_{12}$ is the work of adhesion, commonly denoted in terms of the surface energies γ_1, γ_2 of the two bodies and the interfacial energy γ_{12} [127, 128]. Elastic deformation of the spheres with adhesion was introduced by Johnson, Kendall and Roberts ('JKR model') in 1971 [109], and by Derjaguin, Muller and Toporov ('DMT model') in 1983 [108]. The JKR and DMT models were derived from the classic Hertz contact theory [3]. The JKR model postulates that both short-ranged tensile and compressive interactions contribute to the size of the contact radius, and that these interactions occur only within the contact zone [109]. In the DMT model, the long-ranged molecular forces act in a ring-shaped zone, wherein the deformation profile is constrained to be the same as that predicted by the Hertz model [3]. In general, the JKR model is considered valid for "soft" elastic materials with large radii of curvature and high surface energy whilst the DMT model is more appropriate for "hard" stiff solids with small radii of curvature and low surface energy. A comparison of the force displacement curves prescribed by the DMT and JKR models is shown in Figure 1.3(b). A discrepancy between the pull-off forces predicted by the DMT and JKR models was addressed by Tabor [129], who showed that the DMT and JKR models represented two extreme cases in adhesive interactions and proposed a dimensionless number to decide the applicability of either model for a given system. Later, Maugis [130] developed a theory that showed a continuous transition between the DMT and JKR models.

Both the DMT and JKR models are based on the earlier analysis by Hertz [3] and are valid for small deformations within the elastic limit. However, due to stress concentrations at the contacts, even low loads can induce yielding and plastic deformation in atleast one of the contacting bodies [131]. A number of contact models have been developed to include

plasticity effects, such as the Maugis-Pollock (MP) model [132] which generalizes the JKR theory to allow yielding, and the Thornton model [133] which provides an analytical solution for the normal contact between two elastic-perfectly plastic spheres. Other studies have used the finite element method (FEM) to describe elasto-plastic contact between a sphere and a flat substrate and between two identical spheres [134–141] and developed empirical relations for the force-displacement response in the elastic, elasto-plastic and fully plastic regimes. Pal and coworkers developed a finite element model to study the effect of large deformation at multiple load-unload cycles and also included friction at the contact [142]. Johnson derived an analytical model for the unloading of an elastic-plastic spherical contact considering a completely elastic unloading [119]. Other studies based on FEM also investigated the unloading behavior of an elasto-plastic contact [136, 143, 144] and also considered the effect of adhesion during the loading and unloading of an elasto-plastic spherical contact [137, 138]. A fundamental understanding of contact mechanics at the microscale is therefore central to the study of contact-based wave phenomena in microscale granular crystals. Contact models that include the effects of adhesion and plasticity at the microscale could also be used to predict the magnitude of contact-based resonances in low-dimensional granular crystal systems.

1.2 Significance of This Work

This dissertation aims at filling in the deficiencies in the current state of understanding of the contact-based dynamics and wave tailoring phenomena in granular crystals when scaling down from millimeter- and centimeter- to micron- and submicron- characteristic length scales. Although the frontier of microscale granular crystals was recently opened [11], wherein the dispersion of surface acoustic waves induced by a contact-based local resonance of a microsphere monolayer was demonstrated, this work aims to further strengthen our knowledge of microscale granular crystals. In particular, we explore wave phenomena in self-assembled

single- and few-layer microscale granular crystals subject to dynamic excitations using laser ultrasonic techniques. The granular crystals investigated in this dissertation comprise of micron- and submicron-sized spherical particles that interact via geometric contact, without any connecting ligands or molecular tethers. The dispersion induced coupling of the adhesion-induced contact resonances with surface acoustic waves (SAWs) and Lamb waves is studied in the context of developing a new class of self-assembled, locally resonant acoustic metamaterials that operate in the ultrasonic frequency regime. A novel method to extract the effect interparticle contact stiffness from the longitudinal eigenvibrations of few-layer microscale granular crystals is also presented. Mechanisms to tune the particle-substrate and interparticle contact stiffness in microscale granular crystals are also discussed with an overall aim of taking a step closer towards tunable, dynamically responsive granular metamaterials. For the purpose of this thesis, we confine our investigation to modes below 1 GHz.

The self-assembled granular metamaterials investigated in this work can offer considerable advantages over other types of locally resonant metamaterials employing micron-scale structures fabricated using conventional lithographic and robotic pick-and-place techniques. Self-assembly offer potential for manufacturing metamaterials inexpensively, and on a roll-to-roll basis. Using pick-and-place methods, the manufacturing time to fabricate a device of dimension d with locally-resonant elements of size r is proportional to $(d/r)^3$. It is evident from the scaling that pick-and-place techniques are inefficient and impractical for manufacturing devices of macroscopic dimensions with micro- or nanoscale building blocks. For instance, if it took a millisecond to place a 1 μm sized building block on a panel, it would take ~ 32 years to assemble 10^{12} such building blocks on a 1 m x 1 m panel. Using self-assembly, the same panel could be assembled in a much shorter time, dictated by the evaporation time of the solvent.

This dissertation also addresses fundamental open questions regarding the scaling of the in-

terparticle and particle-substrate contact stiffness at reduced length-scales, and assesses the applicability of adhesive contact models derived from the Hertz contact theory [3]. The effect of plasticity induced by adhesive forces on subsequent dynamic load and unload cycles is also considered. The characterization techniques presented in this dissertation are non-contact and non-destructive, and also offer unique insight into the adhesive contact network of self-assembled microparticle arrays. While this dissertation focuses on the contact-based dynamics of microscale granular crystals for ultrasonic wave tailoring, this work also opens the door for studying similar material systems with acousto-optic [145] and acousto-plasmonic [146] functionalities. Finally, the wave propagation phenomena presented in this work could have applications in shock mitigation, energetic materials, powder processing, and acoustic signal processing and sensing, and also have implications for future studies of colloidal crystal systems [147, 148].

1.3 Colloidal Self-Assembly

Colloidal crystals are ordered arrays of monodisperse colloidal particles, analogous to a crystalline lattice whose repeating sub-units are atoms or moleculres [149]. The size of a typical colloidal particle is on the order of 0.1 to 1 μm [149]. In the context of mechanical wave tailoring, microscale granular crystals can be thought of as a type of colloidal crystal. One of the advantages of using microscale granular crystals as phononic structures and metamaterials is that they can be fabricated on a large-scale via colloidal self-assembly, a technique that is relatively simple, cost-effective and fast when compared to conventional "top-down" micro- and nano-fabrication techniques such as electron-beam lithography [150] and photolithography [151] as well as automated robotic pick-and-place methods to position micro-objects [152]. Comprehensive reviews of the experimental approaches to colloidal self-assembly are provided in [58, 60, 61, 153]. The most experimentally studied and used examples of colloidal particles are silica colloids and polymer latexes such as polystyrene

microparticles, which are also the particles used for self-assembly in this dissertation. Two dimensional colloidal crystals, also referred to as monolayer colloidal crystals, have been used as arrays of microlenses in imaging [154, 155], and as masks for lithography [156, 157]. Three-dimensional colloidal crystals, also referred to as synthetic opals [158], have been used in several applications such as templates for fabricating porous silica structures or inverse opals [159, 160], wafer-scale photonic band gap materials [161, 162] and diffractive elements in optical systems [163].

The self-assembly process entails the migration of colloidal particles from a disordered state in an aqueous (or otherwise liquid) solution, to close-packed, ordered crystalline structures in the dry state. It is worth noting that the availability of colloidal particles of highly uniform size and shape is very important for the self-assembly of crystalline arrays of large sizes (i.e., long range order at the centimeter length scale), since disorder and defects can affect the optical or other functional properties of the colloidal crystal. Several forces such as convective, capillary, van der Waal's attraction, and friction/ lubrication are typically, based on the self-assembly technique being used [59, 124]. In the sections below, we describe three self-assembly techniques used for the fabrication of microscale granular crystals investigated in this dissertation. An overiew of the colloidal self-assembly techniques used in this work is also presented in Figure 1.5.

1.3.1 Wedge-Cell Convective Self-Assembly

This technique involves the evaporation of a volume of colloidal solution confined within a wedge-shaped cell formed by holding together two glass slides [4, 164]. Flat, clean and homogeneous substrate surfaces are required to generate highly ordered arrays of large domain sizes. In this work, the substrates were rinsed with deionized (DI) water, and then soaked in an isoproponal bath for ten minutes, and rinsed with acetone and DI water and dried

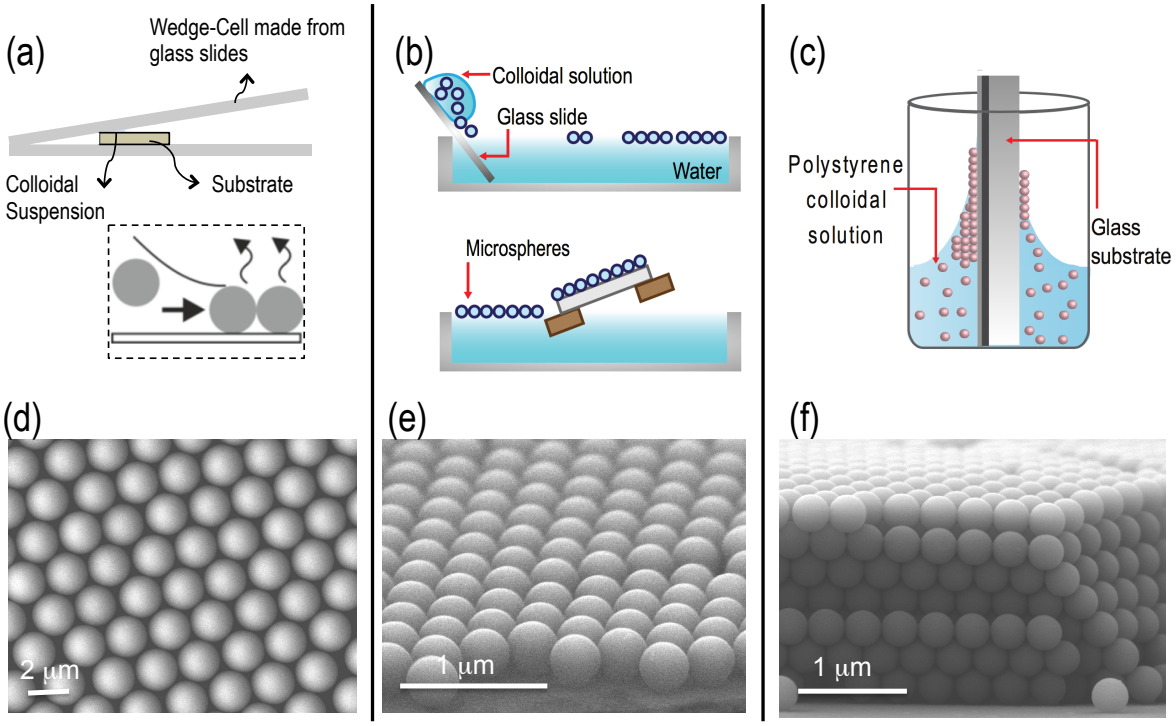

Figure 1.5: (a) Schematic of the wedge-cell convective self-assembly technique for monolayer fabrication based on reference [4]; (b) Schematic of the modified Langmuir-Blodgett technique based on reference [5]; (c) Schematic of the vertical deposition technique for multilayer fabrication based on references [6, 7]. (d) Representative scanning electron microscope (SEM) image of a 2 μm silica sphere monolayer fabricated using the wedge-cell technique; (e) Representative view of a monolayer of 390 nm polystyrene microspheres fabricated using the modified Langmuir-Blodgett technique; (e) View of a seven-layer-thick multilayer of 390 nm polystyrene microspheres fabricated using the vertical deposition technique.

under nitrogen flow. Direct microscopic observation in previous studies have shown that the crystalline ordering of a core array nucleus starts when the thickness of the evaporating liquid layer becomes commensurate with the diameter of the spheres, i.e., when the spheres start to protrude from the liquid surface [61]. It is therefore important that for monolayer fabrication, the contact angle between the colloidal solution and the substrate is as low as

possible. To achieve low contact angles during self-assembly, we treated our substrates either with oxygen plasma or in a hot hydrogen peroxide bath (at 80 °C) to increase their hydrophilicity. A small volume (typically 40 μL) is inserted on the substrate within the wedge-shaped cell, and the entire set-up is placed on a tilt of 10°. The colloidal particles are driven by convective and evaporative forces during the drying process, and line up along the drying front. The wedge-shaped cell ensures a flat meniscus, which results in the colloidal particles being aligned straight along the drying front [4]. It is important to note that in this technique, the pinning and depinning of the mensiscus often leads to a "stick-slip" motion, and can lead to regions with no particle deposition [153]. In this work, the apparatus was left to dry in ambient laboratory conditions. After complete drying, centimeter sized hexagonal-close-packed domains (arranged as a monolayer of microspheres) are obtained. Figure 1.5(a) illustrates the wedge-cell set-up, with a schematic of the drying front. Figure 1.5(d) shows a scanning electron microscope (SEM) image of a monolayer of 2 μm silica spheres deposited on an aluminum-coated glass slide using the wedge-cell technique

1.3.2 Modified Langmuir-Blodgett Self-Assembly

This technique is based on the Langmuir-Blodgett method [165] and uses an approach proposed by Vogel and coworkers [5] to produce close-packed monolayers over large areas, without the need for any special equipment. In this technique, the colloidal suspension (typically 5% by weight) is purified by centrifugation and diluted with ethanol to form a 50% by volume dispersion of ethanol. The colloidal suspension is then introduced into a beaker of water via a partially immersed hydrophilic glass slide with a tilt of 45°. The microspheres float and spread along the surface of the water in the beaker, and readily self-assemble into a close-packed-monolayer at the air/water interface. A hydrophilic substrate is then immersed into the sub-phase and elevated at a shallow angle to transfer the monolayer. The substrate is dried by holding it at an angle of $\sim 45°$. Figure 1.5(b) illustrates the steps in the modified

Langmuir-Blodgett self- assembly technique. A representative SEM image of a monolayer of 390 nm polystyrene microspheres assembled using this technique is shown in Figure 1.5(e). It should be noted that in this technique, it is essential to use colloidal particles with density similar to or less than that of water (or that of the liquid being used as the sub-phase), or modify the spheres so to be only partially immersed into the surface of the water [61]. Furthermore, the formation of an ordered colloidal monolayer requires that the interparticle attraction be sufficiently weak to allow the formation of ordered domains which can deform during drying [61, 166]. Retsch and coworkers [167], and Vogel and coworkers [5], both reported that adding small quantities of a surfactant, namely sodium dodecylsulfate (SDS), below their critical micelle concentration, led to accumulation of the surfactant at the air/water interface and constituted a soft barrier in the monolayer fabrication process, which influenced capillary forces and facilitated the packing of particles in a hexagonal crystal lattice. In this study, however, surfactant was not used in the self-assembly fabrication process.

1.3.3 Vertical Deposition Convective Self-Assembly

Direct self-assembly on solid substrates is one of the most widespread and simplest methods for two- and three-dimensional colloidal crystal fabrication [153]. Originally introduced by Denkov and coworkers for the fabrication of monolayer colloidal crystals [168], this technique has since been extended for the assembly of three-dimensional colloidal crystals [6,7]. A glass scintillation vial is filled with the colloidal suspension, and the substrate is then held still vertically in the vial while being immersed in the suspension. The substrate and suspension are then left to dry in an oven or in ambient laboratory conditions. After complete drying, millimeter-sized colloidal crystals of varied thicknesses are obtained. In this technique, the interplay of convective drag force driven by non-uniform solvent evaporation, electrostatic repulsion, and capillary attraction caused by the evaporation of solvent at the liquid meniscus

in contact with the solid substrate typically leads to highly ordered structures [61,153]. Like in the case of the wedge-cell convective self-assembly technique described in Section 1.3.1, the solvent should wet the surface of the solid substrate in this technique to ensure a low contact angle at the meniscus, and the interaction between the substrate and the particles needs to be sufficiently low to provide mobility to the particles in contact with the substrate to organize themselves into a hexagonal array [153]. The thickness of the resulting crystal film is then determined by a range of parameters such as temperature, humidity and colloidal suspension concentration, and can be tuned from single monolayers to several tens of microns [6,153]. A modification of the vertical deposition convective self-assembly technique is a vertical lifting deposition method wherein the target substrate is continuously removed from the colloidal suspension at a slow speed [169,170]. Like in the case of the wedge-cell technique, a common drawback of the vertical deposition convective assembly method is the prevalence of inhomogeneities in the colloidal crystal film thickness, which are caused by pinning and slipping of the meniscus at the three phase contact line between the substrate, the colloidal suspension, and air [153,171]. Furthermore, the quality of three-dimensional colloidal crystals fabricated using the vertical deposition technique is often limited by the prevalence of cracks on the order of microns, particularly, in the case of colloidal crystals which are several tens of microns in thickness [153]. The formation of these cracks in thick multilayer colloidal crystals has been attributed to stress release upon drying [153,171]. Approaches to fabricate large-area crack-free colloidal crystals have also been studied in recent years, and include the addition of a silica or sol-gel precursor in the colloidal suspension to fill up the voids and avoid crack formation [172,173]. In this study, we use the vertical deposition self-assembly technique to assemble three-dimensional colloidal crystals of a few layers in thickness (up to about fifteen layers). The substrates were held still without the use of substrate withdrawal methods discussed above. The concentration of the colloidal suspension was chosen so was to obtain few-layer-thick colloidal crystals. Since only a few layers were desired, few cracks were observed, and therefore, precursors to limit crack formation were not used. The colloidal suspensions using ethanol as a solvent were allowed to

dry in air, while those in water were dried in an oven set to 60 °C. The deposition setup was placed in a containment to avoid the influence of airflow or vibrations during the deposition process. For the colloidal suspension drying in ambient air, molecular mesh beads (Sigma Alrich Type 4A) were used as a desiccant to maintain a constant evaporation rate. Figure 1.5(c) shows the set-up for the vertical deposition convective self-assembly technique. A representative side-view SEM image of a 7-layer-thick multilayer granular crystal of 390 nm diameter polystyrene spheres is shown in Figure 1.5(f).

1.4 Laser Ultrasonics

The field of laser ultrasonics entails the generation and detection of ultrasound in solid, liquid or even gaseous samples using the energy of laser light [62]. Typically, a pulsed laser beam is used to induce ultrasound by rapid thermal expansion or by ablating the medium. The ultrasonic wave propagating in the sample is measured using an optical probe by different techniques that are sensitive to the time-dependent change in reflectivity of the sample induced by the excitation laser pulse, change in slope or curvature of the sample as the wave travels in the sample, interferometric techniques that measure the displacement of the wave, or the time-dependent diffraction off the surface ripples on the sample induced by the excitation laser pulse, among others. These techniques that involve an excitation laser source ('pump' beam) and a detection laser source ('probe' beam) are referred to as 'pump-probe' laser ultrasonic techniques.

Laser ultrasonic techniques are particularly attractive over other ultrasonic characterization methods because - i) they are non-contact; ii) they are non-destructive if the pulse energy of the pump laser beam is kept sufficiently low; iii) generally, the spot sizes are relatively small, giving high lateral resolution; and iv) they are highly-sensitive broadband systems providing information from the kHz to the THz range [174].

In the sections below, we describe the laser ultrasonic techniques that are used to characterize the contact-based dynamics of microscale granular crystals in this study. The pump laser for all techniques presented below is an actively Q-switched pulsed diode-pumped solid-state (DPSS) laser (Coherent Helios $532-3-50$) with 532 nm wavelength, 440 ps pulse duration and 60 μJ maximum pulse energy. The repetition rate can be adjusted from 0.1 kHz to 50 kHz, or also be configured for single shot pulsing. The energy of the optical pulses from the pump laser could be adjusted by a variable neutral-density (ND) filter and a half-wave plate (HWP) used with a polarizing beam splitter (PBS). The probe laser is a continuous wave (CW) beam Coherent Genesis Nd:YAG laser (Model MX-514) with optical wavelength 514 nm and maximum power 1 W. In some experiments, the probe output was modulated using an electro-optic modulator (EOM - ConOptics $350-50$ with 302 RM high voltage source) in conjunction with an arbitrary function generator (Tektronix AFG3022B) to obtain a 50 μs probe "on" window, synced with the pump pulse arrival. The CW probe beam was modulated to avoid sample heating effects induced from the probe beam.

1.4.1 Laser-induced Transient Grating (TG) Spectroscopy

The laser-induced transient grating (TG) technique, also called impulsively stimulated thermal scattering (ISTS), uses a four-wave mixing process to generate and detect coherent material excitations. This technique takes advantage of the periodic intensity profile generated from crossing two spatially and temporally coincident laser pulses to set the wave vector q of the excitation [175,176]. The setup for the TG technique in reflection geometry is based on the previous work by Johnson and coworkers [8] and is illustrated in Figure 1.6(a). The pump beam of wavelength λ_e is incident on a phase-mask (also known as a diffraction grating). The phase masks used in this study had binary square surface relief patterns etched in a fused silica wafer, and were obtained from Nanoptron Inc. (Redwood City, CA) and from

collaborators (Nelson Research Group at MIT). Each phase mask contained patterns over a 5 mm by 5 mm area on a fused silica wafer separated by 250 μm with period ranging from 2.2 μm to 260 μm. The etch depth was optimized for transmission at 532 nm optical wavelength (i.e., the pump laser optical wavelength) such that 80 % of the incident pump energy is directed into the +1 and −1 diffraction orders. A telescope imaging system with Thorlabs achromatic doublets was used to cross the +1 and −1 diffraction orders of the pump beam on to the sample with an angle θ using to create a spatially sinusoidal temperature profile (thermal grating) onto the sample. The period (or spacing between peaks) L of this thermal profile is given by:

$$L = \frac{2\pi}{q} = \frac{M\Lambda_0}{2} = \frac{\lambda_e}{2\sin(\theta/2)} \tag{1.5}$$

Here, $M = f_2/f_1$ is the magnification of the telescope system with achromatic lenses of focal length f_1 and f_2, and Λ_0 is the period of the phase mask. The periodic heating caused by absorption of the pump results in rapid thermal expansion that launches counter-propagating surface acoustic waves of wavelength L (or wave vector magnitude q). The 'transient grating' on the sample has two parts - i) a steady-sate 'thermal grating' that remains until the heat diffuses away; and ii) an oscillating, standing-wave grating that remains until the surface acoustic waves damp out, or simply leave the probing region [8]. The excitation generated by the crossed pump beams is manifested as surface displacement and/or transient changes in the reflectivity [8]. It is worth noting that if two beams are crossed with perpendicular polarizations, e.g. vertical and horizontal, the generated interference pattern has a periodic polarization profile rather than a periodic intensity profile [177].

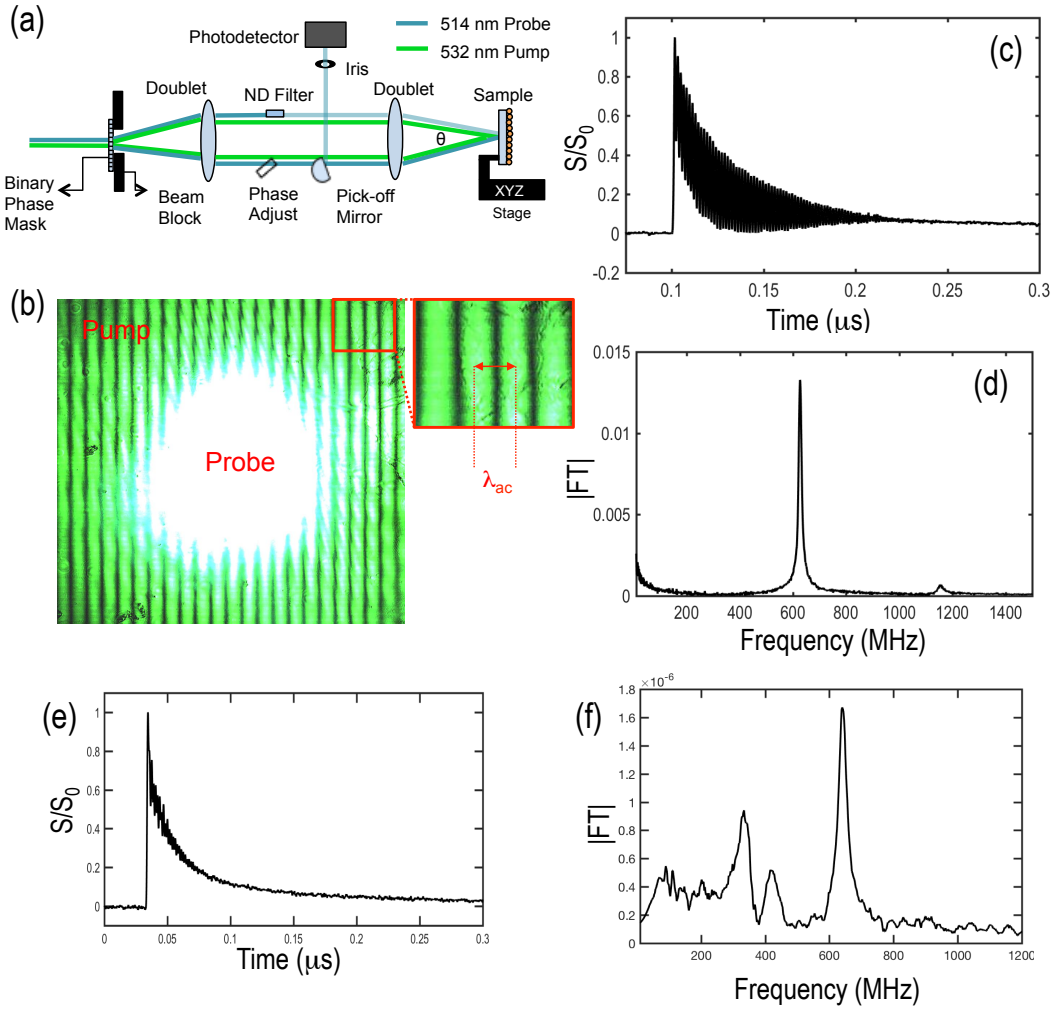

Figure 1.6: (a) Schematic of the transient grating (TG) spectroscopy technique with phase-controlled heterodyne detection where pump and probe laser beams are incident on a binary phase mask and then focused on the sample using a set of telescope lenses, based on reference [8]; (b) CCD camera image of the interference fringe pattern formed by the crossing pump laser beams on the sample and the probe beam focused at the center of the fringe pattern; (c) Representative time-domain TG signal generated at acoustic wavelength 5 μm on a bare aluminum-coated glass substrate and (d) its corresponding Fourier spectrum illustrating Rayleigh wave and surface skimming longitudinal wave peaks. (e) Time-domain TG signal generated at acoustic wavelength 4.95 μm at the interface of a glass substrate and a 3-layer-thick microscale granular crystal, along with its (f) corresponding Fourier spectrum that shows additional peaks corresponding to guided wave modes.

Detection of the material response is achieved using a probe beam, that goes through the same set of optics as the pump beam, and is focused on the 'transient grating' generated on the sample by the crossing pump beams. The probe beam is incident on the phase mask at a slight angle below the normal, thereby allowing the pump and probe beams to be spatially separated in the vertical plane. We employ the optical heterodyne detection technique introduced by Maznev and coworkers [176], which has several advantages such as overcoming noise from the detection electronics or from parasitically scattered light, in addition to signal linearity with respect to the material response amplitude and retention of phase information that would otherwise be lost [176]. In the heterodyne detection technique, the CW laser beam is also split into $+1$ and -1 orders by the phase mask to create a probe beam and a reference (or local oscillator) beam. The reference beam is attenuated using an absorptive neutral density filter (Thorlabs ND 2.0), while a highly parallel fused silica window (from OptoSigma Inc.) was placed in the path of the probe beam. The relative phase ϕ between the probe and reference beams was controlled by adjusting the angle of the window using a Thorlabs Z612 motorized actuator with TDC001 Servo controller. Changing the angle of the window results in a relative change in the optical path length between the probe and reference beams. In general, to avoid issues from probe lasers with short correlation length, the thickness of the glass slide and ND filter should be well matched [177]. The probe beam that is diffracted off the 'transient grating' on the sample (referred to as the signal beam) is spatially overlapped with the reference beam, and is directed to a fast, avalanche silicon photodetector (Hamamatsu C5658) where the time-dependent intensity is measured. The output of the photodiode is digitized using a digital phosphor oscilloscope (Tektronix DPO7254), and averaged typically over 10,000 pump pulses. The diffracted signal and reference beams are overlapped and interfere to give the following intensity [176]:

$$I_{s+r} = I_s + I_r + 2\sqrt{I_s I_r}\cos(\phi) \tag{1.6}$$

Here I_s is the intensity of the diffracted beam, and I_r is the intensity of the reference beam.

In the case where $I_r >> I_s$, the intensity of the measured signal, I_{s+r} is linearly dependent on $\sqrt{I_r}$, because I_s is negligible and I_r has no time dependence. Data can be collected at $\phi = 0$ and $\phi = \pi$, and by subtracting the two traces, any signals not dependent on the heterodyne phase, such as signals from low-frequency electromagnetic sources or scattered pump light, are eliminated [176, 177]. A representative transient grating signal, generated at an acoustic wavelength of 5 μm and measured on a bare aluminum-coated glass slide, is illustrated in Figure 1.6(c). The sharp-rise corresponds to the arrival of the pump pulse, while the slow decay is associated with the thermal diffusion in the sample. The high-frequency oscillations correspond to the displacement of the surface acoustic wave propagating in the sample. Figure 1.6(d) shows the corresponding Fourier spectrum of the TG signal, after removing the slow thermal decay. The dominant peak at $\sim$ 625 MHz corresponds to the Rayleigh wave frequency, while the smaller peak at $\sim$ 1.2 GHz is associated with a surface-skimming longitudinal wave in the substrate. Figure 1.6(e) illustrates a TG signal excited at an acoustic wavelength of 4.95 μm at the interface between an aluminum-coated glass substrate, and a three-layer-thick microscale granular crystal. The corresponding Fourier spectrum of the TG signal, shown in Figure 1.6(f), shows additional acoustic modes associated with the guided waves. Switching phase mask patterns changes the crossing angle θ of the pump beams, and therefore the wavelength of the surface acoustic waves that are generated in the sample. Probing the response of surface acoustic waves at multiple wavelengths enables the construction of the dispersion of SAWs in the sample.

In collaboration with the Nelson Research Group at MIT, we assisted in the development of a novel modification to the TG technique to add the capability of a continuously tunable thermal grating on the sample, achieved by rotating the phase mask [178]. As stated previously, the material response at multiple wave vectors is measured by switching phase mask period patterns achieved by translating a substrate with multiple phase patterns etched on it. However, the TG period can be only varied in fixed steps dictated by the available set

of phase mask patterns. A typical setup [8, 179] employs a set of 15-30 phase mask patterns with a TG period step size of 10-20% between adjacent patterns. The new technique, based on the rotation of the phase mask, is particularly useful for applications that require a finer control of the TG period, such as in acoustic measurements, where one may wish to set the wave vector precisely at the Brillouin zone boundary of a phononic crystal [180] or to look for a narrow resonance of an acoustic metamaterial [11]. The introduction of an angle between the incident excitation beam and the phase mask normal, changes the angle between the first diffraction orders and consequently, changes the period of the interference pattern at the sample. The angle between the probe and reference beams also changes such that the heterodyne detection is preserved. The advantage of the proposed method is that it does not require any modifications of the setup other than putting the phase mask on a rotation stage [178].

1.4.2 Phase-mask-based Interferometry

We use a phase-mask-based interferometer, developed by Glorieux and coworkers [181], to preferentially detect out-of-plane motion. The phase-mask-based interferometer is a versatile and sensitive optical interferometer based on diffractive optics. An advantage of using a phase-mask interferometer over other types of interferometers such as the Michelson interferometer [182] is the absence of the need for active stabilization. The compact common-path design of the phase-mask interferometer requires only two optical elements [181], making this type of interferometer robust against air currents or vibrations of the optical elements in the beam path. For material excitation, the pump laser is focused on the sample, typically as a circular Gaussian beam spot. Absorption of the pump pulse energy by the sample induces a rapid thermal expansion that excites a bulk longitudinal wave propagating through the thickness, as well as a broadband surface wave. Out-of-plane displacements are detected with the phase-mask-based interferometer in which a single CW laser is incident on a phase-mask

and split into $+/-1$ diffraction orders to produce probe and reference beams. Splitting the probe and reference beams by diffraction, rather than by partial reflection, is particularly advantageous, since the wave fronts of the probe and reference beams propagate parallel to each other, which in turn enables the retrieval of a centrosymmetric interferogram that greatly eases analysis [181]. The phase-mask and the sample are placed on either side of a lens at the focal distance, allowing the probe and reference beams to arrive at the sample parallel and focused to circular spots. The pump and probe beams are aligned such that they are collinear and concentric. The separation between the probe and reference beams is kept as low as possible to increase phase stability (typically 1 - 5 mm). Upon reflection from the sample, the probe and reference are re-crossed onto the phase mask, are collinear, and re-combine interferometrically onto an amplified silicon photodetector (EOTech 2030A) where the signal is digitized and recorded using an oscilloscope, and averaged typically over 10,000 pump pulses. Like in the case of the transient grating setup, the relative phase between the reference and probe beams is controlled by adjusting the angle of a glass window placed in the path of the either the probe or the reference beam. The voltage of the interferometric signal V_{sig} measured by the photodiode is proportional to the intensity of the interference pattern, which in turn depends on the optical path difference ξ between the probe and the reference beams [181], and is expressed as,

$$V_{sig}(\xi) = \frac{V_{max} + V_{min}}{2} + \frac{V_{max} - V_{min}}{2} \cos(2\pi\xi/\lambda) \tag{1.7}$$

Here, λ is the optical wavelength of the probe and reference beams, V_{max} is the maximum voltage measured by the photodiode, and is obtained when $\xi = 0, \lambda, ...$ (constructive interference), and V_{min} is the minimum measured voltage obtained when $\xi = \lambda/2, 3\lambda/2, ...$ (destructive interference). The sensitivity of the interferometer ($dV_{sig}/d\xi$) is expressed as,

$$\frac{\partial V_{sig}}{\partial \xi} = -(V_{max} - V_{min})\frac{\pi}{\lambda} \sin(2\pi\xi/\lambda) \tag{1.8}$$

The maximum sensitivity is reached when the optical path difference is $\xi = \lambda/4, 3\lambda/4, ...$, and the signal level is midway between V_{max} and V_{min},

$$\left|\frac{\partial V_{sig}}{\partial \xi}\right|_{max} = -(V_{max} - V_{min})\frac{\pi}{\lambda} \tag{1.9}$$

The maximum and minimum values of the voltage level could be determined by rotating a glass window placed in the path or either the probe or reference beams [181].

In this dissertation, we use this technique to measure the out-of-plane axial contact resonance of microspheres in a two-dimensional granular crystal, or the fixed-free normal eigenmodes of multilayer three- dimensional granular crystals. The set-up of the interferometer, and a representative signal is illustrated in Figure 1.7(a). A representative time-domain interferometric signal measured on a bare aluminum-coated glass slide is shown in Figure 1.7(b). The sharp rise (denoted by the blue dash line) corresponds to the rapid thermal expansion of the aluminum film induced by the pump pulse, while the low frequency wave is associated with a broadband surface wave that leaves the probing region. The inset in Figure 1.7(b) highlights the longitudinal and shear wave pulse echoes, detected via partial reflection off the glass slide, denoted by L_0 and S_0, respectively. The echoes denoted by L_1 and S_1 correspond to the round-trip echoes of the longitudinal and shear wave pulses, respectively.

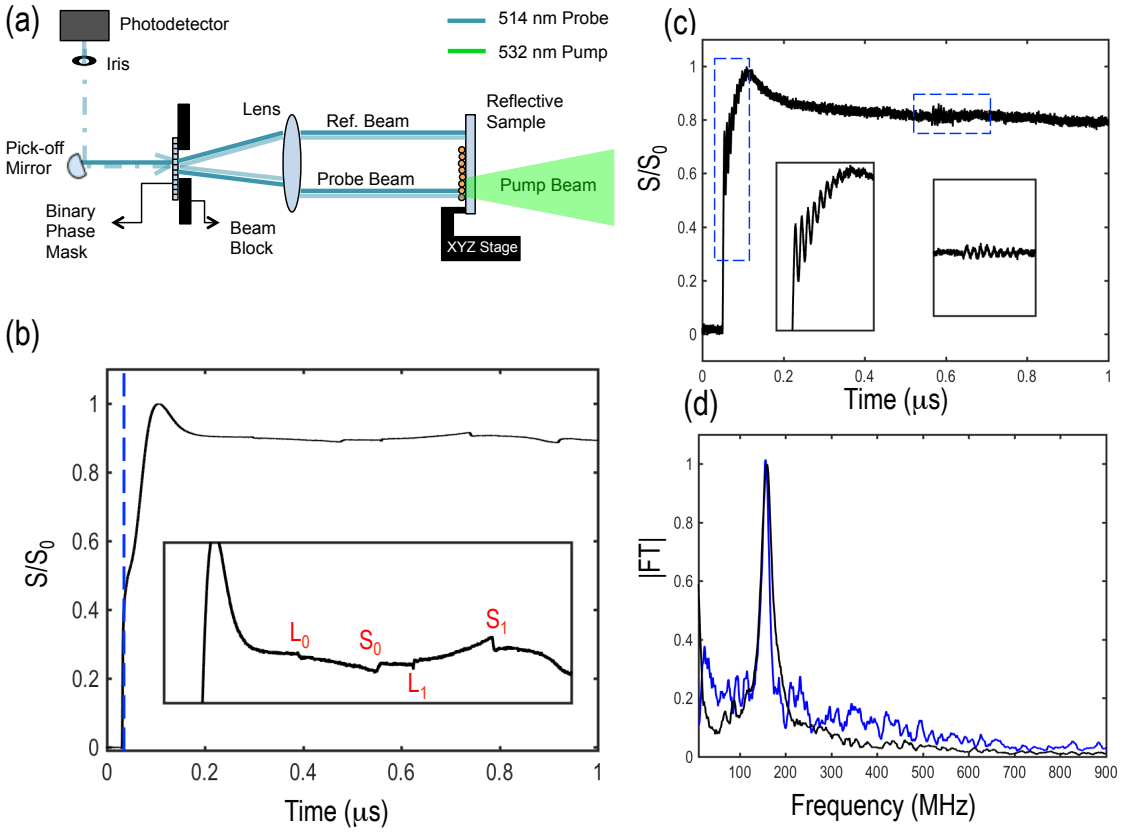

Figure 1.7: (a) Schematic of the phase-mask-based interferometer in reflection set-up; (b) Representative time-domain interferometric signal measured on a bare aluminum-coated glass slide. The dash blue line corresponds to the arrival of the pump pulse, and the subsequent rapid thermal expansion of the aluminum film. $L_{0,1}$ and $S_{0,1}$ denote the echoes of the longitudinal and shear wave pulses in the substrate. (c) Representative time-domain interferometric signal measured on a monolayer of 1 μm polystyrene microspheres. The initial high frequency oscillations (highlighted by the dash blue box) represent the axial contact vibrations of the microspheres and the low frequency pulse is the surface wave leaving the probe region. The echo denoted by the dash blue box indicates acoustic energy radiated by the microspheres in the bulk. (d) Fourier transform of the initial microsphere oscillations (denoted by the black curve), and the echo wave packet (denoted by the blue curve).

A representative time-domain interferometric signal measured on a monolayer of 1 μm polystyrene microspheres is shown in Figure 1.7(c). The high frequency oscillations (highlighted by the blue dash box) represent the axial contact vibrations of the microspheres superimposed over the surface wave leaving the probe region. A second wave packet containing oscillations is seen in the signal (denoted by the blue dash box), which arrives at the time corresponding to the round-trip travel time of the longitudinal wave in the substrate. These oscillations are associated with the acoustic energy radiated into the bulk by the microspheres. The frequency spectrum of the initial acoustic oscillations is shown in Figure 1.7(d) with the black curve. The frequency spectrum of the radiated acoustic oscillations is also shown in Figure 1.7(d) with the blue curve. We see that the frequency of the acoustic wave packet radiated into the bulk by the microspheres that travels a round-trip distance in the substrate is the same as the original contact resonance frequency of vibration. We note that in the phase mask-based interferometer, the out-of-plane displacement component of the microspheres is be the dominant contributor to an optical path difference between the probe and reference beams, which results in a shift of the interference fringe pattern and is manifested in the form of a change in intensity in the measured signal. In-plane horizontal or rotational motion of the microspheres may also contribute to the measured signal, but to much smaller extent compared to the contributions of the out-of-plane oscillations. Scattering of the incident probe beam by the microsphere array may also contribute to the interferometric signal. Shen and coworkers calculated the intensity and the angular distribution of the light scattered by a monolayer of spheres in a two-dimensional plane perpendicular to the direction of radiation [183]. The authors found that the light scattered by a monolayer of spheres is a result of the interference between fractions of light scattered by single particles. The monolayer packing density was also found to influence the angular dependence of the scattered light [183]. Dick and coworkers experimentally studied the angular structure of radiation scattered by non-absorbing microsphere suspended in solution [184]. The measurements showed that the single scattering approximation could be used to describe the structure of radiation scattered by monolayers of particles [184]. In our experiments, we

assume the axial contact vibrations are the dominant contributors to the measured signal, while other sources such as rotational and horizontal vibrations, and scattering effects, result in a much smaller contribution to the signal. It is worth noting that while the majority of interferometric techniques have been used for detecting out-of-plane or longitudinal vibration detection (including the phase-mask-based interferometer in this dissertation) [182], new interferometric methods and tools that are sensitive to in-plane motion have also been developed [185].

1.4.3 Knife-edge Photodeflectometry

The laser deflectometry technique has been widely used to detect megahertz acoustic waves generated by nanosecond laser pulses [62, 186–188]. This technique is based on the measurement of the variation of the probe beam direction after reflection on the sample surface. Pulsed heating of the interface region leads to the excitation of a surface acoustic wave as a result of thermoelasticity. As the surface wave propagates, the sample surface undulates, causing the probe laser beam to be deflected [188]. The time-dependent changes in the angular deflection of the probe beam, induced by the change in the local curvature as well as the refractive index of the sample due to the propagating surface acoustic wave, are monitored by steering the reflected probe beam towards a photodetector. To enhance the sensitivity of the detection, a knife screen is typically placed in front of the photodiode detection area that partially blocks the reflected beam.

In our studies, the photodeflectometry technique was used to measure the resonant attenuation of surface acoustic waves by a two-dimensional microscale granular crystal (led by collaborator M. Hiraiwa). The subnanosecond laser pump pulse was focused to a line of dimensions 1.2 mm x 20 μm (axis length, at $1/e^2$ intensity level) on the sample using a cylindrical lens. The absorbed laser light launches broadband SAW pulses that propagate

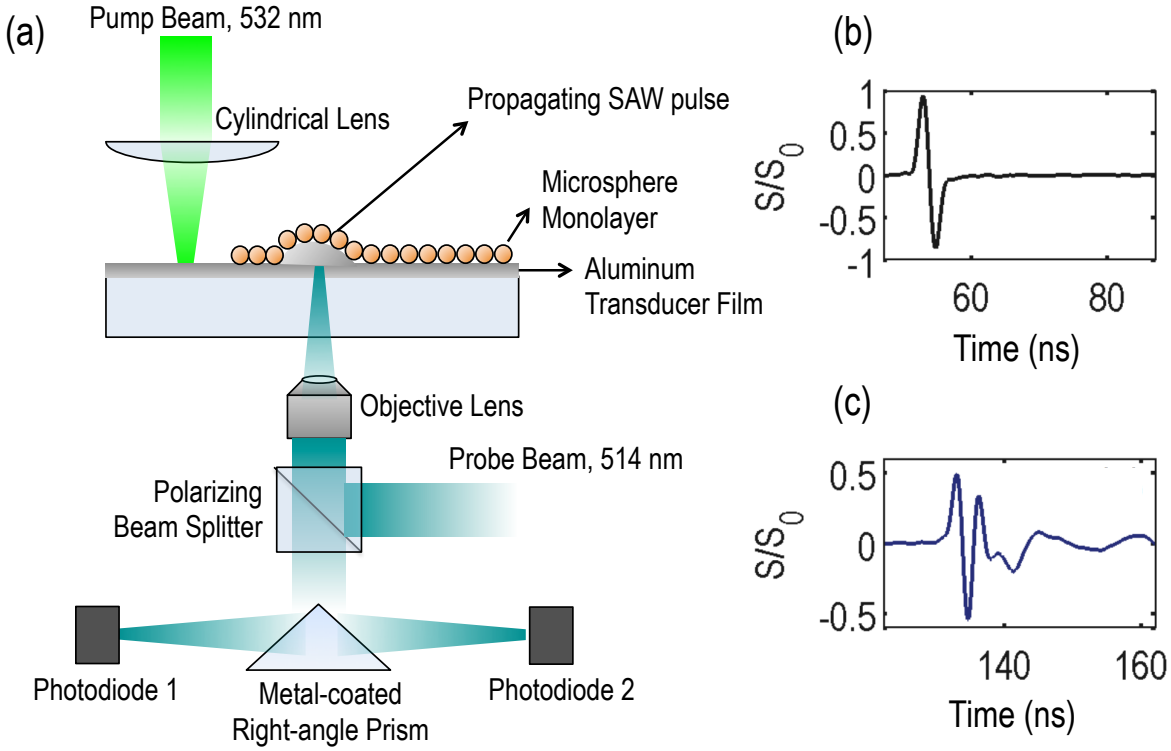

Figure 1.8: (a) Schematic of the knife-edge photodeflectometry setup used to generate and detect surface acoustic waves. A balanced detection scheme is illustrated with the use of the metal-coated right-angle prism and two photodiodes. Representative normalized time-domain signal of a surface acoustic wave pulse detected on (b) a bare aluminum-coated glass slide, and (c) 132 μm inside a monolayer of 2 μm silica spheres [9].

as plane waves perpendicular to the line source. The probe beam is focused to a 6 μm spot on the aluminum transducer film of the sample from the opposite side using an objective lens. A balanced detection scheme is used, in which a metal coated right-angle prism acts as the knife edge for two photodetectors. The two photodetectors used were silicon amplified photodiodes (EOTech 2030A) with a bandwidth of 2 GHz. A schematic of the knife-edge photodeflectometry is illustrated in Figure 1.8(a). A representative normalized time-domain signal of a surface acoustic wave pulse generated by the line source on a blank substrate

(without microspheres), and 132 μm inside a monolayer of 2 μm silica spheres is shown in Figure 1.8(b) and Figure 1.8(c), respectively.

1.5 Numerical Tools

In this dissertation, the finite element method was used to simulate the contact mechanics between a microsphere and a flat substrate. The force-displacement relationship of the indentation of a microsphere into a flat substrate was simulated numerically using the 2D Mechanics interface in COMSOL Multiphysics ® using the Structural Mechanics Module. The model accounts for geometric nonlinearity and assumes frictionless contact. The Structural Mechanics Module supports contact boundary conditions using contact pairs. The contact pair is defined by a source boundary and a destination boundary. The destination boundary is coupled to the source boundary if contact is established, and receives its displacements from the source boundary. As a result, the contact pressure variable is available on the destination boundary. The numerically obtained force-displacement relationships were compared to those predicted analytically using the Hertz contact theory [3]. The force-displacement behavior in the elasto-plastic regime is of particular interest, since even small deformations can induce significant localized stresses at the contact points. The effect of plasticity in the contact zone on subsequent load and unload cycles is studied numerically. Previous studies utilizing the finite element to study a sphere-substrate contact have included the effect of adhesive interactions using the Lennard-Jones potential in the finite element model [138, 189, 190]. However, in this study, while adhesion was not incorporated in the finite element model, the contact stiffness was extracted from the force-displacement curves at various levels of deformation of the sphere.

A two dimensional axisymmetric model was developed in which a quarter of a circle was used to model the sphere. The contact pairs were defined between the lower contour of the

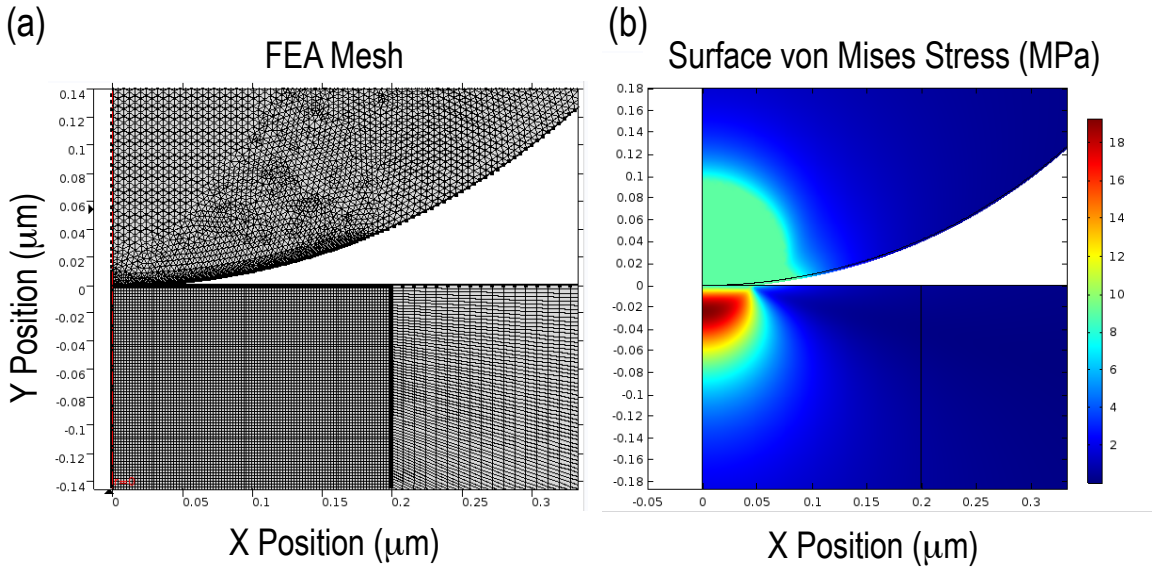

Figure 1.9: (a) Finite element model implemented in COMSOL Multiphysics to simulate the contact deformation of a polystyrene microsphere indented into an aluminum substrate. Free triangular elements were used to mesh the sphere, while quadrangular elements were used to mesh the substrate. The mesh density was refined in the vicinity of the contact. (b) Surface von Mises stress representation of a 1 μm polystyrene sphere indented 7.2 nm into the substrate.

sphere and the edge of the substrate directly beneath the sphere. Free triangular elements were used to mesh the sphere, while mapped quadrangular elements were used for meshing the substrate. The mesh density was increased in the vicinity of the contact for both the sphere and the substrate. Figure 1.9(a) shows the model setup in COMSOL with the meshed sphere-substrate geometry. Displacement steps were prescribed to the top edge of the sphere. The reaction force on the same edge at each displacement step was obtained to construct the force-displacement relationship. The force-displacement relationship was model for a 1 μm and 10 μm diameter polystyrene sphere indented into an aluminum substrate. The Augmented Lagrangian method was used as the contact pressure method [191].

Figure 1.9(b) illustrates the von Mises stress contour of a 1 μm diameter polystyrene sphere indented 7.2 nm into the substrate. Plastic yielding of the sphere in vicinity of the contact is observed. Additional details regarding the finite element modeling of the elasto-plastic contact between a sphere and a flat substrate are provided in Chapter 4.

1.6 Conceptual Organization of This Thesis

The remainder of the thesis is organized as follows: Each chapter describes a specific project related to the contact-based dynamics of single- and few-layer microscale granular crystals. The necessary background for each chapter is included in its introduction. Due to the collaborative nature of this work and to acknowledge the input from members of various research groups (including the Boechler Research Group), a short summary of the contributions of each collaborator for each of the projects is provided at the end of each chapter.

- In Chapter 2 "Resonant Attenuation of Surface Acoustic Waves by Two-Dimensional Microscale Granular Crystals", the interaction of surface acoustic waves (SAWs) with the contact resonances of a monolayer of microspheres is investigated. The first part of this chapter is based on reference [10] and describes the attenuation of surface acoustic waves by a strip of microspheres adhered to an aluminum-coated glass substrate. Measurements of the transmission of surface wave packets generated using the transient grating technique show a distinct resonant attenuation at the axial contact resonance frequency of the microsphere monolayer. In the second part of this chapter, measurements of the resonant attenuation of surface acoustic wave pulses generated by a laser line source are investigated, and reveal three collective vibrational modes that involve displacements and rotations of the microspheres, as well as interparticle and particle-substrate interactions. This section is based on reference [9]. This chapter extends the original work by Boechler and coworkers on the interaction of surface acoustic waves by

an axial contact resonance of a microsphere monolayer [11]. Finally, the measurements of the resonant attenuation of surface waves was used to recover the complex wave number, using a technique based on the spatial Laplace transform of the scanned data developed by Geslain and coworkers [192]. The last section of the chapter is based on reference [192]. The author of this dissertation fabricated the samples for the studies in the chapter, and participated in the discussion and interpretation of experimental results.

- In Chapter 3 "A Microscale Granular Crystal-based Metamaterial for Lamb Waves", the first experimental demonstration of a self-assembled metamaterial for ultrasonic wave tailoring of Lamb Waves is presented. This metamaterial comprises of a two-dimensional microscale granular crystal made of 1 μm polystyrene microspheres adhered to a silicon membrane. The microspheres act as locally resonant inclusions and couple with the Lamb Wave modes of the membrane. This chapter is based on reference [12]. The author fabricated the sample, performed the laser ultrasonic experiments and analyzed the experimental results in this study.

- In Chapter 4 "Scaling of Micro- to Nanosphere Contact Stiffnesses Studied via Vibrations of Two-Dimensional Microscale Granular Crystals", the scaling of the normal stiffness of the sphere-substrate contact, for colloidal particles ranging from 400 nm to 4.16 μm in diameter is studied. The normal contact stiffness calculated from the measured axial contact resonance of the monolayer of spheres is compared with predictions made by adhesive elastic contact models derived from the Hertz contact model. The scaling of the measured contact stiffness and the contact size is compared to adhesive contact models. The author fabricated the samples, performed the laser ultrasonic experiments, along with scanning electron and atomic force microscopy of the samples. The author also analyzed the experimental data, and improved the finite element model for elasto-plastic contact dynamics.

- In Chapter 5 "Tuning the Axial Contact Resonance of Microspheres via Microlensing",

a novel mechanism to tune the axial contact resonance of a monolayer of microspheres is investigated. A two-dimensional colloidal crystal comprised of close-packed silica microspheres acts as a microlens array, in which each silica sphere focuses the incident pump pulse light down to the contact area, and locally ablates the metal film directly beneath the sphere. This results in the formation of "pits" in the contact area, which change the contact geometry, and in turn, stiffen and increase the axial contact resonance. The author fabricated the sample, performed the experiments and SEM imaging, and analyzed the results in this chapter.

- In Chapter 6 "Longitudinal Eigenvibration of Few-layer Granular Crystals and the Effect of Nanoscale Contact Bridges", the longitudinal contact-based vibrations of three-dimensional colloidal crystals up to twelve layers thick, and composed of 390 nm polystyrene spheres, is studied. The particle-substrate and the effective interlayer contact stiffness is extracted from the measured eigenvibrations. Our findings show that the contact stiffnesses are drastically affected by the presence of nanoscale solid bridges between the colloidal particles, which are also seen using scanning electron microscopy (SEM) and atomic force microscopy (AFM). The author fabricated some samples in this study, performed experiments and analyzed the results.

- Finally, in Chapter 7 "Guided Surface Acoustic Waves in Few-layer Granular Crystals", the dispersion of guided surface acoustic waves propagating along the granular multilayer/substrate interface is studied using the transient grating technique. The measured guided wave dispersion curves obtained from three- and five-layer-thick granular crystals are fitted to those predicted by an analytical model of a classical elastic layered half-space [193]. The effective longitudinal and transverse sound speeds in few-layer, three-dimensional granular crystals are extracted using this approach. The author fabricated some samples in this study, performed experiments and analyzed the results.

Chapter 2

RESONANT ATTENUATION OF SURFACE ACOUSTIC WAVES BY TWO-DIMENSIONAL MICROSCALE GRANULAR CRYSTALS [1]

2.1 Introduction

In this chapter, we study the frequency-selective attenuation of surface acoustic waves by two-dimensional microscale granular crystals adhered to elastic substrates. As stated in Section 1.1.4, a spherical particle adhered to a solid substrate yields a "mass-spring" axial contact resonance due to the Hertzian contact between the sphere and the substrate [11,110]. A previous study had demonstrated that an axial contact resonance of a monolayer of micron-sized spheres strongly interacts with surface acoustic waves (or Rayleigh waves [194]) in the substrate [11], yielding a locally resonant metamaterial for SAWs [11]. In this work, we study the attenuation of surface acoustic waves in two cases. In the first case, we consider the transmission of laser-generated surface acoustic wave packets through a thin strip (170 μm wide) of 1 μm sized polystrene spheres adhered to a glass substrate. Monochromatic surface wave packets are generated on the blank region of the substrate using the transient grating technique, and detected on the bare region of the substrate on the other side of the microsphere strip after the wave packet travels through the strip. In the second case, we measure of the resonant attenuation of laser-generated surface acoustic waves pulses using the photodeflectometry technique. The sample is progressively scanned, allowing us to measure the SAW pulse as it propagates further inside the monolayer of microspheres.

[1] This chapter is based on references [9, 10, 192]. Copyright 2016 by the American Institute of Physics [10, 192] and the American Physical Society [9].

Our measurements reveal three collective, contact-based vibrational modes of the granular crystal, that involve displacements and rotations of the microspheres, as well as interparticle and particle-substrate interactions.

2.2 Resonant attenuation of SAW packets by a strip of microspheres

As discussed in Section 1.1.3, granular media yield a range of unusual linear and non-linear acoustic phenomena of both fundamental and practical importance [48, 53, 195]. Natural granular materials such as sand have long been known to exhibit strong broad-band attenuation of acoustic waves [196]. More recently, studies of acoustic attenuation by model granular media comprised of monodisperse spherical particles offered insights into longstanding problems such as Anderson localization of elastic waves [197] and Cosserat elasticity [198]. Transmission of sound through ordered granular chains at the macroscale has been shown to yield narrow-band spectral features such as phononic band gaps [49, 199]. In this section, we study a different aspect of acoustic attenuation by a granular material, namely, the resonant attenuation of surface acoustic waves (SAWs) traveling in a solid substrate induced by a monolayer of microparticles on the substrate surface.

2.2.1 Experimental Details

The sample used in this study comprised a strip of microspheres adhered to a 1.5 mm thick soda-lime glass substrate coated with 100 nm of aluminum. A floating monolayer of 1.02 μm diameter monodisperse polystyrene spheres was self-assembled at an air/water interface using a modified Langmuir-Blodgett technique [5], and subsequently transferred onto the aluminum-coated side of the substrate. A micro-contact printing technique [200], using a poly(dimethylsiloxane) (PDMS) stamp, was employed to selectively remove the micro-

spheres from the glass substrate using a lift-off process, leaving behind a 170 μm-wide strip of microspheres with bare substrate on either side of the strip, as shown in Figure 2.1(a). A magnified image in Figure 2.1(a) shows considerable disorder in the monolayer packing inside the strip.

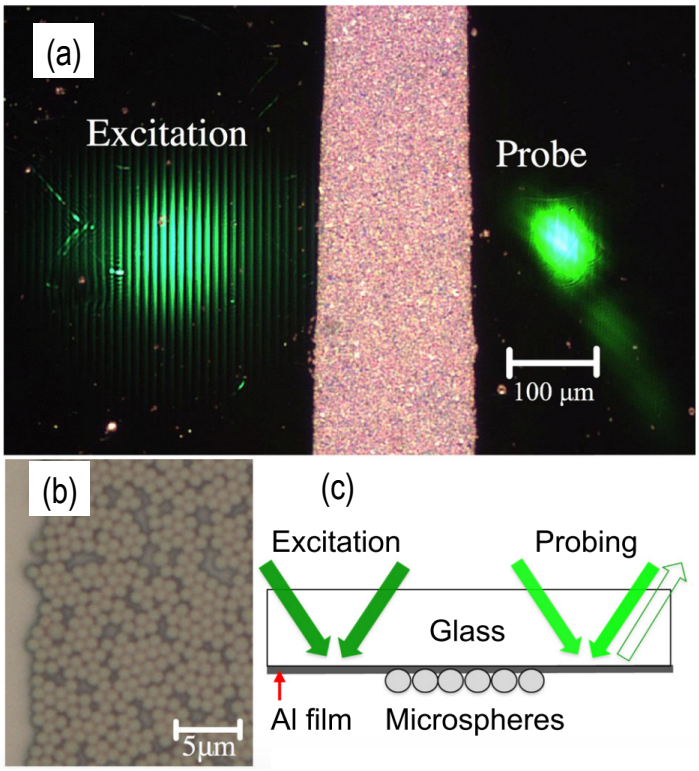

Figure 2.1: (a) Photograph of the sample; excitation and probe spots on either side of the microsphere strip are visible due to partial transmission of light through the aluminum layer. (b) Magnified view of the spheres. (c) Schematic diagram of the measurement: SAWs are excited by a pair of crossed excitation pulses, travel through a microsphere-coated region and are detected via diffraction of the probe beam. The reference beam used for heterodyne detection is overlapped with the probe. Figure is taken from reference [10]. Copyright 2016 by the American Institute of Physics.

Measurements were performed using the laser-induced transient grating technique [175] modified to spatially separate the excitation and detection of SAWs and to enable a fine control of the SAW wavelength. These measurements were performed by collaborators from the Nelson Research Group at MIT. The basic setup was similar to that used in references [8, 11]. Additional details of the experimental setup are provided in reference [10] and in the thesis of J. Eliason [177]. The SAW excitation spot can be clearly seen in Figure 2.1(a). The absorption of laser light in the aluminum film led to rapid thermal expansion that generated counter-propagating SAW wave packets at wavelength L. The detection of SAWs was done via diffraction of a probe laser beam focused to a spot of 90 μm in diameter at a distance 440 μm from the excitation spot.

2.2.2 Results and Discussion

SAW packets were generated and detected at different wavelengths with and without the microsphere strip in between the excitation and probe spots (this was done by translating the sample to move the relative location of the microsphere strip with respect to the laser spots). The frequency-dependent attenuation of SAWs by the microsphere strip was performed by calculated by normalizing the Fourier transform (FT) of the SAW wave packet transmitted by the strip at different wavelengths with respect to those that were measured without the presence of the strip. The presence of the microsphere strip resulted in moderate attenuation of SAW wave packets at 130 and 422 MHz whereas the SAW wave packet at 235 MHz was completely blocked by the strip. By contrast, surface skimming longitudinal waves are not affected by the presence of the spheres. Figure 2.2 shows the dependence of the attenuation on the SAW frequency, which reveals a deep dip in transmission around 240 MHz. Varying the frequency in the small steps necessary to trace the attenuation peak was made possible by rotating the phase mask in the transient grating setup [178]. The maximum attenuation could not be measured as the transmitted SAW signal was below the noise level; the filled

circles in Figure 2.2 show the upper bounds for the transmission at about 43 dB. This corresponds to an attenuation length of 17 μm at the $1/e$ intensity level, which amounts to only 1.3 SAW wavelengths (on the substrate without microspheres).

To elucidate the origin of the sharp peak in the attenuation, we measured dispersion of SAWs inside the microsphere-coated area by overlapping the excitation and probe spots inside the microsphere strip. The measured acoustic dispersion showed a clear splitting of the Rayleigh wave around 240 MHz. The measured hybridized dispersion can be described by the analytical model developed in reference [11], which assumes the substrate to be an elastic half-space, and the top surface of which is connected to an array of linear surface oscillators with a single axial degree of freedom.

For a more realistic description of the attenuation observed in Figure 2.2, the original model presented in reference [11] was modified in reference [10] with the addition of a damping term. The modified model describes the hybridized dispersion of SAWs that relates the angular frequency ω and the wave number k as follows,

$$\left(\frac{\omega^2}{{\omega_0}^2}+\frac{2i\omega\gamma}{{\omega_0}^2}-1\right)\left[\left(2-\frac{\omega^2}{k^2{c_T}^2}\right)-4\left(1-\frac{\omega^2}{{c_T}^2}\right)^{\frac{1}{2}}\left(1-\frac{\omega^2}{{c_L}^2}\right)^{\frac{1}{2}}\right]=\frac{mN}{\rho}\frac{\omega^4}{{c_T}^4k^3}\left(1-\frac{\omega^2}{k^2{c_L}^2}\right)^{\frac{1}{2}} \tag{2.1}$$

Here, c_L and c_T are the longitudinal and transverse sound speeds, respectively, in the substrate, m is the mass of the microsphere, N is the average number of microspheres per unit area, ω_0 is the contact resonance frequency, ρ is the density of the substrate, and γ is the gamma coefficient. The damped contact resonance model was fitted to the observed attenuation of SAWs, and is represented by the dashed curve in Figure 2.2. We note that in the case of a Bragg bandgap of a phononic crystal, the maximum of attenuation is typically located in the middle of the band-gap [201], whereas in the local resonance case, the attenuation

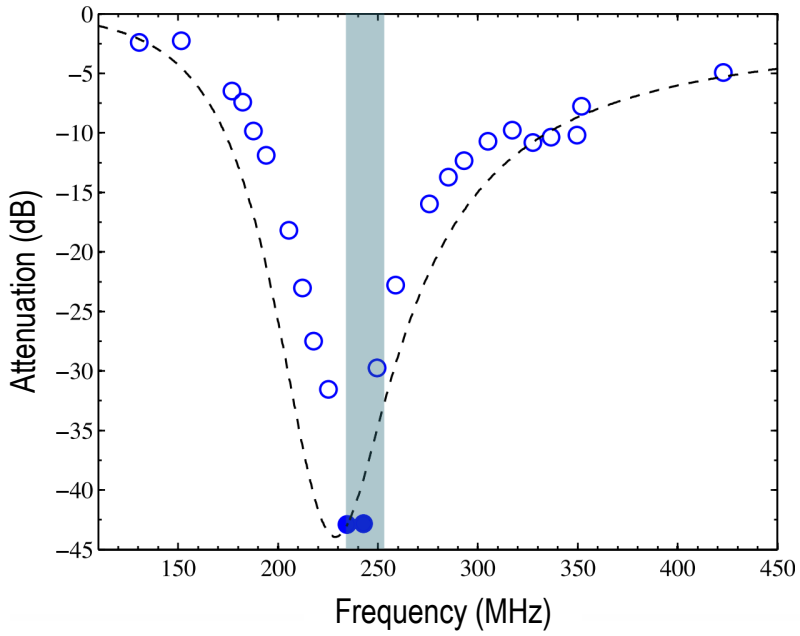

Figure 2.2: Measured SAW attenuation vs. frequency (open symbols). Solid symbols show upper bounds (transmitted SAWs were below the noise level). The dashed curve has been calculated based on the imaginary part of the wave vector obtained an analytical model that includes a damping term [10]. The shaded region corresponds to the acoustic bandgap, i.e., the frequency range yielding a complex wave vector in the analytical model without damping [11]. Figure is taken from reference [10]. Copyright 2016 by the American Institute of Physics.

curve is close to a Lorentzian centered at the resonant frequency, as is well known from the Lorentz oscillator model in optics [202]. In general, the attenuation caused by a local resonance should not be interpreted as a consequence of the band-gap, particularly when the line width exceeds that of the band-gap, as is the case in our experiment. As shown in reference [203], depending on the damping and oscillator strength, the avoided crossing may or may not form, whereas the attenuation peak at the resonant frequency is always present (this is also well known in optics where the locally resonant band-gap corresponds to a band

of negative dielectric constant above the resonant frequency [202]).

2.3 Resonant attenuation of SAW pulses by a monolayer of microspheres

The results presented in references [10,11], as well as those discussed previously in Section 2.2, could be well described with a simple model where the particle motion was restricted to the vertical (out-of-plane) degree of freedom and the interaction between the particles was disregarded. However, models involving both rotations and interparticle interactions [204, 205] predicted more complex dynamics. For motion in the sagittal plane, a close-packed monolayer of spheres on a solid substrate is expected to yield three collective contact-based vibrational modes: one predominantly vertical, and two of mixed horizontal-rotational character, all of which should interact with SAWs [204].

In this section, we present experimental results that reveal the presence of all three contact resonances predicted for the microsphere monolayer, by measuring the attenuation of SAWs using a scanned laser ultrasonic technique. We test the model developed by Wallen and coworkers in reference [204] by changing the interparticle contact stiffness via the deposition of a thin aluminum film on top of the spheres, which shifts the horizontal-rotational contact resonance frequencies upwards. We further confirm the nature of the modes using a complementary laser-ultrasonic technique that preferentially excites the vertical contact resonance. In addition to providing direct evidence of the rotational-vibrational dynamics of microgranular media, our work opens a new approach for the study of micro- to nanoscale particle contact mechanics by enabling measurements of both the interparticle and particle-substrate contact stiffness and offering insight into the role of shear contact rigidity.

2.3.1 Experimental Details

Our sample is a monolayer of $D = 2.0$ μm diameter silica microspheres deposited on an aluminum-coated glass substrate, as shown in Figures 2.3(a) and (b). The aluminum layer is 100 nm thick, and the glass is 1.5 mm thick. The monolayer of microspheres is assembled using the wedge-shaped cell convective self-assembly technique, discussed in Section 1.3.1. To obtain a planar interface between substrate regions with and without the microsphere monolayer (hereafter referred to as the monolayer and blank regions, respectively), we use a microcontact-printing method, wherein a soft polydimethylsiloxane (PDMS) stamp is pressed into conformal contact with the microsphere monolayer and then is removed, such that the spheres detach from the substrate in the stamped region [200]. A representative optical microscope image of the resulting interface is shown in Figure 2.3(b).

To generate and measure SAW propagation in our sample, we utilize a scanning laser-ultrasonic technique, as shown in Figure 2.3(c), and discussed in Section 1.4.3. The measurements were conducted by co-author of reference [9], M. Hiraiwa. We focus a subnanosecond laser pulse, which serves as a "pump" into a line on the aluminum surface of the blank region of the substrate. The absorbed laser light launches broadband SAW pulses that propagate as plane waves perpendicular to the line source. The acoustic response of the sample is measured via the knife-edge photodeflection technique (see Section 1.4.3). A "probe" beam is incident through the substrate and focused to a small spot on the aluminum film using an objective lens. The reflected probe light is focused onto a fast photodetector, after being partially blocked by a knife edge. Changes in the surface slope and refractive index caused by the SAWs deflect the probe beam, which translates to a change in intensity on the photodetector. To obtain spatial information, the sample is automatically scanned in the direction of the SAW propagation. Both the pump and probe are initially focused onto the blank region, then moved progressively closer to the interface, with the probe crossing into the monolayer region. Additional details on the laser ultrasonic experiment are provided in

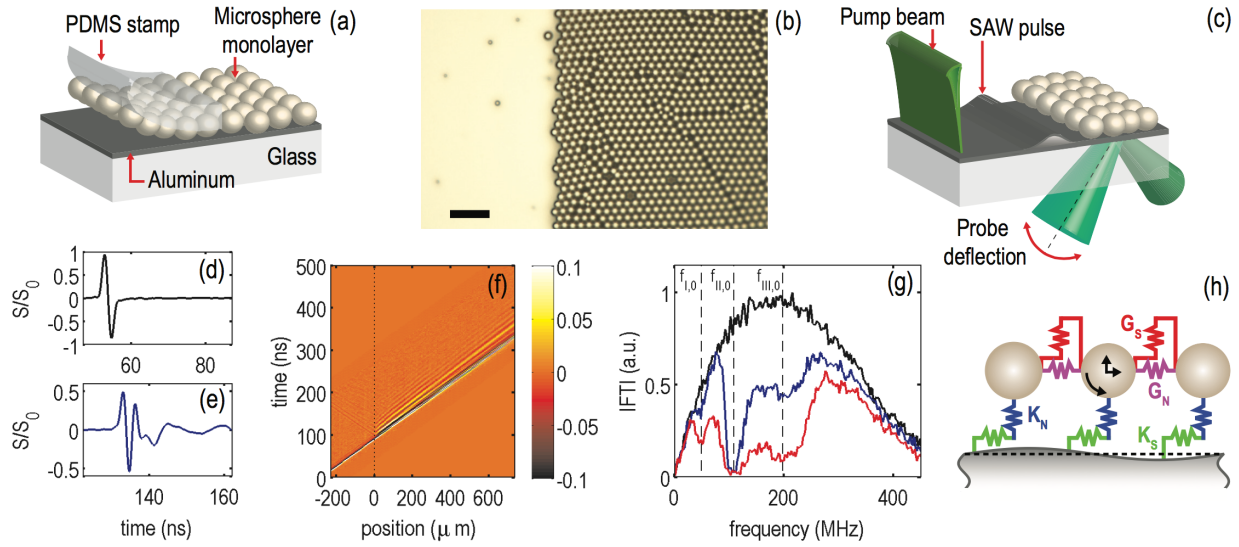

Figure 2.3: Overview of the experiment. (a) PDMS stamp is used to remove a portion of a microsphere monolayer deposited on aluminum-coated glass microscope slide. (b) Microscope image of the interface between monolayer and blank sample regions. The scale bar is 10 μm. (c) Schematic of the scanned laser ultrasonic experimental setup. (d) Normalized signal measured in the blank region. (e) Normalized signal measured 132 μm inside the monolayer region. (f) Spatiotemporal plot of the normalized measured signals. Position denotes distance from the interface. The vertical dotted line denotes the interface. (g) Normalized Fourier spectra of the signals in (d) and (e) using the same colors. The red curve is the spectrum of a signal measured 400 μm inside the monolayer region. Vertical dashed lines denote the identified contact resonance frequencies. (h) Schematic of the dynamical model. Figure is adapted from reference [9]. Copyright 2016 by the American Physical Society.

reference [9].

2.3.2 Results and Discussion

Figures 2.3(d) and (e) show typical measured signals S, normalized to the maximum signal amplitude S_0 measured during the scan. Figure 2.3(d) corresponds to a probe position in the blank region, and Figure 2.3(e) corresponds to a probe position 132 μm inside the monolayer region. The distortion of the signal in Figure 2.3(e) is a result of dispersion and dissipation induced by the monolayer. Figures 2.3(f) presents a spatiotemporal plot of the signals measured throughout the scan, which shows the distortion of the pulse as it propagates through the monolayer region. The Fourier spectra of the normalized signals in Figures 2.3(d) and (e) are shown in Figure 2.3(g). The spectrum corresponding to the signal in the monolayer region shows a sharp dip at 108 MHz. We also observe two smaller dips surrounding this resonance, and denote the three dips with vertical lines drawn at $f_{I,0} = 49$ MHz, $f_{II,0} = 108$ MHz, and $f_{III,0} = 197$ MHz. We also show a third spectrum, corresponding to a location 400 μm inside the monolayer region, which demonstrates the evolution of the attenuation zones.

To obtain position-dependent transmission spectra of SAWs traversing the interface, we normalize the Fourier spectra at each position by the average Fourier spectra of the incident SAW (averaged over all positions in the blank region). Figures 2.4(a) shows the measured transmission spectra as a function of distance from the interface. Three distinct attenuation maxima are evident, corresponding to the identified dips in Figure 2.3(g). We interpret the measured attenuation maxima as being caused by the interaction of SAWs with contact resonances of the microsphere monolayer, as described by the model developed by Wallen and coworkers in reference [204]. In this model, the microspheres are considered as rigid bodies, and the sphere-substrate and sphere-sphere contacts are represented as normal and shear springs, as is shown in Figure 2.3(h). This model predicts three collective vibrational modes of the monolayer involving vertical, horizontal, and rotational motion of spheres in the sagittal plane [204].

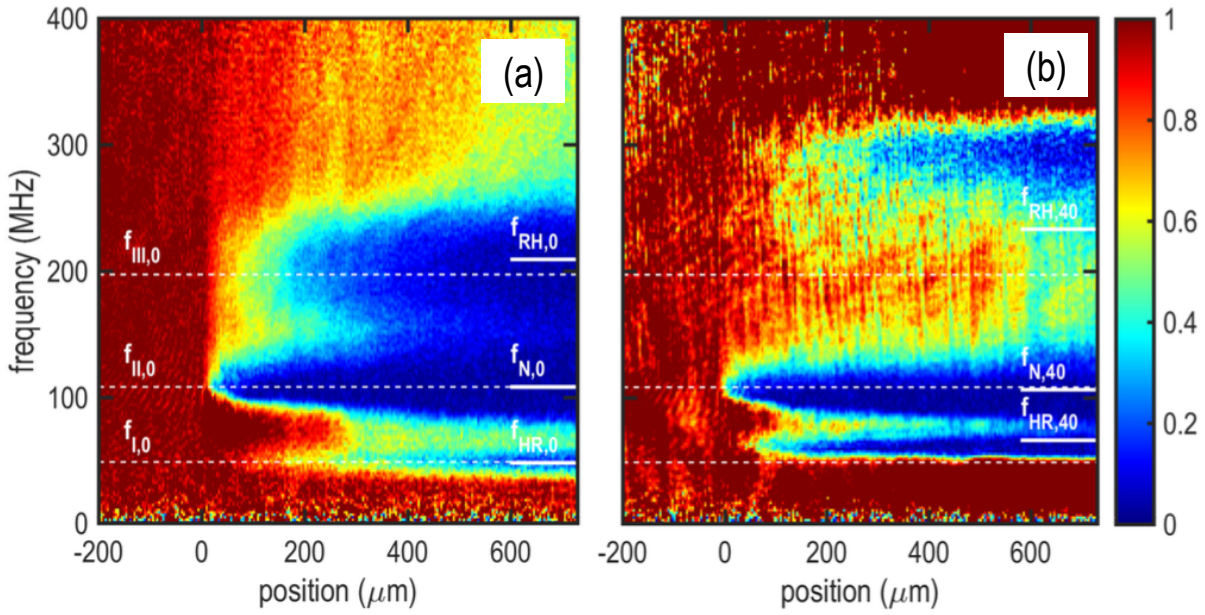

Figure 2.4: Transmission spectra for SAWs propagating across the interface between blank and monolayer regions in (a) the uncoated microsphere monolayer, and (b) monolayer coated with40 nm of aluminum. The color bar denotes the magnitude of the transmission coefficient. Horizontal dashed lines denote the identified contact resonance frequencies for the uncoated monolayer. Short horizontal lines on the right of the panel are the fitted contact resonance frequencies. Position denotes distance from the interface. Figure is adapted from reference [9]. Copyright 2016 by the American Physical Society.

The model developed by Wallen and coworkers in reference [204] predicts that at long wavelengths (compared to the particle spacing), one of the modes is purely vertical, with a frequency given by:

$$f_N = \frac{1}{2\pi}\left[\frac{K_N}{m}\right]^{1/2} \tag{2.2}$$

while two others are of mixed horizontal-rotational character,with frequencies given by:

$$f_{RH} = \frac{1}{2\pi}\left[\left(\frac{K_S}{4m}\right)\left(20\gamma + 7 + \sqrt{400\gamma^2 + 120\gamma + 49}\right)\right]^{1/2} \tag{2.3}$$

$$f_{HR} = \frac{1}{2\pi}\left[\left(\frac{K_S}{4m}\right)\left(20\gamma + 7 - \sqrt{400\gamma^2 + 120\gamma + 49}\right)\right]^{1/2} \tag{2.4}$$

where $m = \rho\pi D^3/6$ is the microsphere mass, K_N is the particle-substrate normal stiffness, K_S is the particle-substrate shear stiffness, G_S is the interparticle shear stiffness, and $\gamma = G_S/K_S$. The interparticle normal contact stiffness G_N does not affect these resonances at long wavelengths. The frequency f_{RH} corresponds to the predominantly rotational mode and is always higher than the frequency of the predominantly horizontal mode f_{HR}. If the monolayer is placed on an elastic substrate, all three modes are predicted to interact with SAWs [204]. As can be seen from equations 2.2 and 2.3, f_N is determined solely by the particle-substrate contact, whereas f_{RH} and f_{HR} are affected by both contacts. Hence, if we increase the interparticle contact stiffness, only f_{RH} and f_{HR} are expected to increase.

To test the model and verify the nature of the observed contact resonances, we coat the microsphere monolayer with a thin aluminum layer using electron beam evaporation, which stiffens the interparticle contact without affecting the particle-substrate contact. This is because the particle-substrate contact remains in the "shadow" of deposition. Figure 2.4(b) show transmission spectrum of the monolayer coated with 40 nm of aluminum. The highest and the lowest attenuation maxima shift upwards upon the deposition of the aluminum, while the middle maximum remains nearly unaffected. The relatively small downshift of the middle resonance, which is approximately consistent with the predicted frequency downshift of approximately 4% due to extra mass loading, confirms our assignment of the middle resonance to f_N. In all cases, the middle zone has the largest attenuation, indicating stronger coupling of this resonance to the propagating SAWs.

2.4 Analysis of Acoustic Attenuation using Spatial Laplace Transform

In collaboration with researchers at the Langevin Institute and the University of Maine in Le Mans, we used the attenuation of SAWs by the microsphere monolayer, presented in Section 2.3, for the recovery of complex wave number information [192]. A new technique was developed by Geslain and coworkers for the analysis of complex attenuation phenomena in scanned spatiotemporal measurements [192]. The technique presented in reference [192] is based on a spatial Laplace transform of the measured acoustic wave field in the frequency domain, instead of the usual spatial Fourier transform. The Laplace transform provides information on both the real and imaginary parts of the poles, and is analyzed by the minimization of a chosen cost function. This allows the reconstruction of complex wavenumbers (as well as the complex amplitude) of the modes, even when they are interacting with other modes [192]. The complex dispersion curves (comprising of real and imaginary components of the wave number) were obtained using the spatial Laplace transform technique. The two rotational-translational resonances were both clearly visible in the dispersion curves corresponding to the imaginary part of the wavenumber. This method therefore provides information that cannot be obtained from 2D Fourier transforms.

2.5 Conclusion

In the first part of this chapter, we have studied the resonant attenuation of SAW packets as they propagate through a thin strip of microspheres adhered to a solid substrate. We have observed a strong peak in the attenuation of SAWs by a microsphere strip at the axial contact resonant frequency of the Hertzian contact between the microspheres and the substrate. While the use of the contact resonance of microspheres is not the only way of fabricating a

locally resonant metamaterial for SAWs, as is evidenced by previous works utilizing arrays of pillars or ridges for surface wave control [82,83], our granular crystal is unique in that the microspheres are only weakly connected to the substrate by van der Waals adhesion forces [57]. The microspheres can easily be removed (for example, by the stamping technique used to fabricate the sample for in this work, or even by high amplitude SAWs [206]), which could be used to make a reconfigurable SAW filter [28]. Furthermore, the resonant frequency can be controlled by affecting the stiffness of the Hertzian contact; for example, it could be tuned by temperature near the glass transition of the polymer used to make microspheres or as a layer between the microspheres and the substrate. It could also be tuned by any factor affecting the adhesion force; for example, the surface of the substrate or the microspheres could be functionalized to make the adhesion force sensitive to a certain chemical or biological agent.

In the second part of the chapter, we have studied the resonant attenuation of SAW pulses as they propagate through a microsphere monolayer. Our measurements reveal three collective vibrational modes that involve displacements and rotations of the microspheres, as well as interparticle and particle-substrate interactions. This study reveals the critical role of particle rotations: for instance, without rotations, the upper rotational-horizontal resonance would not be present [204]. Our characterization method is complementary to existing techniques [110–112, 207], as it is noncontact and nondestructive, offers information about equilibrium contact stiffnesses, and, in contrast to other dynamic techniques involving isolated particles [110–112], enables the measurement of the interparticle contact stiffness in a microscale multiparticle assembly. Finally, the sensitivity to contact forces in the microgranular monolayer may be used in sensors for bioanalytical [208] and other applications.

2.6 Collaborator Contributions

The results presented in this chapter have been made possible by contributions from several collaborators. The author of this dissertation fabricated the samples used for the ultrasonic measurements in this chapter, as well as participated in the discussion and interpretation of experimental results. The experiments described in Section 2.2 of this chapter were performed by J. Eliason, A. Vega-Flick and A. Maznev in the group of Prof. K. Nelson at MIT. J. Eliason, A. Vega-Flick and A. Maznev also analyzed the experimental data and developed the dissipative model that is described in reference [10]. The experiments described in Section 2.3 were performed by M. Hiraiwa and M. Abi Ghanem in the group of Prof. N. Boechler at the University of Washington. The spatial Laplace transform technique described in Section 2.4 was developed by A. Geslain and J.-P. Groby from the University of Burgundy and the Langevin Institute, respectively.

Chapter 3

A MICROSCALE GRANULAR CRYSTAL-BASED METAMATERIAL FOR LAMB WAVES [1]

3.1 Introduction

In this chapter, we report the design and characterization of a self-assembled, locally resonant acoustic metamaterial for Lamb waves, composed of a monolayer of 1.02 μm polystyrene microspheres adhered to a 1.27 μm thick free-standing silicon membrane. As discussed in Section 1.1.1, locally resonant acoustic metamaterials are a type of composite material that have been the subject of intense study over the past eighteen years [32] due to their ability to exhibit extreme [80,209], anisotropic [210], negative [79,211,212], strongly absorbing [213], and locally tailorable [214] effective properties. These unique properties stem from the interaction of propagating acoustic waves with typically subwavelength resonant elements forming the composite, although related phenomena are also observed when the metamaterial unit cell is of suprawavelength dimension [215]. This can present fabrication challenges as wavelengths are reduced, including challenges involved with constructing the resonators themselves and in making large areas of composite with complex microstructure. In this respect, colloidal self-assembly is a promising solution, as it has been shown to enable the simple, inexpensive, and fast fabrication of complex, ordered structures composed of nano- or microscale elements in one to three dimensions [153,216–218]. These advantages have driven the use of self-assembly strategies in multiple areas, particularly in the design of phononic crystals [74,219], photonic crystals [219–221], plasmonic sensors and nanostructures [222–224] and surfaces with tailored wettability [225]. Despite this wide use, there remain few examples of locally resonant

[1] This chapter is based on reference [12]. Copyright 2015 by the American Institute of Physics [12].

acoustic metamaterials fabricated using self-assembly techniques [11, 226–229].

Lamb waves are a type of acoustic waveguide mode that occur in thin elastic plates and membranes [230] and play an important role in nanomechanical resonator [231] and sensing applications [232]. They have also been utilized in studies of sub-THz phonon transport with implications for the understanding of nanoscale thermal phenomena [233]. Recently, several examples of locally resonant metamaterials for Lamb waves have been explored in both theoretical [234–236] and experimental [237, 238] settings. However, in each of the experimentally realized cases, the resonant elements forming the metamaterial had frequencies ranging from the audible regime to a few megahertz and were made using conventional machining or microfabrication techniques.

In this chapter, we present the realization of a self-assembled, locally resonant metamaterial for Lamb waves. As also discussed previously in Section 1.1.4, the microspheres have a contact resonance where the microsphere oscillates like a rigid body as a result of adhesion, with a localized region of elastic deformation around the point of contact with the substrate. In our system, the contact resonance plays the role of the metamaterial locally resonant element and has a frequency of 200 MHz. . This type of metamaterial may have potential future advantages for acoustic wave tailoring applications, as arrays of macroscale spherical particles have been shown to support unique nonlinear dynamical phenomena due to the Hertzian relationship [3] between spherical elastic particles in contact [48, 53].

3.2 Experimental Details

The metamaterial is composed of a monolayer of $D = 1.02$ μm diameter polystyrene microspheres deposited on, and adhered to, the aluminum side of an aluminum-coated (100)

silicon membrane of thickness $2H = 1.27$ μm, as shown in Figure 3.1. The thickness of the membrane was measured with ellipsometry. The aluminum film is 50 nm thick and serves as a medium to absorb the optical pump light. To fabricate the metamaterial, we utilize a self-assembly procedure, in which polystyrene microspheres are assembled at the air/water interface and then transferred to the membrane, as shown in Figure 1.5(b) [5]. The resulting monolayer covers nearly the entire area of the membrane, which has dimensions of 4.8 mm x 4.8 mm. A representative microscope image of the monolayer packing is shown in Figure 3.1(b).

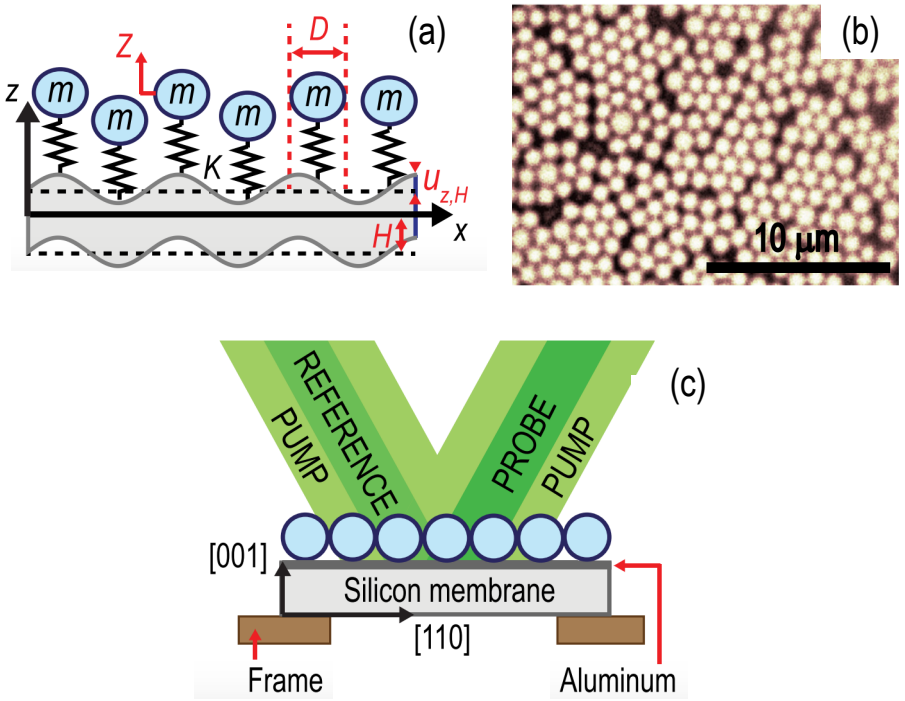

Figure 3.1: (a) Schmatic of the locally resonant metamaterial with indicated sphere and plate dimensions. (b) Representative image of the polystyrene microsphere monolayer.(c) Transient grating experimental setup used to generate and detect Lamb Waves. Figure is adapted from reference [12]. Copyright 2015 by the American Institute of Physics.

The laser-induced transient grating technique, discussed in Section 1.6, is used in this chapter to generate and detect Lamb Waves in the silicon membrane, and is summarized as follows. The configuration of the beams and the sample is illustrated in Figure 3.1(c). Two optical pump beams derived from a pulsed laser source (532 nm wavelength, 440 ps pulse duration, and 1 kHz repetition rate) are overlapped at the aluminum layer in the metamaterial and form a periodic interference pattern. The pump spot has a 500 μm diameter at $1/e^2$ intensity level. Absorption of the pump pulse light by the metamaterial induces a rapid thermoelastic expansion, which induces counterpropagating acoustic waves with a wavelength equal to the optical interference pattern that is defined by the crossing angle of the beams. The acoustic wavelength is controlled by changing a phase mask pattern used to split the pump beam into $+/-1$ diffraction orders. The detection of the metamaterial acoustic response is accomplished with a quasi-cw probe beam (wavelength 514 nm and average power 10.7 mW at the sample) chopped to 50 μs pulses with an electro-optic modulator. The probe beam passes through the same set of optics as the pump beam and is focused at the center of the interference pattern to a spot of 300 μm diameter. Pump-induced surface ripples and refractive index variations caused by the propagating acoustic waves (including contributions from the silicon membrane, aluminum film, and microspheres) lead to a time-dependent diffraction of the probe beam. The diffracted probe light is superimposed with an attenuated reference beam and is directed to a photodiode where it is recorded with an oscilloscope.

Using this technique, we measured the acoustic response of the aluminum-coated membrane before the microspheres were deposited (the "without-spheres" case). In this case, the pump pulses have an energy of 19 μJ and both pump and probe beams are incident on the aluminum-silicon interface in the metamaterial, such that they pass through the silicon membrane. As a result, the measured signal for the without-spheres case includes contributions from surface ripples from both the aluminum film and the silicon membrane, and refractive index variations in the silicon. After the microsphere deposition, we measured the

acoustic response of the metamaterial (the "with-spheres" case). In this case, both the pump and probe beams enter the metamaterial from the opposite side, such that they are incident on the aluminum-microsphere interface, and the pump pulse energy is reduced to 5.6 μJ. Measuring the side with the microspheres provides enhanced sensitivity to microsphere motion,16 in addition to signal contributions from surface ripples of the aluminum film.

3.3 Results and Discussion

Figure 3.2 shows the normalized Fourier spectra of the acoustic oscillations corresponding to the without- and with-spheres cases at $k = 0.78\ \mu\text{m}^{-1}$. In the without-spheres case, two peaks are clearly observed. We identify the low frequency peak at 270 MHz as the A_0 mode of the membrane, and the second peak at 1040 MHz, as the S_0 mode. Because of the presence of the aluminum film, we predominantly excite antisymmetric modes, as can be seen by the relative amplitude of the A_0 and S_0 modes [239]. We measure the dispersion of these two modes by varying the acoustic wavelength, and plotting the peaks identified in the Fourier spectra, as shown in Figure 3.3. The measured spectra and their identified peaks for all wavelengths can be found in the supplementary section of reference [12]. Using a silicon density of $\rho = 2.33\ \text{g/cm}^3$, and typical wave speeds in silicon [240] of $c_L = 9133$ m/s, (longitudinal) and $c_T = 5844$ m/s (transverse), corresponding to a propagation in the [110] direction with a transverse displacement along [001], the theoretical dispersion curves for the A_0 and S_0 modes in the membrane were calculated [12] using an isotropic model [193]. The experimental measurements agreed well with the calculated dispersion curves, as seen in Figure 3.3. The measured frequencies are slightly lower than predicted, which we attribute to the of an isotropic model in reference [12] instead of the fully anisotropic model [241]. Calculations accounting for the presence of the aluminum layer showed that the variation in the A_0 and S_0 dispersion curves due to the presence of the aluminum does not exceed 1% [12, 242]. A clear difference between the with- and without-spheres cases can be seen by

comparing the two spectra in Figure 3.2. In the with-spheres case, each of the A_0 and S_0 modes identified in the without-spheres case is surrounded by two peaks. In this case, we also see an additional peak near 70 MHz. We observe this peak to be present in both the without- and with-spheres cases for multiple wavelengths, and we do not consider it further for this study.

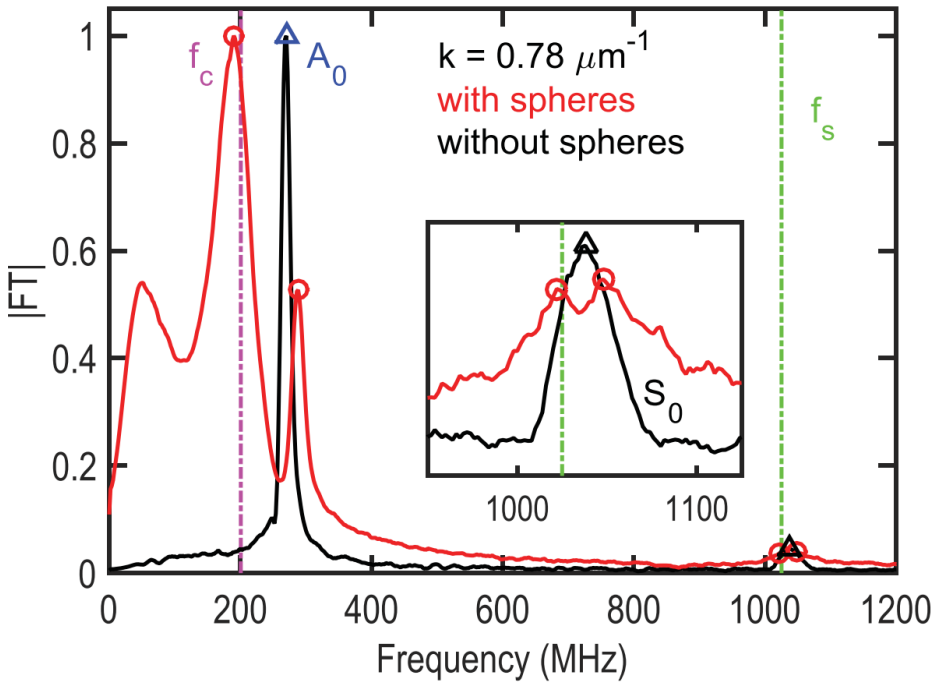

Figure 3.2: Spectra of Fourier transform magnitudes where the black curve corresponds to the without-spheres case, the red curve corresponds to the with-spheres case, and each spectrum is normalized to its maximum amplitude. The markers denote the identified peaks, which are plotted also in Figure 3.3 using the same markers and colors. The vertical lines denote the frequencies of the fitted microsphere contact resonance (f_c) and spheroidal resonance (f_s). The inset shows a closer view of the peaks corresponding to the spheroidal and dilatational modes. Figure is taken from reference [12].

The measured dispersion curves for the with-spheres case are plotted in Figure 3.3. The with-spheres dispersion curves reveal "avoided crossing" behavior between the A_0 branch and the microsphere contact resonance. The dispersion curves also show a flat branch at $f_s = 1030$ MHz that intersects with the S_0 branch, which we attribute to a microsphere spheroidal resonance. The spheroidal resonance frequency is obtained by averaging frequencies of the peaks identified along this branch. We note the presence of two peaks at $k = 0.78$ μm^{-1}. This suggests either a hybridization between the between the S_0 branch and the microsphere spheroidal resonance or simultaneous detection of the S_0 peak and the spheroidal resonance.

We compare the measured spheroidal resonance frequency with the frequency of the lowest frequency spheroidal mode $f(1,2)$ of a free homogeneous isotropic polystyrene sphere, where the first index denotes the mode number and the second the harmonic number. Applying the elastic equation for spheroidal modes [243], we calculate a frequency of $f(1,2) = 1030MHz$ using standard longitudinal and shear velocities for polystyrene of $c_{L,p} = 2350$ m/s and $c_{T,p} = 1200$ m/s [74], and a polystyrene density of $\rho_s = 1.06$ g/cm^3 as provided by the microsphere manufacturer (Corpuscular, Inc.). As the calculated frequency is in close agreement with the measured frequency, we utilize velocities $c_{L,p}$ and $c_{T,p}$ and density ρ_s to solve for the polystyrene microspheres elastic modulus $E_s = 4.04$ GPa and Poissons ratio $\nu_s = 0.32$. The simultaneous identification of both the spheroidal resonance and the contact resonance offers an opportunity to study the variation of each within the same microsphere array, as has previously been demonstrated for isolated nanospheres [110].

To describe Lamb wave propagation in our metamaterial, an analytical model was developed by Wallen and coworkers [13], using a similar approach as the e one used previously to describe the interaction of a contact resonance of microspheres with Rayleigh SAWs [11]. Details about the formulation of this analytical model for Lamb waves and their interaction

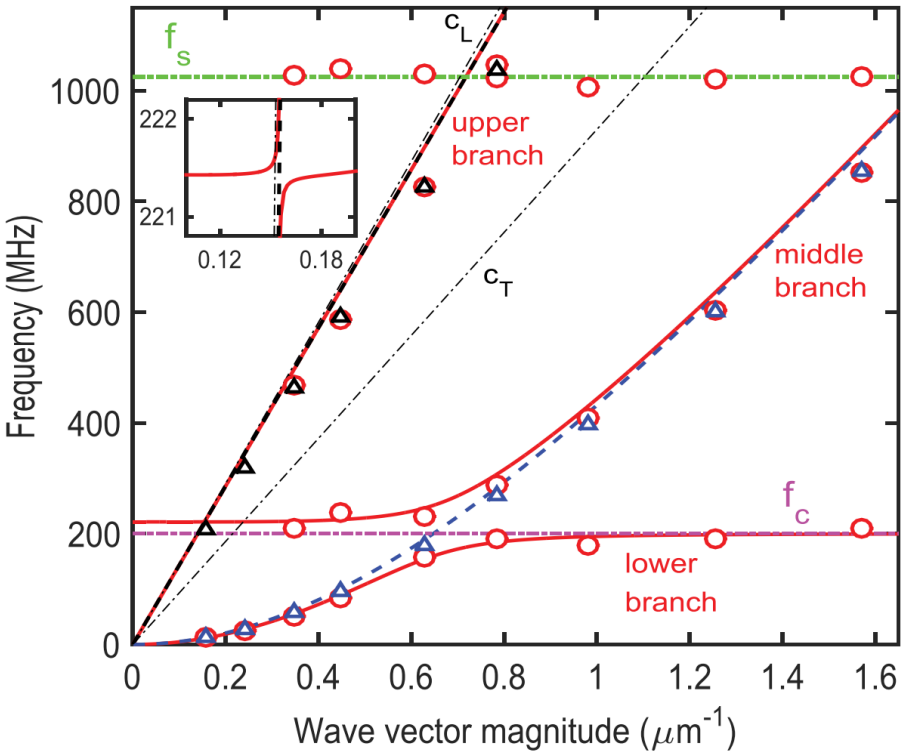

Figure 3.3: Dispersion relations. The circle and triangle markers are the measured frequency peaks for the with- and without-spheres cases, respectively. The solid red line is the dispersion calculated using the model developed by Wallen [13]. The dashed black line corresponds to the calculated S_0 mode and the dashed blue line to A_0 mode in the without-spheres case. The black dashed-dotted lines correspond to bulk waves in silicon. The horizontal lines denote the frequencies of the fitted microsphere contact resonance (f_c) and identified spheroidal resonance (f_s). The inset shows a closer view of the predicted avoided crossing with the S_0 branch. Figure is taken from reference [12]. Copyright 2015 by the American Institute of Physics.

with the contact resonance of the microspheres can be found in references [12, 13]. We note that the spheroidal resonance may similarly couple to SAWs in the substrate; however, we do not consider this in the current model [12,13]. Recently, Vega-Flick and coworkers experimen-

tally studied the low-frequency contact-based modes of a granular crystal monolayer, along with the high-frequency modes originating from spheroidal vibrations of the microspheres, and the surface Rayleigh waves in the substrate [125]. The authors in reference [125] observe a spheroidal resonance splitting caused by the symmetry breaking due to the substrate, as well as an avoided crossing between the Rayleigh and spheroidal modes.

By taking the frequency of the contact resonance as the only fitting parameter, and using least squares minimization between the measured dispersion curves and those predicted by the analytical model developed by Wallen and coworkers [12,13], we find the frequency of the contact resonance to be $f_c = 200$ MHz. We plot the theoretical dispersion curves calculated using the fitted contact resonance frequency in Figure 3.3. The theoretical dispersion curves show coupling between the flexural and dilatational modes due to the presence of the spheres adhered to one side of the membrane. In contrast to the coupling between Rayleigh SAWs and the microsphere contact resonance [11], the middle branch (as denoted in Figure 3.3) does not stop at the line corresponding to transverse polarized bulk waves and remains non-leaky due to the confinement of the membrane. This results in a second hybridization between the middle and the S_0 branch. The inset in Figure 3.3 shows a closer view of this intersection, which is smaller than the avoided crossing near the A_0 branch. The larger avoided crossing with the A_0 branch demonstrates stronger coupling between flexural motion and the contact resonance than with dilatational motion. This stronger coupling is a result of flexural modes having large out-of-plane displacement that couples with the vertical motion of the surface oscillators, in contrast to dilatational modes with predominantly in-plane displacements.

Finally, we estimate the frequency and stiffness of the microsphere contact resonance using the Derjaguin-MullerToporov (DMT) contact model [11, 108] assuming van der Waal's adhesion, and compare with the measured values. We obtain a contact resonance, $f_{c,DMT} = (1/2\pi)(K_{DMT}/m)^{1/2} = 108$ MHz, where $K_{DMT} = 0.27$ kN/m, is the stiffness of the contact.

To obtain the stiffness, we linearize the DMT contact model around its equilibrium position, as no anharmonic behaviors are observed for these pump powers, and we estimate the displacement of the surface to be much smaller than the equilibrium overlap of the microspheres [12]. In comparison, using the microsphere mass and the fitted contact resonance frequency fc, we obtain an experimentally derived contact stiffness of $K_c = 0.93\,\mathrm{kN/m}$. As for previous measurements on micron-sized silica [9, 11] and polystyrene [10] spheres adhered to thick aluminum coated fused glass substrates, we find that the contact stiffness derived from our measurement is larger than the predicted contact stiffness. The use of Johnson-Kendall-Roberts (JKR) elastic contact model [109] (assuming smooth particles with van der Waals interactions) results in little variation in the predicted contact resonance frequency. Within this context, uncertainties in parameters such as the work of adhesion between polystyrene and oxidized aluminum [57], may contribute to the lower predicted stiffness. More generally, measurements of microparticle adhesion are highly varied and depend on a wide range of factors outside of this context, such as the presence of surface roughness, plastic and viscoelastic deformation, solid impurities, surface functional groups, and capillary condensation [27, 57, 111, 244–246]. The latter is of special importance as it can lead to the formation of liquid [27, 247] or solid bridges [248] that strongly increase the stiffness of the contact.

3.4 Conclusion

We have presented a self-assembled, locally resonant metamaterial for Lamb waves. With their high characteristic frequencies and small length scales, these metamaterials hold promise for the development of new types of devices involving Lamb waves. Since the response is sensitive to the state of the contact, these metamaterials may have potential applications as sensors for humidity, temperature, and micro/nanoscale material properties, and serve as a platform for the exploration of microscale contact mechanics. Because of the scalability enabled by self-assembly, this type of metamaterial may enable future studies that explore

the interaction of local mechanical resonances with even higher-frequency phonon transport. Finally, the use of self-assembly approaches may also offer significant potential advantages for producing acoustic metamaterials inexpensively and on a large scale.

3.5 Collaborator Contributions

The author of this dissertation fabricated the sample used for ultrasonic measurements. The experiments were performed by the author, together with M. Abi Ghanem. M. Abi Ghanem and the author analyzed the experimental data. The analytical model used to describe the Lamb wave dispersion was developed by S. Wallen.

Chapter 4

SCALING OF MICRO- TO NANOSPHERE CONTACT STIFFNESSES STUDIED VIA VIBRATIONS OF TWO-DIMENSIONAL MICROSCALE GRANULAR CRYSTALS

4.1 Introduction

In this chapter, we study how the normal stiffness of the sphere-substrate contact scales with particle radius, for colloidal particles ranging from 400 nm to 4.16 μm in diameter. Using a sub-nanosecond laser pulse, we excite axial contact vibrations of monodisperse monolayer colloidal crystals. From the measured axial contact resonance of the monolayer of spheres, we then calculate the normal contact stiffness, and compare it with predictions made by adhesive elastic contact models derived from the Hertz contact model. We further compare equilibrium contact radii measured using atomic force microscopy (AFM) and scanning electron microscopy (SEM) imaging, and study the scaling of the measured axial contact stiffness with the equilibrium contact radius, as well as the respective values predicted by adhesive elastic contact models. Finally, the effects of adhesion-induced plasticity on the initial deformation, and the normal contact stiffness, are also discussed.

As described in Section 1.1.5, a number of models have been developed to describe the force-displacement relationship, and the deformation profile, of bodies in contact under the influence of adhesion. To verify the applicability of these contact models, several contact and non-contact-based experimental techniques have been used to investigate the adhesion between micron and sub-micron sized particles by measuring contact parameters such as the pull-off force, the force-displacement relationship, the change in the contact area with

applied load as well as the contact area at equilibrium. The atomic force microscope (AFM) colloidal probe technique emerged as popular method to characterize the microparticle adhesive contact in the early 1990s [27, 249]. Pioneered by Ducker [250] and Butt [251], this technique involves the direct attachment of the microparticle to be examined to an AFM cantilever, and has been widely used to measure the pull-off force of individual micron-sized polystyrene (PS), glass, metal [106, 252] and metal oxide particles [253] from flat substrates. While the pull-off force was found to scale linearly with the sphere size (in good agreement with the JKR and DMT contact models), the measured pull-off forces were lower than the expected JKR model predictions [106, 252]. The lower pull-off forces measured using this technique were attributed to surface roughness, which tends to increase the mean separation between the two interacting bodies, and therefore, decrease the net adhesion [254]. While the AFM-based colloidal probe technique has provided insight into the contact mechanics at the microscale, the contact-mode AFM technique imposes a high local pressure as well as shear stresses on the surface, and further increases the system complexity [255]. Fuchs and coworkers extended the idea of the colloidal probe technique to a nanoindenter setup to allow testing larger particles at higher maximum normal loads, as well as characterizing the rolling and torsional friction of individual microparticles [207]. Paul and coworkers evaluated the force-deformation behavior of isolated silica microspheres in the elastic and plastic regimes using a custom-built compression device supported in a scanning electron microscope (SEM) [105]. While these contact-based techniques have provided quantitative insight into the nature of the microcontact, contact-based techniques that require particle detachment are disruptive in nature, and involve several complex physical effects such as energy release, plastic deformation, and mass transfer at the nano-/micro-scale [27].

To overcome these complexities, several non-contact techniques have been developed to study contact mechanics at the micro- and nano-scale. Rimai and coworkers [256–261] and Wang and coworkers [262–264] visually observed the sphere-substrate [256–262] and the sphere-

sphere contacts [263, 264] of individual particles ranging from 60 nm to 100 μm in diameter. They compared the scaling of the visually observed equilibrium contact radii with the sphere size to the power law exponents predicted by adhesive elastic and elasto-plastic contact models. In their studies [258, 261], Rimai and coworkers found that the scaling of the contact radius with the sphere radius was consistent with that predicted by the DMT and JKR models for glass particles between 5 and 60 μm on polyureathane substrates, while particles less than 5 μm scaled with an anomalous power law. In other cases [257, 262–264], the contact size scaling was consistent with the power law dependence given by the MP model, indicating plastic deformation induced by adhesive forces. Recently, Nicolet and Meli investigated the scaling of the equilibrium contact radius with sphere size, for PS particles (ranging from 150 nm to 700 nm in diameter) adhered to mica substrates [265]. As opposed to measuring the contact radii from visual observations via SEM, the authors estimated the contact radii using AFM measurements of the "footprint" of the spheres left on the substrate. Contrary to theoretical models, the authors found a linear relationship between the contact radius and the sphere size [265].

Vibrational resonances of micro- and nanoparticles, formed as a result of adhesion and measured via dynamic excitations, have also been used to evaluate the contact mechanics. Experimental setups involving particles adhered to quartz crystal microbalances (QCM) have been used to evaluate the coupling strength of the particle-substrate contact by measuring the change in the resonance frequency of the QCM [112]. Cetinkaya and coworkers extracted the work of adhesion from the rocking motion of microparticles on a transducer, and found good agreement with theoretical values [111, 266]. The authors also observed nonlinear dynamics of the rocking resonance [267]. As described in the previous chapters in this dissertation, recent studies investigating the collective contact-based axial vibrations of silica [9, 11] and polystyrene [10, 12] microsphere monolayers adhered to elastic substrates (a class of "micro-scale granular crystals") have found the sphere-substrate axial contact

stiffness to be about two times higher and the equilibrium contact radius [268] to be about five times higher than the corresponding DMT and JKR model predictions using theoretical work of adhesion values. Factors such as uncertainties in the work of adhesion or plasticity at the contacts [9, 268, 269] were postulated as reasons for these discrepancies. Dynamic measurements of the vibrational resonances of microparticles have provided a non-contact means of studying the nature of the contact and adhesion at the micro-scale; however, such measurements have not shed light into the possible nonlinearity of the contact as predicted by the DMT and JKR models. Guillet and coworkers used an optical pump-probe spectroscopy technique to study the scaling of the axial contact stiffness with the particle size of single gold nanoparticles (60 to 700 nm in diameter) deposited on a glass substrate [110]. While the authors found the measured contact stiffness/sphere radius scaling to be in excellent agreement with the power law dependence given by the DMT and JKR models, the absolute values of the measured contact stiffness were not compared to those predicted by the DMT and JKR models by using the theoretical sphere-substrate work of adhesion computed using the Lifshitz theory of van der Waal's adhesion [57]. The scaling of the contact stiffness with the contact radius at equilibrium was also not explored.

In this chapter, we study the scaling of the normal stiffness of the sphere-substrate contact with the sphere and contact radius for polystyrene spheres, ranging from 400 nm to 4.16 μm in diameter, adhered to flat substrates. We compare the observed scaling with power law exponents predicted by adhesive elastic and elasto-plastic contact mechanics models. The normal contact stiffness is calculated by exciting and detecting the out-of-plane, resonant axial contact vibrations of the spheres about their equilibrium displacements using a laser ultrasonic technique. We estimate the equilibrium contact radii by measuring the size of polymeric "rings" deposited around the sphere-substrate contacts, and supplement these measurements by estimates made from visual observations of the sphere-substrate contacts made using scanning electron microscopy. We find that the scaling of the sphere-substrate

normal contact stiffness with the sphere radius is in good agreement with the power law dependence predicted by the DMT and JKR models of adhesive elastic contact, although the measured stiffnesses are over two times higher than those predicted by the DMT and JKR models with the work of adhesion calculated using the Lifshitz theory of van der Waal's adhesion [57]. The measured equilibrium contact radii are in reasonable agreement with those calculated using the MP elaso-plastic contact model, but higher than elastic models, which suggests large displacements and possible plastic deformation [131] as a result of adhesive forces. We note that the MP model does not capture the observed scaling of the equilibrium contact radii with the sphere radius. We develop a finite element model to simulate the elasto-plastic force-displacement behavior of contact between a polystyrene sphere and an aluminum substrate by assuming elastic perfectly-plastic response for the polystyrene sphere. From the FEM model, we calculate the contact stiffness during load-unload cycles at various levels of deformation, and find that the stiffness at equilibrium corresponds to that predicted by elastic models at the simulated contact radius. Using this observation in conjunction with the Maugus-Pollock model, we find that the magnitude of the measured stiffnesses also agrees well with the stiffnesses predicted when the effects of plasticity are taken into account, due to the increased contact area. However, the scaling of the stiffness with particle size does not match the predicted trend. Finally, we compare the scaling of the measured normal contact stiffness with the measured equilibrium contact radius, and find good agreement with the linear relationship predicted by the DMT and Hertz contact theories, as well as by the FEM model.

4.2 Experimental Details

The samples in our study comprise of hexagonal-close-packed (HCP) monolayers of polystyrene spheres adhered to an aluminum-coated glass substrate of thickness 1.5 mm. The aluminum film on the glass substrate is 100 nm thick and serves as a transducer layer in the laser ultra-

sonic experiments. Colloidal crystal monolayers are fabricated with twelve different sphere sizes ranging from 400 nm to 4.16 μm in diameter, with polydispersity less than 5 %. The spheres were obtained from Corpuscular Inc. (Cold Springs, NY), or were synthesized by the group of N. Vogel using an emulsion-polymerization process (referred to as "in-house" spheres) [270]. In the case of the particles obtained from Corpuscular Inc., the diameters of the particles were provided by the manufacturer, while for the in-house particles, the average particle diameter was determined from SEM images. The PS sphere monolayers were assembled on top of the substrate using a modified Langmuir-Blodgett technique described in Section 1.3.2, in which a floating monolayer was pre-assembled at an air-water interface and subsequently transferred to the substrate [5]. This technique resulted in semi-ordered monolayers, with notable line and point defects. A top-down view optical microscope image of a representative monolayer of 1 μm spheres is shown in Figure 4.1(a). Table 4.1 summarizes the details of the colloidal particles investigated in this study, which include the sphere diameter and supplier.

Table 4.1: Details of colloidal particles whose contact properties were evaluated in this study. The particle sizes were provided by the manufacturer, or for the case of in-house samples, determined from SEM images.

S. No.	Sphere Diameter [μm]	No. of Replicates	Supplier
1	0.4	2	In-house
2	0.5	3	Corpuscular Inc.
3	0.6	2 1	In-house Corpuscular Inc.
4	0.7	3	Corpuscular Inc.
5	0.802	2	Corpuscular Inc.
6	0.93	3	Corpuscular Inc.
7	1	1 2	In-house Corpuscular Inc.
8	1.45	3	Corpuscular Inc.
9	2	3	Corpuscular Inc.
10	2.89	3	Corpuscular Inc.
11	3.5	3	Corpuscular Inc.
12	4.16	3	Corpuscular Inc.

The collective axial contact vibrations of the sphere monolayers were excited using the all-optical, non-contact laser ultrasonic technique shown in Figure 4.1(b). Optical pump pulses of 440 ps duration of wavelength 532 nm, pulse energy 1 μJ and repetition rate 1 kHz, were focused to a circular spot of 500 μm on the aluminum film of the sample either through the glass substrate, or directly through the spheres. Absorption of the pump pulse energy

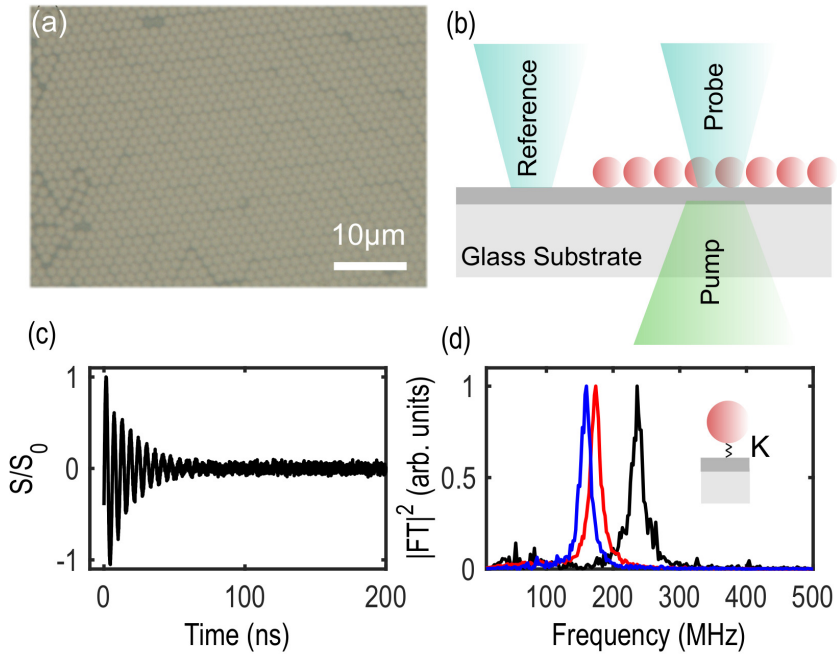

Figure 4.1: (a) Representative optical microscope image of a monolayer of 1 μm diameter PS spheres. (b) Schematic of the laser ultrasonic technique used to excite and detect axial contact vibrations of the micro- to nano-scale spheres on an aluminum-coated glass substrate. (c) Interferometric signal (normalized to its maximum amplitude after removal of the slow thermal decay) showing the out-of-plane oscillations of the monolayer of 1 μm diameter PS spheres. (d) Power spectra with peaks corresponding to the axial contact resonance of three separate 1 μm diameter PS sphere samples.

by the aluminum film and its subsequent rapid thermal expansion excites the vertical contact resonance of the spheres, while rotational and transverse vibrations are not excited due to symmetry constraints [9]. The sphere vibrations were detected with a phase-mask-based interferometer, described in Section 1.4.2, which is sensitive to out-of-plane displacements [181], by focusing a continuous wave (CW) probe beam (wavelength 514 nm, average power 10 mW) to a 200 μm diameter spot on the sample. The interferometric signal was

digitized and recorded using an oscilloscope, and averaged over 10^4 pump pulses. A representative time-domain trace measured on a 1 μm diameter monolayer, after the removal of the slow thermal decay, is shown in Figure 4.1(c). The slowly-decaying oscillations are associated with the axial vibrations of the spheres. Representative power spectra from measurements on three different 1 μm diameter monolayer samples are shown in Figure 4.1(d), where the peak corresponds to the axial contact resonance frequency. Measurements of the axial contact resonance frequency were performed on two or three replicate samples for a given sphere size. Interferometric signals were recorded at a positive and negative phase setting by varying the optical path difference between the probe and the reference beams. Waveforms of 1 μs duration were acquired at a 20 GHz sampling rate and averaged over 10^4 pump pulses. The net signal was obtained by subtracting the waveforms collected at positive and negative phase settings. A segment of 0.55 μs of the signal starting from the sharp initial rise (corresponding to the arrival of the pump pulse) was used for further signal processing, except in the case of the signals measured on the 2 μm, 2.89 μm, 3.5 μm and 4.16 μm diameter spheres, where a longer signal of up to 0.98 μs was used. A low-frequency smoothing function was used to subtract the thermal decay component from the normalized signal, as well as ensure that the signal has a zero mean amplitude. The Fast Fourier Transform (FFT) was applied to this low-frequency filtered, normalized signal to reveal its spectral components. Since the phase-mask-based interferometer is sensitive to out-of-plane vibrations, the peak in the frequency spectrum was identified as the axial contact resonance of the spheres.

4.3 Results and Discussion

Figure 4.2 shows the measured spectra for the twelve different sphere sizes. We assume the spheres act as mass-spring oscillators, and estimate the normal contact stiffness K from the measured collective axial contact resonance frequency f of the sphere monolayer using the

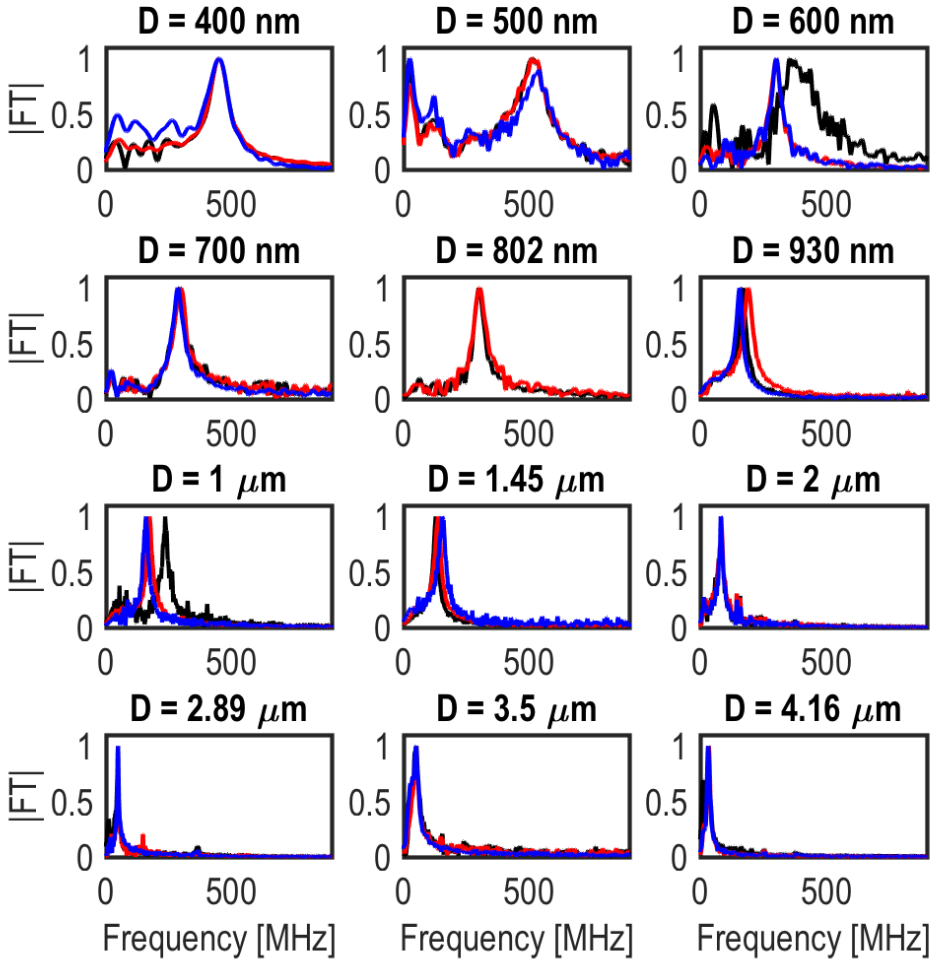

Figure 4.2: Frequency spectra of the axial contact vibrations measured using the phase-mask-based interferometer for the different sized colloidal particles. The black, red and blue curves represent different samples for the same sphere size.

relation $K = (2\pi f)^2 m$, where m is the mass of the sphere calculated using the volume of the sphere of radius R and the density of polystyrene $\rho = 1060$ kg/m^3 [12,268]. The scaling of the normal contact stiffness with the sphere radius, which shows a trend of increasing stiffness with increasing sphere size, is shown in Figure 4.3. The open circle markers represent the

average measurement of two or three samples for a given sphere size, while the error bars denote the minimum and maximum values. The best fit line through the twelve measured points, denoted by the dashed black line in Figure 4.3, has a slope of 0.66 ± 0.25 (R^2 value of 0.77). The uncertainty denoted in the slope is obtained from the upper and lower limits of the 95 % confidence interval using linear regression analysis. We compare the measured contact stiffnesses with those predicted by the DMT and JKR adhesive elastic contact models. The contact stiffnesses are calculated by linearizing the force-displacement relations prescribed by these models about the equilibrium displacement (i.e., when the net force is zero). For the DMT model, the contact stiffness K_{DMT} is obtained by linearizing the DMT model force-displacement relation around the point of equilibrium [11], and is expressed as,

$$K_{DMT} = (3/2)(2\pi w R^2 E^{*2})^{1/3} \tag{4.1}$$

where R and E^* are the effective radius and effective modulus, respectively, defined in Section 1.1.3. In the case of the JKR model, differentiating the force F and the contact radius a in Equation 1.4 yields,

$$\frac{dF}{da} = \frac{3E^* a^2}{R} - \frac{3}{2}(6\pi w E^*)^{\frac{1}{2}} \tag{4.2}$$

Similarly, differentiating the axial displacement δ with respect to the contact radius a using the relation in Equation 1.4, we obtain,

$$\frac{d\delta}{da} = \frac{2a}{R} - \frac{1}{3}\left(\frac{6\pi w}{E^*}\right)^{\frac{1}{2}} a^{-\frac{1}{2}} \tag{4.3}$$

From the force - contact radius relation in Equation 1.4, we obtain the contact radius at equilibrium predicted by the JKR model, as $a_{0,JKR} = (6\pi w/E^*)^{1/3} R^{2/3}$. The contact stiffness predicted by the JKR model about the equilibrium position, K_{JKR} can be expressed as the derivative of the JKR force to the displacement, evaluated at the equilibrium displacement

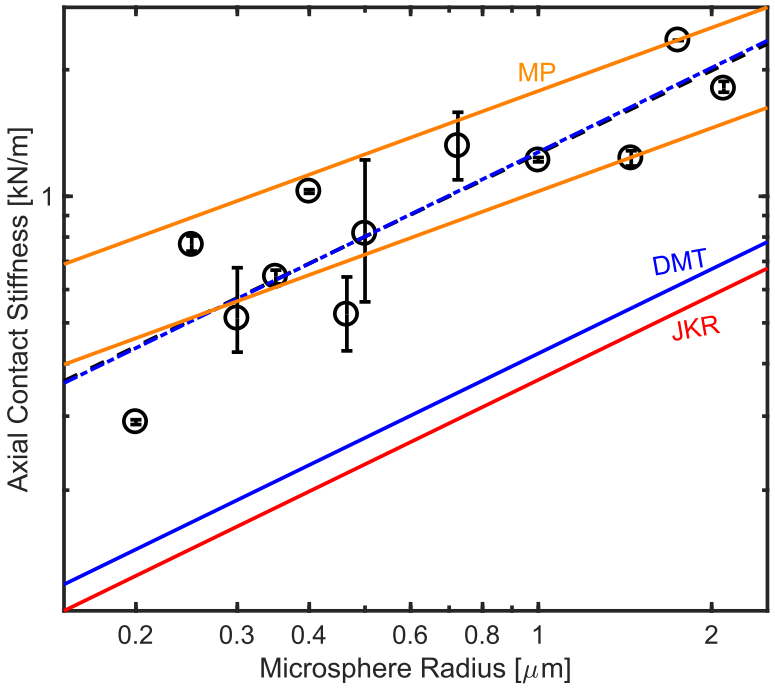

Figure 4.3: Scaling of the normal contact stiffness with sphere radius calculated from the collective axial contact resonance of the monolayer samples with sphere radius ranging from 200 nm to 2.08 μm (shown with open markers). The contact stiffness predicted by adhesive elastic contact models (DMT and JKR) using the theoretical work of adhesion obtained from the Lifshitz theory of van der Waals adhesion between polystyrene and alumina, are shown with the solid blue and red lines, respectively. The dashed black line represents the best fit line through the measured points. The upper and lower bounds of the scaling of the contact stiffness with sphere radius obtained by combining the MP model with the DMT model is shown with the solid orange curves.

$\delta_{0,JKR}$, i.e., $K_{JKR} = dF/d\delta|_{\delta=\delta_{0,JKR}}$. The derivative of the JKR force to the displacement can be obtained by combining Equations 4.2 and 4.3, to give,

$$\left.\frac{dF}{d\delta}\right|_{a=a_{0,JKR}} = \frac{9}{10}\left(6\pi w\right)^{\frac{1}{3}} E^{*\frac{2}{3}} \cdot R^{\frac{2}{3}} \tag{4.4}$$

From Equations 4.1 and 4.4, we see that the power law exponent of the scaling of the axial contact stiffness with particle radius in the DMT and JKR models is 2/3. The solid blue and red lines in Figure 4.4 show the scaling of the contact stiffness with sphere size predicted by the DMT and JKR models, respectively, using a theoretical work of adhesion $w = 0.11$ J/m^2 between polystyrene and alumina (assuming a native oxide layer on the aluminum film), and Young's modulus and Poisson's ratio $E_p = 4.04$ GPa, $\nu_p = 0.32$, $E_s = 62$ GPa, $\nu_s = 0.24$ of the particle and the substrate, respectively [12]. From Figure 4.3, it is clear that although the slope of the best fit through the measured stiffnesses is in reasonable agreement with the slope of ²/₃ predicted by the DMT and JKR models, the measured stiffnesses are over two times higher than the model predictions. Our results are consistent with previous observations of the scaling of the axial contact stiffness with sphere size measured on gold nanoparticles [110]. Using the work of adhesion as a free variable, we fit our measured stiffnesses to the DMT and JKR models, and find the fitted work of adhesion for the DMT and JKR models to be $w_{\mathrm{DMT,fit1}} = 3.1$ J/m^2 and $w_{\mathrm{JKR,fit1}} = 4.8$ J/m^2, respectively, which are over an order of magnitude higher than the work of adhesion between polystyrene and alumina, $w = 0.11$ J/m^2, calculated using the Lifshitz theory of van der Waals adhesion [57]. While uncertainties in predicting the work of adhesion, particularly in the case of reactive metals, have been reported previously for adhesion across metal-ceramic interfaces where the measured work of adhesion was found to be over twice the theoretical value for adhesion between reactive metals bonded to alumina [269], the unrealistically high work of adhesion obtained by fitting the measured stiffnesses to the DMT and JKR model predictions suggests that other factors such as increased contact area due to plasticity might be responsible for the higher contact stiffness. It is also worth noting that a significant scatter in the measured surface energies of metals has been reported, ranging an order of magnitude from 0.4 to 4 J/m^2 [57], compared to the surface energy of ≈ 0.2 J/m^2 obtained using a Hamaker con-

stant that is appropriate for metals [57]. The presence of long-range adhesive forces between polystyrene and aluminum, that could act beyond the native oxide layer, could also introduce significant uncertainty in the work of adhesion between the spheres and the substrate.

We estimate the adhesive force from the DMT model with the theoretical work of adhesion using the relation $F_{adh} = 2\pi wR$. We find the adhesive force to range between 0.14 μN for the case of the 400 nm diameter spheres to 1.5 μN for the 4.16 μm diameter spheres. The axial displacement at the onset of yielding δ_y is calculated using the relation $\delta_y = (4\pi^2/9)(1.6\sigma_y/E^*)^2 R$, where $\sigma_y = 9$ MPa is the yield strength of polystyrene [264], and E^* is the effective modulus of contact defined in Section 1.1.3. The constant 1.6 is determined by maximizing the $J2$ invariant of the axisymmetric stress distribution with respect to both angle and depth below the surface [141, 142]. The corresponding force at the onset of yielding F_y is calculated from the Hertzian law using $F_y = E^* R^{1/2} {\delta_y}^{3/2}$ [142]. It is clear that the ratio of the force at the onset of yield to the theoretical adhesive force, $F_y/F_{adh} = [\{(6.4\pi^2\sigma_y/9)^{3/2} E^{*-1/2}\}/(2\pi w)]R$ is proportional to the radius R of the particle. We find the force at the onset of yielding to be 0.035 nN for the case of the 400 nm diameter spheres, and 3.8 nN for the 4.16 μm diameter spheres. The estimated adhesive force using the theoretical work of adhesion is 4000 times the contact force at the onset of yielding for the 400 nm diameter sphere, and $\sim$ 400 times the contact force at the onset of yielding in the case of the 4.16 μm diameter spheres. This further supports the possibility of adhesion-induced plasticity at the micro-scale.

To further scrutinize the possible reasons for the discrepancy between the measured contact stiffnesses and the stiffnesses predicted by adhesive elastic contact models, we also investigate the scaling of the contact radius at equilibrium a_0 with the sphere size. Visual observations were of the sphere-substrate equilibrium contact radii were made by fragmenting the sample, mounting it to a sample holder, and viewing the sphere-substrate contact under an SEM. A

10 kV accelerating voltage was used for the electron beam. Spheres located on the edge of the sample were viewed and imaged from an angle of 89° to the normal to the plane of the substrate. Representative side-view SEM images of the sphere-substrate contact of a 930 nm and a 2.89 μm diameter sphere are illustrated in Figure 4.4(a) and Figure 4.4(b), respectively. Measurements of the equilibrium contact radii were performed on five spheres per sample, resulting in ten or fifteen measurements for each sphere size. In addition to estimates from visual observations, we used an AFM-based technique to estimate the equilibrium contact radii of a larger number of spheres located over a wider area of the substrate and not just on the edge of the sample. In this technique, the samples were immersed in an aqueous solution (0.5% wt./vol.) of polyvinyl alcohol (PVA) and then allowed to dry by placing them at an angle of 45° in ambient laboratory conditions. Upon drying, the PVA particles are dragged towards the spheres due to meniscus pinning, and are eventually deposited around the sphere-substrate contact. After the sample was completely dry, the spheres were removed from the substrate using an adhesive tape. The surface topography of the substrate after removal of the spheres was imaged using an atomic force microscope (AFM). A typical AFM image on a 5 μm x 5 μm area of a sample after removing a monolayer of 500 nm diameter spheres is shown in Figure 4.4(c). The PVA particles can be seen as distinct "ring-like" features on the substrate. The contact radii are estimated estimated from the inner radii of the PVA rings. Figure 4.4(d) shows a distribution of the contact radii estimated from the AFM image in Figure 4.4(c).

The equilibrium contact radii estimated using the SEM images of the sphere-substrate contacts and AFM scans of the substrate surface topography after depositing PVA around the contacts and removing the spheres, for the range of spheres sizes, are shown in Figure 4.5 with red and black open markers, respectively. The markers represent the average values of the estimated contact radius. For the case of the SEM estimates, the error bars represent the minimum and maximum value of the contact radius, while for the AFM estimates, the error

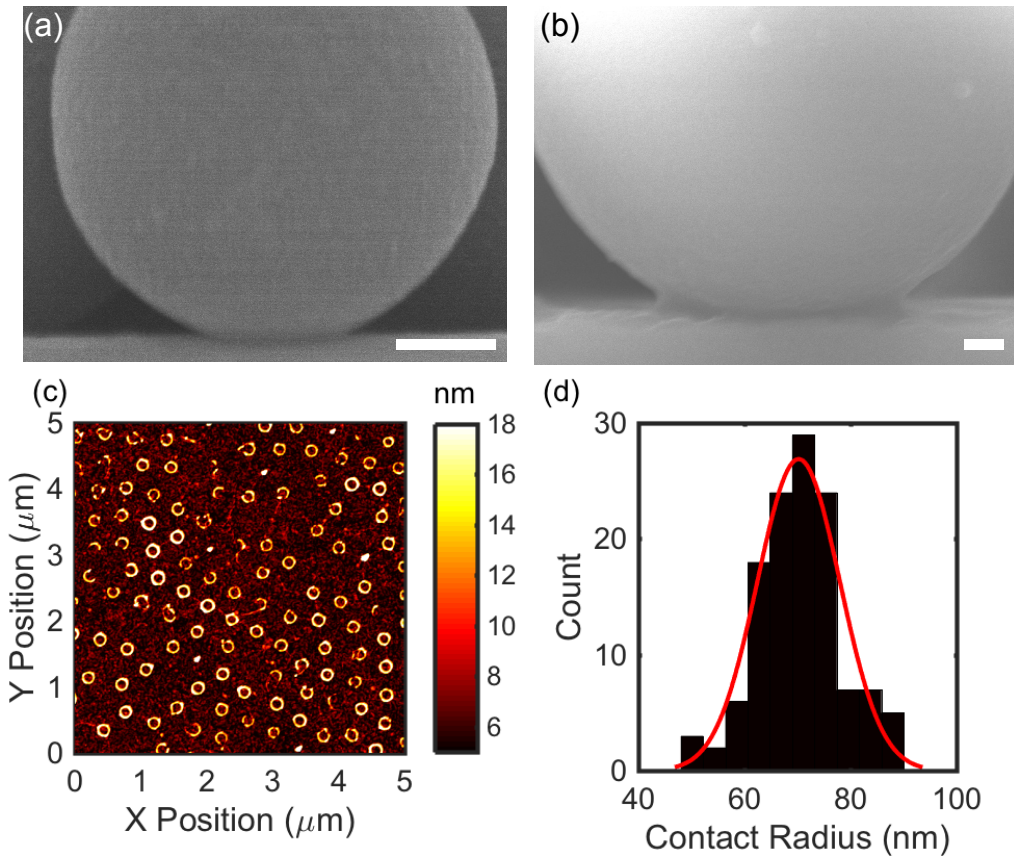

Figure 4.4: Side-view SEM images of individual spheres of diameter (a) 930 nm and (b) 2.89 μm (the scale bar represents 200 nm in both panels). (c) AFM image of the substrate after removal of a monolayer of 500 nm diameter spheres, highlighting the rings formed by the PVA aggregated around the contact. (d) Distribution of the contact radii estimated from the size of the PVA rings in the 500 nm monolayer sample, shown in panel (c). The bin size of the histogram is 4.2 nm. The red line depicts a normal distribution with the mean and standard deviation of the same data set.

bars denote the standard deviation of the data set. We find that the equilibrium contact radii estimated using the SEM images scale with the sphere size with a slope of 0.74 ± 0.21 (R^2 value of 0.86), while the corresponding estimates made from the AFM scans scale with a

slope of 0.64 ± 0.15 (R^2 value of 0.91). The intervals of the slope through the SEM and AFM data points are obtained from the upper and lower bounds of the 95 % condidence interval. The best fit lines through the SEM and AFM estimates are represented in Figure 4.5 by the dash green and the dash black lines, respectively. We note that the scaling exponents are obtained from the average experimental values only. The SEM estimates show a larger scatter compared to the estimates made using the AFM technique. We also see that the upper and lower bounds of the scaling exponents (within the 95 % confidence interval) overlap for the SEM and AFM data points, such that we can not meaningfully distinguish between the two slopes. Although the scaling exponents from the SEM and AFM data points are close, the small discrepancy in the data obtained from the two measurement techniques may be attributed to the higher uncertainty in the SEM estimates originating from the fewer spheres used for the estimations when compared to the AFM estimates, as well as other factors such as the true contact area being partially obscured from view by the sphere curvature, the spheres not being perfectly on the edge of the sample, or distortion of the electron beam during imaging.

The scaling of the equilibrium contact radii predicted by the DMT and JKR contact models, assuming the same theoretical work of adhesion and elastic properties of the sphere and the substrate, is also shown in Figure 4.5 with the solid blue and red lines, respectively. Both the DMT and JKR models predict that the equilibrium contact radius scales with the sphere radius with a $^2/_3$ slope. We see that the JKR model predicts a higher contact radius at equilibrium compared to the DMT model. Despite this, we see from Figure 4.5 that the contact radii estimated from the SEM and AFM techniques are over two times higher than the JKR model predictions. We find that using the work of adhesion as a free parameter to fit the DMT and JKR models through the estimated contact radii using the AFM technique yields $w_{\mathrm{DMT,fit2}} = 3.9$ J/m^2 and $w_{\mathrm{JKR,fit2}} = 1.3$ J/m^2, respectively. The work of adhesion obtained by fitting the estimated contact radii to the DMT model is very close to that ob-

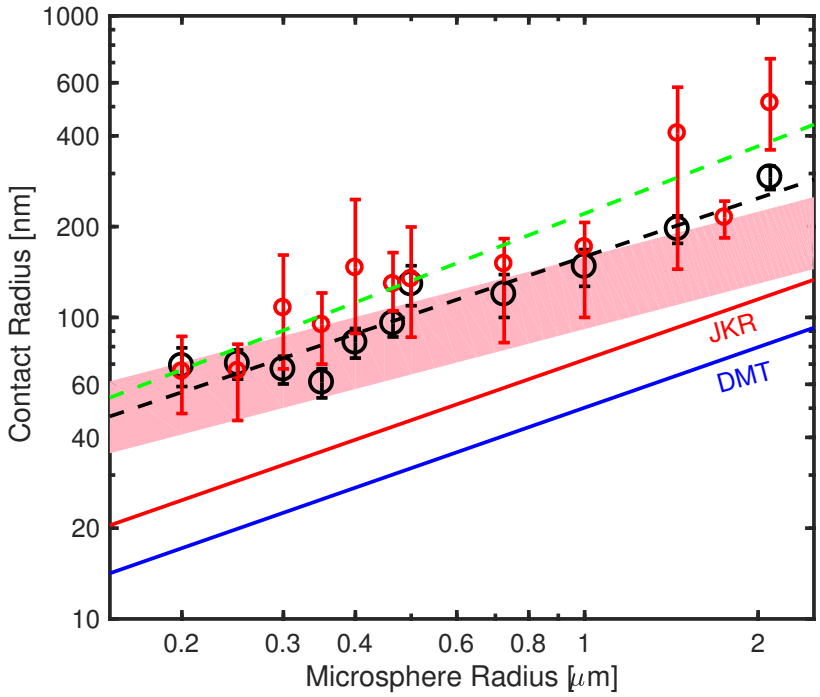

Figure 4.5: Scaling of the equilibrium contact radius with sphere radius. The black and red open markers represent the estimates made using AFM and SEM, respectively. The error bars for the AFM measurements correspond to the standard deviation of the distribution, while those for the SEM measurements denote the minimum and maximum estimated contact radius. The solid red and blue lines denote the contact radii predicted by the JKR and DMT models, respectively, using the theoretical work of adhesion from the Lifshitz theory of van der Waals adhesion between polystyrene and alumina. The shaded pink region denotes the upper and lower bounds of the contact radii predicted by the MP model by assuming a theoretical work of adhesion, and the limiting cases of the hardness (one to three times the yield strength of PS). The dashed black and green lines denote the best fit through the AFM and SEM measurements, respectively.

tained by fitting the measured contact stiffnesses to the DMT model ($w_{DMT,fit1} = 3.1$ J/m^2)

and is about thirty five times the theoretical value of $w = 0.11$ J/m^2 in both cases. On the other hand, the work of adhesion obtained by fitting the estimated contact radii to the JKR model ($w_{\text{JKR,fit2}} = 1.3$ J/m^2) is much lower than the work of adhesion obtained by fitting the measured contact stiffnesses to the JKR model scaling ($w_{\text{JKR,fit1}} = 4.8$ J/m^2), yet this value is about twelve times the theoretical work of adhesion.

We compare the scaling of the estimated contact radii with that predicted by the MP model of elasto-plastic contact [132]. Since the Young's modulus of polystyrene is much lower than that of aluminum, we assume that contact related deformations take place primarily in the sphere. The MP model states that the mean contact pressure becomes constant when the contact area has reached full plasticity, and is equal to the hardness of the material H. The material hardness was expressed in terms of the yield strength of the material $H = 3\sigma_y$. In the absence of any external force, i.e., at equilibrium, the contact radius at full plasticity is expressed as $a_{0,MP} = (2wR/3\sigma_y)^2$ [132]. It is clear from this expression that the power law exponent for the relationship between the equilibrium contact radius and the sphere radius is 1/2, in contrast to the 2/3 power law scaling predicted by the DMT and JKR models. While the MP model prescribes the hardness of the material to equal three times the yield strength when the contact area has completely yielded, recent numerical studies have shown that for relatively large displacements, the mean contact pressure is uniform across the contact area and is equal to 2.5 times the yield strength of the material [142]. Jackson and Green [135] showed using finite element analysis of the contact between an elasto-plastic hemisphere and a rigid flat that the mean contact pressure, commonly approximated as three times the yield strength, in fact varies with the deformed contact geometry, and can equal the yield strength when the contact radius approaches the radius of the sphere. In our case, the maximum ratio of the contact radius (a_0) to the sphere radius (R) occurs in the case of the 400 nm diameter spheres, with $a_0/R = 0.35$, while the minimum value of (a_0/R) is in the case of the 4.16 μm diameter spheres, with $a_0/R = 0.14$. We note that Jackson and Green

found that the hardness equals the yield strength in the limiting case of $a_0/R = 1$ [135]. In our study, although we do not approach this limiting case, we note that the hardness as a function of equilibrium contact radius (and consequently, a function of the sphere radius), could affect the scaling of the contact radius with the sphere radius. We plot the upper and lower bounds of the scaling of the contact radius with the sphere radius predicted by the MP model using the theoretical work of adhesion, by assuming the hardness to equal to three times the yield strength (for the lower bound) and to be equal to the yield strength (for the upper bound). The upper and lower bounds are enclosed by the pink shaded region shown in Figure 4.5. The power law exponent of the upper and lower bounds in the MP model remains 0.5. We see that most of contact radii estimates made using the AFM technique lie within this shaded region. A larger number of the estimates made from the SEM images lie outside this region. Using the work of adhesion as a free parameter to fit the estimated contact radii to the MP model, we obtain $w_{\text{DMT,fit-upper}} = 0.12$ J/m^2 when fitting to the upper bound of the MP model prediction, and $w_{\text{DMT,fit-lower}} = 0.36$ J/m^2 by fitting to the lower bound. We note that the work of adhesion extracted by fitting our estimates to the lower bound of the MP model predictions is much closer to the theoretical value $w = 0.11$ J/m^2, assuming the mean contact pressure is three times the yield strength, than the extraordinarily high work of adhesion values obtained by fitting to elastic contact models.

Despite the better agreement between the measured and predicted contact radii when using an elasto-plastic model versus an elastic model, the large scatter in the observed scaling with particle size does not provide conclusive distinction between elastic and elasto-plastic scaling exponents [slope of 0.64 ± 0.15 from AFM (R^2 value of 0.91), and 0.74 ± 0.21 from SEM (R^2 value of 0.86)], in contrast to the predicted 0.5 slope from the Maugis-Pollock model). Anomalous scaling of the equilibrium contact radii was observed for the case of polystyrene and glass spheres ranging from 0.5 μm to 6 μm in diameter adhered to compliant polyurethane substrates [260], although the scaling of the equilibrium contact radii of

polystyrene spheres between 1.5 μm and 10 μm on silicon substrates agreed well with the MP model power law dependence [260]. In another study, a transition from the $^3/_4$ anomalous power law scaling of the contact radius to the DMT and JKR model $^2/_3$ power law dependence was observed for glass particles on polyurethane substrates [261]. For particles less than 10 μm in diameter, the contact radius varied with the particle radius to the 0.78 power, while for larger particles the contact radius varied approximately to the $^2/_3$ power with particle radius. Nonlinear elastic, viscoelastic or partially plastic deformations were proposed as possible explanations for these anomalies [261]. A more thorough investigation with larger number of data points in the range of the sphere sizes in our study may provide a power law dependence with more certainty and also indicate the presence of any transition. Plastic models which account for the change in curvature of the particle at large deformations may also explain the anomalous power law dependence of the contact radius with the particle radius.

We combine the contact stiffness measurements with the contact radii estimates to investigate the scaling of the contact stiffness with the equilibrium contact radius. We see from Figure 4.6(a) that the measured contact stiffness increases with the estimated contact radius, where the black and red open markers represent the contact radii estimates using the AFM and SEM techniques, respectively. The error bars in the ordinate and abscissa are the same as those corresponding to the contact stiffness measurements shown in Figure 4.3 and the contact radii sestimates in Figure 4.5, respectively. The scaling of the contact stiffness is represented only with the AFM estimated contact radii in Figure 4.6(b). We compare our measured contact stiffness with contact radius scaling with that determined by the DMT model. The DMT model predicts a linear relationship between the linarized contact stiffness and the equilibrium contact radius, $K_{DMT} = 2E^* a_0$. This relationship is independent of the work of adhesion, and depends only on the elastic properties of the particle and the substrate. The scaling of the contact stiffness with the contact radius provides more insight

since it eliminates errors from uncertainties in the work of adhesion. The relation between contact stiffness and the contact radius as predicted by the DMT model is shown with the solid blue line in Figure 4.6(a) and Figure 4.6(b).

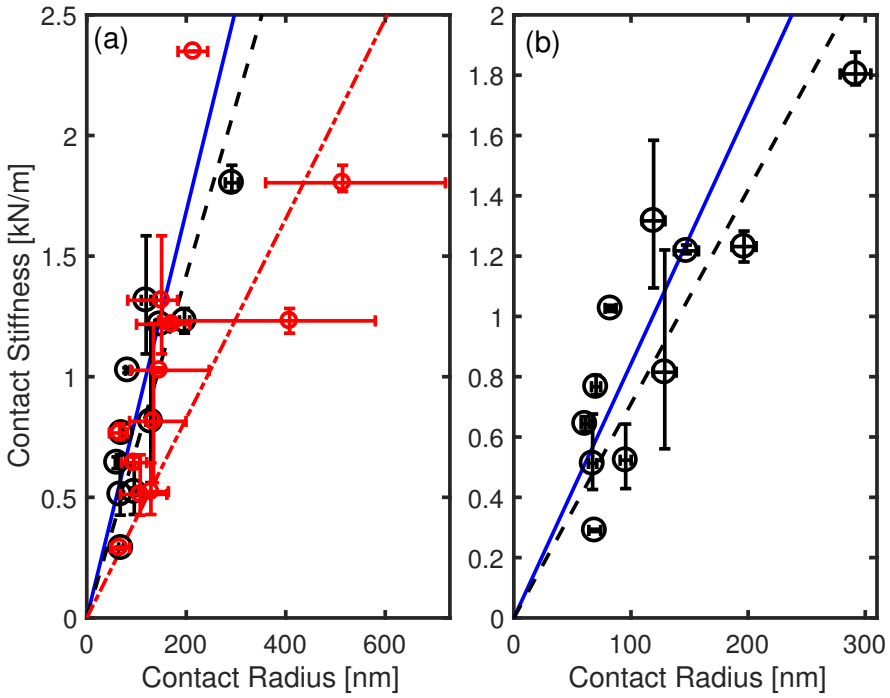

Figure 4.6: (a) Normal contact stiffness versus the equilibrium contact radius. The contact radius measured using AFM and SEM are denoted by the black and red markers respectively. The relation between the normal contact stiffness and the equilibrium contact radius predicted by the DMT contact model is denoted by the solid blue line. The dashed black and the red dashed-dot lines denote the DMT prediction with the effective elastic modulus fitted to the AFM and SEM measurements of the contact radii, respectively. (b) Scaling of the axial contact stiffness with the contact radii measured only using the AFM.

The measured data points are in good agreement with the linear relationship between the contact stiffness and the contact radius predicted by the DMT model, with the exception of

the SEM estimates of the contact radii of the 2.89 μm and 4.16 μm diameter spheres, which appear to be outliers to the linear trend. Using the effective modulus as a free parameter, we fit the measured stiffness and contact radii data points to the Hertzian model scaling. We obtain an effective modulus of 3.6 GPa by fitting the AFM data to the Hertzian model (R^2 value of 0.63), and 2.1 GPa by fitting the SEM data to the Hertzian model (R^2 value of 0.06). We note that the theoretical effective modulus is 5.6 GPa. The effective modulus obtained by fitting the AFM data to the Hertzian model is 84% the theoretical effective modulus, while that obtained from the SEM data is only 49% of the theoretical value. We note that the two outliers in the SEM data skew the fitted modulus, since the effective modulus fitted without the two outliers is 80% of the theoretical value. Using the fitted effective modulii in the adhesive elastic models, we notice that the work of adhesion extracted by fitting the DMT model using the effective modulus obtained from the AFM data to the measured contact stiffness scaling with sphere size shows a $\sim$ 40 % increase, which further increases the discrepancy between the predicted and measured quantities.

To investigate the effect of plasticity on the scaling of the contact stiffness with the contact radius, we implement a finite element model in COMSOL Multiphysics and simulate the elasto-plastic nature of the contact between a polystyrene hemisphere with a flat elastic aluminum substrate. We follow the methodology presented in [142], but model a sphere-flat contact instead of the contact between identical spheres. A two-dimensional axisymmetric model was used in which the hemisphere was meshed with triangular elements, while quadrilateral elements were used to mesh the substrate. The mesh was refined in the vicinity of the sphere-substrate interface. A representative mesh of a 1 μm hemisphere model is shown in Figure 4.7(a).

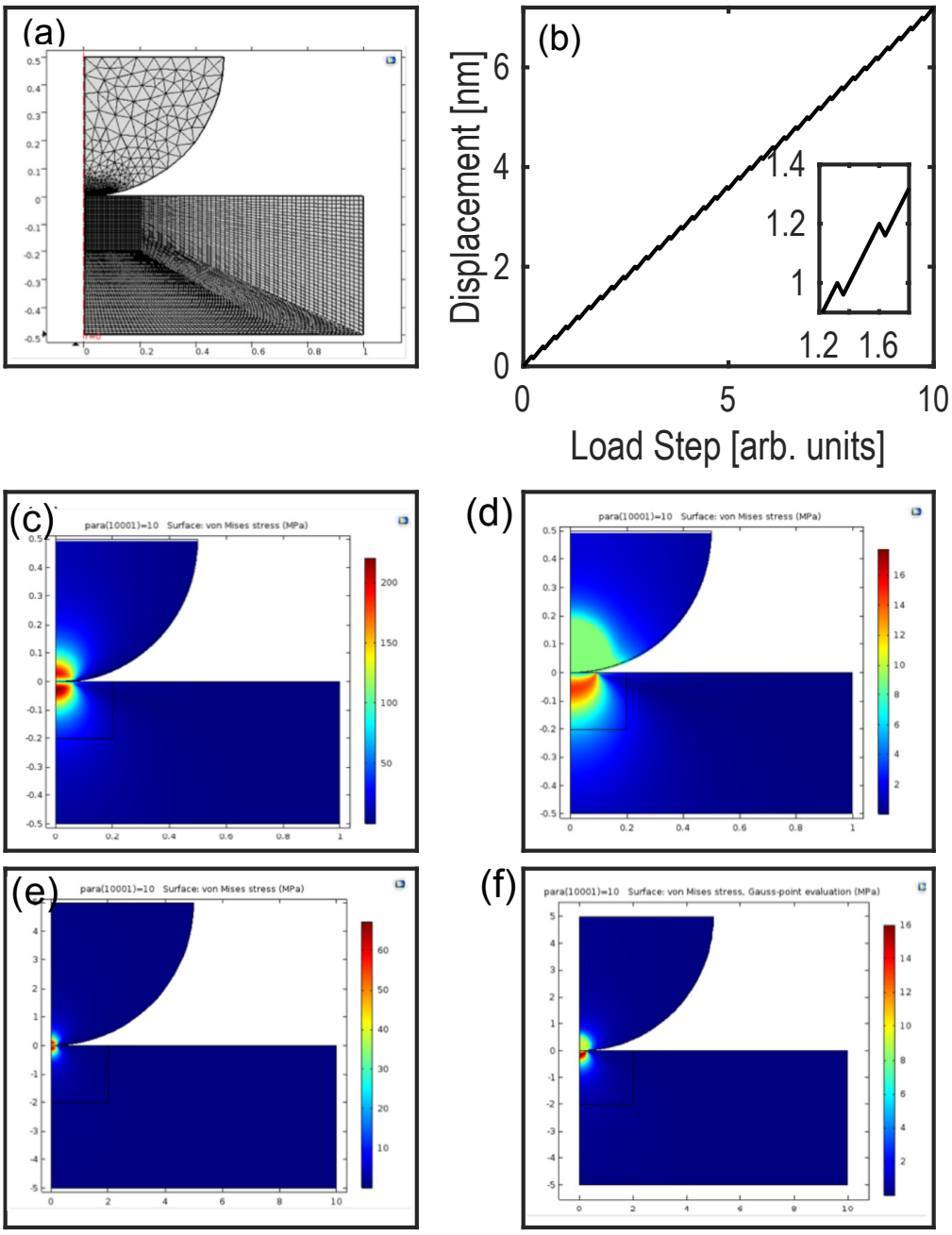

Figure 4.7: (a) Representative FEM model of the axisymmetric contact problem highlighting the triangular and quadrangular elements used to mesh the geometry. (b) Variation of prescribed displacement over the loading history used in the simulation. The von Mises stress contours for 1 μm sphere in the elastic and elasto-plastic cases are shown in (c) and (d), respectively. The corresponding plots for the 10 μm are illustrated in panels (e) and (f).

The contact between the hemisphere and the substrate was kept frictionless. The force-displacement response in the elasto-plastic regime was studied for 1 μm and 10 μm diameter spheres. The polystyrene sphere was modeled as an elastic-perfectly plastic material with the same yield strength of polystyrene define previously, $\sigma_Y = 9$ MPa, along with theoretical values of the Young's modulus and Poisson's ratio of polystyrene and aluminum. A 'saw-tooth' displacement function was prescribed to the top-edge of the hemisphere for the 1 μm and 10 μm diameter spheres with a maximum displacement of 7.2 nm. The displacement profile prescribed to the top-edge of the hemisphere is shown in Figure 4.7(b). The sphere was unloaded by prescribing a displacement of 0.04 nm away from the substrate, as opposed to complete unloading in [142]. The saw-tooth function allowed the sphere to be unloaded and reloaded at multiple points in the displacement ramp up to 7.2 nm, and mimicked the resonant axial vibration of the particles in our experiments. The contact stiffness was extracted at each of unload points by evaluating the local derivative of the force-displacement curve at those points. The von Mises stress contours for the 1 μm sphere in the elastic and elasto-plastic cases are shown in Figures 4.7(c) and (d), respectively. The corresponding plots for the 10 μm are illustrated in panels Figures 4.7(e) and (f).

The force displacement curves obtained from the FEM models for the 1 μm and 10 μm hemisphere models in the elastic and elasto-plastic regimes are shown in Figures 4.8(a) and (b), respectively. The FEM elastic force-displacement curve is shown with a dash blue line, while the FEM elasto-plastic curve is shown with a solid red line. The FEM results are compared to the force-displacement given by the Hertz theory, shown with the solid black curve in Figures 4.8(a) and (b). The elastic force-displacement curves obtained from the FEM model are in excellent agreement with the Hertz theory. We see that for the case of the 1 μm diameter hemisphere, the FEM model results start to diverge from the Hertz theoretical prediction, due to violation of the assumption of small deformations in the Hertz theory. At the unload and subsequent reload cycles, the force-displacement curves completely overlap, indicating

no hysteresis, which is expected for loading, unloading and reloading in the elastic regime. In the case of the elasto-plastic contact, the FEM results show that the force-displacement curves in both the 1 μm and 10 μm hemisphere models start along the elastic curve at very low displacement levels, but then start to diverge and eventually, becomes linear, which is characteristic of plastic deformation in the contact area [141, 142]. During unloading, the force-displacement curve deviates from the loading curve and follows a path similar to the Hertz elastic case. Upon reloading, the force-displacement relation follows the same unloading curve, up until the point of the start of the unloading, beyond which it continues to follow the linear force-displacement relationship expected in the fully plastic regime. This is consistent with the elastic unloading phenomenon described by Thornton [133, 142].

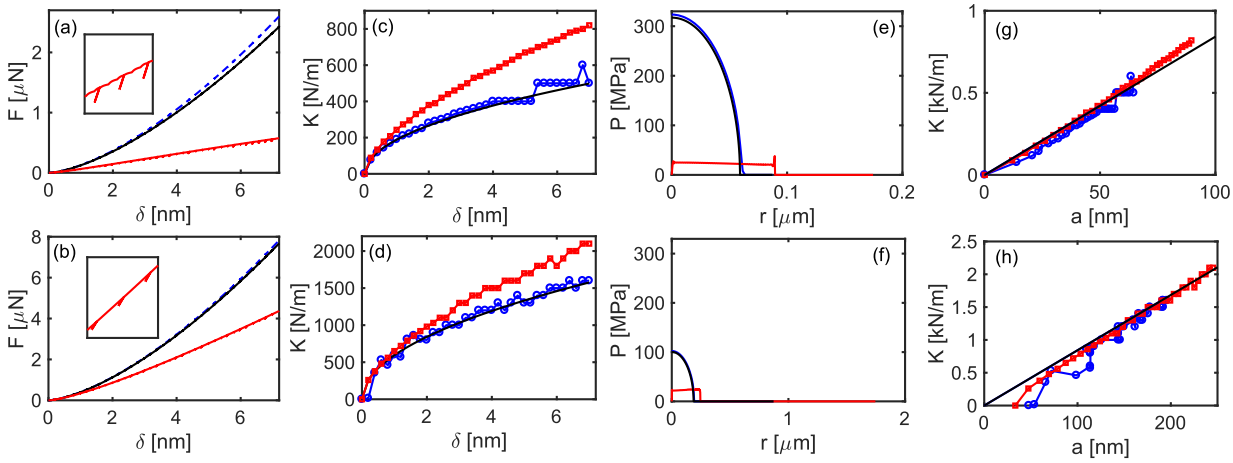

Figure 4.8: Panels (a) and (b) highlight the force-displacement relations obtained from the FEM model for the 1 μm and 10 μm diameter hemispheres, respectively, along with the Hertz theory (solid black line). The dash blue line represents the results from the elastic case, while the solid red lines show the elasto-plastic results. The insets highlight the hysteretic unloading in the elasto-plastic case. Panels (c) and (d) show the contact stiffness-displacement relation for the 1 μm and 10 μm diameter hemispheres, respectively, obtained by taking the derivative of the force-displacement relations at the unload points only in (a) and (b). The contact pressure distribution along the radial direction is shown in panels (e) and (f) for the 1 μm and 10 μm diameter hemispheres, respectively. The blue, red and black curves correspond to the FEM elastic, FEM elasto-plastic and the Hertz analytical results, respectively, when the hemisphere is indented 7 nm into the substrate. Panels (g) and (h) show the relation between the contact stiffness and the contact radius, estimated from the radial distance where the contact pressure vanishes, for the 1 μm and 10 μm diameter hemispheres, respectively. The blue and red markers correspond to the FEM elastic and elasto-plastic cases, respectively, while the solid black line represents the Hertz theory prediction.

The variation of the contact stiffness with displacement of the sphere towards the substrate is plotted in Figures 4.8(c) and (d) for the 1 μm and 10 μm hemisphere models, respectively. The contact stiffness-displacement curve is obtained by taking the derivative of the force-displacement curves in Figures 4.8(a) and (b). The FEM model results for the elastic and elasto-plastic cases are shown with the blue and red markers, respectively. The markers represent the contact stiffness computed at each of the unload and reload cycles. The solid black line shows the contact stiffness relation with displacement that is given by the Hertz theory. As expected, we find good agreement between the FEM elastic model results and the Hertz theory. The contact stiffness at the unload and reload points in the elasto-plastic case is higher than in the elastic case for the same axial displacement. This is also expected, since the geometric contact area is higher in the elasto-plastic case for the same displacement when compared to the elastic case, and that the unloading and subsequent reloading up to the unloading point is considered to be an elastic process.

Figure 4.8(e) and (f) show the variation of the contact pressure along the radial length, r, when the hemisphere is displaced 7 nm into the substrate, for the cases of the 1 μm and 10 μm hemisphere models, respectively. We find an elliptical variation of the contact pressure in the elastic cases, which is in good agreement with the Hertz model. For the elasto-plastic cases, we find a uniform distribution of the contact pressure, which is equal to about ~ 2.7 the yield strength of polystyrene for the case of the1 μm diameter sphere, and ~ 2.4 times the yield strength of polystyrene for the case of the 10 μm sphere. This further confirms that the deformation is in the regime where the hardness (or average contact pressure) is three times the yield strength, and does not approach the yield strength, as suggested by Jackson and Green when a_0/R tends to unity [135]. We estimate the contact radius in the elastic and elasto-plastic cases at various displacement steps by measuring the radial distance at which the contact pressure goes to zero.

We use the contact radii estimated from the FEM models by measuring the radial distance at which the contact pressure goes to zero, and the contact stiffness, at the same displacement steps, to obtain a contact stiffness versus contact radius relation. This relation is plotted in Figures 4.8(g) and (h) for the 1 μm and 10 μm hemisphere models, respectively. The elastic model results are plotted with the blue markers, while the red markers represent the FEM results from the elasto-plastic model. We find the elastic and elasto-plastic markers obtained from FEM to be in excellent agreement with the Hertz theory, denoted by the solid black line. This indicates that despite initial plastic yielding of the contact zone, the stiffness of the contact at subsequent low-amplitude unload and reload cycles can be accurately described by Hertzian contact models, provided a contact radius is given. The higher stiffnesses at the same axial displacement in the elasto-plastic case are result of a larger contact area resulting from plastic deformation of the spheres at the points of contact by adhesive forces. We note that the jaggedness of the plots from the FEM results may arise from the resolution of the load step in the simulation. We also observe good agreement in the scaling of the contact stiffness with the contact radius, which bypasses uncertainties in the work of adhesion, and depends only on the effective modulus of contact. The fitted effective moduli using the AFM and the SEM data points (after removing the two outliers) are close to the theoretical effective modulus of contact. The small discrepancy could be explained by a factors such as a lower elastic modulus of the polystyrene spheres due to porosity of the spheres, variations between spheres that are purchased from an external supplier and those that are synthesized in-house, or softening of the spheres after initial plastic deformation.

From Figures 4.8(g) and (h), it is clear that despite plastic deformation, the linear relationship between the contact stiffness K and the contact radius a predicted by the DMT model, $K = 2E^*a$, remains applicable. We use this linear relationship between the contact stiffness K and the contact radius a, and combine it with the equilibrium contact radius a and sphere radius R given by the MP model, $a = \sqrt{2wR/H}$, where H is the hardness. Considering

both the upper and lower bounds, with the hardness being equal to the yield strength, and being equal to three times the yield strength, respectively, we plot the contact stiffness as a function of the sphere radius, using the MP model and the theoretical work of adhesion, $w = 0.11$ J/m^2, as indicated by the solid orange lines in Figure 4.3. Although the MP model predicts that the contact stiffness scales with the square root of the sphere radius, we observe better agreement between the absolute values of the measured and predicted contact stiffnesses.

4.4 Adhesion Measurements using Laser-induced Spallation [1]

In the previous sections, we have discussed different ways of obtaining the work of adhesion by fitting our measured scaling of the contact stiffness and contact radius with sphere radius to elastic and elasto-plastic contact models. In a separate study [268], the delamination of semiordered 1 μm diameter polystyrene microsphere monolayers adhered to glass substrates was studied using a laser-induced spallation study. Microsphere monolayer samples were fabricated using a modified Langmuir-Blodgett technique (discussed in Section 1.3.2), in which the microspheres were self-assembled at an air-water interface and then transferred to the substrate. This process resulted in a semiordered monolayer, with hexagonal-close-packed (HCP) crystalline domains of differing orientations as well as highly disordered regions. The laser-induced spallation experiments, performed by collaborators M. Hiraiwa from the Boechler Research Group, and M. Stossel from the Wang Research Group at the University of Washington, used a pump laser (1064 nm wavelength, 5 ns pulse duration) to ablate the aluminum layer coated on the side of the substrate opposite the side where the spheres were adhered. Surface displacements were monitored with a Michelson interferometer. The energy threshold at which the microspheres spallation occured was determined by gradually increasing the pump pulse energy, and observing the irradiated spots under an optical micro-

[1] Reproduced in part with permission from [268]. Copyright 2016 American Chemical Society.

scope. By taking the maximum surface deceleration, and applying an inertial microsphere model [268], the adhesion force was estimated to be $F_{spall} = 0.22 \pm 0.07$ μN [268]. Details on the experimental setup and the inertial model can be found in reference [268]. Scanning electron microscope images of detached monolayer regions revealed a unique morphology, namely, partially detached monolayer flakes composed of single hexagonal close packed crystalline domains.

The adhesion force obtained from the laser-induced spallation experiments was compared with that estimated from the out-of-plane microsphere contact resonance measured on a different region of the same sample. The contact resonance of the microsphere monolayer was excited by a broadband bulk longitudinal acoustic pulse using a configuration similar to the spallation experiment, but at an amplitude significantly below the microsphere detachment threshold. The adhesive force F_{CR} was obtained from the contact resonance by linearizing the Hertzian contact model about the equilibrium contact area, such that, $F_{CR} = (2K/3)^3/RE^{*2} = 3.8$ μN. The adhesion force estimated from the contact resonance measurements was significantly larger than the force estimated from the spallation measurements. Side-view SEM images of different microspheresubstrate contacts revealed an average contact radius of 150 ± 20 nm, which is significantly larger than predicted by both spallation and contact resonance measurements. We calculate an adhesive force of $F_{DMT} = 2\pi wR = 0.36$ μN and a contact radius of 32 nm, where $w = 0.11$ J/m^2 is the estimated work of adhesion between PS and alumina (assuming a native oxide layer). As also discussed in previous sections in this chapter, the size of the contact radius measured from the SEM measurements would require unrealistically large adhesive forces in the context of an elastic contact model. The large, measured contact radius may instead indicate the presence of plastic deformation near the contact. However, independent of potential plastic deformation of the contact, it is surprising that the adhesion force estimated from the spallation experiments, which did not involve the assumption of any contact model, is

so low, given the large contact radii observed in the SEM images. This difference may be due to assumptions used in the spallation adhesion force estimation process, such as the microspheres being approximated as rigid bodies. In addition, the discrepancy between the adhesion force estimated from the contact resonance and spallation measurements highlights a potential fundamental difference between the two methods related to variations in particle size and particle-substrate adhesion. For instance, in the spallation experiments, a few particles of larger size or weaker particle-substrate adhesion may pull adhered neighboring particles away from the substrate at lower accelerations, and result in the identification of an effectively lower detachment threshold. In contrast, in the contact resonance measurements the observed resonance is representative of the average contact stiffness across the measurement area, and would see the effect of polydispersity in broadening of the resonance.

4.5 Intra-sample Variations in the Contact Resonance Frequency

A number of factors can affect the magnitude of adhesion between the microspheres and the substrate, and in turn, affect the contact stiffness and the contact resonance frequency of the granular crystal monolayer. Our measurements of the collective contact resonance of the granular crystal entail the vibrational response of thousands of microparticles. Sphere-to-sphere variations in the contact resonance result in broadening of the line width of the measured collective contact resonance of the microsphere monolayer. Since the resonance frequency is inversely proportional to the square root of the microsphere mass (or the sphere radius to the 3/2 power), variations in the size of the individual microparticles will lead to a broadening of the contact resonance frequency of the monolayer. Surface roughness variations in the spheres as well as the substrate can also contribute to inhomogeneities in the adhesion between microparticles and the substrate. As discussed previously, uncertainties in the work of adhesion between the contacting surfaces can yield drastically different values of the contact resonance frequency when compared to estimates made using the Lifshitz van

der Waal's theory of adhesion. In particular, significant uncertainties have been reported for metal-ceramic interface [269, 271]. Furthermore, the large scatter in the measured surface energies of metals that range over an order of magnitude [57] could also add further uncertainties in the work of adhesion between the spheres and substrate, for the case of long-range attractive forces between the polystyrene spheres and the aluminum film, that could act beyond the depth of the alumina layer.

Eliason and coworkers measured the dispersion of surface acoustic waves induced by their interaction with the axial contact resonance of micron-sized silica microsphere monolayers at multiple regions within the same sample [177]. The authors found less variation within the same sample, although sample-to-sample variations were much higher. Although no definitive explanation for the disparity was provided, the authors speculated that minor variations in the substrate cleaning and treatment methods could result in sample-to-sample variations in the magnitude of the microparticle-substrate adhesion [177]. The authors also studied the effect of humidity on the contact resonance, and found a difference of only 5 % in the measured resonance frequency between spheres in the evacuated environment and the humid environment [177]. It was thus concluded that humidity was not a dominant factor in determining the stiffness of the contact, but the noticeable peak shift indicated that microsphere-based systems could be used as humidity sensors.

To quantify the variation in the axial contact resonance frequency across a microsphere monolayer sample, we performed a map scan of the resonance frequency peak across a 0.5 mm x 4 mm region. The sample comprised of a monolayer of 1 μm diameter polystyrene spheres adhered to an aluminum-coated glass substrate. The contact resonance of the microsphere monolayer was measured at different regions via the hybridization of the resonance with surface acoustic waves generated using the laser-induced transient grating (TG) technique. Surface acoustic waves with 10 μm wavelength were generated by crossed pump beams. The

pump beam was 500 μm in diameter, while the probe had a diameter of 200 μm. The pump and probe beams were incident through the glass and focused on the side of the aluminum film opposite to that of the spheres. The sample was mounted on a motorized X-Y stage, and was scanned in 50 μm steps in the X- and Y-directions. Note that the larger probe spot (compared to the motor step size) resulted in an oversampling of the resonance frequency measurements. Figure 4.9 shows the 0.5 mm x 4 mm scanned region, where each pixel is represented by the frequency of the contact resonance peak.

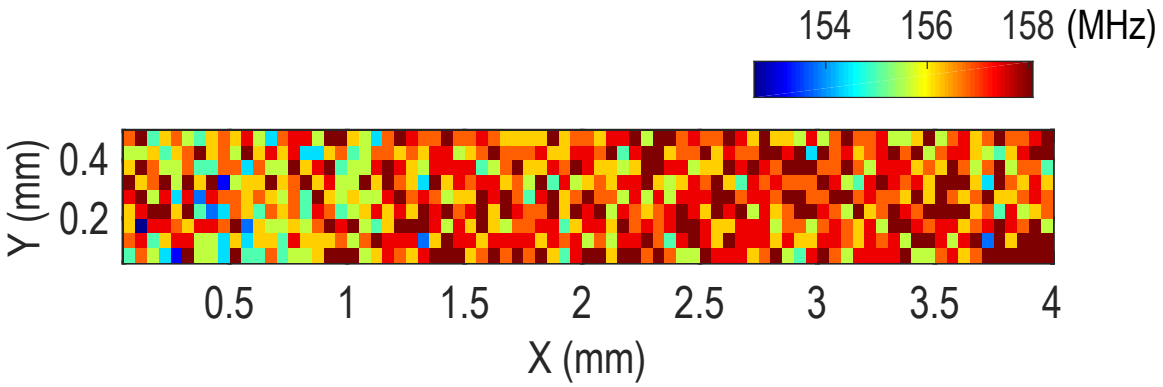

Figure 4.9: Map scan of a 0.5 mm x 4 mm region of the sample highlighting the variation in the axial contact resonance frequency of a monolayer of 1 μm diameter polystyrene spheres adhered to an aluminum-coated glass substrate. The pixel size is 50 μm x 50 μm.

The map scan in Figure 4.9 shows that the axial contact resonance frequency measured in the 0.5 mm x 4 mm region of the sample varies between 150 MHz to 158 MHz, and corresponds to a 5 % variation. This is consistent with previous measurements by Eliason and coworkers [177]. We have observed high sample-to-sample variations of up to 20 %, while variations within the same sample have not exceeded 5 %. Our findings suggest that our measurements may be sensitive to variations in the average particle size of spheres obtained from different batches and from different sources, as well as to substrate treatment and cleaning methods. A systematic study that takes into account various factors, including

the surface energies of the contacting bodies, the surface roughness, the level of impurities on the surface and between the contacts, may shed greater light on the sources that could contribute to variations in sphere-substrate adhesion, and the contact resonance frequency of microsphere monolayers.

4.6 Conclusion

In this chapter, we have studied the scaling of the normal contact stiffness of sphere-substrate contacts with the sphere radius and the contact size for spheres ranging between 400 nm and 4.16 μm in diameter. The contact stiffness is calculated from laser-induced axial contact vibrations of monodisperse monolayer colloidal crystals comprising of polystyrene spheres adhered to an aluminum-coated glass substrate. We introduce a novel technique to estimate the contact radii of the spheres at equilibrium by measuring the size of polymer "rings" deposited around the sphere substrate contacts, and supplement these with estimates made from visual observations of the contacts. While previous studies have investigated either the scaling of the contact radius at equilibrium with the sphere radius [256–264], or that of axial contact stiffness with sphere radius [110] to further understand the applicability and validity of contact mechanics models at the microscale, we combine the two to investigate the scaling of the contact stiffness with the equilibrium contact radius, which is independent of the work of adhesion between the sphere and the substrate. We find that although the measured stiffnesses are higher than those predicted by adhesive elastic contact models using the theoretical work of adhesion, they scale with the sphere radius with the same power law exponent predicted by adhesive elastic models. We attribute the increase in stiffness to the large contact radii at equilibrium resulting from plastic deformation of the spheres in the contact region by adhesive forces. In addition, despite the initial plastic deformation of the spheres by adhesive forces, the scaling of the axial contact stiffness with the contact size is accurately predicted by the DMT adhesive elastic model. This scaling is independent of the sphere radius and the work of adhesion, and therefore bypasses the difficulties

in experimentally determining the work of adhesion between contacting surfaces [269]. Our observations of the elastic unloading and reloading after initial plastic deformation of the spheres are consistent with previous theoretical [133, 142, 272] and experimental works at the macroscale [141, 273].

We have also studied the spallation of microsphere monolayers, and using an inertial model, estimated the adhesion force of a 1 μm diameter polystyrene microsphere monolayer [268]. Microscope images of the spalled monolayer regions revealed a unique morphology, namely, partially detached monolayer flakes composed of single hexagonal close packed crystalline domains. The unique monolayer flakes may find future application in laser-induced particle transfer applications [274], and provide an opportunity to study the in-plane fracture mechanics of microsphere monolayers. Finally, via scanning transient grating spectroscopy, we have quantified the variations in the contact resonance across a sample.

Our results can also guide future directions aimed at studying the dynamics of microscale granular crystals. Several nonlinear phenomena such as solitary wave propagation [275, 276] and acoustic rectification [93] stemming from the Hertz contact law [3] have been reported in macroscale granular crystals. In such systems, the contact area was much smaller than the characteristic dimensions of the granular crystal unit cells and could be assumed to be point contacts. Studying microscale analogs of such phenomena could be challenging given the high magnitude of adhesive forces at reduced length scales, but could be realized with the use of stiff spheres with high yield strength. There has also been considerable interest in exploring the impact and shock wave mitigation abilities of macroscale granular via elasto-plastic wave propagation studies [277–279]. This work could also direct future studies on investigating the effects of adhesion-induced plasticity for exploring similar shock and high-amplitude phenomena at the microscale. It could also lay the foundation for the further experimental validation of contact mechanics models. While we have studied the collective axial vibrations

of monolayers for small amplitudes (relative to the equilibrium displacement), the present study also opens avenues to explore the effects of high amplitude displacements after initial plastic deformation including hysteresis, with an overall aim of developing nonlinear locally resonant, micro- and nano-scale granular metamaterials.

4.7 Collaborator Contributions

The author of this dissertation fabricated the samples, conducted the laser ultrasonic experiments, performed the AFM and SEM measurements, and analyzed the experimental data. Some of the colloidal particles, described as "in-house" spheres, were fabricated by the group of N. Vogel. N. Vogel also suggested the use of PVA to measure contact radii. Guidance of the interpretation of the experimental results and the applicability of contact models was provided by M. Abi Ghanem. A. Lele developed the initial finite element model, upon which further modifications were made by the author. A. Emery provided guidance on the contact mechanics and FEM modeling tasks. The laser-induced spallation experiments were performed by M. Hiraiwa and M. Stossel. The scanning contact resonance frequency measurements were performed by M. Abi Ghanem and the author.

Chapter 5

TUNING THE AXIAL CONTACT RESONANCE OF MICROSPHERES VIA MICROLENSING

5.1 Introduction

In this chapter, we explore a novel mechanism to tune the axial contact resonance of a monolayer of microspheres via a nanostructural contact geometry modification induced by optical microlensing. The monolayer of microspheres acts as an array of lenses, resulting in a "microlens", each of which focuses the incident optical energy from the pump laser beam to a region confined to the contact area between the sphere and the substrate. By varying the energy of the incident pump laser pulse, we tune the axial contact resonance frequency. Using scanning electron microscopy (SEM), we observe the formation of 'nanoholes' in the sphere-substrate contact region that correlates with the energy of the laser pulse. Using microlensing as a tuning mechanism, we observe an increase of over three times the original axial contact resonance using microlensing as a tuning mechanism. Our results show that microlensing can be used as a novel multi-step mechanism to tune the contact-based axial resonance of a microscale granular crystal.

As discussed in Section 1.1.3, numerous studies have demonstrated the tunability of macroscale granular crystals by the application of a variable static load to enable a response in the linear, weakly nonlinear, and highly nonlinear regimes [48, 49, 131, 280, 281]. In a recent study by Hiraiwa and coworkers [282], the dynamic response of a disordered microscale granular system was tuned by changing the magnitude of static compression applied to the material.

At small length scales, application of uniform static compression to tune the response of a microscale granular crystal can present numerous challenges, particularly in the case of monolayer microscale granular crystals, where a single defect particle in the monolayer can introduce geometrical difficulties in the application of a uniform external load. Controlling the interparticle and particle-substrate interactions using mechanisms such as electrophoresis [283], electric fields [284], magnetic fields [285] or particle sintering [114,145] are promising mechanisms to tune the dynamic behavior of microscale granular crystals. The contact resonance frequency of microspheres could also be tuned by changing the mass and shape of the spheres using plasma-assisted etching [5]. The microlensing-based tuning mechanism discussed in this chapter is an all-optical technique that does not affect the geometry or mass of the spheres.

Micro-/nano-spherical lens photolithography (SLPL) has emerged as an inexpensive, inherently parallel, and high-throughput approach to the creation of highly ordered nanostructures. SLPL based on monolayer colloidal crystals of self-assembled colloidal micro-/nano-spheres have recently made remarkable progress in overcoming the constraints of conventional photolithography in terms of cost, feature size, tunability, and pattern complexity [154]. However, while the SLPL technique is particularly appealing due to its low-cost when compared to manufacturing and using conventional photomasks, this technique is sensitive to small defects in the colloidal crystal, which also affect the quality of the nanostructures to be fabricated. Furthermore, patterns etched using the SLPL technique are typically limited to hexagonal close packed features. Despite these challenges, the SLPL technique has enabled the fabrication of a variety of highly ordered nanostructures with applications in light emitting diodes, nano-patterning semiconductors, and localized surface plasmon resonance devices [154]. The use of monodisperse colloidal crystals for patterning using microlensing-based projection lithography was first proposed by Whitesides and coworkers [286–290]. These works showed that the use of an array of transparent micro-/nano-spheres could gen-

erate periodic, sub-micron structures in photoresist, over centimeter-scale distances, without the use of photomasks. Ma and coworkers demonstrated that both silica and polystyrene have optical indices that are close to the optimum value at the wavelengths used by conventional UV light photolithography, making silica and polystyrene colloidal particles suitable for microlensing-based patterning [291]. Mohseni and coworkers showed that the the capabilities of the SLPL technique could be extended by changing the angle of the incident laser beam with respect to the colloidal crystal, resulting in the formation of "photonic nanojects", whose geometry could be controlled by the angle of incidence of the exposure beam [292]. Besides fabricating ordered two-dimensional nanostructures, the SLPL technique has also been used to fabricate highly three-dimensional ordered nanostructures by harnessing the volumetric nature of the intensity distribution generated by a 2D nano-sphere lenses array [293]. The SLPL technique has also been employed in the construction of photonic crystal structures [154, 294]. Besides the fabrication of patterned nanostructures, the microlensing phenomenon has also been used for imaging [155]. Despite the vast demonstrated applications of the use of ordered colloidal particles as lens arrays, the use of the microlensing phenomenon to tailor the contact-based dynamic response of particles adhered to substrates has remained unexplored.

In this chapter, we discuss the use of microlensing as a novel mechanism to tune the axial contact resonance frequency of monolayer microsphere arrays. The spheres focus the pump energy to a spot size that is within the contact area of the sphere-substrate contact. For a 1 μm diameter silica sphere, the contact diameter at equilibrium, using the DMT model and theoretical work of adhesion, is $\sim$ 28 nm. As discussed in Chapter 2, the equilibrium contact radius a scales with $R^{2/3}$ for the DMT and JKR models, where R is the radius of the particle. The change in geometry of the substrate beneath the sphere, incurred due to ablation of the metal film of the substrate, stiffens the contact, and as a result, increases the resonance frequency of the microsphere. We excite the axial resonance of the microspheres using a

laser ultrasonic technique, and detect the microsphere vibrations using a phase-mask-based interferometer. We evaluate the change in the resonance frequency with increasing pump pulse energy, and also study the dependence on the resonance frequency with the number of pump pulses. We correlate the changes in resonance to the size of the 'nanoholes' formed by the microlensing effect on the substrate, in addition to mechanisms such as material build-up around the contact.

5.2 Experimental Details

The microsphere monolayer in this study was fabricated with monodisperse silica microspheres with diameter $D = 2$ μm. Close-packed monolayers were assembled on titanium-coated glass slides using the wedge-cell convective self-assembly technique, described in Section 1.3.1. The titanium film was 200 nm thick, and was deposited on the glass substrate using electron beam evaporation. A representative scanning electron microscopy image of the top-down view of the microsphere monolayer is shown in Figure 5.1(a).

The axial contact resonance of the microsphere monolayer was excited using a laser ultrasonic technique, described previously in Section 4.2. In summary, optical pump pulses of 440 ps duration, emitted from a diode-pumped solid state laser (wavelength 532 nm, pulse energy 0.7 μJ and repetition rate 1 kHz), were focused to a circular spot of 360 μm on the titanium film of the sample directly through the spheres. Absorption of the pump pulse energy by the titanium film and its subsequent rapid thermal expansion excites the vertical contact resonance of the spheres, while rotational and transverse vibrations are not excited due to symmetry constraints [9]. The sphere vibrations were detected with a phase-mask-based interferometer, described in Section 1.4.2, which is sensitive to out-of-plane displacements [181], by focusing a continuous wave (CW) probe beam (wavelength 514 nm, average power 10 mW) to a 280 μm diameter spot through the glass substrate on the titanium film.

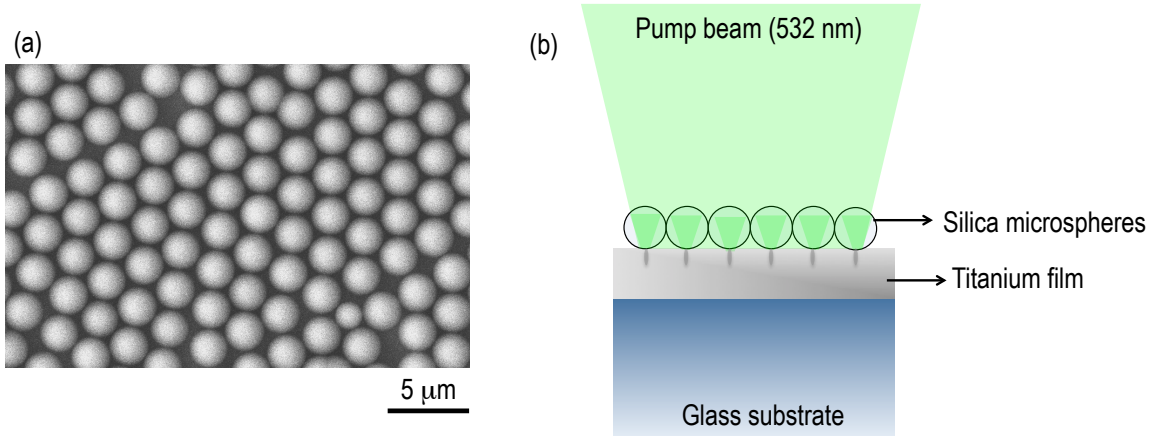

Figure 5.1: (a) Representative SEM image of a monolayer of 2 μm diameter silica spheres on a titanium-coated glass substrate. (b) Schematic of the microlensing experiment that shows the incident pump pulse being focused by spheres in the contact region.

The interferometric signal was digitized and recorded using an oscilloscope, and averaged over 10^4 pump pulses.

The original contact resonance of the microsphere monolayer was measured by focusing the pump laser beam through the glass substrate on the side of the titanium film opposite the spheres. Following the initial measurement of the contact resonance from the back, the geometry of the sphere-substrate contact was altered with single or multiple pump laser pulses incident through the spheres, and focused by the silica spheres to form the nanoholes in the titanium film. A schematic of the microlensing event is illustrated in Figure 5.1(b). Table 5.1 lists the pulse energies of the single pulses used for microlensing. Following the microlensing event, the contact resonance of the spheres was measured with excitation pump pulses incident through the spheres, at a 1 kHz repetition rate, each with pulse energy of 0.7 μJ. Each microlensing experiment was performed on a unique location of the sample, in order to examine the pulse energy-dependent changes in the substrate after each microlensing event.

The nanholes formed as a result of ablation of the titanium film due to microlensing by the silica spheres were examined after the laser ultrasonic experiments under a scanning electron microscope by removing the spheres were removed using an adhesive tape.

In addition to microlensing induced by single ablative pulses, the effect of multiple microlensing pulses on the contact resonance of the microsphere monolayer was also examined. Table 5.2 summarizes the experiments performed with multiple microlensing pulses. Like in the case of the single pulse microlensing experiments, the resonance measurements were performed following the microlensing pulses with excitation laser pulses with 0.7 μJ energy and repetition rate 1 kHz incident on the side of the spheres.

Table 5.1: Details of microlensing experiments with single pulses.

Spot	Single Pulse Energy (μJ)
1	0.7
2	2.4
3	4
4	4.9
5	7.5
6	8.7
7	11
8	13
9	13.9
10	16
11	20.6
12	26.7

Table 5.2: Details of microlensing experiments with multiple pulses.

Spot	Pulse Energy (μJ)	No. of Pulses
13	8.7	10
14	8.7	100
15	8.7	100
16	8.7	1,000
17	8.7	10,000
18	8.7	Continuous Train of Pulses ($\sim$ 100,000)

5.3 Results and Discussion

Measurements of the original contact resonance of the microsphere monolayer were performed on multiple regions of the sample with the pump laser beam focused through the glass substrate on the side of the titanium film opposite the spheres. The pump pulse energy was 5.4 μJ for the initial measurements of the resonance from the back. These initial measurements showed that the contact resonance varied between $\sim$ 73 - 79 MHz. Following these initial measurements, the contact resonance of the monolayer was measured from the front, with the pump pulses incident on the side of the spheres. For the front side measurements, the pump pulse energy was reduced to 0.7 μJ. Measurements from the front with 0.7 μJ pump pulse energy revealed resonances that varied between $\sim$ 73 - 79 MHz, indicating that low energy pulses of 0.7 μJ, focused through the spheres, did not affect the resonance of the monolayer.

5.3.1 Single-pulse Microlensing

The microlensing experiments were subsequently performed with single pulses of increasing energy on different regions of the sample. The resonance was measured before and after the

microlensing pulse. Figure 5.2(a) shows the change in the axial contact resonance frequency power spectra of the microsphere monolayer after irradiating the monolayer with single microlensing pulses of increasing energy. The resonance frequency as a function of microlensing pulse energy is plotted in Figure 5.2(b).

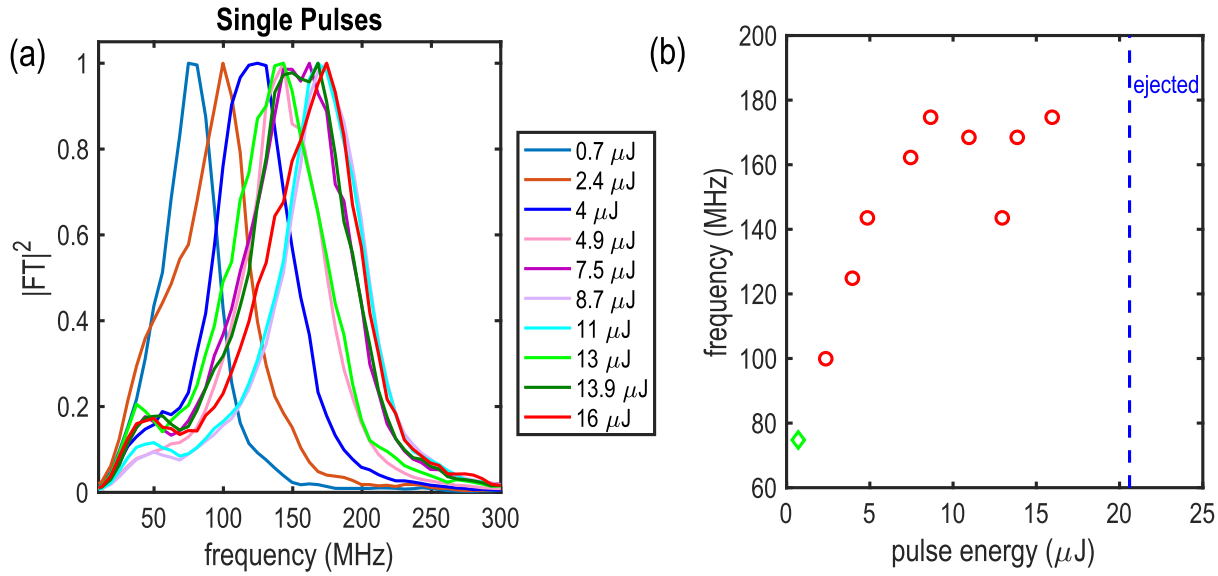

Figure 5.2: (a) Power spectra of the axial contact resonance of the microsphere monolayer which highlight the change in the resonance after irradiation with single microlensing pulses of increasing energy. (b) The change in the resonance as a function of single pulse energy. The dashed blue line denotes the threshold energy beyond which the spheres ejected from the substrate. The green diamond marker represents the original resonance frequency of the monolayer.

The green diamond symbol in Figure 5.2(b) represents the original average contact resonance frequency of the monolayer measured at different regions of the sample. The contact resonance increases to $\sim$ 175 MHz when irradiated with a single pulse of 8.7 μJ energy. Further increasing the energy of the microlensing pulse does not show a corresponding increasing

in the resonance frequency of the monolayer. Beyond pulse energies of 20 μJ, we observed that the spheres had sufficient energy to detach from the substrate, which prevented the measurement of the resonance after irradiation with pulses greater than 20 μJ in energy.

As stated previously, each microlensing experiment was performed on a different region of the sample. Following the dynamic measurements of the contact resonance, the spheres were removed from the substrate, and the morphology of the substrate as a result of ablation of the titanium film was observed using scanning electron microscopy. The SEM images of each spot after irradiation with a single pulse are illustrated in Figure 5.3.

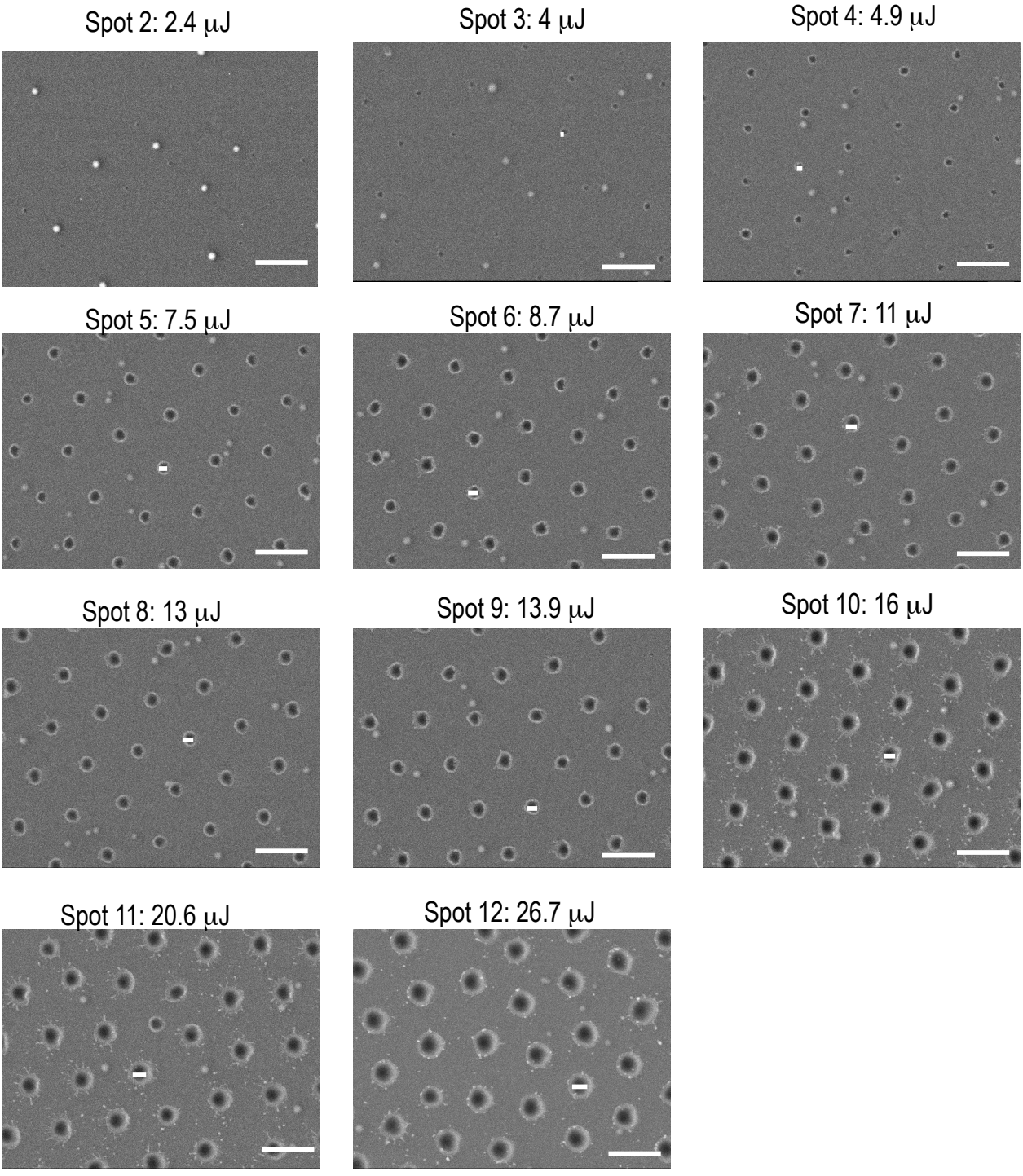

Figure 5.3: Scanning electron microscope images showing top-down views of nanholes formed in the titanium film by microlensing with single pulses that ablate the titanium film beneath the sphere. The scale bar is 2 μm in all panels.

We see the presence of nanoholes in the titanium film whose inner diameter increases with increasing pulse energy. Although we see an increase in the axial resonance, from the original 75 MHz to 100 MHz after irradiation with a single pulse of 2.4 μJ, we do not observe any distinct nanoholes in the titanium film from the SEM images. It is likely that the nanholes could be very small, and have not been detected at the magnification used in the SEM images. Imaging this spot at higher magnification under the SEM, or the use of atomic force microscopy, may reveal the presence of nanoholes in this spot. At Spot 3, which was irradiated with a single pulse of 4 μJ energy, we see distinct nanholes with inner radius $\sim$ 125 nm. Irradiating the sample with a single 4.9 μJ pulse results in nanoholes on the substrate with an average inner radius of $\sim$ 127 nm. Spot 9, which was irradiated with a 13.9 μJ pulse, had nanoholes with an average inner radius of $\sim$ 283 μm. Nanholes with an average inner radius of $\sim$ 351 nm were seen in Spot 10, which was irradiated with a single 16 μJ pulse. We also see "splashes" of titanium around the nanholes for pulse energy greater than 16 μJ. The average inner radii of the nanoholes, estimated from the SEM images, are plotted in Figure 5.4. The error bars denote an uncertainty of $\pm$10 % in the measured inner radii. The blue dash-dot line indicates the threshold pulse energy for sphere detachment from the substrate.

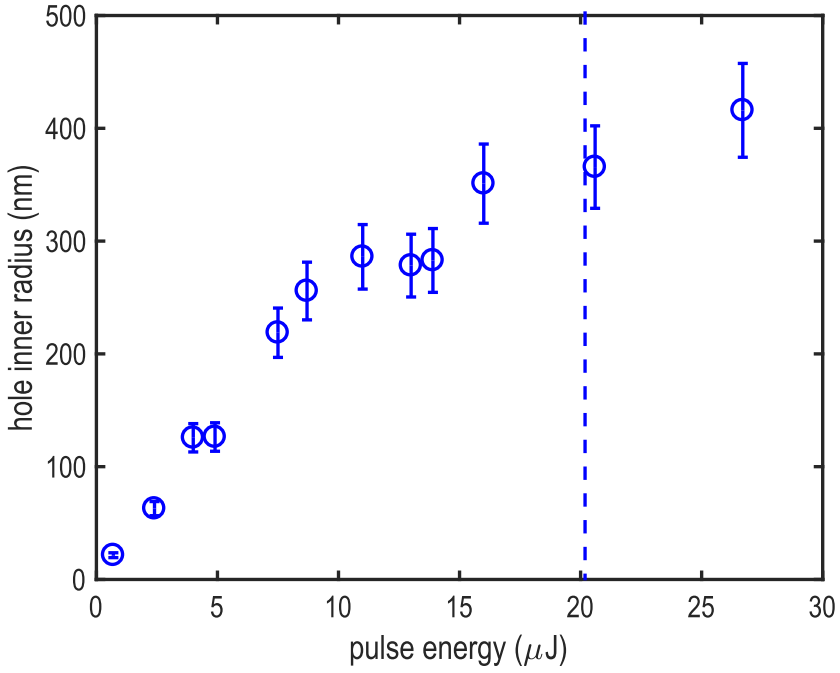

Figure 5.4: The average inner radius of the nanholes formed in the titanium film from single-pulse microlensing as a function of the microlensing pulse energy. The dash-dot line indicates the pulse energy limit beyond which the spheres detached from the substrate.

5.3.2 Multi-pulse Microlensing

Following the single-pulse microlensing experiments, we investigated the effect of microlensing with a train of multiple pulses on the monolayer resonance. We irradiated the microsphere samples with multiple pulses at a fixed pulse energy of 8.7 μJ, and observed an increase of over three times the original monolayer contact resonance. Figure 5.5(a) shows the power spectra of the contact vibrations after irradiating the sample starting with a single pulse, and going up to 10,000 pulses and finally, a continuous train of pulses ($\sim$ 100,000 pulses) with 8.7 μJ energy. The excitation pulse energy for measuring the resoannce was 0.7 μJ. The dependence of the axial contact resonance of the monolayer with the number of microlensing

pulses is shown in Figure 5.5(b). We see that the contact resonance increases from $\sim$ 75 MHz to 175 MHz after irradiation with a single 8.7 μJ pulse. The resonance further increases after irradiating with larger number of pulses, and goes up to 267 MHz after microlensing with 1,000 pulses. It is interesting to see that the resonance measured with continuous pulses is about the same as that after microlensing with 1,000 pulses. We note that in the case of Spot 18, the interferometric measurements of the contact vibrations were made with the microlensing pulses (of energy 8.7 μJ) acting as the excitation pulses.

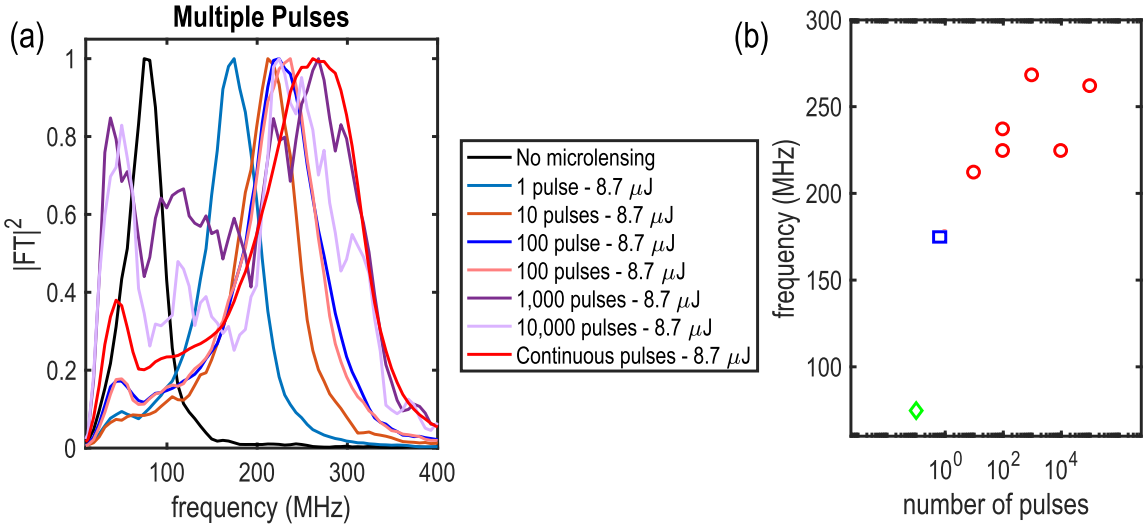

Figure 5.5: a) Power spectra of the axial contact resonance of the microsphere monolayer which highlight the change in the resonance after irradiation with a train of multiple microlensing pulses of fixed energy (8.7 μJ). (b) The change in the resonance as a function of number of microlensing pulses. The green diamond marker represents the original resonance frequency of the monolayer. The blue rectangular marker in panel (b) is the same as the single pulse microlensing event.

SEM images of the substrate in the regions irradiated with multiple pulses of fixed energy (8.7 μJ) are illustrated in Figure 5.6. The images reveal a clear dependence of the size and

shape of the nanhole on the number of microlensing pulses. In the multi-pulse microlensing experiments, we observe nanoholes with geometry similar to those observed with the single pulse irradiation experiments, albeit with some "channel" formation that protrudes above the plane of the substrate. The average inner radii of the nanoholes formed by irradiation with different number of pulses is shown in Figure 5.7. The error bars denote an uncertainty of ± 10 % in the measured inner radii. We see that the average inner radius of the nanohole drops from single pulse irradiation to irradiation with ten pulses, and gradually increases from ten-pulse-irradiation to irradiation with $10,000$ pulses. We note that the average inner radius of the nanohole when irradiated with $10,000$ pulses is slightly less than the nanohole average inner radius from a single microlensing event. It is also interesting to note that although the average inner hole radius does not increase a large amount from microlensing with a single pulse to microlensing with $10,000$ pulses, the axial resonance frequency increases from 175 MHz to 225 MHz (which corresponds to a ~ 30 % increase). We also note that Spot 18, which was irradiated with a continuous train of $\sim$ 100,000 pulses of 8.7 μJ energy, shows features with morphology very different from other irradiated spots. Instead of distinct periodic nanoholes imprinted in the titanium film, we observe channels carved in the titanium in random geometries.

In the case of the microlensing experiments with multiple pulses, we see that although the inner radius of the nanoholes do not increase significantly with number of microlensing laser pulses, the measured resonance increases by $\sim 30\%$ from the single microlensing pulse case, to microlensing with a train of continuous pulses. We attribute the increase in axial resonance of the microspheres observed with increasing the number of pulses at fixed energy to the build-up of material around the nanoholes seen in Figure 5.6 that "piles-up" around the sphere-substrate contact. We note that the increase in the nanohole size is the dominant mechanism for the increased stiffness in the single pulse microlensing experiments, where minimal material "pile-up" was observed around the nanoholes. The "pile-up" of the

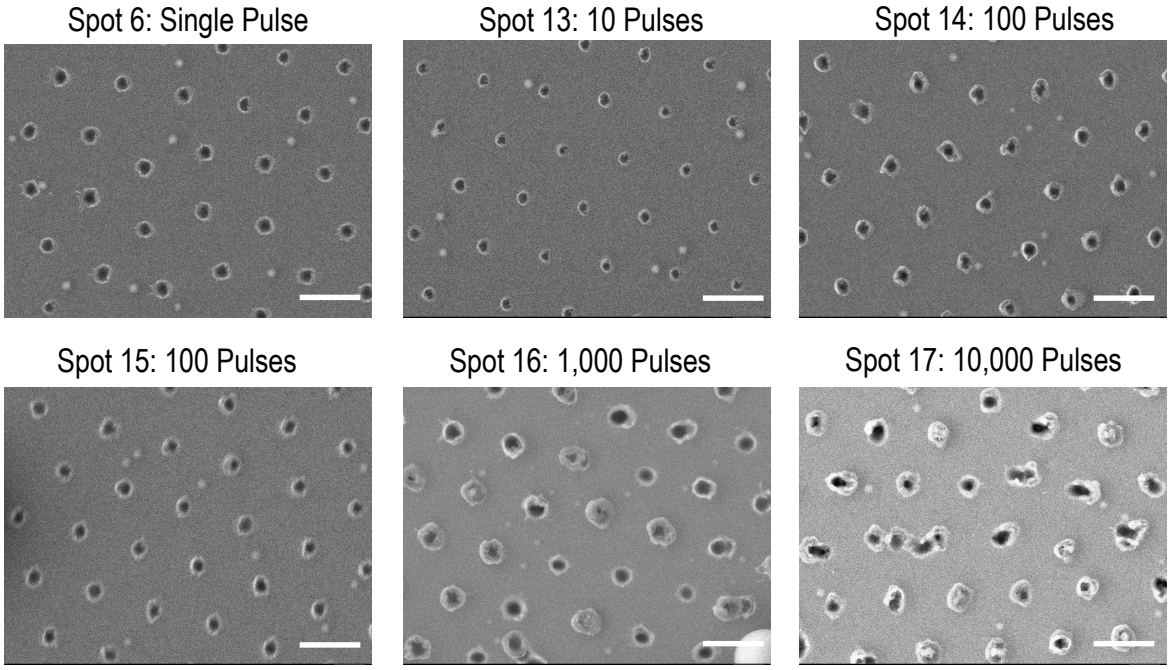

Figure 5.6: Scanning electron microscope images showing top-down views of nanholes formed in the titanium film by microlensing with a single pulse and multiple pulses of fixed energy (8.7 μJ) that ablate the titanium film beneath the sphere. The scale bar is 2 μm in all panels.

titanium film around the nanohole is analogous to pile-up patterns observed during nanoindentation experiments [295, 296]. Correlations between the height of the material piled up, and the measured axial resonance could provide greater insight into the relationship between contact stiffness and nanohole geometry. Measurements of the "pile-up" height, as well as the depth of the nanoholes, can be made with atomic force microscopy, and can present new directions for designing nanoholes with a desired granular crystal response. Contact mechanics models which account for the nanoholes beneath the spheres could also predict the contact stiffness and the resonance frequency for a given nanohole geometry.

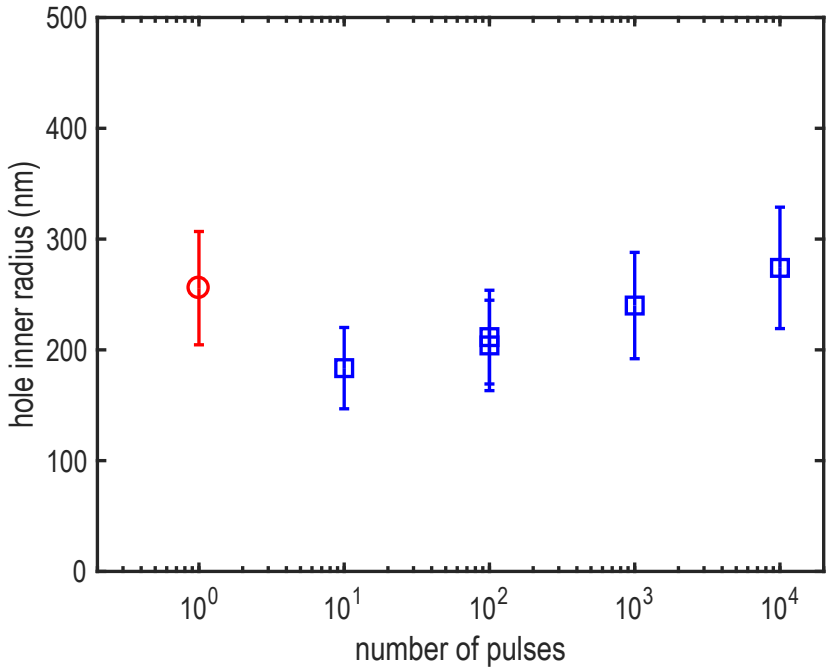

Figure 5.7: The average inner radii of the nanholes formed in the titanium film from microlensing as a function of the the number of microlensing pulses of fixed energy (8.7 μJ). The red circular marker represents the average inner radius of the nanoholes created from a single 8.7 μJ microlensing pulse.

5.4 Conclusion

In this chapter, we have presented a novel all-optical multi-step mechanism to tune the axial contact resonance of microsphere monolayers using the microlensing technique. In this technique, each sphere acts as a lens to focus the incident pump pulse energy to a small small within the contact area. The resultant rise in the energy density ablates the metal film on the substrate, and consequently, alters the sphere-substrate contact geometry. We observe an increase of over three times in the resonance frequency, which is affected not only by the energy of the microlensing pulse, but also by the number of pulses used for

microlensing. We attribute the increase in resonance frequency to the increase in the contact stiffness between the sphere and the substrate. The increased contact stiffness arises from an increase in the contact area, which evolves from a circular to ring-like geometry during the microlensing event. The contact stiffness is also increased by material build-up around the nanoholes, which further increases the effective contact area. Investigating the morphology of the holes using SEM or AFM, along with developing a contact model for the modified geometry, will provide a greater understanding of the stiffness increase, and consequent change in the contact-based dynamics. Contact models that account for the geometry change from a classical Hertzian profile to a sphere-hole contact, can be used to predict relationship between the resonance frequency and nanohole diameter. Our results show the potential of tuning microscale granular crystals in a variety of ultrasonic wave tailoring applications which demand a versatile, tunable platform.

5.5 Collaborator Contributions

The samples were fabricated by the author of this dissertation. The microlensing experiments were performed by M. Abi Ghanem and the author. The SEM images were captured by the author.

Chapter 6

LONGITUDINAL EIGENVIBRATION OF FEW-LAYER GRANULAR CRYSTALS AND THE EFFECT OF NANOSCALE CONTACT BRIDGES

6.1 Introduction

As discussed in Section 1.3, colloidal self-assembly has emerged as a "bottom-up" approach to manufacturing nanostructured materials with controlled hierarchical architectures, and has enabled their fabrication inexpensively and on a large scale [153]. Primarily investigated for their unprecedented features in areas like photonics [145, 221], plasmonics [224], and biosensing [222, 297], self-assembled colloidal crystals, which consist of ordered, close-packed lattices of micro- to nanoscale spherical particles [6], have also shown promise in the context of their vibrational dynamics or "phononic" properties [74, 219].

Macroscale analogues of dry colloidal crystals, often referred to as "granular crystals", have also been a topic of significant interest due to their unique dynamics, as described in Section 1.1.3 and references [47, 48, 53]. In granular crystals, spheres arranged in close packed arrays can be thought to move similar to rigid bodies and interact via small contact regions (compared to the particle size) that elastically deform and act as massless springs. Such contact-based dynamics have underlied the large interest in granular crystals, as the interplay of the contact nonlinearity, typically modeled by the Hertzian contact model [3], coupled with dispersion induced by mechanisms such as structural periodicity [53] and local resonances [50, 198, 298] have been shown to enable new acoustic wave tailoring strategies [47, 53]. However, until recently, studies concerning the contact-based dynamics of

granular crystals have been restricted to systems composed of millimeter to centimeter-sized spheres. Acoustic studies of colloidal crystals, on the other hand, mostly focused on colloids in a host medium [74, 114, 226]. Until recently, the dynamics of dry colloidal crystals or "micro- to nanoscale granular crystals" remained an unexplored territory.

In previous chapters, the contact-based dynamics of dry, two-dimensional (2D) colloidal crystal monolayers have been examined. It was shown that adhesive van der Waals forces [57] statically compress the interparticle and particle-substrate contacts, and effectively linearized the crystal dynamics for small displacements (relative to the static deformation). This compression resulted in the formation of multiple contact resonances of the crystal, including modes with both translational as well as coupled translational-rotational motion [9, 125, 204, 299]. In contrast, the contact-based dynamics of three-dimensional (3D) colloidal crystals remain largely unexplored. Using a Brillouin Light Scattering spectroscopic technique, a previous study exploring 3D colloidal crystal dynamics revealed a single resonant peak that was attributed to a band of contact-based modes, however, the individual eigenmodes were not resolved [114]. Laser ultrasonic techniques have also been used to measure the transmission of hypersonic acoustic waves traveling through dry, sintered 3D colloidal crystals [145], although the measurements provided limited information concerning the acoustic modes of the crystal. In addition, due to the sintering of the crystal in reference [145], we expect limited dynamic deformation of the particle contacts was involved. Several studies have also explored the contact-mediated acoustics of 3D colloidal films, however these were either disordered [115, 300], or the spheres were separated by large ligands [116–118] or polymer tethers [113] that approach the particle size and result in non-Hertzian contact mechanics.

In this chapter, we study the longitudinal contact-based vibration of self-assembled, dry, 3D colloidal crystals with long range order of varied thicknesses, and measure multiple,

discrete eigenmodes of the crystal. In contrast to prior studies, using our laser ultrasonic technique (described previously in Section 1.4.2), we are able to access the low-frequency, contact-based modes of the 3D crystals, and our spheres are not functionalized with large connective ligands that can cause deviation from the Hertzian mechanics of elastically deforming spheres in contact. We correlate the resulting contact stiffnesses, extracted by way of a coupled oscillator model, with scanning electron microscopy (SEM) and atomic force microscopy (AFM) observation of the contacts, and find that nanometric bridges surrounding the contacts, which are much smaller than the particle size, can more than triple the contact stiffness. In all cases, we find higher contact stiffnesses for our self-assembled crystals than those predicted using adhesive elastic contact models [108,301]. We find also that the bridge sizes and contact stiffness vary with sample fabrication method, and that the contact stiffness can decrease with increasing numbers of crystal layers. By studying the quality factors of the measured eigenmodes, and comparing them with an analytical model that estimates acoustic energy radiation into the substrate based on the estimated impedance mismatch between the colloidal crystal and the substrate, we gain insight into energy loss mechanisms in our system. From this comparison, we suggest that energy leakage plays a large role for low frequency modes but is surpassed by disorder- or material-induced losses as the modal frequency increases.

6.2 Experimental Details

We use monodisperse polystyrene spheres of diameter $D = 390$ nm that form a colloidal crystal with high order. The colloidal crystal is assembled on a substrate that consists of a 1.5 mm glass microscope slide, which is coated with a 100 nm thick layer of aluminum to absorb the optical pump energy and then a 20 nm thick silica layer to facilitate the self-assembly process. The polystyrene spheres are synthesized using a surfactant-free emulsion polymerization process [270]. The crystals are fabricated using the vertical convective

self-assembly technique (see Section 1.3.3 and references [6, 7]) using varied solvents and purification strategies, as is detailed in Table 6.1. A schematic of the self-assembly technique is illustrated in Figure 6.1(a). A 20 mL capacity glass scintillation vial is filled with 10 mL of the colloidal suspension. The substrate is then held vertically while being immersed in the suspension. The substrate and suspension are then left to dry in an oven or in ambient laboratory conditions (see Table 6.1). After complete drying, colloidal crystals with millimeter areas of defined and uniform thicknesses are obtained. Regions with uniform layer thickness can be easily identified under a microscope from their different coloration, as is illustrated in Figure 6.1(c). In the most densely packed case, this geometry represents perfectly registered stacks of hexagonally close-packed (HCP) colloidal monolayers. A representative SEM image of our colloidal crystal can be seen in Figure 6.1(d). The distinct structural coloration enables us to identify regions with defined layer thickness and thus study, in detail, the thickness-dependent contact-based acoustic properties of the crystals.

To characterize the out-of-plane acoustic response of the colloidal crystals, we use a laser ultrasonic technique that is illustrated in Fig. 6.1(b). Optical pump pulses (440 ps pulse duration, 532 nm wavelength, 7 μJ pulse energy, and 1 kHz repetition rate) incident through the glass slide are focused onto the aluminum film. The pump pulse is focused to an elliptical spot (436 μm x 76 μm at $1/e^2$ intensity level) or a 200 μm diameter circular spot, depending on the size of the layer being characterized. Absorption of the pump pulse energy by the aluminum film induces a rapid thermal expansion that excites mechanical vibration of the colloidal crystal and acoustic waves in the substrate. In the colloidal crystal, longitudinal vibrations with out of plane motion are predominantly excited, as the excitation of transverse vibrations are hindered by symmetry constraints. These vibrations are detected with a phase-mask-based interferometer [181], which is preferentially sensitive to out-of-plane displacements [9]. In the phase-mask-based interferometer, a single continuous wave (CW) laser beam (514 nm wavelength and 52 mW average power) is incident on a phase-mask and split

Table 6.1: Details of sample fabrication parameters for the multilayer samples.

Sample	Conc. (% v/v)	Solvent	Environ.	Centrifuged	Layers Thicknesses
1	0.2	Ethanol	Ambient	3x	1, 2, 3, 4, 5, 7, 8, 12
2	0.01	DI Water	Oven, 75° C	1x	1, 2, 3, 4, 5, 9, 12
3	1	Ethanol	Ambient	3x	6, 7
4	0.5	Ethanol	Ambient	3x	2, 3, 4, 5, 6, 7, 8, 9
5	0.3	Ethanol	Ambient	3x	2, 3, 4, 5, 6, 7, 9
6	0.01	DI Water	Oven, 75° C	3x	2, 3, 4
7	0.01	DI Water	Oven, 75° C	3x	2, 3, 4, 5, 6

into +/1 diffraction orders to produce probe and reference beams focused to 40 μm diameter spots. The probe is focused through the colloidal film onto the aluminum surface, while the reference beam is incident directly on the aluminum surface of a blank region of the substrate. The separation between the probe and reference beams is 4 mm. Upon reflection from the sample, the probe and reference are recrossed onto the phase mask, and recombined interferometrically onto an amplified silicon photodetector where the signal is digitized and recorded using an oscilloscope, and averaged over 10^4 - 10^6 pump pulses.

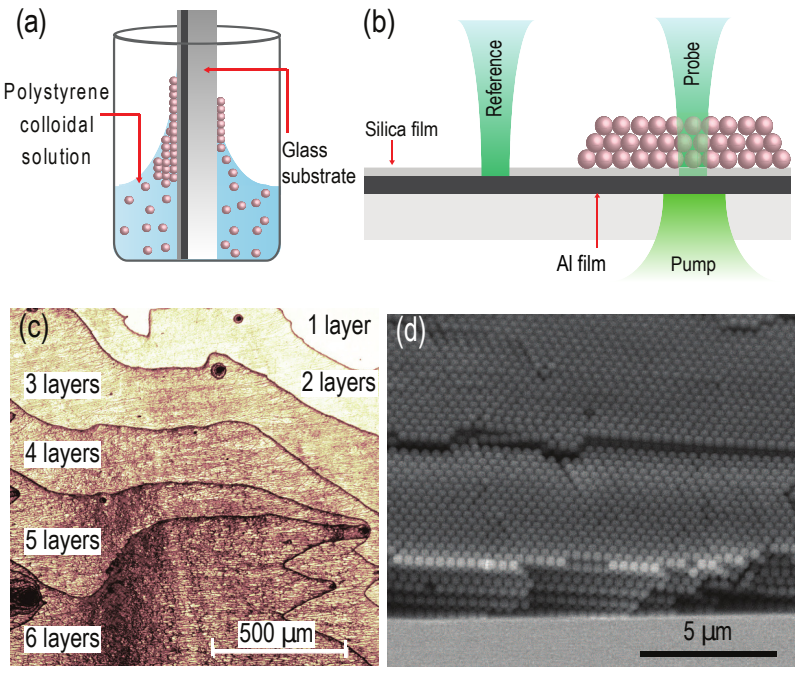

Figure 6.1: (a) Schematic of the multilayer convective self-assembly technique. (b) Illustration of the laser ultrasonic technique used to excite and measure eigenmodes of the colloidal crystal. (c) Optical microscope image showing multiple regions of the colloidal crystal with different layer thicknesses. (d) Representative SEM image of the colloidal crystal.

6.3 Results and Discussion

Figure 6.2(a) shows a signal acquired on a twelve-layer-thick region of a colloidal crystal sample, using the optical characterization method shown in Figure 6.1(b). A sharp initial rise due to the arrival of the pump pulse at the sample followed by a slow decay associated with thermal diffusion is observed. The periodic oscillations in the signal represent the out-of-plane longitudinal vibrations of the colloidal crystal. The power spectrum (amplitude squared of the Fourier transform spectrum) of the time-derivative of the signal in Figure 6.2(a) is shown in Figure 6.2(b), wherein five spectral peaks can be distinguished. The fundamental peak has a frequency $f_1 = 70$ MHz. The intensities of the subsequent peaks decrease with increasing

frequency, such that the intensity of the fifth peak is over three orders of magnitude lower than that of the fundamental peak. We suggest that this is due, in part, to the step-like nature of the excitation, which more efficiently excites modes at lower frequencies, and the increased susceptibility of shorter-wavelength, higher-frequency modes to disorder-induced scattering [195]. Each of the modes identified in the spectrum shown in Figure 6.2(b) are denoted by open diamond markers, and are plotted as function of mode number in Figure 6.2(d) using the same markers. We compare the measured frequencies to the modal frequencies of a continuous film with boundaries that are fixed on one side and free on the other, given by $f_i = (2i1)c/4H$, where i is the mode number, and c and H are the longitudinal sound speed and thickness, respectively of the film [118]. The modal frequencies of the fixed-free film are plotted using blue filled circle markers in Figure 6.2(d), where the sound speed of the film is chosen such that the frequency of the fundamental mode of the continuous film matches the experimentally measured fundamental mode. From Figure 6.2(d), we see that the five measured modes approximately follow the linear trend of the calculated fixed-free film modes as the mode number increases. Similar observations have been made in previous studies on nanocrystal superlattices interacting via ligands that have shown equally-spaced modes [118].

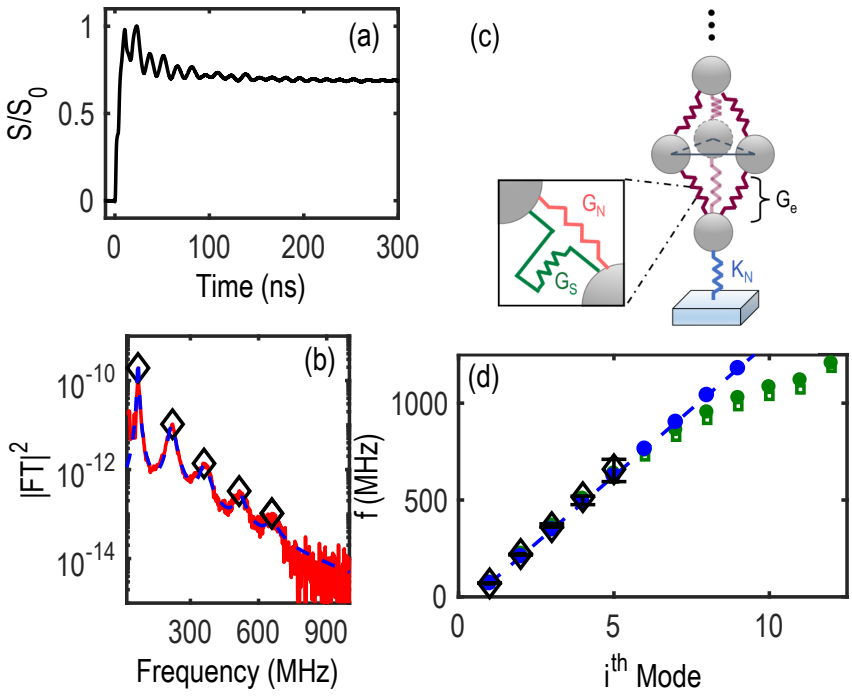

Figure 6.2: (a) Time domain signal corresponding to the out-of-plane eigenvibrations of a 12-layer-thick colloidal crystal. The signal amplitude S is normalized to its maximum amplitude S_0. (b) The solid red line denotes the power spectrum of the time-derivative of the signal in (a), and the dashed blue line denotes the sum of five Lorentzians fitted to the measured spectrum. (c) Schematic of the quasi-one-dimensional coupled oscillator model. (d) Modal frequencies as a function of mode number. Black diamond markers are the modes identified in (b) denoted by the same marker type. The blue circle markers represent the calculated modal frequencies for a fixed-free continuum film adhered to a rigid substrate, where the first mode is matched to the measured fundamental mode. The green markers represent the calculated modal frequencies of the coupled oscillator system using a particle-substrate stiffness obtained via a monolayer region of the same sample measured in (a,b) and an interlayer contact stiffness fitted to the fundamental measured mode (open square markers), and to all five measured modes (filled circle markers). The error bar half-widths in the measured spectral peaks denote the maximum shift in the position of the peaks when the power spectrum time window is adjusted by up to 4 ns.

While the observed modes are well described by the linear relationship corresponding to the continuous film model, we develop a quasi-one-dimensional coupled oscillator model to describe our system and analyze the contact stiffnesses, in which we treat the spheres as rigid bodies connected by massless springs. Similar springs-in-series models (without the lumped masses) have been previously used to study the quasi-static nanoindentation of multilayer colloidal crystals composed of hollow silica nanospheres [302]. We implement a discrete element model because the measured frequencies are lower than the lowest intrinsic spheroidal mode of the particles (2.62 GHz) [243] and the discrete model enables us to separately describe particle-substrate and interlayer contact stiffnesses. A schematic of our quasi-one-dimensional coupled oscillator model is illustrated in Figure 6.2(c). The particle-substrate contact between the first layer and the substrate is represented by an axial contact spring of stiffness, K_N, while the interparticle normal and shear contacts involved in subsequent layers are represented by axial and transverse springs of stiffness G_N and G_S, respectively. The normal and shear stiffnesses are modeled using linearized Hertzian [3] and Hertz-Mindlin contact models [301]. We define an effective interlayer contact stiffness G_e oriented along the the out-of-plane direction, which incorporates the contributions from the three pairs of interparticle normal and shear contact springs, and can be expressed as,

$$G_e = G_N(2 + \nu^*) \tag{6.1}$$

where for statically compressed Hertzian and Hertz-Mindlin contacts, $\nu^* = G_S/G_N = 2\frac{1-\nu_P}{2-\nu_P}$, is the ratio of the interparticle shear and normal contact stiffnesses, and ν_P is the Poissons ratio of the polystyrene spheres [301, 303]. Using Equation 6.1, the colloidal crystal can be simplified to a quasi one-dimensional coupled oscillator system, where each of the oscillators have mass per unit area M, and are connected to one another by springs of stiffness per unit area G. Here, $M = m/A_p$ and $G = G_e/A_p$, where m is the mass of one of the spheres and $A_p = \sqrt{3}D^2/2$ is the area of the primitive unit cell in the HCP lattice. The crystal may also be in the face-centered cubic (FCC) configuration, however, we assume HCP packing in

this chapter. The equivalent one-dimensional coupled oscillator system reduces to a chain of spheres of mass m connected to one another by springs of stiffness G_e, and connected to the substrate by a spring of stiffness K_N. The mass of the sphere is calculated using the density $\rho = 1060$ kg/m^3 of polystyrene [12]. Since our measurements are sensitive to the out-of-plane direction only and we excite primarily longitudinal plane waves, we neglect adhesive contact forces in the transverse direction between neighboring spheres within the same layer.

We first apply our quasi-one-dimensional coupled oscillator model to the spectrum shown in Figure 6.2(b). Using a single oscillator model, we first determine the particle-substrate contact stiffness K_N by measuring the out-of-plane contact resonance frequency $f_{1,m}$ for a monolayer region of the same sample and using the relation $K_N = (2\pi f_{1,m})^2 m$. Using our coupled oscillator model and the experimentally determined particle-substrate contact stiffness KN, we then solve for the effective interlayer contact stiffness G_e of the measured twelve layer region (assuming that all interlayer effective contact stiffnesses are the same), by matching each of the measured modes shown in Figure 6.2b) to the corresponding eigenfrequency. Taking the average value of these effective interlayer stiffnesses, determined for each mode, we obtain a value of $G_e = 0.42$ kN/m. If only the fundamental mode is used, we obtain an effective interlayer thickness $G_e = 0.38$ kN/m, which is 8% lower than the corresponding stiffness obtained by fitting all five measured modes. We note that these effective contact stiffnesses are similar to the stiffness found in reference [114] for colloidal crystals composed of similar-sized PS spheres with face-centered cubic packing. Using these effective interlayer stiffnesses, we then recalculate and plot the resulting modes in Figure 6.2(d), where the green open squares were calculated using the stiffness found by fitting only the fundamental mode and the closed circles using all five measured modes. In both cases, that the highest calculated mode deviates from the dispersion trend defined by the lower frequency modes due to the defect caused by the differing particle-substrate contact stiffness.

To similarly characterize the contact stiffnesses of colloidal crystals of different layer thicknesses, we perform systematic measurements on multiple samples with defined layer thicknesses, ranging from one to twelve layers, as is shown in Figure 6.3. Each sample was also fabricated using different fabrication parameters, including particle concentration, solvent (deionized water or ethanol), temperature of the drying environment, and number of times the colloidal suspension was centrifuged and the supernatant discarded to remove impurities from the solution. The tabulated list of the fabrication parameters used for each sample is indicated in Table 6.1. We note that, in contrast to the spectrum shown in Figure 6.2(b), fewer peaks were observed for other measurement regions and samples. In addition to being a result of the higher number of averages (10^6) used for this measurement location, the presence of the additional peaks in Figure 6.2(b) suggests reduced dissipation, which consequently may indicate lower disorder within that measurement area. This is further supported by an observed higher quality factor of the fundamental mode for this region ($Q \sim 12$), compared to other measured regions ($Q \sim 3 - 7$). The quality factor is obtained by fitting a Lorentzian distribution to the fundamental mode in the measured power spectra.

Figure 6.3(a) shows the Fourier spectra measured for regions of different layer thicknesses across the two samples where we could obtain a measurement of the out-of-plane contact resonance in the monolayer region. The red curves in Figure 6.3(a) correspond to the sample characterized in Figure 6.2, which we refer to as "Sample 1", and the blue to a different sample, which we refer to as "Sample 2". Figure 6.3(b) shows the frequency of the fundamental mode for all regions measured, as a function of the number of layers in that region. Each marker type corresponds to a different sample. The red and blue markers in Figure 6.3(b) correspond to the spectra denoted by the same markers in Figure 6.3(a).

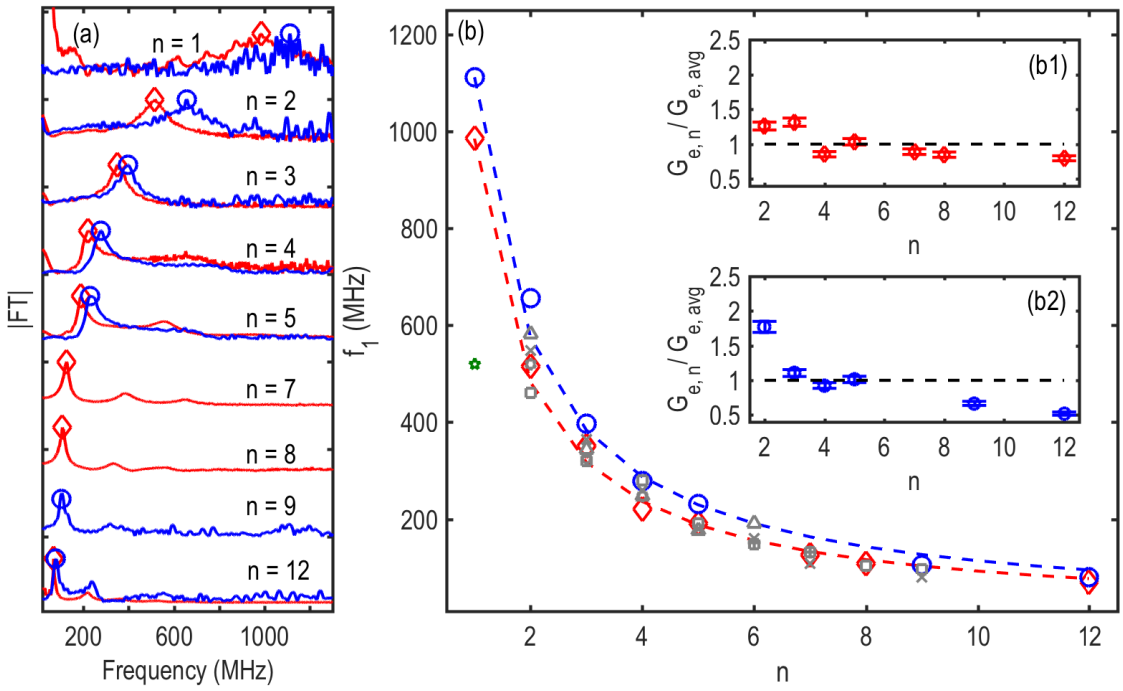

Figure 6.3: (a) Fourier Transform spectra of the time-resolved interferometric signals recorded from measurements on two colloidal crystal samples with thickness ranging from one to twelve layers. The Fourier Transform amplitude is plotted in linear scale, and offset for each layer thickness. (b) Frequencies of the fundamental mode plotted for colloidal crystals of varying number of layers (n) in the two samples from the peaks in the spectra in (a). The blue and red dashed lines indicate the frequencies of the fundamental eigenmode of a coupled oscillator system using the particle-substrate contact stiffness from the monolayer measurement (K_N) and the measured mean effective interlayer contact stiffness ($G_{e,avg}$). The gray markers represent frequencies of the fundamental modes on colloidal crystals fabricated with differing self-assembly parameters, but for which a monolayer resonance could not be measured. The green star marker represents the frequency measured on a monolayer that was pre-assembled at an air/water interface and subsequently transferred to a solid substrate. The inset highlights the variation of the effective interlayer contact stiffness for different layer thicknesses ($G_{e,n}$) in the two samples shown in (a). Red makers and lines correspond to Sample 1 and blue markers and lines to Sample 2 in all panels.

The gray markers denote samples for which a resonance was not detected in the monolayer region. For all samples we observe a similar, and expected, trend of decreasing fundamental mode frequency with increasing layer thickness. We suggest that this may be due to a combination of low quality factors observed for many of the monolayer regions, as can be seen by the broad peaks of the monolayer spectra in Figure 6.3(a), and the possibility that the monolayers have frequen- cies above our detection bandwidth of $\sim$ 1 GHz. As a point of comparison to the samples fabricated using the vertical deposition convective self-assembly technique and prior studies on monolayer contact resonances [9–12], we fabricated and measured a sample consisting entirely of a colloidal crystal monolayer using a modified Langmuir-Blodgett technique involving pre-assembly of the monolayer at an air/water interface and subsequent transfer to a solid substrate (as described in Section 1.3.2). The monolayer contact resonance on this air/water monolayer sample is found to be significantly lower than those measured for the samples fabricated using the vertical convective self-assembly technique, and is denoted by the green star marker in Figure 6.3(b).

We repeat the previously described process to determine the effective interlayer contact stiffness for the different layer thicknesses tested on Sample 1 and 2. As the effective interlayer contact stiffness estimated using the fundamental and higher order modes was found to be reasonably close, and we do not have access to higher order modes for many of the regions tested, we fit only using the measured fundamental mode and the particle-substrate contact stiffness, determined from the monolayer region on the same sample, to find the effective interlayer contact stiffness for each thickness ($G_{e,n}$). The resulting effective interlayer contact stiffnesses, normalized by the average interlayer contact stiffness ($G_{e,avg}$) (across all layer thicknesses for the corresponding sample), are plotted in the insets Figure 6.3(b1,b2) as a function of thickness. The half-width error bars for each marker in the insets represent the 8% error in the effective interlayer stiffness calculated using the fundamental mode only or the first five eigenmodes in the coupled oscillator model. Each sample is denoted with the

same marker type and color throughout Figure 6.3.

The insets, Figures 6.3(b1,b2), highlight the variation of the effective interlayer stiffness in regions of differing thicknesses within the same sample. The effective interlayer stiffness measured on different layer thicknesses in Sample 1 shows little variation, with an average value of 0.44 kN/m. On the other hand, we find that the effective interlayer stiffness decreases with increasing layer thickness in Sample 2, ranging from 1.2 kN/m in the bilayer region to 0.35 kN/m in the twelve-layer region of the sample. We speculate the decrease in stiffness could be due to increased disorder or a reduced density of impurities near the contact with increasing layer thicknesses. Regarding the latter mechanism, we note that the colloidal suspension for Sample 2 was centrifuged three times, while the suspension for Sample 1 was only centrifuged once, as indicated in Table 6.1. The average interlayer stiffness calculated from measurements on all regions of Sample 2 is 0.68 kN/m.

The red and blue dashed lines in Figure 6.3(b) indicate the resulting fundamental eigenfrequencies of coupled oscillator systems with two to twelve masses connected to each other via contact springs having stiffness equal to the measured average interlayer stiffness Ge,avg and to the substrate via a contact spring of stiffness equal to the measured particle-substrate contact stiffness K_N for Sample 1 and 2, respectively. We find that the measured frequencies follow the trend predicted by the coupled oscillator model, including in the case of the samples where a monolayer resonance was not detected.

We find considerable disparity between the monolayer contact resonance frequency measurements for the two colloidal crystal samples ($\sim$ 1 GHz) and that for the monolayer fabricated by the pre-assembly at the air/water interface (520 MHz). Table 6.2 lists the average effective interlayer stiffness and the particle-substrate contact stiffness calculated from the measured frequencies for the two multilayer samples and the air/water monolayer sample. Potential

causes for this disparity, as well as comparisons with adhesive contact models are discussed below.

Table 6.2: Measured and DMT Model predicted particle-substrate and average interlayer contact stiffness. DMT model assumes $w_{P-S} = 0.06$ J/m^2 and $w_{P-P} = 0.06$ J/m^2.

	K_N (kN/m)	$G_{e,avg}$ (kN/m)
Sample 1	1.3	0.4
Sample 2	1.6	0.7
Air/water monolayer	0.4	-
DMT Model	0.1	0.1

We compare the average effective interlayer stiffness and the particle-substrate contact stiffness obtained from our measurements to estimates made using the Derjaguin-Muller-Toporov (DMT) adhesive elastic contact model [108]. The DMT adhesive elastic contact model is derived from the Hertz contact model [3], with the addition of a static adhesive force. Based on the DMT model contact mechanics, the linearized normal contact stiffness around the equilibrium displacement is expressed as, $K_{DMT} = \frac{3}{2}(2\pi w R_e^2 E^{*2})^{1/3}$ [11], where w is the work of adhesion between the two surfaces in contact [57], R_e is the effective radius (equal to the radius of the colloidal particle for the particle-substrate contact, and half the radius of the colloidal particle for the particle-particle contact) and $E^* = [\frac{3}{4}((1-\nu_P^2)/E_P + (1-\nu_S^2)/E_S)]^{-1}$ is the effective modulus of the contact. Using a work of adhesion between the polystyrene colloidal particles and the silica-coated substrate obtained using the Lifshitz theory of van der Waals forces [57] of $w_{P-S} = 0.06$ J/m^2, and $\nu_P = 0.32$, $\nu_S = 0.17$, $E_P = 4.04$ GPa and $E_S = 73$ GPa as the Poisson's ratio and Young's modulus of the polystyrene colloidal particle [12] and the substrate [304], respectively, we estimate the linearized normal contact stiffness between the particle and the substrate to be $K_{N,DMT} = 0.1$ kN/m. Similarly, we find $G_{e,DMT} = 0.1$ kN/m, using a work of adhesion between the particles of $w_{P-P} = 0.06$ J/m^2.

From Table 6.2, we observe that the particle-substrate and the effective interlayer stiffnesses predicted by the DMT model are much lower than all the corresponding measured contact stiffnesses. The discrepancy between measured contact stiffnesses and those predicted by the DMT model has been reported previously for silica [9, 11] as well as polystyrene microspheres [10, 12], and could be explained by the uncertainty in the work of adhesion between contacting surfaces [57], plastic deformation [264], or solid [248] or liquid [27, 247, 305] material bridges around the contacts.

To gain insight into the source of the difference between the measured contact stiffnesses of the multilayer samples and the air/water monolayer sample, as well as that between the measurements and DMT model prediction, we analyze the contact surface by means of scanning electron microscopy. Representative side-view SEM images of the particle-substrate contacts in the air/water monolayer sample, and the monolayer regions of the two multilayer colloidal crystal samples investigated in Figure 6.3(a) (i.e., Sample 1 and Sample 2) are shown in Figures 6.4(a)-(c). The SEM image of the air/water monolayer sample, shown in Figure 6.4(a), indicates a large particle-substrate contact diameter (of ~ 150 nm), which is significantly higher than that predicted by the DMT model (28 nm). The large contact diameter in the air/water monolayer sample suggests that the spheres may have plastically deformed under the action of adhesive forces during the self-assembly process [264]. The SEM image of the monolayer region of Sample 1, shown in Fig. 4(b), reveals a similar particle-substrate contact diameter as in the air/water monolayer sample. Although the particle-substrate contact diameters in the air/water monolayer sample and Sample 1 appear to be comparable, the particle-substrate contact stiffness measured in Sample 1 being over three times that measured in the air/water monolayer sample suggests that there may be other mechanisms responsible for the added stiffness of the contacts. Side-view SEM images of the particle-substrate contacts in the monolayer region of Sample 2, shown in Fig-

ure 6.4(c), appear considerably different from the previous two cases. The spheres seem to be partially embedded in a solid matrix that forms a 'well'-like structure around the particle. The cup-like structures appear to be formed from a thin film on the substrate. However, although the particle-substrate contacts in Samples 1 and 2 appear qualitatively different, the contact stiffnesses measured on these samples were comparable.

To further explore potential causes for the differing contact stiffnesses, we investigate the topography of the surface of the substrate after removal of the spheres by tapping-mode AFM. The spheres in the monolayer regions were removed by placing a piece of adhesive tape on the monolayer region, followed by gentle application of pressure on the surface of the tape. The spheres adhered to the tape when it was peeled off, leaving a region of blank substrate on the sample. The AFM images of the regions of the substrate where the monolayer was peeled off on the three sam- ples are shown in Figures 6.4(d)-(f). For the case of the air/water monolayer sample, the AFM image in Figure 6.4(d) shows variations in the surface height within 3 nm, which we attribute, in part, to the roughness of the silica film deposited on the substrate. However, the AFM image also reveals ring-like patterns of diameter $\sim 150 - 200$ nm at the sites previously occupied by the spheres, suggesting that these patterns could be due to residue on the surface. The corresponding AFM images of the multilayer colloidal crystal samples show a similar, but more pronounced, substrate surface topography. The AFM image of the substrate in Sample 1, shown in Figure 6.4(e), shows very pronounced ring-like structures, $\sim 5 - 16$ nm in height, with hemispherical openings. Even more pronounced ring-like structures are seen in the AFM image of Sample 2, which is illustrated in Figure 6.4(f), and complements the relatively larger observed contact stiffness. The diameter of the hemispherical openings of the ring-like structures in Samples 1 and 2 is $\sim 160 - 200$ nm, similar to that of the ring-like structures observed on the air/water monolayer sample.

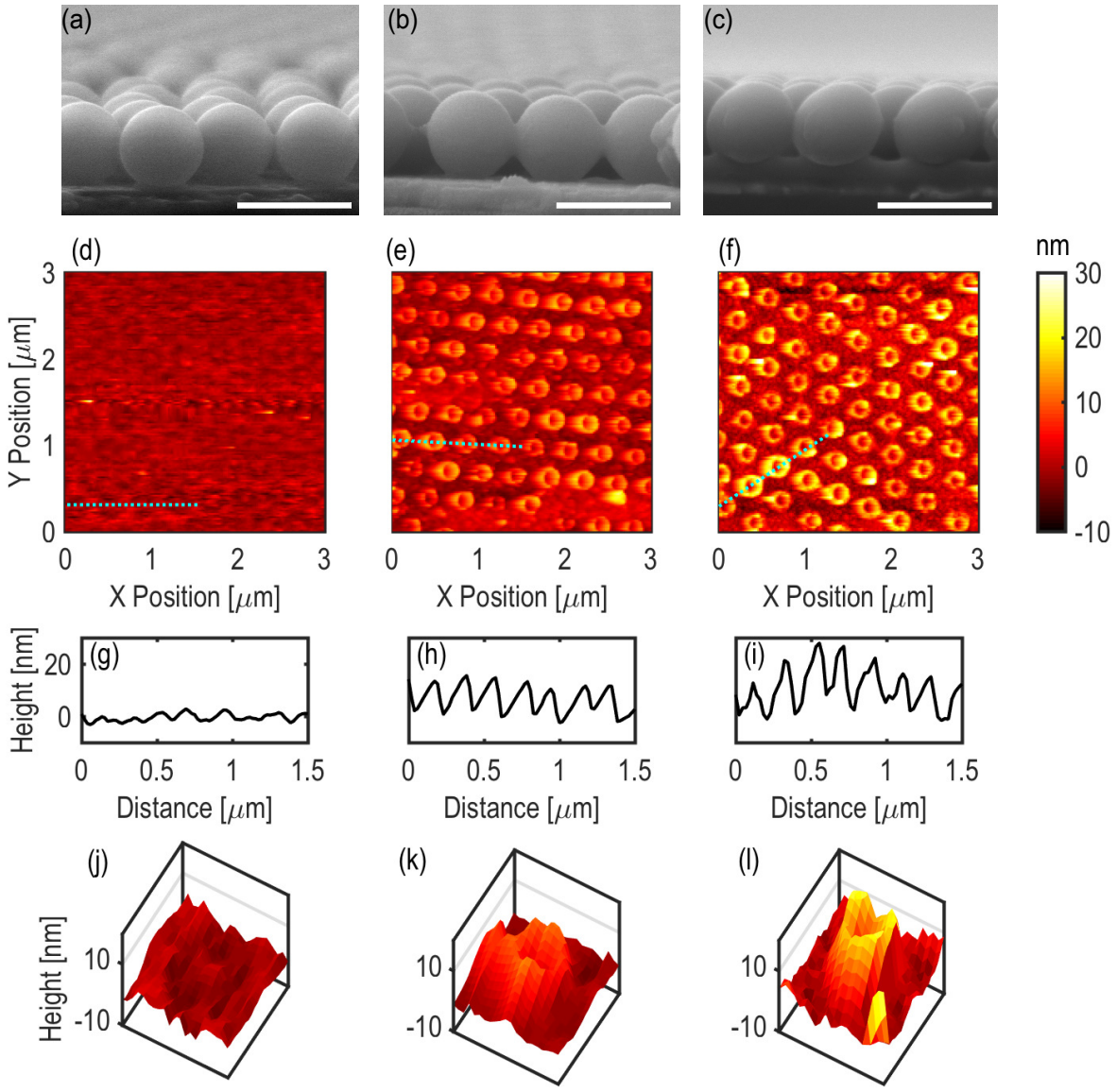

Figure 6.4: Scanning electron microscopy images of the monolayer regions in: (a) the air/water monolayer sample; (b) Sample 1; and (c) Sample 2. We note some minor lateral image distortion in the SEM image in panel (c). Scale bars represent 500 nm in all panels. (d) - (f) Tapping-mode Atomic Force Microscopy images of the substrate after removal of the colloidal particles. (g) - (i) The surface topology of the substrate along the dashed line is shown in the corresponding panel directly above. (j) - (l) Isometric views of the AFM images of single 'well'-like features on a 0.4 μm x 0.4 μm area of the substrate. All panels in the same column correspond to the same sample.

Representative profiles of the surface height in the three samples are plotted in Figures 6.4(g)-(h). Isometric close-up views of the ring-like structures revealed by the AFM images are shown in Figures 6.4(j)-(l). A clear meniscus shape of solid material around a central depletion caused by the removed sphere is seen.

The SEM and AFM images of the regions around the particle-substrate contacts in the colloidal crystals compliment the contact stiffnesses obtained from the laser ultrasonic measurements, and provide possible explanations for the discrepancies in the particle-substrate contact stiffness between the air/water monolayer and multilayer samples, as well as discrepancies between our measurements and predictions made by the DMT contact model. The presence of the hemispherical contacts in the ring-like structures in Samples 1 and 2 suggests that the particle-substrate con- tact cannot be modeled as that between a sphere and a flat substrate, but instead may follow a non-Hertzian contact law.

The previously described bridging can also be observed in the interparticle and particle-susbtrate contacts in the multilayer regions of the colloidal crystal samples. Representative views of the particle-substrate and interparticle contacts in the multilayer regions of Samples 1 and 2 are illustrated in Figures 6.5(a) and (b), respectively. For both samples, a thin 'bridging' material ($\sim$ 10 nm in width) is seen in the region around the particle-substrate contact, as well in the interstitial space between neighboring spheres. As before, the 'bridging' material is more evident in Sample 2 (shown in Figure 6.5(b)), which can be seen as a continuous thin film along the substrate that forms cup-like structures around the particle-substrate contact. Similar to the case of the monolayer regions, the material is also deposited at the contact points between neighboring spheres. We attribute these solid bridges to the presence of solid impurities within the colloidal suspension.

The differences between the various samples in this study, as seen from measurements of the

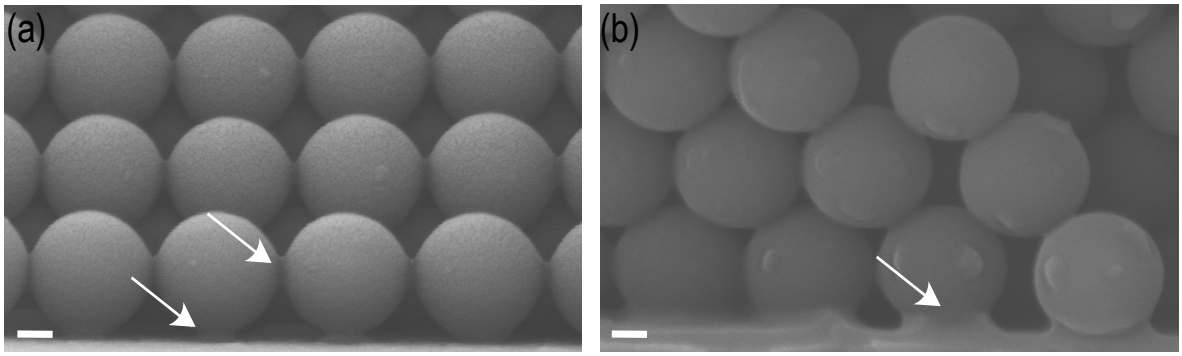

Figure 6.5: Scanning electron microscopy images illustrating particle-substrate and interparticle contacts in (a) a seven-layer-thick region of Sample 1 and (b) a six-layer-thick region of Sample 2. The scale bar is 100 nm in both panels. The arrows indicate representative material bridges observed between the contacts.

contact stiffnesses via laser ultrasonic characterization as well as in the SEM and AFM images of the contacts, can be attributed to the different nature of the self-assembly fabrication process. In the modified Langmuir-Blodgett technique, a floating monolayer of spheres is pre-assembled at an air/water interface, which is then transferred onto a substrate [5]. Solid impurities in the colloidal suspension, such as water-soluble polystyrene oligomers, other reaction side-products from the emulsion polymerization process [270], or polymer impurities that may leach from the vials containing the colloidal solution, are much more diluted as the water subphase provides an enormous reservoir. This may explain the smaller ring-like structures seen in the AFM images of the air/water monolayer sample, Figure 6.4(d). On the other hand, the 'bridging' material seen between the sphere contacts in Samples 1 and 2 may be formed by solid impurities occupying interstitial sites in the crystal lattice. Unlike the case of the air/water pre-assembly technique, it is possible that the solid impurities in the vertical deposition technique are pulled towards spheres that have already deposited on the substrate by convective forces. Subsequently, these impurities are concentrated in liquid capillary bridges that form in between the spheres and the substrate, where they finally

solidify upon drying. As a result, the purity of the assembly suspension (i.e., the amount of impurities) will determine the quality of the colloidal crystal sample, which in turn would be expected to affect the contact properties, wherein cleaner suspensions should give less solid bridges and suspensions with more solid impurities should result in colloidal crystals with more solid bridges. As suggested earlier, multiple cycles of centrifuging the colloidal suspension and removing the supernatant prior to self-assembly deposition can alter the quantity of impurities in the colloidal suspension. The use of repeated centrifuge purification steps in the preparation of Sample 1 readily explains the slightly higher particle-substrate contact stiffness in Sample 2 over Sample 1, and the thicker film on the surface of the substrate. In addition to affecting the average interlayer contact stiffness of the multilayer, an increased density of impurities at the lower layers may also contribute to the observed decrease in stiffness with increasing layer thickness shown in Figure 6.3(b2). Our measurements, therefore, open avenues to potentially assess the packing and contact quality in three-dimensional colloidal crystals.

For further insights into the mechanical wave propagation properties in our colloidal crystals, we estimate the long wavelength longitudinal sound speed v in the colloidal crystal samples from the measured average interlayer contact stiffnesses using the relation, $v = \sqrt{\frac{G_{e,avg}}{m}} D^*$, where $D^* = \frac{\sqrt{6}}{3} D$ is the unit cell spacing, and find $v_1 = 1166$ m/s and $v_2 = 1445$ m/s for Samples 1 and 2, respectively. Our estimated values are about half the longitudinal sound speed in bulk polystyrene, $v_{PS} = 2350$ m/s [12], and about two times higher than the sound speed calculated using the interlayer contact stiffness predicted by the DMT model, $v_{DMT} = 617$ m/s. We note that the long wavelength longitudinal sound speed calculated from the average interlayer contact stiffness is consistent with the sound speed estimated from the observed contact area. This suggests that the contact stiffness can be reasonably estimated from the contact area, even when the force of adhesion is unknown. We also calculate the long wavelength sound speed obtained from the observed contact diameter,

assuming DMT contact mechanics. Using a contact diameter of 150 nm yields a sound speed of 1582 m/s, which is in reasonable agreement with the sound speed calculated from the measured average interlayer stiffness. At the macroscale, an uncompressed granular crystal is often described as a sonic vacuum (i.e., zero sound speed) wherein the particle-particle interactions are purely nonlinear [47]. As this system is further compressed, it can be considered to linearize, with a finite low-amplitude sound speed. Compared to sound speeds as low as $\sim$ 200 m/s measured in slightly compressed macroscale granular crystals [131], the relatively high speeds in our samples suggest a highly linearized system. Strategies to increase the coupling between macroscale spheres in contact and therefore modify their dynamic response have been studied previously, for instance by welding a finite chain of millimeter-sized steel spheres [306], where the contact diameter was $\sim$ 30% of the sphere diameter. Controlling the size of the material bridges between the colloidal particles may therefore be used as an analogous mechanism to tune the coupling between particles at the micro- and nanoscale.

Finally, we also compare the quality factors of the peaks of the measured eigenfrequencies to those estimated from the acoustic impedance mismatch between the colloidal crystal and the glass substrate. We estimate the acoustic impedance of the colloidal crystal to be $Z_1 = \rho_g v_1 = 0.92$ MPa.s/m, where v_1 is the longitudinal sound speed calculated previously for Sample 1 using the average interlayer contact stiffness an effective density of the colloidal crystal of $\rho_c = \phi m/(\pi D^3/6) = 784$ kg/m^3, which is calculated using a solid volume fraction $\phi = 0.74$ assuming HCP packing. Similarly, we calculate the acoustic impedance of the glass substrate to be $Z_s = 13.9$ MPa.s/m. The resulting amplitude reflection coefficient r at the colloidal crystal/ substrate interface is calculated to be $r = (\frac{Z_s - Z_1}{Z_s + Z_1}) = 0.88$ [307]. We estimate the expected quality factor of the fundamental mode, accounting for radiation from the colloidal layer, using the relation $Q_i = \pi(2i-1)/(1-r^2)$, where i is the mode number. For the fundamental mode ($i = 1$), we estimate a quality factor of $Q_1 = 14$, which is slightly larger than the observed quality factor for the fundamental mode of the 12 layer thick region

of Sample 1, and respectively larger than the other measured fundamental modes. Furthermore, for the 12 layer thick region of Sample 1, we note that the measured quality factors of the higher-order peaks varies between $\sim 7-10$, which is in contrast to the increase in quality factor with mode number that is expected for damping stemming from radiation into the substrate. The observed quality factors for the higher-order, shorter-wavelength modes thus suggests additional susceptibility to disorder-related loss mechanisms, including mechanisms arising from variations in the contact stiffnesses.

6.4 Conclusion

In summary, we have studied the contact-based longitudinal eigenvibrations of ordered, three-dimensional colloidal crystals adhered to solid substrates. We identify regions of uniform layer thickness in the colloidal crystal by their structural color. This enables us to measure the longitudinal eigenvibrations of the colloidal crystal as a function of layer thickness. Using non-contact laser ultrasonic measurements, along with a coupled oscillator model, we extract the particle-substrate and effective interlayer contact stiffness in the samples, and in one case find the effective contact stiffness between each layer to decrease with increasing number of layers. The laser ultrasonic measurements, supplemented by SEM and AFM images, show that nanometric-sized bridges around the contacts can drastically affect the contact stiffnesses. In the future, we expect that the rational control of contact stiffness via deposition of solid bridges can be systematically exploited to tailor the acoustic properties of self-assembled structures, which may in turn lead to a new class of tunable 'micro- and nanoscale granular crystals'. This study furthers the understanding of the dynamics of self-assembled micro- and nanoparticulate structures, which may have potential for ultrasonic wave tailoring applications analogous to macroscale granular crystals.

6.5 Collaborator Contributions

The samples used in this study were fabricated by the author and M. Helwig. The colloidal particles used for the samples were fabricated by the group of N. Vogel. The laser ultrasonic experiments were performed by M. Abi Ghanem and the author, who also analyzed the results. S. Wallen provided input on the coupled oscillator model and performed calculations involving the interlayer stiffnesses. The SEM and AFM measurements were performed by the author. A. Maznev provided input on the analytical acoustic radiation estimates. N. Boechler provided guidance on all aspects of this project.

Chapter 7

GUIDED SURFACE ACOUSTIC WAVES IN FEW-LAYER GRANULAR CRYSTALS

7.1 Introduction

In this chapter, we study the propagation of guided surface acoustic waves in few-layer microscale granular crystals adhered to solid substrates. The guided waves are excited and propagate along the granular crystal-substrate interface. We measure the dispersion of the guided surface acoustic waves in the layered half-space system using the laser-induced transient grating technique. We compare and fit the measured guided wave dispersion curves obtained from three- and five-layer-thick granular crystals to those predicted by an analytical model of a classical elastic layered half-space [193]. We estimate the effective longitudinal and transverse sound speeds in the granular crystal in the direction of the surface wave propagation, and compare these estimates to the effective longitudinal sound speed estimated from the average interlayer contact stiffness obtained in Chapter 6. Our results provide an insight into the contact-based interactions and elastic properties of a granular crystal multilayer.

Elastic wave propagation in layered systems is of great importance for several practical applications such as studying seismic wave propagation in the Earth's crust [308], as well as in fields such as composite materials design [309], and thin film metrology [175]. Bromwich first studied steady-state waves in layered half-space systems for waves with wavelength larger than the layer thickness [310]. Love extended the work of Bromwich to include waves of length compared to or smaller than the thickness of the layer on the semi-infinite solid [311].

The theoretical formulation for wave propagation in a semi-infinite solid covered by a solid layer of uniform thickness is presented by Ewing and coworkers in reference [193]. In the following section, we describe the formulation of the equations governing swave propagation in a layered half-space.

7.1.1 Waves in a Layered Half-Space

In continuum mechanics, the mechanical response of an isotropic material with mass density ρ can be expressed in terms of two unique material properties, namely the Young's modulus E and the Poisson's ratio ν, or alternatively, in terms of the Lame´ parameters λ and μ. The Lame´ parameters λ and μ can be expressed in terms of the Young's modulus E and Poisson's ration ν using the relations,

$$\lambda = \frac{\nu E}{(1+\nu)(1-2\nu)}, \ \mu = \frac{E}{2(1+\nu)} \tag{7.1}$$

Or alternatively, the Young's modulus E and the Poisson's ratio ν can be expressed in terms of the Lame´ parameters using the relations,

$$E = \frac{\mu(3\lambda+2\mu)}{\lambda+\mu}, \ \nu = \frac{\lambda}{2(\lambda+\mu)} \tag{7.2}$$

From the wave equation, one can show that two types of disturbances with velocities c_L and c_T propagate through a bulk elastic solid. The velocities can be expressed in terms of the Lame´ parameters and the material density ρ as,

$$c_L = \sqrt{\frac{\lambda+2\mu}{\rho}}, \ c_T = \sqrt{\frac{\mu}{\rho}} \tag{7.3}$$

The velocity c_L is associated with the component of displacement parallel to the direction of propagation (i.e., longitudinal waves), while the velocity c_T is associated with components in any two mutually perpendicular directions normal to the direction of propagation. Thus, a system of plane waves traveling along a specific axis consists of three independent parts corresponding to: i) the longitudinal or compressional wave (also referred to as the P-wave), ii) the vertically polarized shear wave (referred to as the SV-wave), and iii) the horizontally polarized shear wave (referred to as the SH-wave). By introducing a free surface to a bulk elastic medium, Rayleigh theoretically demonstrated that surface-confined waves propagated with a velocity c_R lower than the bulk sound speeds, and the amplitude of these waves decayed rapidly with depth, limited to approximately one wavelength below the surface [194]. The non-trivial solution obtained by setting stress-free boundary conditions in the dilatational and transverse potential functions yields the Rayleigh wave equation,

$$\left\{2 - \frac{c_R^2}{c_T^2}\right\}^2 = 4\left\{1 - \frac{c_R^2}{c_T^2}\right\}^{\frac{1}{2}}\left\{1 - \frac{c_R^2}{c_L^2}\right\}^{\frac{1}{2}} \tag{7.4}$$

It can be deduced that solutions to Equation 7.4 exist when $0 < c_R < c_T < c_L$. Furthermore, the constant velocity of the Rayleigh wave reveals that this type of wave is non-dispersive, and undamped in the direction of propagation, while being damped in the perpendicular direction to propagation.

We consider an isotropic homogeneous solid layer of thickness H and mass density ρ_1 and Lame´ parameters λ_1 and μ_1 adhered to a semi-infinite isotropic elastic solid with mass density ρ_2 and Lame´ parameters λ_2 and μ_2. A schematic of the layered half-space system is illustrated in Figure 7.1. We follow a procedure similar to that used in the previous section to develop the formulation for describing wave propagation in a layered half-space. The set of equations for particle displacements, strain, and stresses must be satisfied in each medium with the additional boundary conditions, namely, i) the continuity of stresses at the

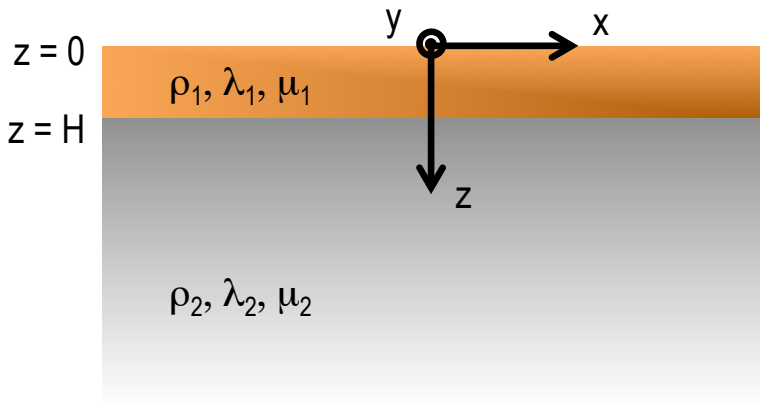

Figure 7.1: Co-ordinate system in a layered elastic half-space.

interface; ii) the continuity of displacements at the interface; and iii) vanishing of stresses at the free interface. Assuming plane waves propagating in both media, the dilatational potential function φ and transverse potential function Ψ in the layer (medium 1) and the half-space (medium 2) are given by,

$$\varphi_1 = Ae^{i(\omega t - kx) - \nu_1 z} + Be^{i(\omega t - kx) + \nu_1 z},\ \Psi_1 = Ce^{i(\omega t - kx) - \nu_1' z} + De^{i(\omega t - kx) + \nu_1' z} \tag{7.5}$$

$$\varphi_2 = Ee^{i(\omega t - kx) - \nu_2 z},\ \Psi_2 = Fe^{i(\omega t - kx) - \nu_2' z} \tag{7.6}$$

where ω is the angular frequency, k and ν_1 are the wave numbers in the x- and z-directions, respectively, and A, B, C, D, E and F are amplitude constants. Like in the case of the semi-infinite half-space, the dilatational and transverse potential functions can be substituted in the stress-free boundary conditions at $z = 0$,

$$p_{zz}\Big|_{z=0} = (\lambda_1 + 2\mu_1)\nabla^2\varphi_1 - 2\mu_1\Big(\frac{\partial^2\varphi_1}{\partial x^2} - \frac{\partial^2\Psi_1}{\partial x \partial z}\Big) = 0 \tag{7.7}$$

$$p_{zx}\Big|_{z=0} = \mu_1\Big(2\frac{\partial^2\varphi_1}{\partial x\partial z} - \frac{\partial^2\Psi_1}{\partial z^2} + \frac{\partial^2\Psi_1}{\partial x^2}\Big) = 0 \tag{7.8}$$

where p_{zz} is the normal stress in the z-direction, and p_{zx} is the shear stress in the xz plane. The dilatational and transverse potential functions can also be substituted in the equations of continuity of displacement and stresses at the interface, i.e., at $z = H$,

$$u_1 = \frac{\partial\varphi_1}{\partial x} - \frac{\partial\Psi_1}{\partial z} = u_2 = \frac{\partial\varphi_2}{\partial x} - \frac{\partial\Psi_2}{\partial z}\Big|_{z=H} \tag{7.9}$$

$$w_1 = \frac{\partial\varphi_1}{\partial z} + \frac{\partial\Psi_1}{\partial x} = w_2 = \frac{\partial\varphi_2}{\partial z} + \frac{\partial\Psi_2}{\partial x}\Big|_{z=H} \tag{7.10}$$

$$(p_{zz})_1 = (p_{zz})_2\Big|_{z=H},\ (p_{zx})_1 = (p_{zx})_2\Big|_{z=H} \tag{7.11}$$

Solving the system of equations yields the dispersion relation of the elastic waves propagating in the layered half-space. From the above boundary condition equations, we obtain six equations:

$$(2k^2 - {k_{\beta 1}}^2)A + (2k^2 - {k_{\beta 1}}^2)B + 2k{\nu_1}'iC - 2k{\nu_1}'iD = 0 \tag{7.12}$$

$$2k\nu_1 A - 2k\nu_1 B + (2k^2 - {k_{\beta 1}}^2)iC + (2k^2 - {k_{\beta 1}}^2)iD = 0 \tag{7.13}$$

$$-kAe^{-\nu_1 H} - kBe^{\nu_1 H} - {\nu_1}'iCe^{-{\nu_1}'H} + {\nu_1}'iDe^{{\nu_1}'H} = -kEe^{-\nu_2 H} - {\nu_2}'iFe^{-\nu_2 H} \tag{7.14}$$

$$-\nu_1 Ae^{-\nu_1 H} + \nu_1 Be^{\nu_1 H} - kiCe^{-{\nu_1}'H} - kiDe^{{\nu_1}'H} = -\nu_2 Ee^{-\nu_2 H} - kiFe^{-{\nu_2}'H} \tag{7.15}$$

$$2k\nu_1 Ae^{-\nu_1 H} - 2k\nu_1 Be^{\nu_1 H} + (2k^2 - {k_{\beta 1}}^2)iCe^{-\nu_1 H} + (2k^2 - {k_{\beta 1}}^2)iDe^{{\nu_1}' H}$$
$$= 2\frac{\mu_2}{\mu_1}k\nu_2 Ee^{-\nu_2 H} + \frac{\mu_2}{\mu_1}(2k^2 - {k_{\beta 2}}^2)iFe^{-{\nu_2}' H} \tag{7.16}$$

$$(2k^2 - {k_{\beta 1}}^2)Ae^{-\nu_1 H} + (2k^2 - {k_{\beta 1}}^2)Be^{\nu_1 H} + 2k{\nu_1}' iCe^{-\nu_1 H} - 2k{\nu_1}' iDe^{-{\nu_1}' H}$$
$$= \frac{\mu_1}{\mu_2}\left[(2k^2 - {k_{\beta 2}}^2)Ee^{-\nu_2 H} + 2k{\nu_2}' iFe^{-{\nu_2}' H}\right] \tag{7.17}$$

where $k_{\beta 1} = \omega/c_{T,1}$ and $k_{\beta 2} = \omega/c_{T,2}$ are the wave numbers associated with the shear waves in medium 1 and 2 with shear wave speed $c_{T,1}$ and $c_{T,2}$, respectively. For the non-trivial solution to the system of the above six equations, the six variables $Ae^{-\nu_1 H}$, $iCe^{-\nu_1 H}$, $Be^{\nu_1 H}$, $iDe^{{\nu_1}' H}$, $Ee^{-\nu_2 H}$, and $iFe^{-{\nu_2}' H}$ must have non-zero values. The system of equations can be written in matrix form and the determinant of the coefficient matrix can be set to zero to solve for the non-trivial solution. A detailed solution to the dispersion relation of a layered half-space can be found in the books by Ewing, Jardetzky and Press [193] and by Farnell and Adler [312]. In this work, we use the form given by Lee [313] that is useful for computation. This form is also provided in reference [193]. We define X, Y, Z, W as follows,

$$X = \frac{\mu_2}{\mu_1}\frac{{k_{\beta 2}}^2}{k^2} - 2\left(\frac{\mu_2}{\mu_1} - 1\right) \tag{7.18}$$

$$Y = \frac{{k_{\beta 1}}^2}{k^2} + 2\left(\frac{\mu_2}{\mu_1} - 1\right) \tag{7.19}$$

$$Z = \frac{\mu_2}{\mu_1}\frac{{k_{\beta 2}}^2}{k^2} - \frac{{k_{\beta 1}}^2}{k^2} - 2\left(\frac{\mu_2}{\mu_1} - 1\right) \tag{7.20}$$

$$W = 2\left(\frac{\mu_2}{\mu_1} - 1\right) \tag{7.21}$$

We also define the variables r_1, r_2, s_1, s_2 as follows,

$$r_1{}^2 = (i\nu_1)^2 = k_{\alpha 1}{}^2 - k^2 = \nu_2{}^2 \tag{7.22}$$

$$r_2{}^2 = k^2 - k_{\alpha 2}{}^2 \tag{7.23}$$

$$s_1{}^2 = (i\nu_1{}')^2 = k_{\beta 1}{}^2 - k^2 \tag{7.24}$$

$$s_2{}^2 = k^2 - k_{\beta 2}{}^2 = \nu_2{}'^2 \tag{7.25}$$

Here, $k_{\alpha 1} = \omega/c_{L,1}$ and $k_{\alpha 2} = \omega/c_{L,2}$ are expressed in terms of the longitudinal sound speed in the layer and the elastic half-space, respectively. The period equation in the form provided by Lee [313] is as follows,

$$\xi_1\eta_2 - \xi_2\eta_1 = 0 \tag{7.26}$$

where,

$$\xi_1 = \left(2 - \frac{k_{\beta 1}{}^2}{k^2}\right)\left[X\cos r_1 H + \frac{r_2}{r_1}Y\sin r_1 H\right] + 2\frac{s_1}{k}\left[\frac{r_2}{k}W\sin s_1 H - \frac{k}{s_1}Z\cos s_1 H\right] \tag{7.27}$$

$$\xi_2 = \left(2 - \frac{k_{\beta 1}{}^2}{k^2}\right)\left[\frac{s_2}{k}W\cos r_1 H + \frac{k}{r_1}Z\sin r_1 H\right] + 2\frac{s_1}{k}\left[X\sin s_1 H - \frac{s_2}{s_1}Y\cos s_1 H\right] \tag{7.28}$$

$$\eta_1 = \left(2 - \frac{k_{\beta 1}{}^2}{k^2}\right)\left[\frac{r_2}{k}W\cos s_1 H + \frac{k}{s_1}Z\sin s_1 H\right] + 2\frac{r_1}{k}\left[X\sin r_1 H - \frac{r_2}{r_1}Y\cos r_1 H\right] \tag{7.29}$$

$$\eta_2 = \left(2 - \frac{{k_{\beta 1}}^2}{k^2}\right)\left[X\cos s_1 H + \frac{s_2}{s_1} Y \sin s_1 H\right] + 2\frac{r_1}{k}\left[\frac{s_2}{k} W \sin r_1 H - \frac{k}{r_1} Z \cos r_1 H\right] \quad (7.30)$$

Positive real values of s_i, r_i are obtained when $k^2 < {k_{\alpha 1}}^2 < {k_{\beta 1}}^2$ and $k^2 > {k_{\beta 2}}^2 > {k_{\alpha 2}}^2$. Equation 7.26 provides an implicit relation between the phase velocity c and the wave number k, through the dimensionless parameters $c/c_{T,1}$ and kH. In the case where the transverse wave speed in the layer is less than that in the elastic half-space, i.e., $c_{T,1} < c_{T,2}$, the phase velocity of the first Rayleigh-like mode decreases with increasing wave number, starting with the Rayleigh wave speed in the substrate at long wavelength (or low wave number). As the wave number increases, the phase velocity of the Rayleigh-like mode decreases, until the wavelength approaches the thickness of the layer, where the mode asymptotically approaches the Rayleigh wave speed in the layer. In this chapter, we study the propagation of guided waves in a layered half-space system comprised of a few-layer microscale granular crystal adhered to a glass substrate that serves as the elastic half-space. The multilayer granular crystal films are ordered, three- and five-layer thick close-packed crystals composed of 390 nm diameter polystyrene colloidal particles. In the case of the five-layer granular crystal, the thickness of the film is $H = 1.74$ μm (assuming hexagonal-close-packed packing). In our experiment, the shortest wavelength that we generate and detect is $\lambda_S = 3$ mum. With the thickness-to-wavelength ratio in our experiment of 0.58, we are in the regime where the Rayleigh wave mode of the substrate will bend, and be affected by the presence of the layer at high wave numbers. It is also worth noting that the shortest wavelength in our experiment is over seven times the particle size. The Brillouin folding zone due to periodicity occurs when the wavelength is twice the unit cell dimension [18]. We, therefore, are not in the regime to see zone folding effects induced by structural periodicity in the granular crystal layer.

7.1.2 Surface Waves in Granular Systems

A number of studies have investigated surface acoustic waves in granular systems. Suiker and coworkers theoretically studied the propagation of surface waves in an elastic stratified half space, which consisted of a granular elastic upper layer resting on a classic elastic substratum [314,315]. The authors considered both the case of an upper layer with second-gradient continuum properties [316], and an upper layer with Cosserat continuum properties [317]. These enhanced continuum formulations are able to describe micro-scale effects as governed by the individual particle displacements and particle rotations. The authors demonstrated that the micro-scale effects become important when the length of the surface waves is of the same order of magnitude as the particle size, which may occur in a high-speed railway track that consists of an upper layer of ballast particles. The dispersion curves resembled those of a classical elastic layered half-space [193], with the emergence of additional non-classical surface modes. More recently, Merkel and Luding presented an enhanced micro-polar model that takes into account all degrees of freedom at the contacts between particles to describe wave propagation in granular materials [318]. Aleshin and coworkers showed the existence of guided surface acoustic waves confined between the surface of the granular materials and in-depth layers with increasing rigidity, in unconsolidated granular materials under gravity [319]. The authors found that in contrast to the Rayleigh wave polarized in the sagittal vertical plane, which is the unique localized mode in a homogeneous solid, an infinite number of modes with sagittal polarization as well as an infinite number of shear horizontal modes were supported in the granular material [319]. Pichard and coworkers studied the existence of surface elastic waves at a mechanically free surface of granular phononic crystals, in which the particles interact by means of normal, shear, and bending contact rigidities [320]. In addition to the Rayleigh-type sagittal surface modes and the shear-horizontal modes, the presence of Rayleigh-type zero-group velocity surface modes were also predicted to exist along the free surface of three-dimensional granular crystals [320].

7.2 Experimental Details

The sample comprises three-dimensional close-packed crystals of $D = 390$ nm diameter monodisperse polystyrene colloidal particles adhered to an aluminum-coated glass substrate. The granular crystal sample labeled as 'Sample 2' in previous chapter was used in this study. This sample was fabricated using the vertical deposition convective self-assembly technique described in Section 1.3.3. The substrate was immersed in an aqueous solution of colloidal particles of concentration 0.01 % (v/v). The setup was left to dry in an oven set to 75 °C. Upon drying, distinct areas of defined layer thickness ranging from monolayer up to twenty layers were obtained. A representative side-view SEM image of a five-layer multilayer region is illustrated in Figure 7.2(a).

We use the laser-induced transient grating (TG) technique to excite guided surface acoustic waves along the granular crystal/substrate interface and measure their dispersion in the sample (see Section 1.6). The set-up is illustrated in Figure 7.2(b). Two optical pump beams derived from the same laser source (wavelength 532 nm, pulse duration 440 ps, pulse energy 3 μJ and repetition rate 1 kHz) are crossed at an angle and focused to an elliptical spot (436 μm x 76 μm) at the $1/e^2$ intensity level through the spheres on the aluminum film of the sample. This results in a spatially periodic interference pattern on the surface of the sample. Absorption of the pump pulses in the aluminum film results in rapid thermoelastic expansion, which subsequently generates counter-propagating surface acoustic waves along the long side of the elliptical pump spot with a wavelength equal to the interference pattern. Switching phase mask patterns gives measurements at multiple acoustic wavelengths ranging from 2.75 to 45 μm in our current TG setup. The detection of the guided wave propagation in the sample is accomplished via a quasi-cw probe beam (wavelength 514 nm and average power 10.7 mW at the sample) chopped to 50 μs pulses with an electro-optic modulator. The probe beam passes through the same set of optics as the pump beam and is focused to a 246 μm x

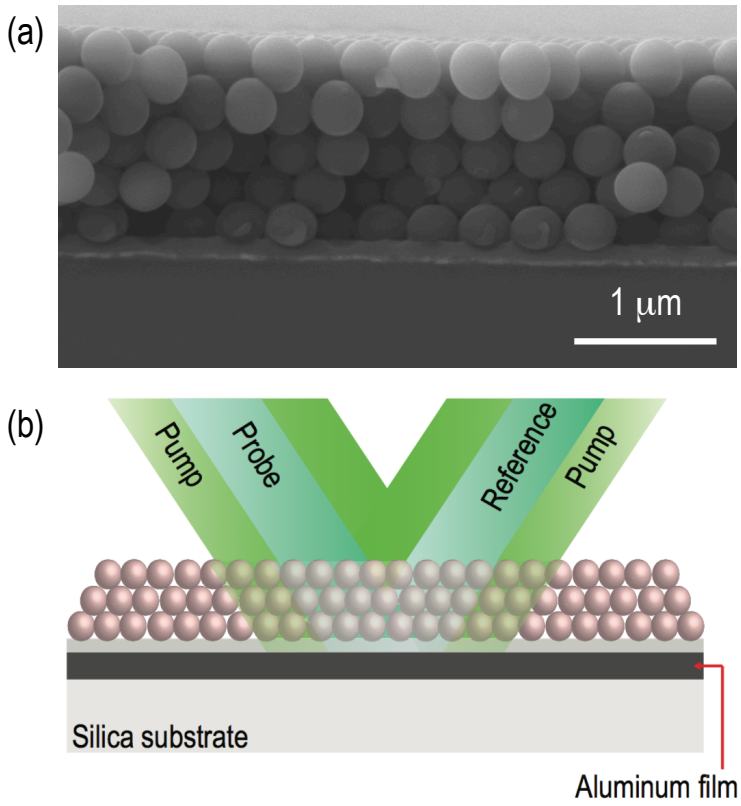

Figure 7.2: (a) Representative side-view SEM image of a five-layer multilayer region. (b) Illustration of the laser-induced transient grating technique used to excite and detect guided surface acoustic waves along the granular crystal/substrate interface.

79 μm elliptical spot at the center of the interference pattern. Pump-induced surface ripples and refractive index variations in the multilayer/aluminum film lead to a time-dependent diffraction of the probe beam. The diffracted probe light is superposed with a reference (local oscillator) beam and is directed to a fast avalanche photodiode with a 1 GHz bandwidth. The signal is recorded using an oscilloscope and averaged over 10^4 repetitions. The dispersion of guided surface acoustic waves was characterized in monolayer, 3-layer and 5-layer regions of the granular crystal. Figure 7.3 illustrates representative time-domain TG signals and their corresponding frequency spectra recorded at acoustic wavelength $\lambda_S = 4.95$ μm

(or wave number $k = 1.27\ \mu\text{m}^{-1}$) on monolayer, three-layer, and five-layer regions.

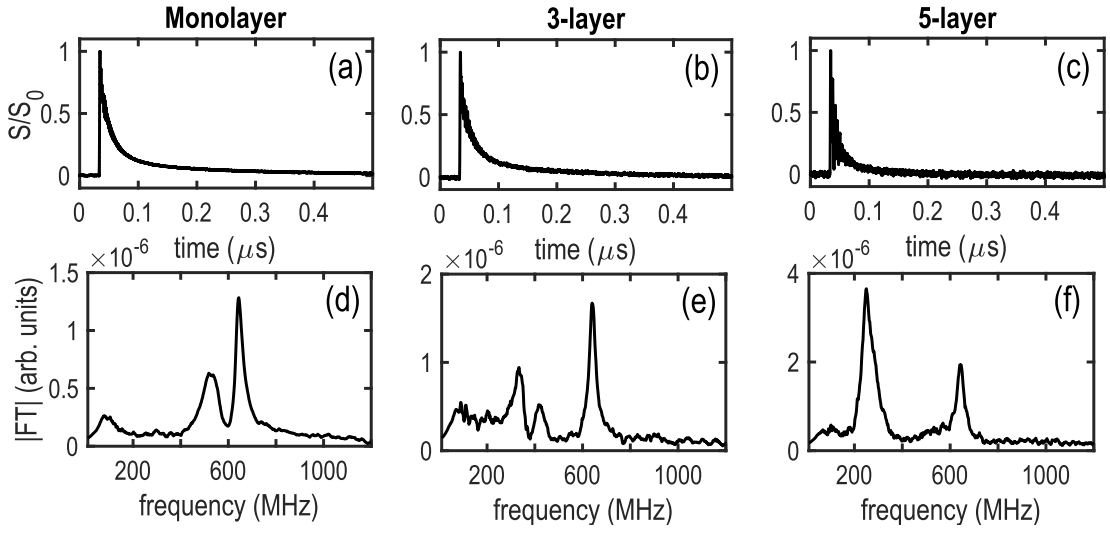

Figure 7.3: Representative time-domain signals recorded at $\lambda_S = 4.95\ \mu$m on a (a) monolayer, (b) 3-layer and (c) 5-layer regions of the granular crystals. The corresponding frequency spectra of the time-traces in panels (a) - (c) are shown in (d) - (f), respectively.

7.3 Results and Discussion

The peaks identified in the frequency spectra at each wave number were used to construct the dispersion curves in our samples. The measured dispersion curves for acoustic waves on the monolayer, three- and five-layer-thick granular crystal multilayers are shown in Figure 7.4. The markers represent peaks identified in the frequency spectrum of a signal recorded at a particular acoustic wavelength. The monolayer dispersion in Figure 7.4(a), shows two 'avoided crossings' in the Rayleigh wave branch - one branch at ~ 600 MHz, while a higher one at ~ 1100 MHz. From the phase-mask-based interferometeric measurement of the resonance on the same monolayer region, shown with the blue curve for the $n = 1$ case in Figure 6.3(a), we measured a monolayer resonance of ~ 1 GHz. We therefore identify the

top branch to be a hybridization with the axial contact resonance, since phase-mas-based interferometer is preferentially sensitive to vibrations in the direction normal to the plane of the sample. We attribute the hybridization of the bottom branch to coupling of the surface acoustic waves with the horizontal-rotational resonance of the monolayer [9]. As discussed in Chapter 6, we attribute the large discrepancy in the measured axial contact stiffness of the monolayer to the presence of solid impurities in the contact regions between the spheres and the substrate. The dispersion curves of three- and five- layer granular crystal multilayers on an elastic substrate are illustrated in Figures 7.4(b) and (c), respectively. Each of the measured dispersion curves start along the Rayleigh wave speed line of the substrate, and hybridize and branch out to approach wave speeds in the granular crystal layer at high wave numbers.

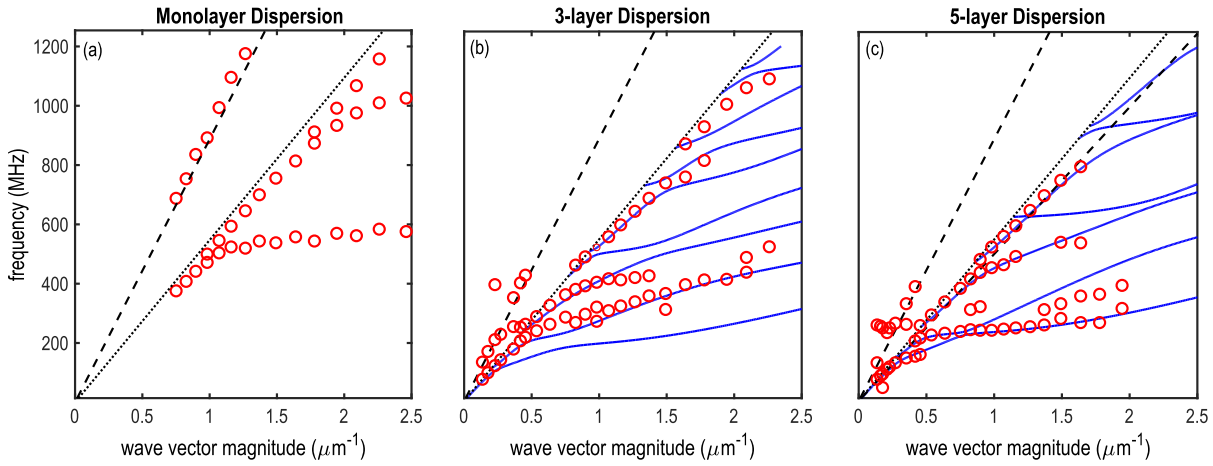

Figure 7.4: Dispersion curves for (a) monolayer, (b) three-layer and (c) five-layer thick granular crystal. The experimentally measured points are represented as markers, while the continuous lines represent the dispersion predicted by the theoretical layered-half-space model. The dashed line denotes the longitudinal sound speed in the substrate, while the dotted line denotes the transverse sound speed in the substrate.

We compare our dispersion curves of the guided waves measured in the three- and five-layer-thick granular crystals to the theoretically derived dispersion curves of a layered half-space [193]. The theoretical dispersion curves are plotted on the same axes as the measured dispersion points in Figures 7.4(b) and (c). In this model, we choose a longitudinal sound speed in the granular crystal, $c_{L,fit3} = 2005$ m/s, and transverse speed, $c_{T,fit3} = 800$ m/s to fit the theoretically-derived dispersion contours to the measured points in the three-layer granular crystal. In the case of the five-layer-granular crystal, we find that using $c_{L,fit5} = 1700$ m/s, and $c_{T,fit5} = 900$ m/s fits the theoretical layered half-space model reasonably well. Note that these fits was performed as an estimate, without the use of a least-squares-minimization routine. In the model, the thickness of the granular film H is calculated using the relation, $H = D \cdot (N + 1 - \sqrt{3}/2)$ where N is the number of layers in the crystal. We find good agreement between the measured guided dispersion and the theoretical prediction. The theoretical model shows that at the long-wavelength limit, the phase velocity of the first mode approaches the Rayleigh wave speed of the half-space, while in all other higher modes, the velocity approached at the long-wavelength limit is that of the shear wave in the half-space. Each mode cuts off at the shear speed of the half-space, below which unattenuated propagation does not occur [193]. Although these modes are 'leaky' past the bulk sound speed threshold, we detect some branches in the 'leaky' region for both the three- and five-layer cases in our experiment.

We note that the theoretical dispersion curve for a layered half-space assumes a continuum film [193], and does not account for individual particle rotations and displacements. Since the lowest SAW wavelength is about seven times greater than the particle size, we also do not observe Bragg band-gaps induced from the periodicity in the granular crystal [74, 145]. Given the wavelength range in our experiment, we find that our measurements fit well with the continuum dispersion case. Accurate models accounting for particle normal and shear interactions, as well as particle rotations, such as those developed in references [314,318–320],

may be more suitable for surface waves with approach the size of the particles. In our experiment, the shortest wavelength at which we could identify peaks in the frequency spectra was $\lambda_S = 2.78$ μm for the case of the three-layer granular crystal, while the shortest wavelength for the five-layer granular crystal was $\lambda_S = 3.23$ μm. This is seen from the fact that the acoustic branches in the dispersion curve of the five-layer granular crystal, shown in Figure 7.4(c), cut off at lower wave numbers when compared to the acoustic branches in the dispersion curves for the three-layer granular crystal, illustrated in Figure 7.4(b). The higher apparent dissipation in the five-layer granular crystal may be attributed to disorder-induced scattering of short wavelength guided waves, from defects such as voids and cracks in the granular crystal.

We utilize the fitted longitudinal wave speeds in the three- and five-layer granular crystals to estimate the elastic modulus of the granular crystal multilayer, following similar estimations for disordered colloidal films [115]. We estimate the density of the hexagonal-close-packed crystal, $\rho = \phi \cdot m/(\pi D^3/6) = 784$ kg/m^3, where $\phi = 0.74$ is the solid volume fraction of an hcp crystal, and m and D are the mass and diameter of the polystyrene spheres. Using the longitudinal sound speed $c_{L,fit,3} = 2005$ m/s, we estimate the elastic modulus of the three-layer granular crystal $M_3 = c_{L,fit,3}^2 \cdot \rho = 2.9$ GPa. This is slightly lower than the elastic modulus of bulk polystyrene, $E_{PS} = 4.04$ GPa [12]. Similarly, we estimate the elastic modulus of the five-layer granular crystal $M_5 = c_{L,fit,5}^2 \cdot \rho = 2.3$ GPa. We note slightly higher longitudinal sound speed in the three-layer granular crystal, when compared to that in the five-layer granular crystal, is consistent with our observation of the decreasing stiffness in the out-of-plane direction, for different granular crystals of different thickneses within the same sample, shown in Figure 6.3(b2). We note that the longitudinal wave speed $v_2 = 1445$ m/s calculated from the average interlayer contact stiffness $G_{e,avg}$ in Chapter 6 is lower than the longitudinal sound speeds for the three- and five-layer granular crystals, $c_{L,fit,3} = 2005$ m/s and $c_{L,fit,5} = 1700$ m/s, obtained by fitting the measured dispersion to that of an classical

layered half-space formulation. The possible variation in the sound speed in the out-of-plane and in-plane directions suggests a stiffness anisotropy in the granular crystal. However, given that these fits were performed as estimates, a least squares minimization routine may provide more certainty in these estimates. As described previously in Chapter 6, solid impurities can greatly influence the interlayer stiffness. The experimental measurements of the guided surface waves along the granular crystal/ substrate interface in this chapter could compliment the longitudinal eigenvibration measurements in the previous chapter, by providing a deeper insight in the direction-dependent stiffness of the granular crystal. Our results also motivate future studies on the stiffness anisotropy of microscale granular crystals, and how solid impurities affect the in-plane and out-of-plane stiffnesses of a three-dimensional granular crystal. Furthermore, our measurements also provide an estimate of the transverse wave speed in the granular crystal, stemming from the shear interactions between the particles.

7.4 Conclusion

We have studied the dispersion of guided surface acoustic waves in granular crystals comprising of single, three, and five layers. The acoustic dispersion measured on the monolayer region of the granular crystal shows hybridization of the Rayleigh wave branch at two distinct frequencies, which we attribute to the horizontal-rotational and the axial contact resonances [9]. We note that solid bridges between the contact, described in Chapter 6, significantly alter the interparticle and particle-substrate stiffnesses, and consequently, affect the dynamic response of the granular crystal. The discrepancy between the measured stiffnesses and those predicted by adhesive elastic contact models can also be explained, in part, by the our observations of solid bridges in the contact regions. We do not measure highest resonance, the rotational-horizontal contact resonance, in our experiment, which may be outside the bandwidth of our experiment.

We have also characterized the dispersion of guided surface acoustic waves propagating along the granular crystal / substrate interface in three- and five-layer-thick granular crystals adhered to homogeneous solid substrates. We estimate effective longitudinal and transverse sound speeds by fitting the measured dispersion curves to those of a classical layered half-space. Our technique provides a novel way to estimate the effective mechanical stiffness of the granular crystal in the direction of propagation of surface waves. Our results indicate that for long wavelengths (compared to the particle size), the continuum approach adequately describes our experimental findings, and can be used to model long-wavelength wave propagation. The use of discrete models, which account for particle rotations and interparticle interactions, can reveal several new dynamic phenomena [314, 315, 318–320], such as zero-group-velocity surface modes, which may have use in novel wave control applications. Guided surface acoustic modes in granular crystals also have potential for designing wave guides based on granular crystal dynamics. While the results presented in this chapter provide an estimate of the wave speeds in few-layer granular crystals, future studies on guided waves in granular crystals, particularly in the short-wavelength regime, can reveal several new wave phenomena.

7.5 Collaborator Contributions

The author of this thesis fabricated the sample in this study. The colloidal particles for sample fabrication were synthesized by the group of N. Vogel. The experiments and data analysis were performed by M. Abi Ghanem and the author.

Chapter 8

CONCLUSION AND FUTURE OUTLOOK

In this dissertation, we have used an experimentally-driven approach to study the contact-based dynamics of self-assembled, microscale granular crystals in monolayer and few-layer configurations, using laser ultrasonic techniques in the sub-gigahertz ultrasound regime. Our results provide an insight into the contact mechanics of isolated particles as well as particulate assemblies at the micron and sub-micron length scale, and open the door towards developing novel, microscale granular crystal-based metamaterials for ultrasonic wave tailoring applications. We have demonstrated experimental concepts of locally-resoant granular crystal-based metamaterials with particle-substrate and interparticle normal and shear contact resonances induced by adhesion. These include microscale granular crystals for tailoring surface acoustic waves and Lamb waves. This work has also explored novel mechanisms to tune the response of microscale granular crystals, by modifying the contact geometry via solid bridges at the contacts and microlensing. Finally, the mechanical properties and effective long-wavelength sound speeds in the granular crystals are estimated from the longitudinal eigenvibrations of the granular crystals and the dispersion of guided surface acoustic waves along the granular crystal/ substrate interface.

In Chapter 2, we have studied the resonant attenuation of surface acoustic waves by monolayer granular crystals. Surface acoustic waves interact and hybridize with the contact-based resonances of the micro-particle arrays. Through the frequency-dependent attenuation measurements, we have quantified the spectral linewidth of the axial contact resonance, and simultaneously detected three resonances stemming from interparticle and particle-substrate

normal and shear contact interactions. Our work has shown the potential of using self-assembled microscale granular systems in surface acoustic wave filtering devices, which could be tuned by modifying the contact properties. The discovery of the collective vibrational modes of microsphere monolayers could also lead to a broader understanding of wave propagation in microscale granular media, with applications in shock mitigation, powder processing and particulate contaminant removal using ultrasound.

In Chapter 3, we report the design and characterization of a self-assembled, locally resonant acoustic metamaterial for Lamb waves, comprising of a monolayer of micron-sized particles self-assembled on a free-standing silicon membrane. Our experiments reveal a microsphere contact resonance, which hybridizes with flexural Lamb waves, and the lowest frequency spheroidal microsphere resonance. This work opens avenues towards developing micro- and nano-mechanical resonators with applications in microelectromechanical and sensing systems.

In Chapter 4, we have studied how the normal stiffness of the sphere-substrate contact scales with particle radius, for particles ranging from 400 nm to 4 μm in diameter. We compare the scaling trends of the particle-substrate normal contact stiffness and the particle-substrate contact diameter at equilibrium with power law exponents predicted by adhesive elastic and elasto-plastic contact mechanics models. This work also reveals the role of adhesion-induced plasticity on the dynamic response of microparticles.

In Chapter 5, we explore a novel mechanism to tune the axial contact resonance of a monolayer of microspheres via a nanostructural contact geometry modification induced by optical microlensing. The monolayer of microspheres acts as an array of lenses, resulting in a "microlens", each of which focuses the incident optical energy from the pump laser beam to a region confined to the contact area between the sphere and the substrate. We demonstrate

an ability to tune the microsphere axial contact resonance by up to three times the original value using microlensing-based ablation of the substrate, which is dependent on the pulse energy and number of microlensing pulses. Our results show the reconfigurability of microscale granular crystals in applications that may require resonance matching with other systems.

In Chapter 6, we have studied the longitudinal, out-of-plane, contact-based eigenvibrations of few-layer microscale granular crystals. We extract the sphere-substrate average interlayer normal contact stiffnesses from the eigenmodes. We find that nanometric-sized solid bridges present in the contact regions drastically alter the contact stiffness, and subsequent dynamical response of the granular crystal. Our findings, and the measurement technique used in this chapter, provide a basis for future investigations of the contact mechanics, dynamics, and disorder of three-dimensional micro- and nano-particulate systems.

In Chapter 7, we study the propagation of guided surface acoustic waves in few-layer microscale granular crystals adhered to solid substrates. We fit the measured dispersion of guided waves to an effective-medium layered half-space model, and extract the long-wavelength longitudinal and transverse sound speeds. Our technique opens avenues to measure the in-plane and out-of-plane mechanical properties and dynamic response of microscale granular crystals in a non-contact and non-destructive approach.

From a fabrication stand-point, this study shows the potential of self-assembly as a technique to manufacture metamaterials for ultrasonic wave applications rapidly, inexpensively, and on a large-scale, and enable the translation of microscale granular metamaterials into chip-scale devices for applications in signal processing, biomedical imaging, and shock wave mitigation, among others. A few recommendations for avenues of future research in the field of microscale granular crystals are discussed below.

The sensitivity of the contact-based resonances to environmental factors such as temperature and humidity could be explored. This could result in granular crystal-based sensors. Furthermore, other tuning mechanisms such as particle sintering, thermal annealing, plasma-enhanced etching and electrophoresis, could be explored as ways of tuning and controlling the contact-based resonances of micro-particle arrays. Using template-driven self-assembly techniques [153], microscale granular crystals could be self-assembled into novel geometries for designing acoustic wave guides which may have applications for focusing ultrasound in biomedical imaging devices. The response of microsphere monolayers to high-amplitude excitations could also be explored to shed light into potential nonlinear phenomena analogous to studies on granular crystals at the macroscale. Although this study shows that adhesion induces significant deformation of the microparticles, using low adhesion material combinations such as silica particles on gold-coated substrates could reveal rich nonlinear dynamics at the microscale. The response of three-dimensional, thick microscale granular crystals to shock and impulse loading could also be explored, particularly with an aim of shock wave mitigation and energy absorption. Finally, the scalability of the self-assembly process shows the potential of extending this work to studying the contact-based modes of nanoparticles, which may have acousto-optic and acousto-plasmonic functionalities, as well as the ability to control high-frequency phonons in the hypersonic regime.

BIBLIOGRAPHY

[1] M. Maldovan, "Sound and heat revolutions in phononics," *Nature*, vol. 503, no. 7475, p. 209, 2013.

[2] P. Hess, "Surface acoustic waves in materials science," *Physics Today*, vol. 55, no. 3, pp. 42–48, 2002.

[3] H. Hertz, "On the contact of elastic solids," *Z. Reine Angew. Mathematik*, vol. 92, pp. 156–171, 1881.

[4] J. Sun, C.-j. Tang, P. Zhan, Z.-l. Han, Z.-S. Cao, and Z.-L. Wang, "Fabrication of centimeter-sized single-domain two-dimensional colloidal crystals in a wedge-shaped cell under capillary forces," *Langmuir*, vol. 26, no. 11, pp. 7859–7864, 2010.

[5] N. Vogel, S. Goerres, K. Landfester, and C. K. Weiss, "A convenient method to produce close-and non-close-packed monolayers using direct assembly at the air–water interface and subsequent plasma-induced size reduction," *Macromolecular Chemistry and Physics*, vol. 212, no. 16, pp. 1719–1734, 2011.

[6] P. Jiang, J. Bertone, K. Hwang, and V. Colvin, "Single-crystal colloidal multilayers of controlled thickness," *Chemistry of Materials*, vol. 11, no. 8, pp. 2132–2140, 1999.

[7] J.-M. Meijer, F. Hagemans, L. Rossi, D. V. Byelov, S. I. Castillo, A. Snigirev, I. Snigireva, A. P. Philipse, and A. V. Petukhov, "Self-assembly of colloidal cubes via vertical deposition," *Langmuir*, vol. 28, no. 20, pp. 7631–7638, 2012.

[8] J. A. Johnson, A. A. Maznev, M. T. Bulsara, E. A. Fitzgerald, T. Harman, S. Calawa, C. Vineis, G. Turner, and K. A. Nelson, "Phase-controlled, heterodyne laser-induced transient grating measurements of thermal transport properties in opaque material," *Journal of Applied Physics*, vol. 111, no. 2, p. 023503, 2012.

[9] M. Hiraiwa, M. A. Ghanem, S. P. Wallen, A. Khanolkar, A. A. Maznev, and N. Boechler, "Complex contact-based dynamics of microsphere monolayers revealed by resonant attenuation of surface acoustic waves," *Physical review letters*, vol. 116, no. 19, p. 198001, 2016.

[10] J. Eliason, A. Vega-Flick, M. Hiraiwa, A. Khanolkar, T. Gan, N. Boechler, N. Fang, K. Nelson, and A. Maznev, "Resonant attenuation of surface acoustic waves by a disordered monolayer of microspheres," *Applied Physics Letters*, vol. 108, no. 6, p. 061907, 2016.

[11] N. Boechler, J. Eliason, A. Kumar, A. Maznev, K. Nelson, and N. Fang, "Interaction of a contact resonance of microspheres with surface acoustic waves," *Physical review letters*, vol. 111, no. 3, p. 036103, 2013.

[12] A. Khanolkar, S. Wallen, M. Abi Ghanem, J. Jenks, N. Vogel, and N. Boechler, "A self-assembled metamaterial for lamb waves," *Applied Physics Letters*, vol. 107, no. 7, p. 071903, 2015.

[13] S. P. Wallen, *Analytical and Computational Modeling of Mechanical Waves in Microscale Granular Crystals: Nonlinearity and Rotational Dynamics*. PhD thesis, 2017.

[14] I. Tamm, "Über die quantentheorie der molekularen lichtzerstreuung in festen körpern," *Zeitschrift für Physik*, vol. 60, no. 5-6, pp. 345–363, 1930.

[15] E. L. Feinberg, "Igor'evgen'evich tamm," *Physics-Uspekhi*, vol. 38, no. 7, pp. 773–789, 1995.

[16] F. Schwabl, R. Hilton, and A. Lahee, *Advanced Quantum Mechanics*. Advanced Texts in Physics, Springer Berlin Heidelberg, 2013.

[17] S. Simon, *The Oxford Solid State Basics*. OUP Oxford, 2013.

[18] T. Gorishnyy, M. Maldovan, C. Ullal, and E. Thomas, "Sound ideas," *Physics World*, vol. 18, no. 12, p. 24, 2005.

[19] G. Chen, *Nanoscale Energy Transport and Conversion: A Parallel Treatment of Electrons, Molecules, Phonons, and Photons*. MIT-Pappalardo Series in Mechanical Engineering, Oxford University Press, 2005.

[20] O. Pahuja, *Solid State Physics*. Laxmi Publications Pvt Limited, 2005.

[21] L. Lou, *Introduction to Phonons and Electrons*. World Scientific, 2003.

[22] C. M. Harris *et al.*, *Shock and vibration handbook*. McGraw-Hill,, 1996.

[23] G. Ter Haar, "Therapeutic applications of ultrasound," *Progress in biophysics and molecular biology*, vol. 93, no. 1-3, pp. 111–129, 2007.

[24] J. Blitz and G. Simpson, *Ultrasonic methods of non-destructive testing*, vol. 2. Springer Science & Business Media, 1995.

[25] B. W. Drinkwater and P. D. Wilcox, "Ultrasonic arrays for non-destructive evaluation: A review," *Ndt & E International*, vol. 39, no. 7, pp. 525–541, 2006.

[26] G. Gale and A. Busnaina, "Removal of particulate contaminants using ultrasonics and megasonics: a review," *Particulate science and Technology*, vol. 13, no. 3-4, pp. 197–211, 1995.

[27] K. L. Mittal and R. Jaiswal, *Particle adhesion and removal*. John Wiley & Sons, 2015.

[28] D. Morgan, *Surface acoustic wave filters: With applications to electronic communications and signal processing*. Academic Press, 2010.

[29] T. L. Bergman, F. P. Incropera, D. P. DeWitt, and A. S. Lavine, *Fundamentals of heat and mass transfer*. John Wiley & Sons, 2011.

[30] T. Tritt, *Thermal Conductivity: Theory, Properties, and Applications*. Physics of Solids and Liquids, Springer US, 2006.

[31] S. A. Cummer, J. Christensen, and A. Alù, "Controlling sound with acoustic metamaterials," *Nature Reviews Materials*, vol. 1, p. 16001, 2016.

[32] M. I. Hussein, M. J. Leamy, and M. Ruzzene, "Dynamics of phononic materials and structures: Historical origins, recent progress, and future outlook," *Applied Mechanics Reviews*, vol. 66, no. 4, p. 040802, 2014.

[33] S. Yang, J. H. Page, Z. Liu, M. L. Cowan, C. T. Chan, and P. Sheng, "Focusing of sound in a 3d phononic crystal," *Physical review letters*, vol. 93, no. 2, p. 024301, 2004.

[34] M. Ke, Z. Liu, C. Qiu, W. Wang, J. Shi, W. Wen, and P. Sheng, "Negative-refraction imaging with two-dimensional phononic crystals," *Physical Review B*, vol. 72, no. 6, p. 064306, 2005.

[35] A. Sukhovich, L. Jing, and J. H. Page, "Negative refraction and focusing of ultrasound in two-dimensional phononic crystals," *Physical Review B*, vol. 77, no. 1, p. 014301, 2008.

[36] A. Sukhovich, B. Merheb, K. Muralidharan, J. Vasseur, Y. Pennec, P. Deymier, and J. Page, "Experimental and theoretical evidence for subwavelength imaging in phononic crystals," *Physical review letters*, vol. 102, no. 15, p. 154301, 2009.

[37] X. Zhang and Z. Liu, "Negative refraction of acoustic waves in two-dimensional phononic crystals," *Applied Physics Letters*, vol. 85, no. 2, pp. 341–343, 2004.

[38] A. Palermo, S. Krödel, A. Marzani, and C. Daraio, "Engineered metabarrier as shield from seismic surface waves," *Scientific reports*, vol. 6, p. 39356, 2016.

[39] S. Brûlé, E. Javelaud, S. Enoch, and S. Guenneau, "Experiments on seismic metamaterials: Molding surface waves," *Physical review letters*, vol. 112, no. 13, p. 133901, 2014.

[40] S. Brûlé, S. Enoch, S. Guenneau, and R. Craster, "Seismic metamaterials: controlling surface rayleigh waves using analogies with electromagnetic metamaterials," *Handbook of metamaterials. World Scientific*, 2017.

[41] M. Miniaci, A. Krushynska, F. Bosia, and N. M. Pugno, "Large scale mechanical metamaterials as seismic shields," *New Journal of Physics*, vol. 18, no. 8, p. 083041, 2016.

[42] A. Colombi, P. Roux, S. Guenneau, P. Gueguen, and R. V. Craster, "Forests as a natural seismic metamaterial: Rayleigh wave bandgaps induced by local resonances," *Scientific reports*, vol. 6, p. 19238, 2016.

[43] E. Kim, J. Yang, H. Hwang, and C. W. Shul, "Impact and blast mitigation using locally resonant woodpile metamaterials," *International Journal of Impact Engineering*, vol. 101, pp. 24–31, 2017.

[44] M. Thota and K. Wang, "Reconfigurable origami sonic barriers with tunable bandgaps for traffic noise mitigation," *Journal of Applied Physics*, vol. 122, no. 15, p. 154901, 2017.

[45] K. Biswas, J. He, I. D. Blum, C.-I. Wu, T. P. Hogan, D. N. Seidman, V. P. Dravid, and M. G. Kanatzidis, "High-performance bulk thermoelectrics with all-scale hierarchical architectures," *Nature*, vol. 489, no. 7416, p. 414, 2012.

[46] S. Strogatz, "Nonlinear dynamics and chaos (cambridge, ma: Westview)," 1994.

[47] M. A. Porter, P. G. Kevrekidis, and C. Daraio, "Granular crystals: Nonlinear dynamics meets materials engineering," *Physics Today*, vol. 68, no. LA-UR-15-21727, 2015.

[48] V. Nesterenko, *Dynamics of heterogeneous materials*. Springer Science & Business Media, 2013.

[49] N. Boechler, J. Yang, G. Theocharis, P. Kevrekidis, and C. Daraio, "Tunable vibrational band gaps in one-dimensional diatomic granular crystals with three-particle unit cells," *Journal of Applied Physics*, vol. 109, no. 7, p. 074906, 2011.

[50] L. Bonanomi, G. Theocharis, and C. Daraio, "Wave propagation in granular chains with local resonances," *Physical Review E*, vol. 91, no. 3, p. 033208, 2015.

[51] N. Boechler, G. Theocharis, S. Job, P. Kevrekidis, M. A. Porter, and C. Daraio, "Discrete breathers in one-dimensional diatomic granular crystals," *Physical review letters*, vol. 104, no. 24, p. 244302, 2010.

[52] G. Theocharis, M. Kavousanakis, P. Kevrekidis, C. Daraio, M. A. Porter, and I. Kevrekidis, "Localized breathing modes in granular crystals with defects," *Physical Review E*, vol. 80, no. 6, p. 066601, 2009.

[53] G. Theocharis, N. Boechler, and C. Daraio, "Nonlinear periodic phononic structures and granular crystals," in *Acoustic Metamaterials and Phononic Crystals*, pp. 217–251, Springer, 2013.

[54] A. Spadoni and C. Daraio, "Generation and control of sound bullets with a nonlinear acoustic lens," *Proceedings of the National Academy of Sciences*, vol. 107, no. 16, pp. 7230–7234, 2010.

[55] J. Yang and C. Daraio, "Nonlinear acoustic metamaterials for sound attenuation applications," tech. rep., CALIFORNIA INST OF TECH PASADENA DIV OF ENGINEERING AND APPLIED SCIENCE, 2011.

[56] K. Runge and P. A. Deymier, "Downsizing granular crystals and their kin," *Physics Today*, vol. 69, no. 6, pp. 12–12, 2016.

[57] J. Israelachvili, *Intermolecular and Surface Forces*. Intermolecular and Surface Forces, Elsevier Science, 2015.

[58] V. Lotito and T. Zambelli, "Approaches to self-assembly of colloidal monolayers: A guide for nanotechnologists," *Advances in colloid and interface science*, vol. 246, pp. 217–274, 2017.

[59] Q. Li, U. Jonas, X. Zhao, and M. Kappl, "The forces at work in colloidal self-assembly: A review on fundamental interactions between colloidal particles," *Asia-Pacific Journal of Chemical Engineering*, vol. 3, no. 3, pp. 255–268, 2008.

[60] J. Zhang, Y. Li, X. Zhang, and B. Yang, "Colloidal self-assembly meets nanofabrication: From two-dimensional colloidal crystals to nanostructure arrays," *Advanced materials*, vol. 22, no. 38, pp. 4249–4269, 2010.

[61] M. Mastrangeli, S. Abbasi, C. Varel, C. Van Hoof, J.-P. Celis, and K. F. Böhringer, "Self-assembly from milli-to nanoscales: methods and applications," *Journal of micromechanics and microengineering*, vol. 19, no. 8, p. 083001, 2009.

[62] C. B. Scruby and L. E. Drain, *Laser ultrasonics techniques and applications*. CRC Press, 1990.

[63] A. Rosencwaig, "Photoacoustic spectroscopy of solids," *The Journal of the Acoustical Society of America*, vol. 58, no. S1, pp. S52–S52, 1975.

[64] I. Newton, "1686, principia-book ii, imprimatur s," *Pepys, Reg. Soc. Præses, London.*

[65] J. Lord Rayleigh, "The theory of sound, vol. 1," 1945.

[66] L. Brillouin, *Wave propagation in periodic structures: electric filters and crystal lattices*. Courier Corporation, 2003.

[67] P. Deymier, *Acoustic Metamaterials and Phononic Crystals*. Springer Series in Solid-State Sciences, Springer Berlin Heidelberg, 2013.

[68] E. Yablonovitch, "Inhibited spontaneous emission in solid-state physics and electronics," *Physical review letters*, vol. 58, no. 20, p. 2059, 1987.

[69] S. John, "Strong localization of photons in certain disordered dielectric superlattices," *Physical review letters*, vol. 58, no. 23, p. 2486, 1987.

[70] J. D. Joannopoulos, P. R. Villeneuve, and S. Fan, "Photonic crystals: putting a new twist on light," *Nature*, vol. 386, no. 6621, p. 143, 1997.

[71] Y. Pennec and B. Djafari-Rouhani, "Fundamental properties of phononic crystal," in *Phononic Crystals*, pp. 23–50, Springer, 2016.

[72] R. Martínez-Sala, J. Sancho, J. V. Sánchez, V. Gómez, J. Llinares, and F. Meseguer, "Sound attenuation by sculpture," *nature*, vol. 378, no. 6554, p. 241, 1995.

[73] T. Gorishnyy, C. Ullal, M. Maldovan, G. Fytas, and E. Thomas, "Hypersonic phononic crystals," *Physical review letters*, vol. 94, no. 11, p. 115501, 2005.

[74] W. Cheng, J. Wang, U. Jonas, G. Fytas, and N. Stefanou, "Observation and tuning of hypersonic bandgaps in colloidal crystals," *Nature materials*, vol. 5, no. 10, p. 830, 2006.

[75] T. Cui, D. Smith, and R. Liu, *Metamaterials: Theory, Design, and Applications*. Springer US, 2009.

[76] V. G. Veselago, "The electrodynamics of substances with simultaneously negative values of and μ," *Soviet physics uspekhi*, vol. 10, no. 4, p. 509, 1968.

[77] J. B. Pendry, A. J. Holden, D. J. Robbins, and W. Stewart, "Magnetism from conductors and enhanced nonlinear phenomena," *IEEE transactions on microwave theory and techniques*, vol. 47, no. 11, pp. 2075–2084, 1999.

[78] D. R. Smith, W. J. Padilla, D. Vier, S. C. Nemat-Nasser, and S. Schultz, "Composite medium with simultaneously negative permeability and permittivity," *Physical review letters*, vol. 84, no. 18, p. 4184, 2000.

[79] Z. Liu, X. Zhang, Y. Mao, Y. Zhu, Z. Yang, C. T. Chan, and P. Sheng, "Locally resonant sonic materials," *Science*, vol. 289, no. 5485, pp. 1734–1736, 2000.

[80] F. Lemoult, M. Fink, and G. Lerosey, "Acoustic resonators for far-field control of sound on a subwavelength scale," *Physical Review Letters*, vol. 107, no. 6, p. 064301, 2011.

[81] A. Maznev, G. Gu, S.-y. Sun, J. Xu, Y. Shen, N. Fang, and S.-y. Zhang, "Extraordinary focusing of sound above a soda can array without time reversal," *New Journal of Physics*, vol. 17, no. 4, p. 042001, 2015.

[82] Y. Achaoui, A. Khelif, S. Benchabane, L. Robert, and V. Laude, "Experimental observation of locally-resonant and bragg band gaps for surface guided waves in a phononic crystal of pillars," *Physical Review B*, vol. 83, no. 10, p. 104201, 2011.

[83] Y. Achaoui, V. Laude, S. Benchabane, and A. Khelif, "Local resonances in phononic crystals and in random arrangements of pillars on a surface," *Journal of Applied Physics*, vol. 114, no. 10, p. 104503, 2013.

[84] R. Pourabolghasem, S. Mohammadi, A. A. Eftekhar, A. Khelif, and A. Adibi, "Experimental evidence of high-frequency complete elastic bandgap in pillar-based phononic slabs," *Applied Physics Letters*, vol. 105, no. 23, p. 231908, 2014.

[85] A. A. Zharov, I. V. Shadrivov, and Y. S. Kivshar, "Nonlinear properties of left-handed metamaterials," *Physical Review Letters*, vol. 91, no. 3, p. 037401, 2003.

[86] S. Strogatz, *Nonlinear Dynamics and Chaos: With Applications to Physics, Biology, Chemistry, and Engineering*. Studies in Nonlinearity, Avalon Publishing, 2014.

[87] M. R. Haberman and A. N. Norris, "Acoustic metamaterials," *Acoustics Today*, vol. 12, no. 3, pp. 31–39, 2016.

[88] B. Liang, B. Yuan, and J.-c. Cheng, "Acoustic diode: rectification of acoustic energy flux in one-dimensional systems," *Physical review letters*, vol. 103, no. 10, p. 104301, 2009.

[89] B. Liang, X. Guo, J. Tu, D. Zhang, and J. Cheng, "An acoustic rectifier," *Nature materials*, vol. 9, no. 12, p. 989, 2010.

[90] N. Kent, *Notes on the Zeeman effect*. Johns Hopkins University., 1901.

[91] R. Fleury, D. L. Sounas, C. F. Sieck, M. R. Haberman, and A. Alù, "Sound isolation and giant linear nonreciprocity in a compact acoustic circulator," *Science*, vol. 343, no. 6170, pp. 516–519, 2014.

[92] B.-I. Popa and S. A. Cummer, "Non-reciprocal and highly nonlinear active acoustic metamaterials," *Nature communications*, vol. 5, p. 3398, 2014.

[93] N. Boechler, G. Theocharis, and C. Daraio, "Bifurcation-based acoustic switching and rectification," *Nature materials*, vol. 10, no. 9, p. 665, 2011.

[94] P. Wang, F. Casadei, S. Shan, J. C. Weaver, and K. Bertoldi, "Harnessing buckling to design tunable locally resonant acoustic metamaterials," *Physical review letters*, vol. 113, no. 1, p. 014301, 2014.

[95] B. Florijn, C. Coulais, and M. van Hecke, "Programmable mechanical metamaterials," *Physical review letters*, vol. 113, no. 17, p. 175503, 2014.

[96] G. Ma and P. Sheng, "Acoustic metamaterials: From local resonances to broad horizons," *Science advances*, vol. 2, no. 2, p. e1501595, 2016.

[97] J. Duran, A. Reisinger, and P. de Gennes, *Sands, Powders, and Grains: An Introduction to the Physics of Granular Materials*. Partially Ordered Systems, Springer New York, 1999.

[98] K. Higashitani, H. Masuda, and H. Yoshida, *Powder technology: fundamentals of particles, powder beds, and particle generation*. CRC Press, 2006.

[99] C. Dominik and A. Tielens, "The physics of dust coagulation and the structure of dust aggregates in space," *The Astrophysical Journal*, vol. 480, no. 2, p. 647, 1997.

[100] H. M. Jaeger, S. R. Nagel, and R. P. Behringer, "Granular solids, liquids, and gases," *Reviews of modern physics*, vol. 68, no. 4, p. 1259, 1996.

[101] V. Nesterenko, "Propagation of nonlinear compression pulses in granular media," *Journal of Applied Mechanics and Technical Physics*, vol. 24, no. 5, pp. 733–743, 1983.

[102] A. Lazaridi and V. Nesterenko, "Observation of a new type of solitary waves in a one-dimensional granular medium," *Journal of Applied Mechanics and Technical Physics*, vol. 26, no. 3, pp. 405–408, 1985.

[103] F. Li, P. Anzel, J. Yang, P. G. Kevrekidis, and C. Daraio, "Granular acoustic switches and logic elements," *Nature communications*, vol. 5, p. 5311, 2014.

[104] J. Tomas, "Mechanics of particle adhesion," *Particles on Surfaces*, vol. 8, pp. 183–229, 2006.

[105] J. Paul, S. Romeis, J. Tomas, and W. Peukert, "A review of models for single particle compression and their application to silica microspheres," *Advanced Powder Technology*, vol. 25, no. 1, pp. 136–153, 2014.

[106] L.-O. Heim, J. Blum, M. Preuss, and H.-J. Butt, "Adhesion and friction forces between spherical micrometer-sized particles," *Physical Review Letters*, vol. 83, no. 16, p. 3328, 1999.

[107] J. Greenwood, "Adhesion of elastic spheres," in *Proceedings of the Royal Society of London A: Mathematical, Physical and Engineering Sciences*, vol. 453, pp. 1277–1297, The Royal Society, 1997.

[108] V. Muller, B. Derjaguin, and Y. P. Toporov, "On two methods of calculation of the force of sticking of an elastic sphere to a rigid plane," *Colloids and Surfaces*, vol. 7, no. 3, pp. 251–259, 1983.

[109] K. Johnson, K. Kendall, and A. Roberts, "Surface energy and the contact of elastic solids," *Proc. R. Soc. Lond. A*, vol. 324, no. 1558, pp. 301–313, 1971.

[110] Y. Guillet, B. Audoin, M. Ferrié, and S. Ravaine, "All-optical ultrafast spectroscopy of a single nanoparticle-substrate contact," *Physical Review B*, vol. 86, no. 3, p. 035456, 2012.

[111] M. M. Peri and C. Cetinkaya, "Non-contact microsphere–surface adhesion measurement via acoustic base excitations," *Journal of colloid and interface science*, vol. 288, no. 2, pp. 432–443, 2005.

[112] E. Vittorias, M. Kappl, H.-J. Butt, and D. Johannsmann, "Studying mechanical mi-

crocontacts of fine particles with the quartz crystal microbalance," *Powder technology*, vol. 203, no. 3, pp. 489–502, 2010.

[113] D. Schneider, M. Schmitt, C. M. Hui, R. Sainidou, P. Rembert, K. Matyjaszewski, M. R. Bockstaller, and G. Fytas, "Role of polymer graft architecture on the acoustic eigenmode formation in densely polymer-tethered colloidal particles," *ACS Macro Letters*, vol. 3, no. 10, pp. 1059–1063, 2014.

[114] M. Mattarelli, M. Montagna, T. Still, D. Schneider, and G. Fytas, "Vibration spectroscopy of weakly interacting mesoscopic colloids," *Soft Matter*, vol. 8, no. 15, pp. 4235–4243, 2012.

[115] A. Ayouch, X. Dieudonné, G. Vaudel, H. Piombini, K. Vallé, V. Gusev, P. Belleville, and P. Ruello, "Elasticity of an assembly of disordered nanoparticles interacting via either van der waals-bonded or covalent-bonded coating layers," *ACS nano*, vol. 6, no. 12, pp. 10614–10621, 2012.

[116] I. Lisiecki, D. Polli, C. Yan, G. Soavi, E. Duval, G. Cerullo, and M.-P. Pileni, "Coherent longitudinal acoustic phonons in three-dimensional supracrystals of cobalt nanocrystals," *Nano letters*, vol. 13, no. 10, pp. 4914–4919, 2013.

[117] P. Ruello, A. Ayouch, G. Vaudel, T. Pezeril, N. Delorme, S. Sato, K. Kimura, and V. Gusev, "Ultrafast acousto-plasmonics in gold nanoparticle superlattices," *Physical Review B*, vol. 92, no. 17, p. 174304, 2015.

[118] C. L. Poyser, T. Czerniuk, A. Akimov, B. T. Diroll, E. A. Gaulding, A. S. Salasyuk, A. J. Kent, D. R. Yakovlev, M. Bayer, and C. B. Murray, "Coherent acoustic phonons in colloidal semiconductor nanocrystal superlattices," *ACS nano*, vol. 10, no. 1, pp. 1163–1169, 2016.

[119] K. Johnson and K. Johnson, *Contact Mechanics*. Cambridge University Press, 1987.

[120] E. H. Lee and J. R. M. Radok, "The contact problem for viscoelastic bodies," *Journal of Applied Mechanics*, vol. 27, no. 3, pp. 438–444, 1960.

[121] G. A. Graham, "The contact problem in the linear theory of viscoelasticity when the time dependent contact area has any number of maxima and minima," *International Journal of Engineering Science*, vol. 5, no. 6, pp. 495–514, 1967.

[122] W. H. Yang, "The contact problem for viscoelastic bodies," *Journal of Applied Mechanics*, vol. 33, no. 2, pp. 395–401, 1966.

[123] D. Spence, "The hertz contact problem with finite friction," *Journal of elasticity*, vol. 5, no. 3-4, pp. 297–319, 1975.

[124] Y. Min, M. Akbulut, K. Kristiansen, Y. Golan, and J. Israelachvili, "The role of

interparticle and external forces in nanoparticle assembly," *Nature materials*, vol. 7, no. 7, p. 527, 2008.

[125] A. Vega-Flick, R. Duncan, S. Wallen, N. Boechler, C. Stelling, M. Retsch, J. Alvarado-Gil, K. Nelson, and A. Maznev, "Vibrational dynamics of a two-dimensional micro-granular crystal," *Physical Review B*, vol. 96, no. 2, p. 024303, 2017.

[126] R. S. Bradley, "Lxxix. the cohesive force between solid surfaces and the surface energy of solids," *The London, Edinburgh, and Dublin Philosophical Magazine and Journal of Science*, vol. 13, no. 86, pp. 853–862, 1932.

[127] Y.-P. Zhao, L. Wang, and T. Yu, "Mechanics of adhesion in memsa review," *Journal of Adhesion Science and Technology*, vol. 17, no. 4, pp. 519–546, 2003.

[128] K. Johnson and J. Greenwood, "An adhesion map for the contact of elastic spheres," *Journal of colloid and interface science*, vol. 192, no. 2, pp. 326–333, 1997.

[129] D. Tabor, "Surface forces and surface interactions," in *Plenary and Invited Lectures*, pp. 3–14, Elsevier, 1977.

[130] D. Maugis, "Adhesion of spheres: the jkr-dmt transition using a dugdale model," *Journal of colloid and interface science*, vol. 150, no. 1, pp. 243–269, 1992.

[131] C. Coste and B. Gilles, "On the validity of hertz contact law for granular material acoustics," *The European Physical Journal B-Condensed Matter and Complex Systems*, vol. 7, no. 1, pp. 155–168, 1999.

[132] D. Maugis and H. Pollock, "Surface forces, deformation and adherence at metal microcontacts," *Acta Metallurgica*, vol. 32, no. 9, pp. 1323–1334, 1984.

[133] C. Thornton, "Coefficient of restitution for collinear collisions of elastic-perfectly plastic spheres," *Journal of Applied Mechanics*, vol. 64, no. 2, pp. 383–386, 1997.

[134] L. Kogut and I. Etsion, "Elastic-plastic contact analysis of a sphere and a rigid flat," *Journal of applied Mechanics*, vol. 69, no. 5, pp. 657–662, 2002.

[135] R. L. Jackson and I. Green, "A finite element study of elasto-plastic hemispherical contact against a rigid flat," *Journal of tribology*, vol. 127, no. 2, pp. 343–354, 2005.

[136] S. D. Mesarovic and K. Johnson, "Adhesive contact of elastic–plastic spheres," *Journal of the Mechanics and Physics of Solids*, vol. 48, no. 10, pp. 2009–2033, 2000.

[137] Y. Kadin, Y. Kligerman, and I. Etsion, "Loading–unloading of an elastic–plastic adhesive spherical microcontact," *Journal of Colloid and Interface Science*, vol. 321, no. 1, pp. 242–250, 2008.

[138] Y. Du, L. Chen, N. E. McGruer, G. G. Adams, and I. Etsion, "A finite element model

of loading and unloading of an asperity contact with adhesion and plasticity," *Journal of colloid and interface science*, vol. 312, no. 2, pp. 522–528, 2007.

[139] H. Peng, Z. Liu, and G. Zhang, "A study of overall contact behavior of an elastic perfectly plastic hemisphere and a rigid plane," *Proceedings of the Institution of Mechanical Engineers, Part J: Journal of Engineering Tribology*, vol. 227, no. 3, pp. 259–274, 2013.

[140] F. Li, J. Pan, and C. Sinka, "Contact laws between solid particles," *Journal of the Mechanics and Physics of Solids*, vol. 57, no. 8, pp. 1194–1208, 2009.

[141] H. A. Burgoyne and C. Daraio, "Strain-rate-dependent model for the dynamic compression of elastoplastic spheres," *Physical Review E*, vol. 89, no. 3, p. 032203, 2014.

[142] R. K. Pal, A. P. Awasthi, and P. H. Geubelle, "Wave propagation in elasto-plastic granular systems," *Granular Matter*, vol. 15, no. 6, pp. 747–758, 2013.

[143] I. Etsion, Y. Kligerman, and Y. Kadin, "Unloading of an elastic–plastic loaded spherical contact," *International Journal of Solids and Structures*, vol. 42, no. 13, pp. 3716–3729, 2005.

[144] L. Vu-Quoc, X. Zhang, and L. Lesburg, "A normal force-displacement model for contacting spheres accounting for plastic deformation: force-driven formulation," *Journal of Applied Mechanics*, vol. 67, no. 2, pp. 363–371, 2000.

[145] A. Akimov, Y. Tanaka, A. Pevtsov, S. Kaplan, V. Golubev, S. Tamura, D. Yakovlev, and M. Bayer, "Hypersonic modulation of light in three-dimensional photonic and phononic band-gap materials," *Physical review letters*, vol. 101, no. 3, p. 033902, 2008.

[146] P. M. Jais, D. B. Murray, R. Merlin, and A. V. Bragas, "Metal nanoparticle ensembles: tunable laser pulses distinguish monomer from dimer vibrations," *Nano letters*, vol. 11, no. 9, pp. 3685–3689, 2011.

[147] P. J. Yunker, K. Chen, M. D. Gratale, M. A. Lohr, T. Still, and A. Yodh, "Physics in ordered and disordered colloidal matter composed of poly (n-isopropylacrylamide) microgel particles," *Reports on Progress in Physics*, vol. 77, no. 5, p. 056601, 2014.

[148] B. Li, F. Wang, D. Zhou, Y. Peng, R. Ni, and Y. Han, "Modes of surface premelting in colloidal crystals composed of attractive particles," *Nature*, vol. 531, no. 7595, p. 485, 2016.

[149] P. Pieranski, "Colloidal crystals," *Contemporary Physics*, vol. 24, no. 1, pp. 25–73, 1983.

[150] C. Vieu, F. Carcenac, A. Pepin, Y. Chen, M. Mejias, A. Lebib, L. Manin-Ferlazzo, L. Couraud, and H. Launois, "Electron beam lithography: resolution limits and applications," *Applied surface science*, vol. 164, no. 1-4, pp. 111–117, 2000.

[151] L. Mosher, B. Morgan, C. Waits, R. Ghodssi, M. U. C. P. D. of ELECTRICAL, and C. ENGINEERING., *Advanced Techniques in 3D Photolithography for MEMS*. Defense Technical Information Center, 2006.

[152] Y. Zhang, B. K. Chen, X. Liu, and Y. Sun, "Autonomous robotic pick-and-place of microobjects," *IEEE Transactions on Robotics*, vol. 26, no. 1, pp. 200–207, 2010.

[153] N. Vogel, M. Retsch, C.-A. Fustin, A. del Campo, and U. Jonas, "Advances in colloidal assembly: the design of structure and hierarchy in two and three dimensions," *Chemical reviews*, vol. 115, no. 13, pp. 6265–6311, 2015.

[154] Z. Zhang, C. Geng, Z. Hao, T. Wei, and Q. Yan, "Recent advancement on micro-/nano-spherical lens photolithography based on monolayer colloidal crystals," *Advances in colloid and interface science*, vol. 228, pp. 105–122, 2016.

[155] S. Hayashi, Y. Kumamoto, T. Suzuki, and T. Hirai, "Imaging by polystyrene latex particles," *Journal of colloid and interface science*, vol. 144, no. 2, pp. 538–547, 1991.

[156] Y. Xia, B. Gates, Y. Yin, and Y. Lu, "Monodispersed colloidal spheres: old materials with new applications," *Advanced Materials*, vol. 12, no. 10, pp. 693–713, 2000.

[157] F. Burmeister, C. Schäfle, T. Matthes, M. Böhmisch, J. Boneberg, and P. Leiderer, "Colloid monolayers as versatile lithographic masks," *Langmuir*, vol. 13, no. 11, pp. 2983–2987, 1997.

[158] D. J. Norris, E. G. Arlinghaus, L. Meng, R. Heiny, and L. Scriven, "Opaline photonic crystals: How does self-assembly work?," *Advanced Materials*, vol. 16, no. 16, pp. 1393–1399, 2004.

[159] O. Velev, T. Jede, R. Lobo, and A. Lenhoff, "Porous silica via colloidal crystallization," *Nature*, vol. 389, no. 6650, p. 447, 1997.

[160] K. R. Phillips, N. Vogel, Y. Hu, M. Kolle, C. C. Perry, and J. Aizenberg, "Tunable anisotropy in inverse opals and emerging optical properties," *Chemistry of Materials*, vol. 26, no. 4, pp. 1622–1628, 2014.

[161] G. A. Ozin and S. M. Yang, "The race for the photonic chip: colloidal crystal assembly in silicon wafers," *Advanced Functional Materials*, vol. 11, no. 2, pp. 95–104, 2001.

[162] Y. Xia, B. Gates, and S. H. Park, "Fabrication of three-dimensional photonic crystals for use in the spectral region from ultraviolet to near-infrared," *Journal of lightwave technology*, vol. 17, no. 11, p. 1956, 1999.

[163] J. M. Weissman, H. B. Sunkara, S. T. Albert, and S. A. Asher, "Thermally switchable periodicities and diffraction from mesoscopically ordered materials," *Science*, vol. 274, no. 5289, pp. 959–963, 1996.

[164] V. Canalejas-Tejero, M. Ibisate, D. Golmayo, A. Blanco, and C. López, "Qualitative and quantitative analysis of crystallographic defects present in 2d colloidal sphere arrays," *Langmuir*, vol. 28, no. 1, pp. 161–167, 2011.

[165] M. C. Petty, *Langmuir-Blodgett films: an introduction*. Cambridge University Press, 1996.

[166] M. Kondo, K. Shinozaki, L. Bergstroem, and N. Mizutani, "Preparation of colloidal monolayers of alkoxylated silica particles at the air-liquid interface," *Langmuir*, vol. 11, no. 2, pp. 394–397, 1995.

[167] M. Retsch, Z. Zhou, S. Rivera, M. Kappl, X. S. Zhao, U. Jonas, and Q. Li, "Fabrication of large-area, transferable colloidal monolayers utilizing self-assembly at the air/water interface," *Macromolecular Chemistry and Physics*, vol. 210, no. 3-4, pp. 230–241, 2009.

[168] N. D. Denkov, O. Velev, P. Kralchevsky, I. Ivanov, H. Yoshimura, and K. Nagayama, "Two-dimensional crystallization," *Nature*, vol. 361, no. 6407, p. 26, 1993.

[169] A. S. Dimitrov and K. Nagayama, "Continuous convective assembling of fine particles into two-dimensional arrays on solid surfaces," *Langmuir*, vol. 12, no. 5, pp. 1303–1311, 1996.

[170] Z.-Z. Gu, A. Fujishima, and O. Sato, "Fabrication of high-quality opal films with controllable thickness," *Chemistry of Materials*, vol. 14, no. 2, pp. 760–765, 2002.

[171] L. Teh, N. Tan, C. Wong, and S. Li, "Growth imperfections in three-dimensional colloidal self-assembly," *Applied Physics A*, vol. 81, no. 7, pp. 1399–1404, 2005.

[172] L. Wang and X. Zhao, "Fabrication of crack-free colloidal crystals using a modified vertical deposition method," *The Journal of Physical Chemistry C*, vol. 111, no. 24, pp. 8538–8542, 2007.

[173] B. Hatton, L. Mishchenko, S. Davis, K. H. Sandhage, and J. Aizenberg, "Assembly of large-area, highly ordered, crack-free inverse opal films," *Proceedings of the National Academy of Sciences*, vol. 107, no. 23, pp. 10354–10359, 2010.

[174] S. Krishnaswamy, *Theory and Applications of Laser Ultrasonic Techniques: Engineering and Biological Material Characterizati*, pp. 435–494. CRC Press, 1 ed., 2003.

[175] J. A. Rogers, A. A. Maznev, M. J. Banet, and K. A. Nelson, "Optical generation and characterization of acoustic waves in thin films: Fundamentals and applications," *Annual Review of Materials Science*, vol. 30, no. 1, pp. 117–157, 2000.

[176] A. Maznev, K. Nelson, and J. Rogers, "Optical heterodyne detection of laser-induced gratings," *Optics letters*, vol. 23, no. 16, pp. 1319–1321, 1998.

[177] J. K. Eliason, *Optical transient grating measurements of micro/nanoscale thermal*

transport and mechanical properties. PhD thesis, Massachusetts Institute of Technology, 2015.

[178] A. Vega-Flick, J. Eliason, A. Maznev, A. Khanolkar, M. Abi Ghanem, N. Boechler, J. Alvarado-Gil, and K. Nelson, "Laser-induced transient grating setup with continuously tunable period," *Review of Scientific Instruments*, vol. 86, no. 12, p. 123101, 2015.

[179] A. Maznev, A. Mazurenko, L. Zhuoyun, and M. Gostein, "Laser-based surface acoustic wave spectrometer for industrial applications," *Review of scientific instruments*, vol. 74, no. 1, pp. 667–669, 2003.

[180] A. Maznev and O. Wright, "Optical generation of long-lived surface vibrations in a periodic microstructure," *Journal of Applied Physics*, vol. 105, no. 12, p. 123530, 2009.

[181] C. Glorieux, J. Beers, E. H. Bentefour, K. Van de Rostyne, and K. A. Nelson, "Phase mask based interferometer: Operation principle, performance, and application to thermoelastic phenomena," *Review of scientific instruments*, vol. 75, no. 9, pp. 2906–2920, 2004.

[182] P. Hariharan, *Basics of Interferometry*. Elsevier Science, 2012.

[183] J. Shen, U. Riebel, and X. Guo, "Scattering and transmission by a monolayer of spheres: A study on the monolayer structure," *Particle & Particle Systems Characterization*, vol. 22, no. 5, pp. 320–328, 2005.

[184] V. P. Dick, V. A. Loiko, and A. P. Ivanov, "Angular structure of radiation scattered by monolayers of particles: experimental study," *Applied optics*, vol. 36, no. 18, pp. 4235–4240, 1997.

[185] J.-Y. Lee, M.-P. Lu, K.-Y. Lin, and S.-H. Huang, "Measurement of in-plane displacement by wavelength-modulated heterodyne speckle interferometry," *Applied optics*, vol. 51, no. 8, pp. 1095–1100, 2012.

[186] O. B. Wright and K. Kawashima, "Coherent phonon detection from ultrafast surface vibrations," *Physical review letters*, vol. 69, no. 11, p. 1668, 1992.

[187] C. Desmet, V. Gusev, W. Lauriks, C. Glorieux, and J. Thoen, "All-optical excitation and detection of leaky rayleigh waves," *Optics letters*, vol. 22, no. 2, pp. 69–71, 1997.

[188] J. Higuet, T. Valier-Brasier, T. Dehoux, and B. Audoin, "Beam distortion detection and deflectometry measurements of gigahertz surface acoustic waves," *Review of Scientific Instruments*, vol. 82, no. 11, p. 114905, 2011.

[189] L. Kogut and I. Etsion, "Adhesion in elastic–plastic spherical microcontact," *Journal of Colloid and Interface Science*, vol. 261, no. 2, pp. 372–378, 2003.

[190] Z. Song and K. Komvopoulos, "Adhesion-induced instabilities in elastic and elastic–plastic contacts during single and repetitive normal loading," *Journal of the Mechanics and Physics of Solids*, vol. 59, no. 4, pp. 884–897, 2011.

[191] *COMSOL Multiphysics Reference Manual*.

[192] A. Geslain, S. Raetz, M. Hiraiwa, M. Abi Ghanem, S. Wallen, A. Khanolkar, N. Boechler, J. Laurent, C. Prada, A. Duclos, *et al.*, "Spatial laplace transform for complex wavenumber recovery and its application to the analysis of attenuation in acoustic systems," *Journal of Applied Physics*, vol. 120, no. 13, p. 135107, 2016.

[193] W. Ewing, *Elastic Waves in Layered Media*. Bibliolife DBA of Bibilio Bazaar II LLC, 2015.

[194] J. Rayleigh, *The Theory of Sound*. No. v. 2 in The Theory of Sound, Macmillan, 1896.

[195] V. Tournat and V. Gusev, "Acoustics of unconsolidated "model" granular media: An overview of recent results and several open problems," *Acta Acustica united with Acustica*, vol. 96, no. 2, pp. 208–224, 2010.

[196] A. C. Kibblewhite, "Attenuation of sound in marine sediments: A review with emphasis on new low-frequency data," *The Journal of the Acoustical Society of America*, vol. 86, no. 2, pp. 716–738, 1989.

[197] H. Hu, A. Strybulevych, J. Page, S. E. Skipetrov, and B. A. van Tiggelen, "Localization of ultrasound in a three-dimensional elastic network," *Nature Physics*, vol. 4, no. 12, p. 945, 2008.

[198] A. Merkel, V. Tournat, and V. Gusev, "Experimental evidence of rotational elastic waves in granular phononic crystals," *Physical Review Letters*, vol. 107, no. 22, p. 225502, 2011.

[199] A.-C. Hladky-Hennion, F. Cohen-Tenoudji, A. Devos, and M. de Billy, "On the existence of subresonance generated in a one-dimensional chain of identical spheres," *The Journal of the Acoustical Society of America*, vol. 112, no. 3, pp. 850–855, 2002.

[200] B. H. Lee, H. Shin, and M. M. Sung, "Patterning a two-dimensional colloidal crystal by water-mediated particle transfer printing," *Chemistry of Materials*, vol. 19, no. 23, pp. 5553–5556, 2007.

[201] V. Laude, *Phononic Crystals: Artificial Crystals for Sonic, Acoustic, and Elastic Waves*, vol. 26. Walter de Gruyter GmbH & Co KG, 2015.

[202] M. Born and E. Wolf, *Principles of Optics: Electromagnetic Theory of Propagation, Interference and Diffraction of Light*. Elsevier Science, 2013.

[203] E. Garova, A. Maradudin, and A. Mayer, "Interaction of rayleigh waves with randomly

distributed oscillators on the surface," *Physical Review B*, vol. 59, no. 20, p. 13291, 1999.

[204] S. P. Wallen, A. A. Maznev, and N. Boechler, "Dynamics of a monolayer of microspheres on an elastic substrate," *Physical Review B*, vol. 92, no. 17, p. 174303, 2015.

[205] V. Tournat, I. Pèrez-Arjona, A. Merkel, V. Sanchez-Morcillo, and V. Gusev, "Elastic waves in phononic monolayer granular membranes," *New Journal of Physics*, vol. 13, no. 7, p. 073042, 2011.

[206] A. A. Kolomenskii, H. Schuessler, V. Mikhalevich, and A. Maznev, "Interaction of laser-generated surface acoustic pulses with fine particles: Surface cleaning and adhesion studies," *Journal of applied physics*, vol. 84, no. 5, pp. 2404–2410, 1998.

[207] R. Fuchs, T. Weinhart, J. Meyer, H. Zhuang, T. Staedler, X. Jiang, and S. Luding, "Rolling, sliding and torsion of micron-sized silica particles: experimental, numerical and theoretical analysis," *Granular matter*, vol. 16, no. 3, pp. 281–297, 2014.

[208] T. M. Gronewold, "Surface acoustic wave sensors in the bioanalytical field: Recent trends and challenges," *analytica chimica acta*, vol. 603, no. 2, pp. 119–128, 2007.

[209] F. Lemoult, N. Kaina, M. Fink, and G. Lerosey, "Wave propagation control at the deep subwavelength scale in metamaterials," *Nature Physics*, vol. 9, no. 1, p. 55, 2013.

[210] Y. Lai, Y. Wu, P. Sheng, and Z.-Q. Zhang, "Hybrid elastic solids," *Nature materials*, vol. 10, no. 8, p. 620, 2011.

[211] N. Fang, D. Xi, J. Xu, M. Ambati, W. Srituravanich, C. Sun, and X. Zhang, "Ultrasonic metamaterials with negative modulus," *Nature materials*, vol. 5, no. 6, p. 452, 2006.

[212] S. Zhang, L. Yin, and N. Fang, "Focusing ultrasound with an acoustic metamaterial network," *Physical review letters*, vol. 102, no. 19, p. 194301, 2009.

[213] J. Mei, G. Ma, M. Yang, Z. Yang, W. Wen, and P. Sheng, "Dark acoustic metamaterials as super absorbers for low-frequency sound," *Nature communications*, vol. 3, p. 756, 2012.

[214] S. Zhang, C. Xia, and N. Fang, "Broadband acoustic cloak for ultrasound waves," *Physical Review Letters*, vol. 106, no. 2, p. 024301, 2011.

[215] M. Rupin, F. Lemoult, G. Lerosey, and P. Roux, "Experimental demonstration of ordered and disordered multiresonant metamaterials for lamb waves," *Physical review letters*, vol. 112, no. 23, p. 234301, 2014.

[216] T. Kraus, D. Brodoceanu, N. Pazos-Perez, and A. Fery, "Colloidal surface assemblies: nanotechnology meets bioinspiration," *Advanced Functional Materials*, vol. 23, no. 36, pp. 4529–4541, 2013.

[217] F. Li, D. P. Josephson, and A. Stein, "Colloidal assembly: the road from particles to colloidal molecules and crystals," *Angewandte Chemie International Edition*, vol. 50, no. 2, pp. 360–388, 2011.

[218] O. D. Velev and S. Gupta, "Materials fabricated by micro-and nanoparticle assembly–the challenging path from science to engineering," *Advanced Materials*, vol. 21, no. 19, pp. 1897–1905, 2009.

[219] J.-H. Lee, C. Y. Koh, J. P. Singer, S.-J. Jeon, M. Maldovan, O. Stein, and E. L. Thomas, "25th anniversary article: ordered polymer structures for the engineering of photons and phonons," *Advanced Materials*, vol. 26, no. 4, pp. 532–569, 2014.

[220] J. F. Galisteo-López, M. Ibisate, R. Sapienza, L. S. Froufe-Pérez, Á. Blanco, and C. López, "Self-assembled photonic structures," *Advanced Materials*, vol. 23, no. 1, pp. 30–69, 2011.

[221] G. von Freymann, V. Kitaev, B. V. Lotsch, and G. A. Ozin, "Bottom-up assembly of photonic crystals," *Chemical Society Reviews*, vol. 42, no. 7, pp. 2528–2554, 2013.

[222] B. Sepúlveda, P. C. Angelomé, L. M. Lechuga, and L. M. Liz-Marzán, "Lspr-based nanobiosensors," *nano today*, vol. 4, no. 3, pp. 244–251, 2009.

[223] M. Grzelczak, J. Vermant, E. M. Furst, and L. M. Liz-Marzán, "Directed self-assembly of nanoparticles," *ACS nano*, vol. 4, no. 7, pp. 3591–3605, 2010.

[224] A. Klinkova, R. M. Choueiri, and E. Kumacheva, "Self-assembled plasmonic nanostructures," *Chemical Society Reviews*, vol. 43, no. 11, pp. 3976–3991, 2014.

[225] W.-L. Min, B. Jiang, and P. Jiang, "Bioinspired self-cleaning antireflection coatings," *Advanced Materials*, vol. 20, no. 20, pp. 3914–3918, 2008.

[226] T. Still, W. Cheng, M. Retsch, R. Sainidou, J. Wang, U. Jonas, N. Stefanou, and G. Fytas, "Simultaneous occurrence of structure-directed and particle-resonance-induced phononic gaps in colloidal films," *Physical review letters*, vol. 100, no. 19, p. 194301, 2008.

[227] M. Caleap and B. W. Drinkwater, "Acoustically trapped colloidal crystals that are reconfigurable in real time," *Proceedings of the National Academy of Sciences*, vol. 111, no. 17, pp. 6226–6230, 2014.

[228] T. Brunet, A. Merlin, B. Mascaro, K. Zimny, J. Leng, O. Poncelet, C. Aristégui, and O. Mondain-Monval, "Soft 3d acoustic metamaterial with negative index," *Nature materials*, vol. 14, no. 4, p. 384, 2015.

[229] P. J. Beltramo, D. Schneider, G. Fytas, and E. M. Furst, "Anisotropic hypersonic phonon propagation in films of aligned ellipsoids," *Physical review letters*, vol. 113, no. 20, p. 205503, 2014.

[230] H. Lamb, "On waves in an elastic plate," *Proceedings of the Royal Society of London. Series A*, vol. 93, no. 648, pp. 114–128, 1917.

[231] T.-T. Wu, J.-C. Hsu, and J.-H. Sun, "Phononic plate waves," *IEEE transactions on ultrasonics, ferroelectrics, and frequency control*, vol. 58, no. 10, pp. 2146–2161, 2011.

[232] V. Yantchev and I. Katardjiev, "Thin film lamb wave resonators in frequency control and sensing applications: a review," *Journal of Micromechanics and Microengineering*, vol. 23, no. 4, p. 043001, 2013.

[233] J. Cuffe, O. Ristow, E. Chávez, A. Shchepetov, P.-O. Chapuis, F. Alzina, M. Hettich, M. Prunnila, J. Ahopelto, T. Dekorsy, *et al.*, "Lifetimes of confined acoustic phonons in ultrathin silicon membranes," *Physical review letters*, vol. 110, no. 9, p. 095503, 2013.

[234] Y. Pennec, B. Djafari-Rouhani, H. Larabi, J. Vasseur, and A. Hladky-Hennion, "Low-frequency gaps in a phononic crystal constituted of cylindrical dots deposited on a thin homogeneous plate," *Physical Review B*, vol. 78, no. 10, p. 104105, 2008.

[235] B. L. Davis and M. I. Hussein, "Nanophononic metamaterial: Thermal conductivity reduction by local resonance," *Physical review letters*, vol. 112, no. 5, p. 055505, 2014.

[236] V. E. Gusev and O. B. Wright, "Double-negative flexural acoustic metamaterial," *New Journal of Physics*, vol. 16, no. 12, p. 123053, 2014.

[237] T.-C. Wu, T.-T. Wu, and J.-C. Hsu, "Waveguiding and frequency selection of lamb waves in a plate with a periodic stubbed surface," *Physical Review B*, vol. 79, no. 10, p. 104306, 2009.

[238] R. Zhu, X. Liu, G. Hu, C. Sun, and G. Huang, "Negative refraction of elastic waves at the deep-subwavelength scale in a single-phase metamaterial," *Nature communications*, vol. 5, p. 5510, 2014.

[239] J. A. Rogers and K. A. Nelson, "Study of lamb acoustic waveguide modes in unsupported polyimide thin films using real-time impulsive stimulated thermal scattering," *Journal of applied physics*, vol. 75, no. 3, pp. 1534–1556, 1994.

[240] H. McSkimin and P. Andreatch Jr, "Elastic moduli of silicon vs hydrostatic pressure at 25.0 c and- 195.8 c," *Journal of Applied Physics*, vol. 35, no. 7, pp. 2161–2165, 1964.

[241] L. Solie and B. Auld, "Elastic waves in free anisotropic plates," *The Journal of the Acoustical Society of America*, vol. 54, no. 1, pp. 50–65, 1973.

[242] J. Jones, "Wave propagation in a two-layered medium," *Journal of Applied Mechanics*, vol. 31, no. 2, pp. 213–222, 1964.

[243] Y. Sato, "Basic study on the oscillation of a homogeneous elastic sphere, 1˜ 3.," *Geophysical Magazine*, vol. 31, no. 1, 1962.

[244] S. Biggs and G. Spinks, "Atomic force microscopy investigation of the adhesion between a single polymer sphere and a flat surface," *Journal of adhesion science and technology*, vol. 12, no. 5, pp. 461–478, 1998.

[245] H. Zhou, M. Götzinger, and W. Peukert, "The influence of particle charge and roughness on particle–substrate adhesion," *Powder Technology*, vol. 135, pp. 82–91, 2003.

[246] R. Tykhoniuk, J. Tomas, S. Luding, M. Kappl, L. Heim, and H.-J. Butt, "Ultrafine cohesive powders: from interparticle contacts to continuum behaviour," *Chemical Engineering Science*, vol. 62, no. 11, pp. 2843–2864, 2007.

[247] J. Damour, J. R. Stålgren, K. Kanazawa, C. Frank, M. Rodahl, and D. Johannsmann, "Capillary aging of the contacts between glass spheres and a quartz resonator surface," *Physical review letters*, vol. 96, no. 5, p. 058301, 2006.

[248] J. Tomas, "Adhesion of ultrafine particlesa micromechanical approach," *Chemical Engineering Science*, vol. 62, no. 7, pp. 1997–2010, 2007.

[249] B. Bhushan, *Handbook of Micro/Nano Tribology, Second Edition*. CRC series mechanics and materials science, Taylor & Francis, 1998.

[250] W. A. Ducker, T. J. Senden, and R. M. Pashley, "Direct measurement of colloidal forces using an atomic force microscope," *nature*, vol. 353, no. 6341, p. 239, 1991.

[251] H.-J. Butt, "Measuring electrostatic, van der waals, and hydration forces in electrolyte solutions with an atomic force microscope," *Biophysical Journal*, vol. 60, no. 6, pp. 1438–1444, 1991.

[252] D. Schaefer, M. Carpenter, B. Gady, R. Reifenberger, L. Demejo, and D. Rimai, "Surface roughness and its influence on particle adhesion using atomic force techniques," *Journal of adhesion science and technology*, vol. 9, no. 8, pp. 1049–1062, 1995.

[253] G. Toikka, R. A. Hayes, and J. Ralston, "Adhesion of iron oxide to silica studied by atomic force microscopy," *Journal of colloid and interface science*, vol. 180, no. 2, pp. 329–338, 1996.

[254] D.-L. Liu, J. Martin, and N. Burnham, "Optimal roughness for minimal adhesion," *Applied Physics Letters*, vol. 91, no. 4, p. 043107, 2007.

[255] J. Drelich and K. Mittal, *Atomic Force Microscopy in Adhesion Studies*. CRC Press, 2005.

[256] D. Rimai, L. DeMejo, and R. Bowen, "Adhesion-induced deformations of polymeric substrates: Particle size dependence of the contact area," *Journal of Applied Physics*, vol. 66, no. 8, pp. 3574–3578, 1989.

[257] D. Rimai, L. DeMejo, and R. Bowen, "Surface-force-induced deformations of monodis-

perse polystyrene spheres on planar silicon substrates," *Journal of applied physics*, vol. 68, no. 12, pp. 6234–6240, 1990.

[258] L. DeMejo, D. Rimai, and R. Bowen, "Adhesion-induced deformations of polyurethane substrates in contact with spherical glass particles: the effect of particle size on the radius of contact," *Journal of adhesion science and technology*, vol. 5, no. 11, pp. 959–972, 1991.

[259] D. Rimai, L. DeMejo, W. Vreeland, and R. Bowen, "Adhesion induced deformations of a highly compliant elastomeric substrate in contact with rigid particles," *Langmuir*, vol. 10, no. 11, pp. 4361–4366, 1994.

[260] D. Rimai, L. Demejo, and R. Bowen, "Mechanics of particle adhesion," *Journal of Adhesion Science and Technology*, vol. 8, no. 11, pp. 1333–1355, 1994.

[261] D. Rimai, D. Quesnel, and R. Bowen, "Particle adhesion to highly compliant substrates: anomalous power-law dependence of the contact radius on particle radius," *Langmuir*, vol. 17, no. 22, pp. 6946–6952, 2001.

[262] X.-D. Wang, Z.-X. Shen, J.-L. Zhang, H.-F. Jiao, X.-B. Cheng, L.-Y. Chen, and Z.-S. Wang, "Submicrometer aluminum spheres adhesion to planar silicon substrates," *Langmuir*, vol. 26, no. 17, pp. 13903–13906, 2010.

[263] X.-D. Wang, Z.-X. Shen, J.-L. Zhang, H.-F. Jiao, X.-B. Cheng, X.-W. Ye, L.-Y. Chen, and Z.-S. Wang, "Contact between submicrometer silica spheres," *Langmuir*, vol. 26, no. 8, pp. 5583–5586, 2009.

[264] X.-D. Wang, B. Chen, H.-F. Wang, and Z.-S. Wang, "Adhesion between submicrometer polystyrene spheres," *Powder technology*, vol. 214, no. 3, pp. 447–450, 2011.

[265] A. Nicolet and F. Meli, "Spherical polystyrene particle deformation measured with the afm," *Measurement Science and Technology*, vol. 28, no. 3, p. 034003, 2017.

[266] M. M. Peri and C. Cetinkaya*, "Rolling resistance moment of microspheres on surfaces," *Philosophical Magazine*, vol. 85, no. 13, pp. 1347–1357, 2005.

[267] A. Saeedi Vahdat, S. Azizi, and C. Cetinkaya, "Nonlinear dynamics of adhesive microspherical particles on vibrating substrates," *Journal of Adhesion Science and Technology*, vol. 27, no. 15, pp. 1712–1726, 2013.

[268] M. Hiraiwa, M. Stossel, A. Khanolkar, J. Wang, and N. Boechler, "Laser-induced spallation of microsphere monolayers," *Langmuir*, vol. 32, no. 31, pp. 7730–7734, 2016.

[269] D. M. Lipkin, J. N. Israelachvili, and D. R. Clarke, "Estimating the metal-ceramic van der waals adhesion energy," *Philosophical Magazine A*, vol. 76, no. 4, pp. 715–728, 1997.

[270] N. Vogel, L. de Viguerie, U. Jonas, C. K. Weiss, and K. Landfester, "Wafer-scale fabrication of ordered binary colloidal monolayers with adjustable stoichiometries," *Advanced functional materials*, vol. 21, no. 16, pp. 3064–3073, 2011.

[271] M. Finnis, "The theory of metal-ceramic interfaces," *Journal of Physics: Condensed Matter*, vol. 8, no. 32, p. 5811, 1996.

[272] D. Ma and C. Liu, "Contact law and coefficient of restitution in elastoplastic spheres," *Journal of Applied Mechanics*, vol. 82, no. 12, p. 121006, 2015.

[273] E. Wang, P. Geubelle, and J. Lambros, "An experimental study of the dynamic elasto-plastic contact behavior of metallic granules," *Journal of Applied Mechanics*, vol. 80, no. 2, p. 021009, 2013.

[274] N. T. Kattamis, P. E. Purnick, R. Weiss, and C. B. Arnold, "Thick film laser induced forward transfer for deposition of thermally and mechanically sensitive materials," *Applied Physics Letters*, vol. 91, no. 17, p. 171120, 2007.

[275] M. A. Porter, C. Daraio, E. B. Herbold, I. Szelengowicz, and P. Kevrekidis, "Highly nonlinear solitary waves in periodic dimer granular chains," *Physical Review E*, vol. 77, no. 1, p. 015601, 2008.

[276] R. Carretero-González, D. Khatri, M. A. Porter, P. Kevrekidis, and C. Daraio, "Dissipative solitary waves in granular crystals," *Physical review letters*, vol. 102, no. 2, p. 024102, 2009.

[277] H. A. Burgoyne, J. A. Newman, W. C. Jackson, and C. Daraio, "Guided impact mitigation in 2d and 3d granular crystals," *Procedia Engineering*, vol. 103, pp. 52–59, 2015.

[278] H. A. Burgoyne and C. Daraio, "Elastic–plastic wave propagation in uniform and periodic granular chains," *Journal of Applied Mechanics*, vol. 82, no. 8, p. 081002, 2015.

[279] R. F. Waymel, E. Wang, A. Awasthi, P. H. Geubelle, and J. Lambros, "Propagation and dissipation of elasto-plastic stress waves in two dimensional ordered granular media," *Journal of the Mechanics and Physics of Solids*, 2017.

[280] C. Coste, E. Falcon, and S. Fauve, "Solitary waves in a chain of beads under hertz contact," *Physical review E*, vol. 56, no. 5, p. 6104, 1997.

[281] C. Daraio, V. Nesterenko, E. Herbold, and S. Jin, "Tunability of solitary wave properties in one-dimensional strongly nonlinear phononic crystals," *Physical Review E*, vol. 73, no. 2, p. 026610, 2006.

[282] M. Hiraiwa, S. Wallen, and N. Boechler, "Acoustic wave propagation in disordered

microscale granular media under compression," *Granular Matter*, vol. 19, no. 3, p. 62, 2017.

[283] M. Trau, D. Saville, and I. Aksay, "Field-induced layering of colloidal crystals," *Science*, vol. 272, no. 5262, pp. 706–709, 1996.

[284] J. Aizenberg, P. V. Braun, and P. Wiltzius, "Patterned colloidal deposition controlled by electrostatic and capillary forces," *Physical review letters*, vol. 84, no. 13, p. 2997, 2000.

[285] J. Ge, Y. Hu, and Y. Yin, "Highly tunable superparamagnetic colloidal photonic crystals," *Angewandte Chemie*, vol. 119, no. 39, pp. 7572–7575, 2007.

[286] M.-H. Wu and G. M. Whitesides, "Fabrication of arrays of two-dimensional micropatterns using microspheres as lenses for projection photolithography," *Applied physics letters*, vol. 78, no. 16, pp. 2273–2275, 2001.

[287] H. Wu, T. W. Odom, G. M. Whitesides, *et al.*, "Generation of chrome masks with micrometer-scale features using microlens lithography," *Advanced Materials*, vol. 14, no. 17, pp. 1213–1216, 2002.

[288] M.-H. Wu, K. E. Paul, and G. M. Whitesides, "Patterning flood illumination with microlens arrays," *Applied optics*, vol. 41, no. 13, pp. 2575–2585, 2002.

[289] M.-H. Wu and G. M. Whitesides, "Fabrication of two-dimensional arrays of microlenses and their applications in photolithography," *Journal of micromechanics and microengineering*, vol. 12, no. 6, p. 747, 2002.

[290] M.-H. Wu, C. Park, and G. M. Whitesides, "Generation of submicrometer structures by photolithography using arrays of spherical microlenses," *Journal of colloid and interface science*, vol. 265, no. 2, pp. 304–309, 2003.

[291] X. Ma, J. Q. Lu, R. S. Brock, K. M. Jacobs, P. Yang, and X.-H. Hu, "Determination of complex refractive index of polystyrene microspheres from 370 to 1610 nm," *Physics in Medicine & Biology*, vol. 48, no. 24, p. 4165, 2003.

[292] A. Bonakdar, S. J. Jang, and H. Mohseni, "Tilted exposure microsphere nanolithography for high-throughput and mask-less fabrication of plasmonic molecules," in *Nanoengineering: Fabrication, Properties, Optics, and Devices X*, vol. 8816, p. 881614, International Society for Optics and Photonics, 2013.

[293] C.-H. Chang, L. Tian, W. Hesse, H. Gao, H. Choi, J.-G. Kim, M. Siddiqui, and G. Barbastathis, "From two-dimensional colloidal self-assembly to three-dimensional nanolithography," *Nano letters*, vol. 11, no. 6, pp. 2533–2537, 2011.

[294] T. Wei, K. Wu, D. Lan, Q. Yan, Y. Chen, C. Du, J. Wang, Y. Zeng, and J. Li, "Selectively grown photonic crystal structures for high efficiency ingan emitting diodes using

nanospherical-lens lithography," *Applied Physics Letters*, vol. 101, no. 21, p. 211111, 2012.

[295] Y. Wang, D. Raabe, C. Klüber, and F. Roters, "Orientation dependence of nanoindentation pile-up patterns and of nanoindentation microtextures in copper single crystals," *Acta Materialia*, vol. 52, no. 8, pp. 2229–2238, 2004.

[296] K. Kese and Z.-C. Li, "Semi-ellipse method for accounting for the pile-up contact area during nanoindentation with the berkovich indenter," *Scripta Materialia*, vol. 55, no. 8, pp. 699–702, 2006.

[297] P. Alivisatos, "The use of nanocrystals in biological detection," *Nature biotechnology*, vol. 22, no. 1, p. 47, 2004.

[298] F. Allein, V. Tournat, V. Gusev, and G. Theocharis, "Transversal–rotational and zero group velocity modes in tunable magneto-granular phononic crystals," *Extreme Mechanics Letters*, vol. 12, pp. 65–70, 2017.

[299] A. Vega-Flick, R. Duncan, S. Wallen, N. Boechler, C. Stelling, M. Retsch, J. Alvarado-Gil, K. Nelson, and A. Maznev, "Contact-based and spheroidal vibrational modes of a hexagonal monolayer of microspheres on a substrate," *Wave Motion*, vol. 76, pp. 122–133, 2018.

[300] J. Avice, C. Boscher, G. Vaudel, G. Brotons, V. Juve, M. Edely, C. Méthivier, V. E. Gusev, P. Belleville, H. Piombini, *et al.*, "Controlling the nanocontact nature and the mechanical properties of a silica nanoparticle assembly," *The Journal of Physical Chemistry C*, vol. 121, no. 42, pp. 23769–23776, 2017.

[301] R. Mindlin, "Compliance of elastic bodies in contact," *J. Appl. Mech. Trans. ASME*, vol. 16, pp. 259–268, 1949.

[302] J. Yin, M. Retsch, E. L. Thomas, and M. C. Boyce, "Collective mechanical behavior of multilayer colloidal arrays of hollow nanoparticles," *Langmuir*, vol. 28, no. 13, pp. 5580–5588, 2012.

[303] A. Merkel, V. Tournat, and V. Gusev, "Dispersion of elastic waves in three-dimensional noncohesive granular phononic crystals: properties of rotational modes," *Physical Review E*, vol. 82, no. 3, p. 031305, 2010.

[304] N. B. R. Doremus, *Handbook of Glass Properties*. Academic Press 1986, 2013.

[305] F. Gallego-Gómez, V. Morales-Flórez, M. Morales, A. Blanco, and C. López, "Colloidal crystals and water: Perspectives on liquid–solid nanoscale phenomena in wet particulate media," *Advances in colloid and interface science*, vol. 234, pp. 142–160, 2016.

[306] A.-C. Hladky-Hennion, A. Devos, and M. de Billy, "Quantitative analysis of the vibra-

tion modes in a finite set of coupled spheres," *The Journal of the Acoustical Society of America*, vol. 116, no. 1, pp. 117–124, 2004.

[307] B. Auld, *Acoustic fields and waves in solids*. A Wiley-Interscience publication, Wiley, 1973.

[308] A. Ben-Menahem and S. Singh, *Seismic Waves and Sources*. Springer New York, 2012.

[309] A. Mal, "Wave propagation in layered composite laminates under periodic surface loads," *Wave motion*, vol. 10, no. 3, pp. 257–266, 1988.

[310] T. Bromwich, "On the influence of gravity on elastic waves, and, in particular on the vibrations of an elastic globe," *Proceedings of the London Mathematical Society*, vol. 1, no. 1, pp. 98–165, 1898.

[311] A. Love, *Some Problems of Geodynamics*. Cambridge University Press, 2015.

[312] G. Farnell and E. Adler, "Elastic wave propagation in thin layers," *Physical acoustics*, vol. 9, pp. 35–127, 2012.

[313] A. Lee, "The effect of geological structure upon microseismic disturbance.," *Geophysical Journal International*, vol. 3, no. s2, pp. 83–105, 1932.

[314] A. S. Suiker, C. S. Chang, R. de Borst, and C. Esveld, "Surface waves in a stratified half space with enhanced continuum properties. part 1: Formulation of the boundary value problem," *European Journal of Mechanics-A/Solids*, vol. 18, no. 5, pp. 749–768, 1999.

[315] A. S. Suiker, C. S. Chang, R. de Borst, and C. Esveld, "Surface waves in a stratified half space with enhanced continuum properties. part 2: Analysis of the wave characteristics in regard to high-speed railway tracks," *European Journal of Mechanics-A/Solids*, vol. 18, no. 5, pp. 769–784, 1999.

[316] C. S. Chang and J. Gao, "Second-gradient constitutive theory for granular material with random packing structure," *International Journal of Solids and Structures*, vol. 32, no. 16, pp. 2279–2293, 1995.

[317] E. Cosserat, F. Cosserat, *et al.*, "Théorie des corps déformables," 1909.

[318] A. Merkel and S. Luding, "Enhanced micropolar model for wave propagation in ordered granular materials," *International Journal of Solids and structures*, vol. 106, pp. 91–105, 2017.

[319] V. Aleshin, V. Gusev, and V. Tournat, "Acoustic modes propagating along the free surface of granular media," *The Journal of the Acoustical Society of America*, vol. 121, no. 5, pp. 2600–2611, 2007.

[320] H. Pichard, A. Duclos, J.-P. Groby, V. Tournat, L. Zheng, and V. Gusev, "Surface waves in granular phononic crystals," *Physical Review E*, vol. 93, no. 2, p. 023008, 2016.